ABSTRACT

Title of Dissertation:	COMPACT ABSORBER FOR ADVANCED ABSORPTION HEAT PUMPS
	Stefan Bangerth, Doctor of Philosophy, 2018
Dissertation directed by:	Professor Michael Ohadi, Department of Mechanical Engineering

Almost half of all energy contained in primary energy carriers is discarded as low temperature waste heat. One of few application areas for low temperature waste heat recovery is to drive absorption cooling systems for conversion of waste heat to cooling energy. However, absorption chillers are often not economical due to their bulky, and hence expensive, heat and mass exchangers; the absorber heat/mass exchanger being the largest among them.

This dissertation introduces original contributions to advance next generation, more economical absorption chillers by utilizing a novel, highly compact absorber. The novel absorber designed in this work enhances absorption performance by combining rotation of the heat transfer surface for solution-side heat and mass transfer enhancement with innovative high-performance heat transfer technology on the water-

side. A numerical model was developed to describe the absorption process and promote design optimization. The replacement of gravitation force by the stronger centrifugal acceleration thins and mixes the solution film and thereby decreases solution-side thermal and mass transfer resistance. The development of an original adaptation of manifold-microchannel technology leads to significant water-side heat transfer enhancement. This dissertation includes the first publication of an experimental characterization of exothermic absorption on a spinning disk. The overall and film-side heat transfer coefficients were 4.7 and 5.5 times higher, respectively, than conventional horizontal tube banks. The absorption rate increased by a factor of 4 to 10 folds over those of the conventional tube absorbers. The power required for spinning the disk was modest and ranged between 1.1% and 2.3% of the cooling capacity. The results suggest that a spinning disk absorber could substantially reduce the size of absorber in the absorption machines.

The technology developed in this dissertation can lead to more compact and hence more economical absorption chillers, thereby easing higher market penetration of absorption chillers which in turn can reduce the amount of primary energy spent on cooling applications. Spinning disk absorbers may be especially useful if combined with a new generation of absorbents that promise improved system efficiency and/or expanded application range but exhibit challenging thermophysical properties.

COMPACT ABSORBER FOR ADVANCED ABSORPTION HEAT PUMPS

by

Stefan Bangerth

Dissertation submitted to the Faculty of the Graduate School of the
University of Maryland, College Park, in partial fulfillment
of the requirements for the degree of
Doctor of Philosophy
2018

Advisory Committee:
Professor Michael Ohadi, Chair
Professor Bao Yang
Professor Yunho Hwang
Professor Siddhartha Das
Professor Keith E. Herold, Dean's Representative

Dedication

To Hanan, who always encouraged and believed in me.

Acknowledgements

The research presented in this dissertation was funded by the Advanced Research Project Agency Energy (ARPA-E) of the U.S. Department of Energy under award DE-AR0000585 as part of Advanced Research in Dry Cooling (ARID) program. The views and opinions expressed in this work do not necessarily state or reflect those of the United States Government or any agency thereof.

First, I would like to acknowledge the contributions of late Dr. Serguei Dessiatoun and express my deep gratitude for his encouragement and guidance in technical matters.

I am sincerely grateful to my advisor Dr. Michael Ohadi for his continued guidance, trust and support. Dr. Ohadi did not only shape my research capabilities but encouraged me to tap my full potential by taking on a variety of projects and leadership roles.

I am also grateful for constructive discussions with friends, colleagues, supervisors and alumnae of the S2TS Laboratory. In particular, I wish to thank Dr. Ratnesh Tiwari for his help and advice during critical phases of the project. Dr. Amir Shooshtari's leadership of the task group over the course of the project is gratefully acknowledged.

Dr. Keith Herold is gratefully acknowledged for providing water/lithium bromide property correlations in Visual Basic, which sped up the programming of respective MATLAB functions substantially. Finally, I would like to thank the Principal Investigator Dr. Bao Yang for his leadership of the overall project. I would also like to thank the members of the dissertation committee, Professors Bao Yang, Yunho Hwang, Siddhartha Das and Keith E. Herold for their contributions and advice.

Table of Contents

List of Tables

List of Figures

Nomenclature

A	Surface area [m^2]
Abs	Absorber
c_p	Specific heat capacity at constant pressure [J/(kg·K)]
C	Mass concentration [kg/kg]
C_S	Mass concentration at free surface [kg/m^3]
C_{in}	Mass concentration at inlet [kg/m^3]
$\tilde{C}$	Molar concentration [mol/m^3]
CHP	Combined heat and power
CCHP	Combined cooling heat and power
COP	Coefficient of Performance [-]
D	Diffusivity [m^2/s]
E	Enhancement [-]
$Ek_{r_{in}}$	Ekman number based on inlet radius [-], $(\nu/(\omega r_{in}^2))$
Ek_{r_o}	Ekman number based on outer radius [-], $(\nu/(\omega r_o^2))$
Ek_δ	Ekman number based on film thickness [-], $(\nu/(\omega\delta^2))$
F	Fourier number for heat transfer [-], $(\alpha t/\delta^2)$
F_m	Fourier number for mass transfer [-], (Dt/δ^3)
f	Rotational speed [rpm]
h	Enthalpy per unit mass of refrigerant [kJ/kg]
h	Convective heat transfer coefficient [$W/(m^2\cdot K)$]
$\bar{h}$	Average convective heat transfer coefficient [$W/(m^2\cdot K)$]
h_c	Collar height [m]
h_{mix}	Enthalpy of mixing per unit mass of refrigerant [kJ/kg]
h_{fg}	Enthalpy of vaporization per unit mass of refrigerant [kJ/kg]
h_m	Mass transfer coefficient [m/s]
H	Height [mm]
I	Current [A]
k	Thermal conductivity [W/(m·K)]
L	Length [mm]
LMTD	Log mean temperature difference [K]
M	Molar mass [g/mol]
$\dot{m}$	Mass flow rate [g/s]
MTC	Mass transfer coefficient [s/m or h/m]
N”	Mass flux [$kg/(m^2s)$]
$\bar{N}$”	Average mass flux [$kg/(m^2s)$]
Nu_r	Local Nusselt number [-], (hr/k)
$\overline{Nu}$	Average Nusselt number [-], $(\bar{h}r_o/k)$
K_1, K_2	Empirical correction factors in Pigford model []
P	Pressure [Pa]
Pe_c	Peclet number [-], $(u_c r_c/\alpha)$
Q	Volumetric flow rate [m^3/s]

q'' Heat flux [W/m^2]
$\dot{Q}$ Heat transfer rate [W]
Q_{cr} Critical volumetric flow rate [m^3/s]
r Radial coordinate [m]
r_c Collar radius [m]
r_{in} Inlet radius [m]
r_o Outer radius of disk
$\tilde{r}$ Normalized radial coordinate, (r/r_c)
R Radius [m]
RTD Resistance temperature detector
Re_x Reynolds number evaluated at particular point x along a surface [-], (xu_∞/ν)
$Re_{r,Q}$ Reynolds number based on local radius and volumetric flow rate [-], $(Q/(2\pi r\nu))$
$Re_{r_o,Q}$ Reynolds number based on disk radius and volumetric flow rate [-], $(Q/(2\pi r_o\nu))$

Re_{ru_c} Reynolds number based on local radius and radial velocity at collar exit [-], $(u_c r/\nu)$
$Re_{r_c u_c}$ Reynolds number based on collar radius and velocity [-], $(u_c r_c/\nu)$
$Re_{\delta,in}$ Reynolds number based on inlet velocity and film thickness [-], $(u_{in}\delta/\nu)$
Re_ω Rotational Reynolds number [-], $(\omega r^2/\nu)$
$Re_{\omega_{r_o}}$ Rotational Reynolds number based on outer radius [-], $(\omega r_o^2/\nu)$
Ro_c Rossby number based on outer collar radius [-], $(u_c^2/\omega^2 r_c^2)$
Ro_{ro} Rossby number based outer disk radius [-], $(u_c^2/\omega^2 r_o^2)$
RTD Residence time distribution
Sc Schmidt number [-], (ν/D)
SDA Spinning disk absorber
SDR Spinning disk reactor

Sh_{ff} Sherwood number used in falling film literature [-], $(h_m(\nu^2/g)^{\frac{1}{3}}/D)$
Sh_{r_o} Sherwood number based on outer disk radius [-], $(h_m r_o/D)$
$\overline{Sh}_{r_o}$ Average Sherwood number based on outer disk radius [-], $(\bar{h}_m r_o/D)$
$\overline{Sh}_{\delta_c}$ Average Sherwood number based on characteristic film thickness [-]
t_e Exposure time [s]
t_{ave} Average residence time [s]
TP Temperature profile
T Temperature [K]
TC Thermocouple
T_{ave} Average temperature [K]
T_w Temperature of wall [K]
T_s, T_{int} Temperature of free surface / interface [K]
T_{sat} Saturation temperature [K]

U	Overall heat transfer coefficient [$W/(m^2K)$]
u	Radial velocity [m/s]
$\bar{u}$	Average radial velocity [m/s]
u_∞	Free stream velocity [m/s]
u_c	Radial velocity at collar exit [m/s]
u_{in}	Radial velocity at inlet [m/s]
u_s	Surface velocity (maximum velocity) [m/s]
v	Tangential velocity [m/s]
V	Voltage [V]
w_p	Pump work per unit mass of refrigerant [W/kg]
W	Width [mm]
x	Distance from start of vertical surface [m]
x	Mass fraction of lithium bromide
z	Coordinate in axial direction, zero at surface [m]

Greek

α	Thermal diffusivity [m^2/s], $(k/(\rho c_p))$
α	Correlation coefficient in Eq. 3-20
β	Correlation coefficient in Eq. 3-20
δ	Film thickness [m]
$\bar{\delta}$	Average film thickness
$\tilde{\delta}$	Normalized film thickness [-], (δ/h_c)
δ_c	Concentration boundary layer thickness [m]
δ_t	Thermal boundary layer thickness [m]
Δ	Difference [-]
γ	Correlation coefficient in Eq. 3-20
ε	Correlation coefficient in Eq. 3-20
μ	Dynamic viscosity [Pa s]
ν	Kinematic viscosity [m^2/s]
ρ	Mass density [kg/m^3]
ϕ	Azimuth
σ	Surface tension [N/m]
ω	Angular velocity [rad/s], rotational speed [rpm]

Subscripts

abs	absorber
ave	average
ch	channel
cc	cooling capacity
cp	copper plate
c	core of the liquid film
cw	cooling water
chw	chilled water

cond	conduction, condenser
conv	convective
evap	evaporator
film	film-side
g	gaseous
gen	generator
htf	heat transfer fluid
int	internal
int	gas-liquid interface
l	liquid
LiBr	lithium bromide
lin	linear profile
lm	log mean
M	electrical motor
par	parabolic profile
rot	rotational
s	free surface of liquid flow
sol	solution of aqueous lithium bromide
tot	total
v	vapor
w	film-side surface of disk

Superscripts

Sat	At saturated (equilibrium) conditions

1. Introduction

1.1. Motivation and background

Far more than half of all energy contained in primary energy sources is rejected as waste. Few economical usage opportunities exist for waste heat because it is mostly available at low temperature. One of few application areas for low temperature waste heat is to drive absorption chillers. Since cooling applications are a significant contributor to energy consumption, the replacement of electricity-based provision of cooling by absorption cooling can make a real impact to reduce energy consumption.

Worldwide, 72% of primary energy consumption is lost as waste heat, and 63% of these losses occur at temperatures below 100ºC [1]. In 2017, the United States consumed a total of 97.7 quadrillion BTU (28.6 million GWh) of primary energy, 68.3% of which were rejected as waste heat [2]. The U.S. Energy Information Administration (EIA) reports that the residential and commercial sectors accounted for 21% and 18% of U.S. primary energy consumption, respectively [3]. Cooling applications within the residential and commercial sector caused 6.6% of total primary energy consumption distributed over space cooling (4.2%), refrigeration (2.2%) and freezers (0.2%) [3]. To put this into perspective, Mexico had a primary energy consumption of 7.45 quads in 2014, only 16% more than the energy used for cooling applications alone in the U.S. [4]. On a global scale, the International Energy Agency (IEA) predicts global energy use for space cooling to triple by 2050. Space cooling is predicted to increase its share of total energy consumption in buildings from 6% to 14%

[5] (Figure 1-1). 21% of the overall growth in world total final electricity consumption between 2016 and 2050 is expected to be caused by space cooling.

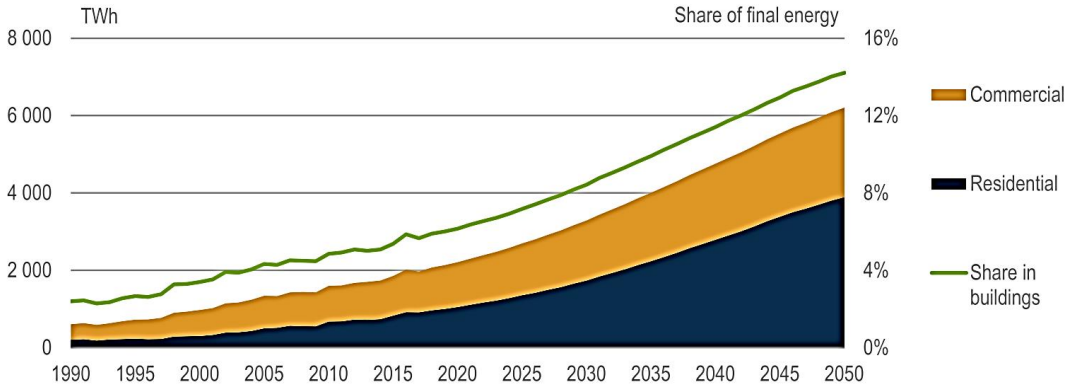

Figure 1-1: World energy use for space cooling and its share in energy consumption of buildings, IEA [5].

All cooling applications involve the transfer of heat from a lower temperature reservoir to a higher temperature reservoir, which requires either the input of work, as in a vapor-compression heat pump cycle, or of heat, as in an absorption heat pump. Both approaches have been widely commercialized and the choice of a certain application depends mainly on economic factors. As of today, these economic factors often favor vapor compression refrigeration systems over absorption systems. However, the need to improve energy efficiency, to reduce carbon dioxide production and prevent the release of refrigerants with high global warming potential has re-emphasized the opportunities offered by absorption heat pumps. A naïve back of the envelope calculation may look as follows: 6.5 Quads of primary energy are used for cooling and two thirds of this primary energy are rejected as waste heat. The coefficient of performance of vapor compression cycle systems easily reaches three, such that it

can be approximated that actually 6.5 Quads of energy are moved from a cold reservoir to a hot reservoir. Still, the total amount of rejected energy in the U.S. economy is roughly a factor of ten higher, raising the question what stands in the way of using this free waste energy to provide all of the country's cooling needs.

There most obvious impediments are the local and temporal discrepancy of waste heat production and cooling needs as well as the quality of waste heat. Absorption chillers require hot water at a minimum temperature of 93 ºC [6], thus only a fraction of low temperature waste heat is recoverable for absorption cooling. Additionally, most waste heat is produced in large central power plants and the transportation sector, while cooling demand is located in individual buildings distributed all over the country. Interestingly, this may change in the near future. According to the EIA's reference scenario, more than 50GW of coal generating capacity will retire between 2015 and 2020 [3]. Between 2015 and 2030, more than 100 GW of natural gas generating capacity will be built. This offers the opportunity to advance a more distributed energy generation system. The U.S. Department of Energy estimates a potential capacity for Combined Heat and Power (CHP) across the industrial and commercial sectors of 241 GW [7]. While existing CHP plants are concentrated at industrial sites, a significant part of the potential is located at commercial facilities. Commercial facilities often have significant space cooling demands and thus would be ideal candidates for Combined Cooling Heating and Power (CCHP), i.e. trigeneration systems.

The deployment of absorption heat pumps is especially attractive if low or medium temperature heat is available at low cost as by- or waste product from other processes.

The demands on working pairs for absorption refrigeration are quite restrictive such that only water/lithium bromide and ammonia/water have gained commercial relevance. In water/lithium bromide systems, water is the refrigerant and aqueous lithium bromide is the absorbent. Advantages of this configuration are high latent heat of the refrigerant and non-volatility of the absorbent. These properties result in a potential for high coefficients of performance and easy separation of refrigerant and absorbent at the outlet of the generator. Although the mixture is highly corrosive, it exhibits low toxicity. However, the minimum temperature that cooling can be provided at is restricted by the freezing point of water. Since this restriction is not relevant for space cooling applications, water/lithium bromide machines are the most widely used heat-activated cooling technology. Water/lithium bromide absorption machines are typically water-cooled which makes them attractive only for larger systems such as large commercial and residential buildings that justify the cost and space requirement of a cooling tower.

The requirement to provide water-cooling is the main disadvantage of the working pair water/lithium bromide. It is caused by the risk of precipitation of salt molecules and subsequent equipment shutdown that result in demands on heat rejection temperature. Lithium bromide crystallizes when its concentration surpasses the solubility limit. The solubility limit is strongly dependent on salt concentration and solution temperature. Generally, higher concentration and lower temperatures lead towards the solubility maximum. If the temperature of the heat sink and approach temperature between heat sink and solution are sufficiently low, the system operates at lower solution concentrations and the risk of crystallization events diminishes.

However, cooling capacity decreases if the heat sink temperature increases. Thus, the machine is pushed to operate at higher concentration to make up for lost capacity. Commonly, this problem is solved by using a cooling tower that guarantees low heat rejection temperatures. Another way to confront the issue to reduce the approach temperature between absorbent solution and cooling medium by using high-performance heat exchangers that provide larger conductance at lower heat exchanger surface area. Given a certain heat sink temperature, a lower approach temperature leads to lower absorbent solution temperature and thus has the same effect as reduced heat sink temperature itself.

Alternatively, high performance heat exchangers can be used to reduce the size of absorption refrigeration systems. Given an overall conductance design target, the higher overall heat transfer coefficient of high performance heat/mass exchangers can be used to reduce heat/mass exchanger surface area. A single stage system requires four heat exchangers with gas-liquid mass transfer that serve as generator, condenser, evaporator and absorber. Conventionally, these heat/mass exchangers are designed as falling film over horizontal tube bundle expect the generator, which is usually built as flooded type [8]. The refrigerant and especially the solution films are relatively thick and thus add considerably to the overall resistance of the heat/mass exchanger. The high resistance requires bulky and hence expensive heat exchangers that render the absorption system as a whole uneconomical. It is commonly accepted that the absorber is the most critical heat exchanger with respect to overall system size [9,10].

1.2. Research concept

The objective of the research outlined in this dissertation is to develop a compact absorber for advanced absorption cooling systems that enhances heat and mass transfer processes. For technology demonstration, a 3kW unit is designed, fabricated, experimentally tested and optimized. The project is related to a future microemulsion-absorbent heat pump system. However, since the microemulsion absorbent is not yet available for substantial testing, the research is carried out with the conventional working pair water/lithium bromide. It is expected that improvement of heat/mass exchangers used with water/lithium bromide will translate into larger enhancement for microemulsion-based systems due to latter's higher mass diffusivity and viscosity and lower thermal conductivity. Experimental testing with conventional fluids further enables direct performance comparison to standard absorber design since data for water/lithium bromide systems is available in the literature.

A spinning disk reactor serves as absorber. Spinning disk reactors are well established as mass transfer devices that facilitate process intensification [11–15]. Spinning disk reactors generate thin liquid films that enhance heat transfer, surface waves that increase mass transfer through intense mixing of the liquid film. Previous research on the use of centrifugal force in absorption heat pumps has proven the potential of this technology [16–19]. However, the effort was an advanced commercial venture and thus performance data and accurate characteristics of heat and mass transfer enhancements were not published.

The spinning disk absorber is operated in a vacuum environment and thus sealing and structural integrity are important parameters in the design process. The disk surface

is cooled by circulating cooling water underneath the surface. It is important to mitigate heat exchange between the entering and exiting cooling water, which both flow through the drive shaft. Corrosion resistance has to be taken into account as water/lithium bromide is very corrosive and even more so in an environment of experimental testing design that may require repeated opening of the system which inevitably introduces oxygen, the cornerstone of metal corrosion.

Once the enhancement of solution-side (i.e. film-side) heat/mass transfer processes is established by centrifugal acceleration, water-side (i.e. internal) heat transfer improvements are progressed. In conventional absorbers, the dominance of film-side resistance results in low effect of water-side improvements [20]. However, process intensification of the solution-side processes can lead to water-side improvements becoming significantly more relevant. Cooling water heat transfer is strongly enhanced by using a novel adaption of high performance manifold microchannel technology. Manifold microchannel heat exchangers are commonly manufactured in rectangular shape and have been shown to achieve equal or better heat transfer performance than conventional microchannels while reducing the pressure drop penalty considerably [21,22].

1.3. Research objectives

The main research objectives of this dissertation are as follows:

- To conduct an experimental investigation of a spinning disk reactor used as absorber in an absorption chiller system by designing and fabricating said absorber and testing it in an absorber/generator test loop. To study the effect of rotational

speed and other operating parameters on film-side and overall heat transfer coefficient as proxy for combined heat and mass transfer processes. To compare performance of spinning disk absorber to commercial absorber and other experimental absorber types as reported in the literature. Assess the trade-off between power consumption and absorber performance.

- To study the potential to further improve aforementioned spinning disk absorber by incorporating and advancing latest type of heat transfer enhancement on the water-side. To study effect of internal enhancement on overall component performance and characterize the absorber performance compare the same with conventional and experimental absorber types. Achieve at least 100% increase in absorption performance compared to conventional falling film on horizontal tubes using water/lithium bromide without surfactants.
- To develop a computer program that mathematically describes exothermic absorption on spinning disk reactor with internal cooling. The goal of the computer model is to project absorber performance based on transport coefficients for heat and mass available in the literature. To compare the design model to experimental data.
- To test aforementioned absorber in full loop absorption chiller system and comparison of system performance when operated with conventional horizontal tube and with spinning disk absorber.
- To develop preliminary scale-up design to commercial scale heat pump system.

1.4. Organization of dissertation

The present chapter 1 discusses reasons for this study and research objectives. A review of the literature on enhancement in conventional water/lithium bromide absorption, spinning disk reactors and the previous development of an absorption heat pump is provided in chapter 2. Spinning disk reactors are discussed with respect to hydrodynamics, mass transfer and sensible/latent heat transfer characteristics. The previous development of a rotary absorption heat pump is debated to the extent that descriptions are available in the open literature. Chapter 0 describes the development experimental testing of a spinning disk reactor used as absorber in an absorber/generator test system. First, the design of the device, which was developed and fabricated by the author, is presented. The chapter further discusses the experimental loop and gives details on data analysis and uncertainty propagation. Next, experimental test results are presented and discussed. Chapter 4 reports the experimental study of an enhanced spinning disk absorber which was developed based on conclusions drawn in the previous chapter. The approach for water-side enhancement is discussed and details of the technical implementation are given. Experimental test results are presented and compared to wide range of literature data. Chapter 5 discusses a theoretical model that was programed to provide insight into the heat and mass transfer performance of the spinning disk absorber. Modelling results are compared to experimental data and a correlation for non-dimensional gas-liquid mass transfer on spinning disks is developed. Results from testing the spinning disk absorber in a full absorption chiller system are given in chapter 6. Chapter 7 presents

conclusions drawn from the research reported in this dissertation0. Recommendation for future work in the area of spinning disk absorbers are discussed in chapter 8.

2. Literature survey

This chapter reviews the literature related to the topic of the dissertation. It provides analysis of the state of research including background, major ideas and current research directions. First, requirements on the absorber in water/lithium bromide absorption heat pumps are discussed. Then, conventional and novel absorber designs are investigated. The final two subchapters are dedicated to the discussion of spinning disk reactors and general and a past effort to develop a rotary heat pump.

2.1. Background: Requirements on absorbers in water/lithium bromide absorption heat pumps

The research reported in this dissertation is carried out with the working pair water and aqueous solution of lithium bromide, shortly referred to as water/lithium bromide or water/lithium bromide, which serve as refrigerant and absorbent, respectively. The literature analyzed in this chapter therefore focuses on water/lithium bromide heat pumps systems in general and on absorbers in water/lithium bromide absorption chillers in particular. For a broader discussion of absorption heat pumps, including water/lithium bromide systems, the reader is referred to the comprehensive treatment of the topic provided in [23].

Absorption cooling cycles operate at a minimum of two pressure levels. At the lower pressure level, the design of both evaporator and absorber has to be thoroughly

adapted to the properties of water at a pressure between 0.75 kPa and 1.5 kPa. At a pressure of 0.85 kPa – equivalent to an evaporation temperature of 4.6 °C – a volumetric flow rate of 182 L/s is required to provide 3 kW of cooling. Thus, it is important to minimize pressure drop in evaporator, absorber and related piping in order to achieve a low chilled water temperature. Ultimately, the target of absorption heat pumps is to provide low temperature cooling in the evaporator and any pressure drop that increases saturation temperature of water on the evaporation coils is directly compromising this target. As a result, absorber and evaporator are usually integrated in the same vessel to keep vapor velocities and viscous losses low. Likewise, pressure drop in the absorber is to be kept at a minimum and design alternatives have to comply with this requirement.

The ability to efficiently reject heat of absorption is the other important design constraint. Capacity and COP suffer from higher heat rejection temperature and thus the temperature approach between heat sink and absorber has to be minimized. This can be achieved through high overall transfer coefficients or large heat/mass transfer surface area. Since heat and mass transfer coefficients in the absorber are lowest among all heat/mass exchangers in the system, absorbers are the largest components within the chiller [24]. Therefore, “the performance of the absorber is the key to the overall system size, performance and cost” [9].

The performance of the absorber depends on its effectiveness in augmenting both heat and mass transfer processes. It has been stated that the rate of absorption is controlled by the slow diffusion of water molecules from the interface into the solution [25]. Thus, induction of mixing of the liquid is one approach to enhance absorption

[23]. On the other hand, Yu et al. [26] showed the importance of thermal resistance of the solution film and hence heat transfer performance for overall performance. In their numerical study, the absorption rate almost tripled when film thickness was reduced by 75%. In real systems, the coupling between heat and mass transfer processes is very strong and therefore it is not possible to define a transfer coefficient for one process that is not influenced by the other process [1]. The processes of mass and heat transfer are coupled through the dependence of equilibrium mass concentration on solution temperature and through the heat of absorption that is caused by the phase change of water and the dilution of the solution. An equilibrium between the vapor pressure of water in the gas phase and the vapor pressure of water in the solution is assumed at the interface (Eq.2-1) [27]).

$$p_{H_2O,(g)} = p_{sol_{int}}(x_{int}, T_{int}) \qquad 2\text{-}1$$

Literature on LiBr absorbers usually gives solution concentration as weight percent of LiBr. However, details of the absorption process are more readily discussed in terms of (molar) concentration of water. With respect to Eq. 2-1), higher vapor pressure in the gas phase leads to lower mass concentration of lithium bromide or higher concentration of water at the interface. Higher water concentration at the interface provides a larger driving force for mass transfer, as Eq. 2-2) shows.

$$\dot{N}_{H_2O} = h_m\left(\tilde{C}_{H_2O,int} - \tilde{C}_{H_2O,c}\right) \qquad 2\text{-}2$$

The coupling between heat and mass transfer and the dependency on concentration and vapor pressure can be explained by analyzing Eq. 2-2). The mass transfer driving force depends both on pressure, through its influence on water concentration at the interface, and on core solution concentration. Interfacial concentration also depends on

interfacial temperature. Thus, sustaining mass transfer requires continuous heat removal from the interface and better cooling will increase the driving force for mass transfer. Naturally, effective heat and mass transfer requires continuous contact between solution and cold wall, which can be challenging to achieve.

Surface wetting can be a problem due to high surface tension – 55%-wt. lithium bromide solution has a surface tension of 0.092 N/m [28]. Nomura et al. [29] measured the wet surface area in a horizontal tube absorber and reported that lower tubes exhibited worse wetting than upper tubes and the ratio of wetted surface area was as low as 0.5. Jeong and Garimella [30] developed an analytical model of heat and mass transfer in horizontal tube water/lithium bromide absorber based on the experimental data by Nomura et al.. Their model best matches experimental data if wetting ratios between 0.6 and 0.8 are assumed. Sasaki et al. [31] also reported wetting issues of the heat/mass transfer surface area. In commercial absorbers, wetting of the tubes is often improved by increasing solution flow rates through recirculation of part of the diluted solution [32].

2.2. Conventional absorbers and their enhancement

Typical heat/mass exchangers in commercial water/lithium bromide absorption machines are of horizontal tube-type arranged in shell and tube fashion (Figure 2-1).

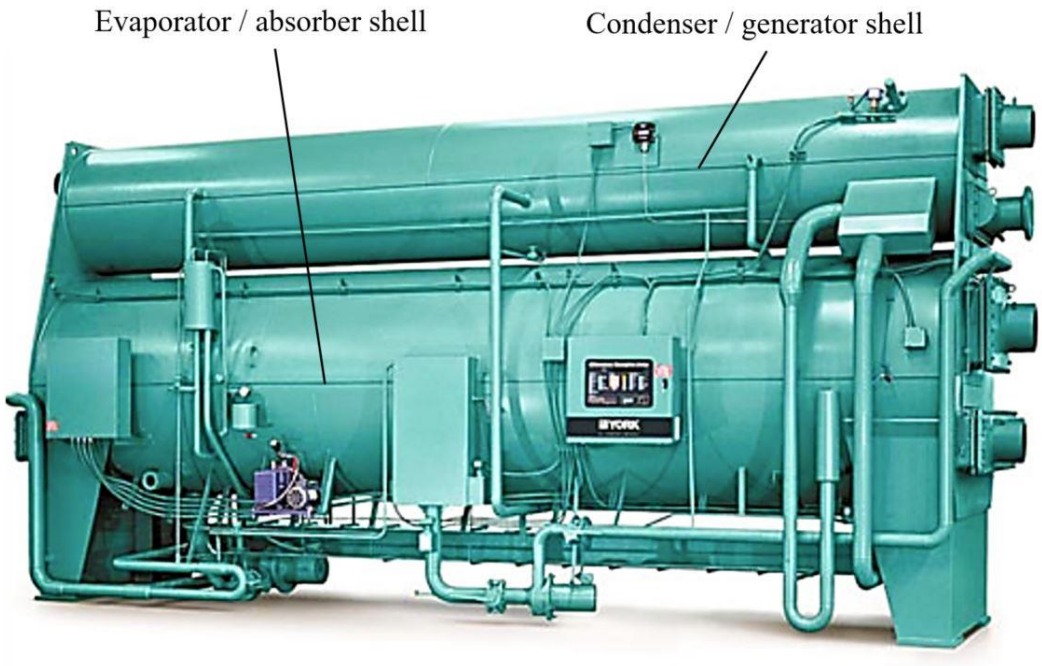

Figure 2-1: Commercial single-stage LiBr-water absorption chiller (adapted from [30]).

According to a manufacturer's data sheet [33], the shell volume of evaporator/absorber is more than three times larger than the shell volume generator/condenser. On the tube side, the volume of the absorber is 30% larger than that of the evaporator and about three times larger than that of generator and condenser. Commercial absorber designs reported in the literature contain hundreds of copper tubes that are each one to few meters long and have a diameter of 19 mm [25,32,34]. The tubes are packed into a tight bundle but a minimum spacing is required to limit the pressure drop of the water vapor as it flows through the bundle. Absorbent solution is sprayed onto the uppermost tube from where it drops onto lower tubes while cooling water inside the tubes flows from bottom to top through the tube bundle. This arrangement is called counter-current due to the counter-current configuration of flow

over an array of tubes. However, the configuration is cross-flow per individual tube. For coil-type absorbers, counter-current arrangement has been estimated to improve absorber performance by 3% to 19% over parallel-flow arrangement [35].

In line with their commercial importance, horizontal tube bundles have been extensively studied. Much of the research was conducted in the 1990's with the goal of better understanding and describing important parameters of the absorption process itself, finding enhancements and developing design correlations [10,20,36–39]. Although commercially less relevant, vertical tube designs can also be grouped into the conventional design concepts. Similar to horizontal tube absorbers, they received plenty attention in the 1990's in relation to better understanding and improvement of heat and mass transfer processes [10,40–42]. In particular, vertical tubes were taken into consideration for air-cooling of absorbers according to a discussion of the Japanese literature by Fujita [25].

The tubes in tube-type absorbers can be modified physically both on the inside and the outside, leading to internal (i.e. water-side) or film-side (i.e. solution-side) enhancement. The main heat transfer resistance is caused on the solution side and the overall effect of water-side enhancement is generally small [20]. Therefore, external enhancement has been studied more extensively. Still, researchers also try to minimize water-side resistance either with physical enhancements or through the use of high cooling water flow rates [9]. Enhanced tube surfaces can have several effects: Obviously, the surface structure increases the effective heat transfer surface area and thus enhances heat transfer. Other important effects are improved wetting behavior through the surface structure [31] and induction of mixing in the film flow [32].

Different surface structures such as pin-fins and a variety of continuous fin arrangements have been investigated.

However, comparison of results achieved with dissimilar operating conditions and sometimes analyzed with differing methods is not always straight forward. Therefore, an effort was made to compile comparable data for absorption rate (Figure 2-2), absorber heat flux (Figure 2-3) and overall heat transfer coefficient (Table 2-3). The results displayed in these overviews was standardized in the following manner: If researchers reported results for a variety of operating conditions, the outcomes closest nominal values for concentration and cooling water inlet temperature of 60 wt.-% and 30 °C, respectively, were chosen. If available, results obtained with saturated solution inlet conditions were selected. Often, researcher study the effect of solution flow rate. In that case, the highest value of the variable of interest at any solution flow rate was chosen. The same procedure was followed if results for different types of enhanced tube were given. Finally, the operating pressure has a large effect on the amount of water vapor that is absorbed. Therefore, the parameters absorber heat flux and absorption rate were plotted versus absorber pressure.

Figure 2-2 and Figure 2-3 show absorption rate and absorber heat flux, respectively. Details on the specifications of the absorbers plotted in these Figures are given in Table 2-1 and Table 2-2. As expected, the performance of individual absorbers increases with pressure through its influence on the mass transfer driving force. However, performance measures at any given pressure spread significantly depending on the test sections. Focusing on results achieved under pressure of less than 1.5 kPa in Figure 2-2 shows that different enhancement methods can yield good results. The highest

absorption rates in this area are reported with tubes with fins, pin-fins, micro-hatched structure and small diameter tubing. With the same experimental setup, Atchley [32] achieved 76% increase in absorption rate with tubes that have internal and external enhancement over smooth tubes. The absorber heat fluxes reported in the literature range in between 5 and 16 kW/m^2 (Figure 2-3). Again, the highest value was achieved with the internally and externally enhanced tubes by Atchley at [32]. However, Kyung and Herold also achieved good results with smooth tubes [43]. The outcome of various studies with respect to overall heat transfer coefficient is given in Table 2-3. Care must be taken in comparing the values for overall heat transfer coefficients because different researchers defined the temperature difference used to calculate the coefficient differently. Unfortunately, most researchers did not list the pressure the experiments were conducted at. The pressure is known for the study by Kyung and Herold who attained a U-value of 768 $W/(m^2 \cdot K)$.

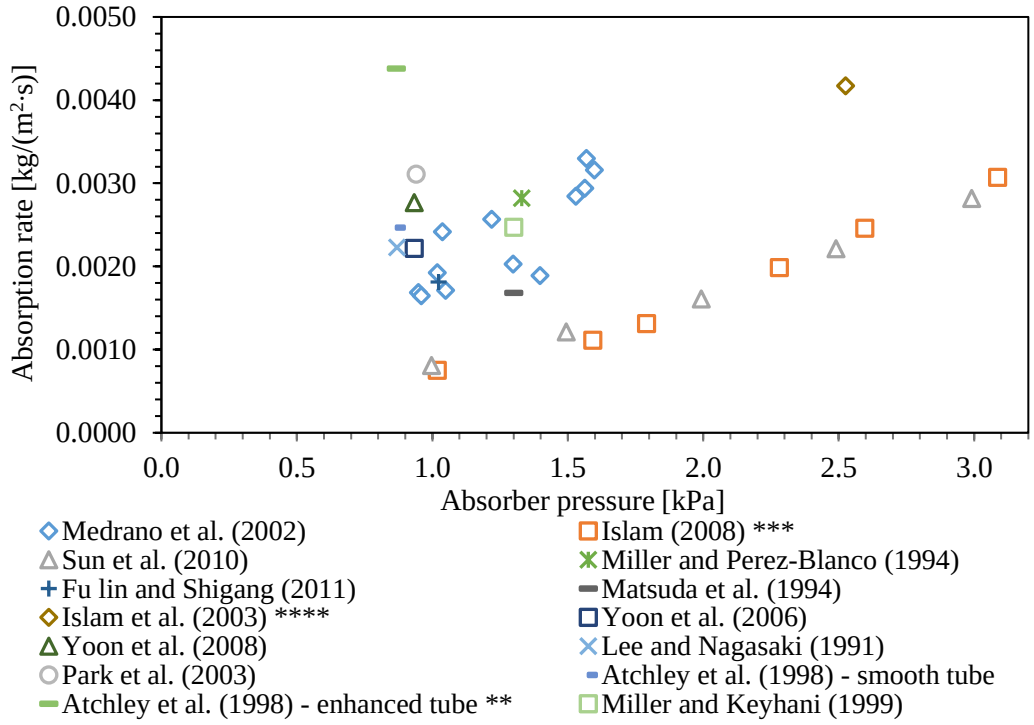

Figure 2-2: Absorption rates reported in the literature for tube-type absorbers.

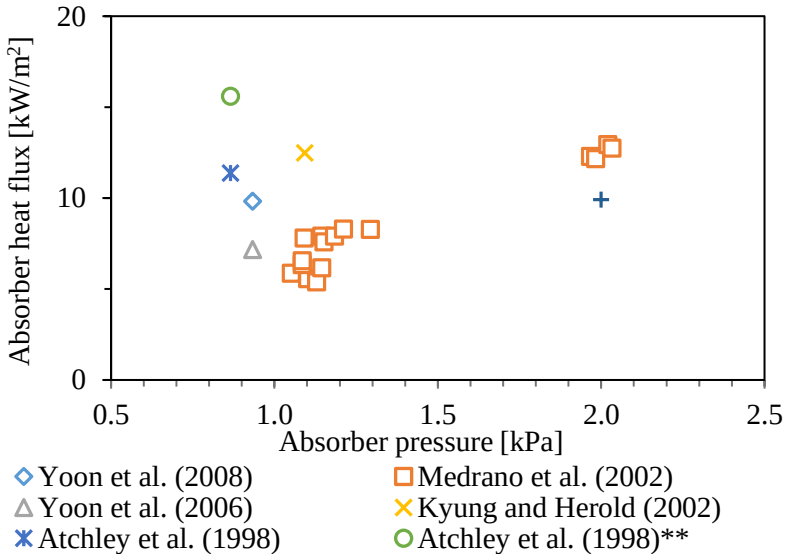

Figure 2-3: Absorber heat fluxes reported in the literature.

Table 2-1: Geometric specifications and operating conditions of studies plotted in Figure 2-2.

Authors	X_{in} [wt.-% LiBr]	$T_{Sol,in}$ [°C] (Condition)	$T_{CW,in}$ [°C]	$\dot{m}_{CW}$ [kg/s]	Abs. type *	Enhancement
Medrano et al. (2002) [44]	60	40 (Sub)	30	N.R.	VT	CW-side (external): Fins
Islam (2008) [45] ***	60.4	39.8 (N.R.)	29.4	0.063	HT	N.R.
Sun et al. (2010) [46]	60-62	39.0 - 49.6 (N.R.)	26 - 35.3	N.R.	HT	N.R.
Miller and Perez-Blanco (1994) [42]	62	56.5 (Sat)	45.7	0.062	VT	Sol.-side: Pin fin
Fu and Shigang (2011) [47]	59.9	40 (Sub)	29.9	N.R.	VT	N.R.
Matsuda et al. (1994) [40]	55	40.7 (Sat)	30.7	N.R.	VT	N.R.
Islam et al. (2003) [48] ****	60.4	39.8 - 49.7 (Sub)	29.3	0.063 - 0.114	HT	Sol.-side: Guiding fins
Yoon et al. (2006) [49]	60	45 (Sat)	30	0.25	Hel. T	N.R.
Yoon et al. (2008) [50]	61	47 (Sat)	32	0.085	HT	Small tube diameter
Lee and Nagasaki (1991) [37]	60	44.2 (Sat)	30	N.R.	HT	Sol.-side: Ridged fins
Park et al. (2003) [51]	61	46 (Sub)	32	N.R.	HT	Sol.-side: Micro-scale hatched
Atchley et al. (1998) [32]	60	N.R (Sat)	29.5	N.R.	HT	None
Atchley et al. (1998) [32]**	62	N.R (Sat)	31.2	(Re_{CW} = 5700)	HT	Sol.-side: Finned, 40 fins per inch CW-side: 30 ridges per turn
Miller and Keyhani (1999) [52]	62	N.R. (N.R.)	35.0	N.R.	VT	N.R.

* HT: Horizontal tube; Hel. T: Helical tube; MB: Membrane; SD: Spinning disk; VP: Vertical plate; VT: Vertical tube

** Surface area of bare tube with outer diameter equivalent to diameter of base of the fins used as heat exchange area.

*** Operating conditions were given for comparison to theoretical model, not stated that valid for experimental part.

**** Only range for pressure given, average value of that range plotted here.

Table 2-2: Geometric specifications and operating conditions of studies plotted in Figure 2-3.

Authors	$Conc._{in}$ [wt.-% LiBr]	$T_{Sol,in}$ [°C] ***	$T_{CW,in}$ [°C]	m_{CW} [kg/s]	Abs. type*	Enhancement
Yoon et al. (2008) [50]	61	47 (Sat)	32	0.085	HT	Small diameter tube
Medrano et al. (2002) [44]	57.9	40 (Sub)	30	N.R.	VT	CW-side: Fins
Yoon et al. (2006) [49]	60	45 (Sat)	30	0.167	Hel. T	N.R.
Kyung and Herold (2002) [43]	60	N.R. (Sat)	30	0.125	HT	None
Atchley et al. (1998) [32]	62	N.R. (Sat)	29.4	Re_{CW} = 8268	HT	None
Atchley et al. (1998) [32]**	62	N.R. (Sat)	31.2	Re_{CW} = 5700	HT	Sol.-side: Finned, 40 FPI CW-side: 30 ridges per turn
Sasaki et al. (1995) [31]	58	40 (Sub)	28.0	N.R.	HT	None

* HT: Horizontal tube; Hel. T: Helical tube; VT: Vertical tube

** Surface area of bare tube with outer diameter equivalent to diameter of base of the fins used as heat exchange area.

*** Condition of solution: Sub = Subcooled, Sat = Saturated (within ± 1.5 °C of saturation temperature)

Table 2-3: Overview of studies that report overall heat transfer coefficient.

Authors	TD***	U-Value [W/(m^2·K)]	P [kPa]	Conc.$_{in}$ [wt.-% LiBr]	$T_{Sol,in}$ [°C] ****	$T_{CW,in}$ [°C]	$\dot{m}_{CW}$ [kg/s]	Abs. type *	Enhance-ment
Hoffmann et al. (1996) [20]	$LMTD_{sat}$	809	N.R.	56	N.R (Sub)	N.R.	N.R.	HT	Sol.-side: Knurled tube CW-side: Helical rod inserts
Beutler et al. (1996) [10]	$LMTD_{sat}$	445	N.R.	59	N.R (Sub)	30	0.045	HT	CW-side: Helical rod inserts
Kyung and Herold (2002) [43]	$LMTD_{sat}$	768	1.09	60	N.R. (Sat)	30	0.125	HT	None
Deng and Ma (1999) [53]	Other	1883	N.R.	63	52.5 (N.R.)	32	N.R.	HT	None
Greiter et al. (1993) [39]	$LMTD_{sat}$	1200	N.R.	N.R.	N.R. (N.R.)	N.R.	N.R.	HT	Sol.-side: Structured tube
Castro et al. (2007) [54]**	LMTD	376	1.02	57	N.R. (Sat)	35	N.R.	VT	CW-side (external): Fins
Sasaki et al. (1995) [31]	LMTD - other	746	2.0	58	40 (Sub)	28	N.R.	HT	None

* HT: Horizontal tube; SD: Spinning disk; VT: Vertical tube
** Direct air cooled
*** Temperature difference based on:
**** Condition of solution: Sub = Subcooled, Sat = Saturated (within ± 1.5 °C of saturation temperature)

The addition of surfactants, such as 2-ethyl-1-hexanol or octanol, constitutes a chemical mass transfer enhancement for water/lithium bromide absorbers. Hoffmann et al. [20] reported several effects of the addition of surfactants: Better wetting because of reduced surface tension, more frequent and smaller drops, and horizontal flow on the tubes. Cosenza and Vliet [36] observed that the addition of surfactants led to full wetting of tubes that had poor wetting behavior without surfactant. An early discussion of reported observations with regards to surface convection through surfactants is given by Fujita [25]. Fujita reported visual observations that describe the effect of surfactants as violent interfacial turbulence and he associated the enhancement with Marangoni convection. A theoretical foundation of the mechanism of enhancement by Marangoni convection has been developed with the vapor surfactant theory [55]. The vapor surfactant theory postulates that surfactants are transported via the refrigerant vapor flow. Where the surfactant adsorbs to the gas-liquid interface, it reduces surface tension. The gradient in surface tension causes a secondary flow, called Marangoni convection. The surface becomes unstable, exposing strong solution and thereby increasing absorption at that location. It has also been shown that the amplitude of enhancement through surfactants depends on the mass flux [43]. Since the surfactant is delivered through the bulk vapor flow, locally higher mass flux increases the surfactant concentration at the interface. The resulting larger surface tension gradient further enhances convection and mass transfer, a process that only comes to an end when the critical micelle concentration is reached and surface tension cannot be lowered further by higher concentration of the surfactant. Although the effect of the enhancement

through surfactants is substantial, researchers tend to disagree on the maximum enhancement: Atchley et al. [32], Cosenza and Vliet [36], Hoffmann et al. [20] and Sasaki et al. [31] (for plain tubes), measured enhancement factors of the film side heat transfer coefficient of up to 3, 3, 2.4 and 2, respectively. A more recent study gauges the heat transfer enhancement lower, at 20% to 70%, depending on the heat flux [43]. There are several possible reasons for the relatively large spread in enhancement factors. The study with the lowest enhancement reported a relatively high transfer coefficient without surfactant [43]. Thus, the lower enhancement may have been caused by good wetting behavior without surfactant and that further enhancement with surfactants was primarily through Marangoni convection, not improved wetting. Also, the outcome of the different studies may have been affected by differences in operating conditions. Still, in summary, it has been proven that the addition of surfactants strongly enhances absorption. However, accurate performance assessment of different absorber types and experimental studies is more difficult when studies with surfactant are included. The effect of the additive may overshadow the underlying performance of the absorber itself, rendering accurate comparisons more difficult. Moreover, the majority of experimental studies reports results without surfactants. For these reasons, all literature results reported in this document and all new experimental studies were undertaken without the additions of additives. However, it is suggested that future studies include the effect of surfactants on the performance of rotating absorbers.

The performance data reported in the literature for conventional absorbers (Figure 2-2 and Figure 2-3) without surfactants ranges within a relatively narrow band. This

shows that conventional enhancement methods will not lead to significantly performance improvements of absorbers and hence better economic viability of absorption chillers. Therefore, radically new designs of absorbers and absorption chillers are needed to find a path to alter the competitive position of absorption chillers.

2.3. Novel absorber designs

To improve absorbers beyond the performance of tube-type designs, recent studies have used flat plates/channels, sometimes in combination with membranes. The novel absorber designs plotted in Figure 2-4 and listed in Table 2-4 are all of vertical plate-type – this development bears resemblance of the successes with high performance plate heat exchangers in pure heat transfer applications. In the case of water/lithium bromide absorbers, the required access to low pressure vapor on the solution side requires novel approaches to plate-type designs. Membrane absorbers can lead to compact designs due to their high mass transfer area to volume ratio [56,57]. Researchers also used membranes to generate thin solution films [58,59]. Instead of relying on gravity to drive solution flow, membrane absorbers pump the solution through channels that are height-restricted by a water vapor-permeable membrane. The membrane hence allows film thickness to be controlled, and with it thermal resistance of the solution film. Other techniques to enhance flat plate absorbers, such as induction of film mixing and improved wetting behavior, are known from tube-type absorbers. To enhance film mixing, the surface structure can be modified to induce mixing of the solution film, which enhances absorption by renewing the surface with fresh solution

[59,60]. The surface can also be modified to lower the solution flow rate needed for good wetting behavior and thereby decrease thermal resistance [61,62]. The application of these methods has led to two to three times higher absorption rates than those for conventional tube bank absorbers. Besides these passive techniques, active methods have been considered for mass transfer enhancement. The mass transfer enhancement potential by active film mixing has been estimated to exceed a factor of 10 [63].

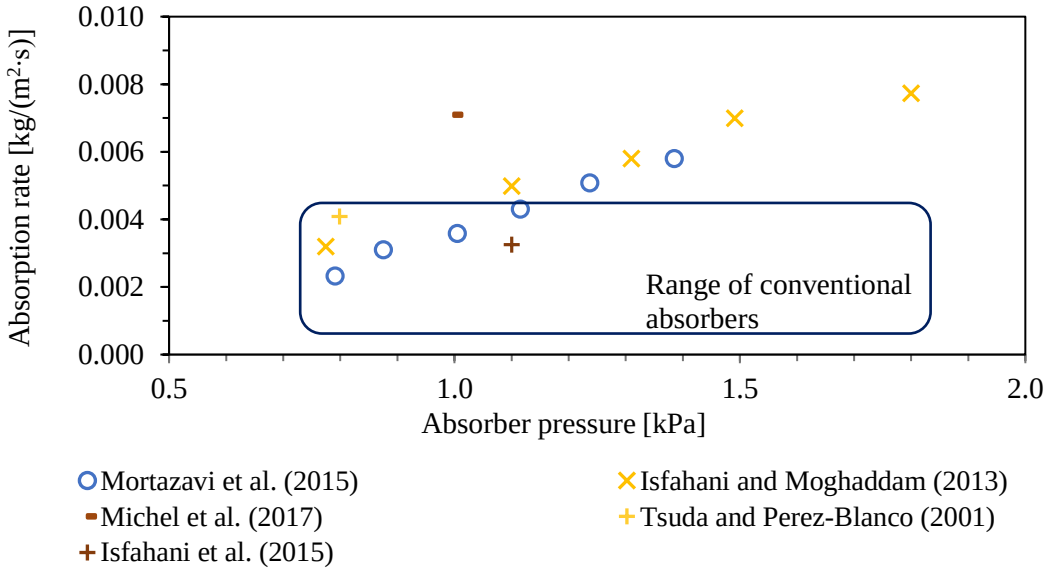

Figure 2-4: Absorption rates of novel absorber concepts.

Table 2-4: Operating conditions and description of absorbers plotted in Figure 2-4.

Authors	X_{in} [wt.-% LiBr]	$T_{Sol,in}$ [°C] (Condition)	$T_{CW,in}$ [°C]	$\dot{m}_{CW}$ [kg/s]	Abs. type*	Enhancement
Mortazavi et al. (2015) [62]	57	25 (Sub)	25	N.R.	VP	Sol.-side: Fins w. microscale surface treatment CW-side: Minichannels (0.4 mm high, 4 mm wide)
Isfahani and Moghaddam (2013) [58]	60	25 (Sub)	25	N.R.	MB, VP	Sol.-side: Microchannels (0.1 mm deep, 1 mm wide) CW-side: Minichannels (0.4 mm high, 4 mm wide)
Tsuda and Perez-Blanco (2001) [64]	62.0	47.99 (Sub)	32.0	N.R.	VP	Sol.-side: Vibrating screen
Isfahani et al. (2015) [59]	60	25 (Sub)	30.0	N.R.	MB, VP	Sol.- side: Microchannels with ridges (0.5 mm deep, 1 mm wide, 195 mm long) CW.-side: Minichannels (0.4 mm high, 4 mm wide)
Michel et al. (2017) [61]	60	30.55 (Sub)	29.9	0.014	VP	Sol.-side: Fins CW-side: Minichannels (2 mm x 4 mm)

* MB: Membrane; VP: Vertical plate;

Another novel absorber design are adiabatic spray absorbers. Adiabatic absorbers separate heat and mass transfer into two independent units. First, the absorbent solution is subcooled in a heat exchanger and then the subcooled solution is fed to an adiabatic absorber. The concept has the advantage that high-performance liquid-to-liquid heat exchangers can be utilized that are substantially smaller than the combined heat and mass exchangers employed in conventional absorbers. Further, mass transfer enhancement concepts not available to conventional absorbers can be employed. The concept was introduced by Ryan [65] in 1993. Ryan used a nozzle / atomizer to generate small droplets and hence a large interfacial area that increases mass transfer per unit volume. However, the heat of absorption quickly heats up the absorbent solution in absence of continuous heat removal. Hence, the solution has to be recirculated through

both heat and mass exchanger. Thus, the strong solution leaving the generator is diluted with leaner solution before the mixed solution is fed to the absorber. The design therefore does not take advantage to full potential for mass transfer driving force. Solution recirculation combined with the pressure drop of the spray nozzle also causes a significant amount of additional pumping power. Analytical models and further experimental results were reported by Warnakulasuriya and Worek [66]. More recently, flat and conical sheet absorbers have been proposed to reduce the amount of mechanical energy required in adiabatic absorbers [67–69].

2.4. Spinning disk reactor

One active process intensification method that achieves very thin films with good wetting behavior is the continuous rotation of the heat transfer surface. Rotation of disk-shaped surfaces can lead to liquid films less than 100 μm thick [70] that breakdown at flow rates up to an order of magnitude lower than theoretically predicted [14]. The first patent on the use of a spinning disk as reaction surface was filed by Ernst Buhtz in England in 1925 and in Germany in 1926 [71]. While prior work proposed to mix chemical substances by rotating small disks very fast and thereby creating a spray-like distribution and mixing process, Buhtz suggested to rotate larger disks rather slowly to accurately control chemical reactions. From a reaction kinetics point of view optimal ratios can be achieved by carefully selecting feed locations. Good mixing of the chemicals is achieved through the rotation of the disk. The speed of rotation

regulates film thickness. The disk surface temperature can be controlled by internal cooling or heating in order to regulate the heat of reaction.

While Buhtz patent concerned chemical reactions, later work often focuses on the heat transfer aspect of the invention. Namely, the replacement of gravitational acceleration by stronger centrifugal acceleration decreases film thickness and thereby increases heat transfer rates. To support development of a spacecraft vapor absorption heat pump system, the NASA Microgravity Fluid Physics Program and Goddard Space Flight Center funded numerical, theoretical and experimental work to better understand the fluid mechanics of liquid flow over rotating disks. An overview of the research resulting from this program is given in Table 2-5. In research originating from this project, a particular collar feed system with jet impingement effects was used, which makes results not readily transferable to systems without this feature. The collar feed arrangement ejects the liquid into radial direction with high inertia which has pronounced effects on fluid flow and heat transfer.

Table 2-6 provides a tabulated overview of another set of research that started with the filing of a patent by Cross and Ramshaw of Imperial Chemical Industries PLC in 1984 [17]. The patent was followed by more than two decades of research that culminated in the production of a rotating absorption heat pump. While early prototypes of the heat pump used metal hydroxides as the working fluid and flat plates for all transfer units [17,72,73], later versions used a rotating coil-type absorber instead of a rotating disk absorber [19,74,75], and the system was driven by aqueous lithium bromide [19,75]. In a double effect configuration, the chiller used a coil-type absorber

and plane surfaces for primary and intermediate generators. The process taking place in the generators is the reversal of the absorption process. The high film heat transfer coefficient of 9 kW/(m^2·K) of the intermediate generator in [75] thus indicates high process intensification potential for disk-type absorbers as well. The intermediate generator operated at a temperature of 107 °C and a pressure of 12 kPa, one order of magnitude higher than the typical pressure for absorbers. While the whole chiller was integrated in one rotating enclosure, it was reported that the highest process intensification was achieved through the flat disk generators. As of 2017, the intensified heat pump has disappeared from the market, and, since its development was driven by private companies, little information on performance testing of its individual components has been made publicly available. So, rather surprisingly given the sustained research interest in the topic, no study has been published describing in detail the performance of a spinning disk absorber in an actual absorption process and comparing it to conventional systems. Thus, the objective of this study is to address this void and to compare the results to published performance data of horizontal tube bank absorbers.

Early studies on spinning disk reactors examined pure condensation without bulk flow of liquid that is present in an absorption process. Sparrow and Gregg [76] attacked the problem analytically and derived heat flux to be uniform over the surface of the disk and proportional to $\omega^{1/2}$. The heat transfer coefficient of rotating condensation was found to surpass the value for condensation on a vertical wall at a distance of 0.3 m from top when rotational speed reaches 33.2 rpm. Experimental studies largely

confirmed the analytical solutions and the therein postulated high heat transfer rates of rotational film condensation [77–79]. Butuzov and Rifert [78] reported condensation heat transfer coefficients of above 90 kW/(m^2·K) at 2139 rpm and the lowest heat flux studied. Typical for film condensation, higher heat fluxes led to thicker films and therefore lower heat transfer coefficients. Sparrow and Gregg also treated the heat and mass transfer characteristics of a disk rotating in quiescent fluid and concluded that the injection of fluid through the disk surface decreases the heat transfer significantly since it adds an additional layer of resistance [80]. This result is further indication of the differences between rotating condensation and absorption, since bulk liquid flow present in absorption also creates an additional resistance that is not present in conventional condensation.

Few studies have incorporated an internal heat sink into the design of a spinning disk reactor. While internal circulation of a heat transfer fluid is the expected mode of operation for most purposes, studies on heat transfer characteristics largely relied on heat flux from an internal electric heater to the outside film [11,13,81,82]. Oxley et al. [83] used a spinning disk absorber with internal cooling for manufacturing chemicals. They calculated internal heat transfer coefficients using a correlation for turbulent flow in tubes although flow at the given conditions should have been laminar. Still, they predicted overall heat transfer coefficients between 4180 W/(m^2·K) and 2240 W/(m^2·K) at radial distances from center of 0.02 m and 0.06 m, respectively, and concluded that calculations agreed with experimental observations. Other studies regarding production of chemicals using spinning disk reactors that included internal cooling emphasized its

effectiveness but did not measure heat transfer rates [84,85]. Burns and Henderson [86] patented profiling the backside of the internal cooling channel such that the width of the channel is not constant in radial direction, thereby controlling heat transfer performance and velocity of the cooling fluid. A similar approach is taken in development of the reactor presented in chapter 3, were the width of the cooling channel is varied to optimize heat transfer rates while keeping pressure drop at acceptable levels.

Table 2-5: Overview of research on spinning disks for space-based vapor-absorption chillers.

Authors	Year of publication	Type of work*	Process investigated	Working fluid	Disk cooled internally	Diameter of disk [m]	Rotational speed [rpm]	Flow rate [mL/s]	Outcome of the study
Thomas et al. [87]**	1990	Num.	Sensible heat transfer	Water	N/A	N/A	N/A	N/A	- Film heat transfer of rotating disk with collar feed arrangement is two orders of magnitude higher than when liquid is ejected from pressurized container onto horizontal plate.
Rahman and Faghri [88]**	1992	Num.	Sensible heat transfer; evaporation heat transfer	Water	N/A	0.39	55 – 300	117 - 250	- Heat transfer coefficient in case with sensible heating larger than in case with sensible heating and evaporation. - Heat transfer coefficient increases with rotational speed. - At 100 rpm, heat transfer coefficient decreases monotonically in radial direction. - At 300 rpm, heat transfer coefficient first decreases, then increases in radial direction.
Rahman and Faghri [89]**	1993	Num. / An.	Gas absorption	CO_2 / water	N/A	0.39	55 - 600	50 - 500	- Gas absorption doubles when rotational speed triples. - Increasing flow rate increases mass transfer at small radii, decreases mass transfer at large radii.
Ozar et al. [90]**	2004	Exp.	Sensible heat transfer; evaporation heat transfer	Water	No	0.41	0 - 500	50 - 250	- Heat transfer increases with rotational speed and flow rate. - Due to the inertial forces when the fluid is leaving the collar feed arrangement, heat transfer is higher closer to the collar.

Rice et al. [91]**	2005	Num.	Sensible heat transfer; evaporation heat transfer	Water	N/A	0.41	50 - 200	50 - 250	- Heat transfer increases with rotational speed and flow rate. - Heat transfer increases when evaporation takes place.
Basu and Cetegen [81]**	2006	An.	Sensible heat transfer	Water	N/A	N/A	50-100	50 - 250	- At low rotational speed, the heat transfer coefficient reduces in radial direction. - At high rotational speed and flow rate, the heat transfer coefficient first increases, then decreases in radial direction.
Quinn and Cetegen [82]**	2011	Exp.	Sensible heat transfer; evaporation heat transfer	Water	No	0.41	0 - 100	50 - 200	- Heat transfer increases with rotational speed, flow rate and inlet temperature. - Evaporation has only small effect on heat transfer.

* Abbr.: An.: Analytical methods; Exp. Experimental; Num.: Numerical simulation.

** Study utilizes a specific two-disk collar feed arrangement that produces a jet impingement effect.

Table 2-6: Overview of development of an integrated rotary absorption heat pump.

Authors	**Year of publication**	**Type of work***	**Working fluid**	**Type and size of absorber**	**Rotational speed [rpm]**	**Outcome of the study**	**Machine configuration ****
Cross and Ramshaw [17]	1985	P.	Refrigerants and organic solvents	Disk with 0.1 – 5 m diameter	N/A	- COP of 1.27 predicted. - Plurality of plates such that absorber and evaporator are on facing surfaces of adjacent plates.	AHP; DF; SE
Ramshaw and	1988	Exp.	H_2O / KOH, NaOH, CsOH	Disk with 0.5 m diameter	500	- Condenser and absorber on opposite faces of same disk. - COP of 1.2 achieved in heating mode at 30 °C temperature lift.	AHP; DF; SE

Winnington [72]							
Lorton et al. [74]	2000	Exp.	H_2O / mixed metal hydroxide	Coil-type; system size: 0.5 m diameter, 0.5 m length	550	- Plate-type intermediate condenser / generator has overall heat transfer coefficient of 6.1 kW/(m^2·K). - COP of 0.76 achieved at 7 °C chilled and to 52 °C cooling water temperatures with 8.8 kW cooling capacity.	AC; DE; DF; DR
Gilchrist et al. [75]	2002	Exp.	H_2O / LiBr-H_2O	Coil-type absorber; system size: 0.5 m diameter, 0.5 m length	500	- Plate-type intermediate condenser/ generator has overall heat transfer coefficient of 6.5 kW/(m^2·K). - Results at operation in double effect at ambient temperature of 32 °C: COP of 0.9, capacity of 10.5 kW. - Results at operation in single effect at ambient temperature of 35 °C: COP of 0.75, cooling capacity of 8.8 kW.	AC; DE/SE; DF; DR
Zaltash et al. [92]	2007	Exp.	H_2O / LiBr-H_2O	Coil-type;	~ 300	Test results of commercial product: - COP of 0.58 and cooling capacity of 3.78 kW at 14.6 °C chilled water temperature and 40 °C cooling water temperature. - 1.8 kW of power consumption.	AC; DR; IF; SE
Izquierdo et al. [93]	2008	Exp.	H_2O / LiBr-H_2O	System volume 0.93 m^3, description and drawings provided in [19]	N/A	Test results of commercial product: - Performance testing for actual space cooling over 20 day test period during summer time. - Average COP recorded at 0.49 without consideration of auxiliary power consumption. - Chilled water temperatures were between 11.3 and 24.3 °C.	AC; DR; IF; SE

*Abbr.: Exp.: Experimental; P.: Patent.

**Abbr.: AC: Absorption chiller; AHP: Absorption heat pump; DE: Double effect; DF: Direct fired; DR: Dry heat rejection via fan coil; IF: Indirect fired; SE: Single effect.

2.4.1. Hydrodynamics

In a simple approximation, the flow field on a rotating disk can be derived from the Nusselt model of laminar film condensation on vertical plates. Important assumptions of the Nusselt model are given in [94] as follows:

- The flow of the liquid is laminar.
- No non-condensables in the gas phase which is at constant temperature. Hence no conduction heat transfer between gas and liquid.
- Negligible shear stress at the gas-liquid interface.
- Negligible momentum and energy transfer by advection in the liquid film. Therefore heat transfer is by conduction only and the temperature profile is linear.

For more detailed discussions of the Nusselt model, the reader is referred to its treatment in standard textbooks (e.g. [94]). The Nusselt model can be adapted to a rotating surface by using the centrifugal acceleration $\omega^2 r$ instead of the gravitational constant [95,96]. Based on this adaption, Wood and Watts [96] and Aoune and Ramshaw [13] develop equations for film thickness, average, maximum and local radial velocity and residence time and the derivation of Eqs. 2-3 to 2-11 is based on theses sources. The shear stress (Eq. 2-3) can be integrated to receive the parabolic radial velocity profile (Eq. 2-4) [13].

$$\tau = \mu \frac{du}{dz} = \omega^2 r \rho (\delta - z) \qquad 2\text{-}3$$

$$u = \frac{r\omega^2\rho}{\mu}\left(z\delta - \frac{z^2}{2}\right) \qquad 2\text{-}4$$

Integration of the velocity profile over the thickness of the film gives the average velocity at a certain radius according to the Nusselt model.

$$\bar{u} = \frac{1}{\delta}\int_0^{\delta} u\, dz \; = \frac{r\omega^2\rho\delta^2}{3\mu} \qquad 2\text{-}5$$

Maximum velocity of the liquid film, found at the gas-liquid interface (z = δ), is 50 % higher than average velocity.

$$u_{int} = \frac{\omega^2 r\rho\delta^2}{2\mu} \qquad 2\text{-}6$$

The average radial velocity can also be expressed in terms of volumetric flow rate (Eq. 2-7):

$$\bar{u} \; = \frac{Q}{2\pi r\delta} \qquad 2\text{-}7$$

The film thickness (Eq. 2-8) follows from equating the two expressions for average radial velocity (Eqs. 2-5 and Eq. 2-7).

$$\delta = \left(\frac{3\mu Q}{2\pi r^2\omega^2\rho}\right)^{\frac{1}{3}} \qquad 2\text{-}8$$

Integration of Eq. 2-8 yields average film thickness, $\bar{\delta}$ (Eq. 2-9).

$$\bar{\delta} = \frac{\int_0^{2\pi}\int_0^{r}\int_0^{\delta} r\, dzdrd\phi}{\pi r^2} = \frac{2\pi\int_0^{r}\delta r\, dr}{\pi r^2} = \left(\frac{81Q\mu}{16\pi r^2\omega^2\rho}\right)^{\frac{1}{3}} \qquad 2\text{-}9$$

The film thickness may be used to express average velocity according to Eq. 2-10.

$$\bar{u} = \left(\frac{Q^2\omega^2\rho}{12\pi^2 r\mu}\right)^{\frac{1}{3}} \qquad 2\text{-}10$$

Eqn. 2-10 can be used to derive the average residence time of liquid on the disk (Eq. 2-11).

$$t_{ave} = \int_0^r \frac{1}{\bar{u}} dr = \left(\frac{81\pi^2\nu}{16\,\omega^2 Q^2}\right)^{\frac{1}{3}} r^{\frac{4}{3}} \qquad 2\text{-}11$$

Since the surface velocity is twice the average velocity, residence time at the free surface (i.e. gas-liquid interface) equals minimum residence time. It is given by Eq. 2-12.

$$t_{int} = \frac{2}{3} t_{ave} \qquad 2\text{-}12$$

Wood and Watts [96] list three assumptions inherent to the application of the Nusselt model to describe the fluid flow over rotating disks. Most importantly, since the Nusselt model is developed for fully developed laminar flow on a vertical wall while fluid thickness and velocity are constantly changing with radial position on spinning disks, the description by the Nusselt model will be a simplification. Besides, it also implicitly assumes that Coriolis forces can be neglected and that the tangential velocity of the fluid is equal to the tangential velocity of the disk, e.g. that there is no slip in angular direction.

The experimental work conducted by Wood and Watts shows the approximate nature of the application of the Nusselt model to the problem. By injection of a dye into the fluid prior to deposition on the disk, they hoped to be able to observe the maximum

velocity of different fluids by following the dye front on the surface of the disk. However, when applying this technique to water, the dye front disappeared due to high mixing. Only a high viscosity fluid indicated laminar flow. Thus, they resorted to the use of small tracer particles of density equal to the density of the fluids. Their experimental results for mean radial velocity show that only the high viscosity fluid follows the trend expected from the Nusselt model. When using water, the mean radial velocity actually increases with increasing radial distance. Further, for lower viscosity fluids, the flow contradicted the no slip assumption in angular direction. They also reported the presence of circumferential waves. The waves were more irregular for a low viscosity fluid.

Woods [97] investigated these surface waves due to their important role in the heat and mass transfer enhancement of spinning disks. He reviewed the earlier literature and identified three distinct surface regimes. In the first regime, flow rates and acceleration or inertia due to rotation are very low which results in laminar flow without wave formation. The second regime is characterized by smooth two-dimensional disturbances that occur at higher flow rates or body forces. Finally, for even higher body forces or flow rates, the smooth waves break up into three-dimensional ripples. Due to the inertial forces created by rotation, the flow is at steady state at every location on the disk but the nature of this steady state is constantly evolving between center and perimeter. This is dissimilar to the case of a fluid flowing down a vertical wall that was the foundation of the Nusselt model. Thus, as the inertial force due to rotation increases in radial direction, all three of the above regimes can be present at the same time on a

rotating disk. He notes that viscosity influences stability of laminar flow as higher viscosity decreases the growth rate of disturbances. Thus, the dampening effect of viscosity influences the critical Reynolds number associated with the transition from laminar flow to breakdown of thereof. Another observation worth mentioning is the complete breakdown of the thin liquid film that can occur at very low flow rates. Under the influence of surface tension, the very thin film can deteriorate into stretched liquid patches and actual dry spots. This phenomenon was also reported by other researchers who developed a correlation of the minimum flow rate at which film breakdown occurs (Eq. 2-13) [98,99]. Experiments conducted by Bell [100] yielded minimum flow rates 30% below the theoretical predictions.

$$Q_c = 5.5 \left(\frac{\nu r^4}{\omega^2}\right)^{\frac{1}{5}} \left(\frac{\sigma}{\rho}\right)^{\frac{3}{5}} \qquad 2\text{-}13$$

Woods [97] further investigated wave propagation on rotating disks. Experimental measurements were based on a dyed fluid and knowledge about the thickness of the film was derived by measuring the intensity of light passing through the thin film. Figure 2-5 shows photographs taken at constant volumetric flow rate but increasing rotational speed. At the lowest speed, the flow seems laminar close to the center before spiral waves, which propagate in opposite direction to the rotation of the disk, appear. At increasing flow rate, the size of the laminar region decreases and an intermediate region of almost concentric waves is observed. Closer investigation yields that the waves in the intermediate zone are indeed spirals as well, and that the laminar region only appears to be laminar while the spiral waves actually start at the distributor. The

small amplitude of the waves close to the middle makes the flow field look laminar although it is not. As the amplitude grows further through the intermediate region, the spiral waves grow closer together and become more irregular. At 400 rpm, the flow looks more orderly again with a spiral extending from the middle to the outer disk at a slightly increasing wavelength. At higher rotational speed, the spiral originating from the middle breaks up into small, three-dimensional waves that appear highly random. Generally, the wave amplitude grows from the central dispersion through the region of waves that appear two-dimensional. When the waves break down into three-dimensional wavelets, the amplitude may decrease slightly but stays almost constant. The ratio of the peak wave amplitude to the mean film thickness increases with rotational speed from close to 1 at 100 rpm to about 5 at 600 rpm.

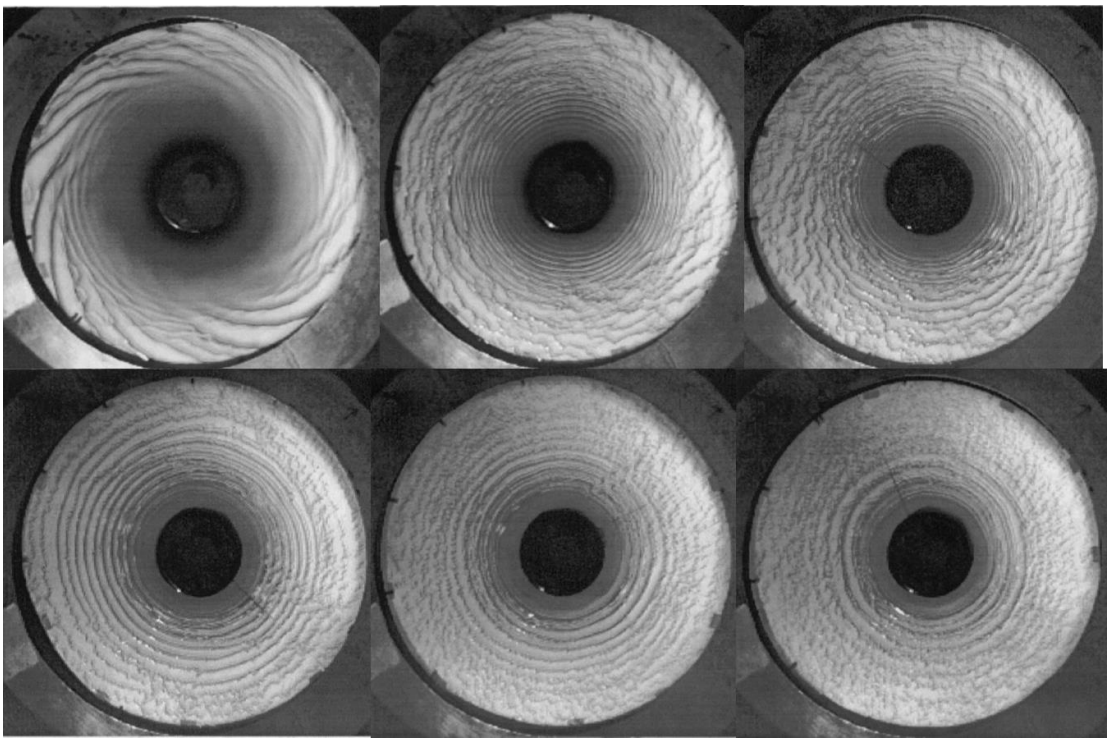

Figure 2-5: Flow pattern of water with dye on rotating disk (diameter: 0.36 m, flow rate 19 mL/s) for rotational speed ranging from 100 rpm (top left) to 600 rpm (bottom right). Adapted from [97].

Burns et al. [70] evaluated the film thickness on a rotating disk using an electrical resistance technique. The method allowed calculating the film thickness at 11 radial positions. Reviewing the literature, they stated that most previously published studies found the mean film thickness to be below the thickness predicted by the Nusselt model. The deviation was explained by the presence of surface waves. However, Burns et al. suggested that a better explanation could be derived from the analysis of the Ekman number (Eq. 2-14).

$$Ek_\delta = \frac{\nu}{\omega\delta^2} \qquad 2\text{-}14$$

The Ekman number in Eq. 2-14 is based on the film thickness, which was previously suggested by [101]. Eqn. 2-15 gives the Ekman number after inserting the film thickness (Eq. 2-8).

$$Ek_\delta = \left(\frac{2\Pi}{3}\right)^{\frac{2}{3}} \left(\frac{r^4\omega\nu}{Q^2}\right)^{\frac{1}{3}} \qquad 2\text{-}15$$

Figure 2-6 shows that the measured film thickness deviated most from the Nusselt model for Ekman numbers below 2. This is explained by the presence of inertial effects and the fact that the liquid has not caught up yet with the rotation of the disk. Interestingly, the average measured film thickness was 9% below the Nusselt prediction, thus the flow was moving slightly faster than expected. A deviation of 9% is fairly small and hence the Nusselt model seems to relay an acceptable approximation of the actual film thickness.

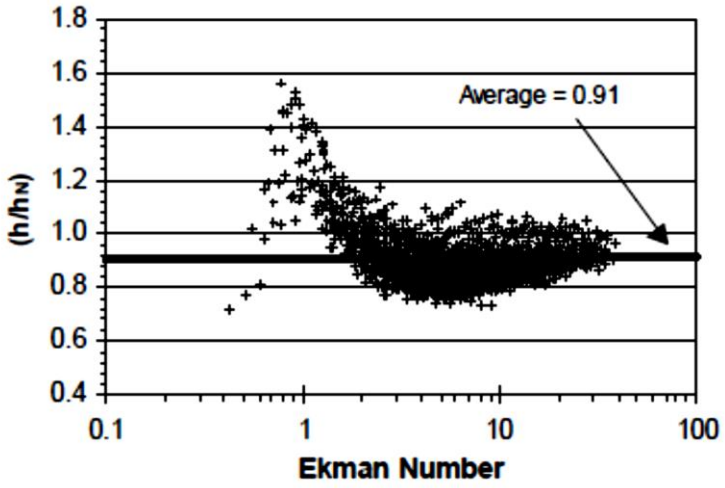

Figure 2-6: Ratio of experimentally determined film thickness to prediction by Nusselt model for different Ekman number. Figure from [70].

Still, Burns et al. [70] suggest an alternative model to better the predictions closer to the center of the disk where the Nusselt model underperforms. By transforming the film thickness measurements into radial velocity measurements, they experimentally validated the reasoning of the model depicted in Figure 2-7. Close to injection of the fluid, the radial velocity decreases due to the viscous drag. In the acceleration zone, the radial velocity increases due to centrifugal acceleration. In the third zone, the rotational speed of disk and fluid is synchronized and the Nusselt model fits well.

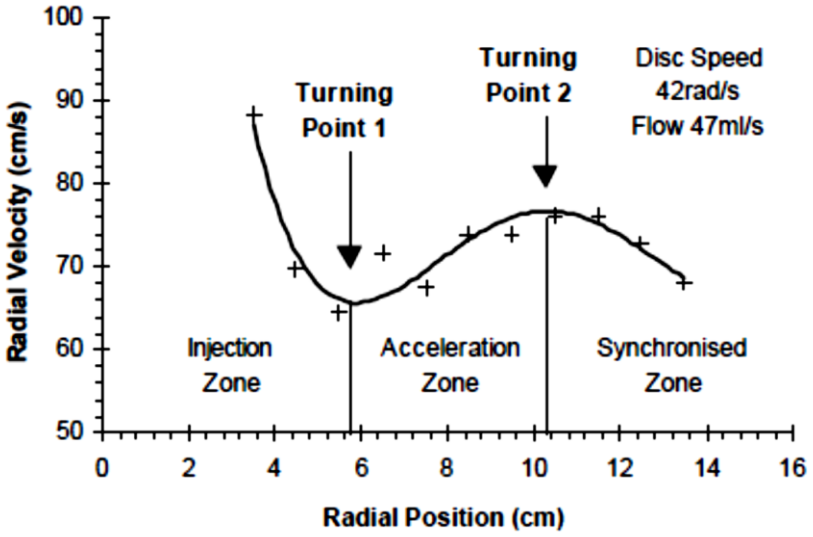

Figure 2-7: Three zone model of radial velocity development incl. experimental values and polynomial fit of radial velocity profile. Figure from [70].

For low Ekman numbers, where the validity of the Nusselt model is weak, they suggest the use of the Pigford model previously described by Wood and Watts [96]. This two-dimensional model includes inertial and viscous terms and is given by the Eqs. 2-16 and 2-17.

$$u\frac{\partial u}{\partial r}-\frac{v^2}{r}=-\frac{12\,\pi^2 r^2 K_1 \nu}{Q^2}u^3 \qquad 2\text{-}16$$

$$u+\frac{uv}{r}=\frac{12\,\pi^2 r^2 K_2 \nu}{Q^2}u^2(r\,\omega-v) \qquad 2\text{-}17$$

The equations can be non-dimensionalized for scaling purposes, using a radial length scale λ that correlates the inertial and viscous forces (Eq. 2-18).

$$\lambda = \left(\frac{Q^2}{\omega \nu}\right)^{\frac{1}{4}} \qquad 2\text{-}18$$

Burns et al. then fit the non-dimensional version of equations 2-16 and 2-17 to experimental data and determined values for the empirical constants K_1 and K_2 within the non-dimensional equations. This allows to give formulas to estimate the size of the spin-up zone, which consists of injection and acceleration zones. For typical speeds and flow rates, the spine-up zone extends a few centimeters from the disk's center and is approximately proportional to $\lambda^{2/3}$.

Mohammadi and Boodhoo [102] studied the residence time distribution (RTD) on spinning disk reactors through pulse injection of a tracer and subsequent conductivity measurements of the fluid exiting the disk. A narrow and symmetrical residence time distribution corresponds to plug flow conditions with high mixing in vertical direction and uniform velocity profile in radial direction. Already at the lowest rotational speed of 300 rpm, strong mixing was recorded. From their parametric studies, it appeared that RTD is narrowing with higher rotational speed, albeit not at the lowest flow rate of 5 mL/s. The effect of volumetric flow rate is more distinct, with the distribution becoming narrower with increasing flow rates for all rotational speeds under investigation. They argued that higher flow rates and rotational speeds lead to increase in intensity of surface waves. The surface waves cause turbulence within the thin film and thereby create a more uniform velocity profile in radial direction. Mixing occurs in transvers direction while radial dispersion is limited. Mohammadi and Boodhoo also investigated the effect of a circular grooves in the surface of the disk. Neglecting a

number of minor different effects, they found that the RTD is narrower for grooved disks due to increase in mixing intensity caused by the film detachment and reattachment as the flow overcomes the ripples. Their experiments also suggest that the use of rippled surfaces can overcome the detrimental effect of viscosity on mixing in transverse direction.

Jacobsen and Hinrichsen [103] employed a system of parallel reactions in order to investigate the mixing properties of a spinning disk reactor. Their setup consisted of a small disk of 0.1 m diameter that spun at up to 6000 rpm. One of the reactions was instantaneous while the other was also fast, but significantly slower than the first one. The reaction details were such that the products of the second reaction were present only for imperfect mixing conditions. Results were reported in terms of a segregation index that takes the value 0 for perfect mixing and 1 for absence of mixing. They found that the segregation index decreased sharply with rotational speed, indicating better mixing. It is argued that higher rotational speed decreased film thickness, which in turn reduced diffusion time. Also, the higher rotational speed caused more surface ripples which increased mixing. Jacobsen and Hinrichsen also found an influence of flow rate, mainly at low rotational speeds, with lower flow rates correlating with lower values of the segregation index. They argued that this behavior showed the correlation of mixing efficiency with film thickness. With regard to the effect of a textured disk surface, their experiments indicated that the rotational speed had to be above a threshold for the textured surface to enhance mixing efficiency. This effect was attributed to the

turbulence caused by textured surface at higher speeds while at lower speeds the liquid is held back inside the grooves.

In conclusion, the simple Nusselt model describes the thickness of the liquid film on spinning disks reasonably well for many conditions. However, it does not capture the effects of inertia that are present at low Ekman numbers. Further, the laminar flow profile assumed in developing the Nusselt model may not be accurate as the high mixing observed in transverse direction indicates a more turbulent flow pattern. Thus, the Nusselt model can be used to predict film thickness and average velocity although the actual velocity profile is uncertain and experimentally observed surface waviness is not treated in the Nusselt model at all.

2.4.2. Sensible external heat transfer

Spinning disk reactors were originally invented to improve the yield of temperature-sensitive reactions by keeping fluids in an optimal temperature range [71]. Accordingly, a number of studies concerning sensible and latent heat transfer characteristics of spinning disks have been published and an overview is provided in Table 2-7.

Table 2-7: Overview of previous work on sensible and latent heat transfer characteristics of spinning disks.

Authors	**Year of publication**	**Type of work***	**Process investigated**	**Working fluid**	**Disk cooled internally**	**Diameter of disk [m]**	**Rotational speed [rpm]**	**Flow rate [mL/s]**	**Outcome of the study**
Buhtz [71]	1928	P.	Chemical reactions	N/A	Yes	N/A	N/A	N/A	- Capability of spinning disk reactor to keep reactants within optimum temperature band leads to higher yield of preferred product.
Sparrow and Gregg [76]	1959	An.	Condensation heat transfer	N/A	N/A	N/A	N/A	N/A	- Analytical prediction of heat transfer coefficient which is valid for most common cases from engineering and fluid properties point of view: $\frac{h\left(\frac{\nu}{\omega}\right)^{\frac{1}{2}}}{k} = 0.904 \left(\frac{Pr}{c_p(\mathrm{T_{sat}} - T_w)/h_{fg}}\right)^{\frac{1}{4}}$
Sparrow and Gregg [80]	1960	An.	Heat transfer; suction/injection mass transfer	N/A	N/A	N/A	N/A	N/A	- Heat transfer decreases when fluid of the same temperature as the disk is injected through the surface of the disk since the fluid covers the surface.
Sparrow and Gregg [104]	1960	An.	Condensation heat transfer	N/A	N/A	N/A	N/A	N/A	- Influence of shear at gas-liquid interface has small effect on heat transfer for most cases.
Nandapurkar and Beatty [77]	1960	Exp.	Condensation heat transfer	Methanol, ethanol, Freon-113	Yes	0.13	400 - 2400	N/A	- Experimental heat transfer results 25 - 30% below prediction. - Mass transfer coefficient proportional to $\omega^{0.45}$.
Espig and Hoyle [105]	1967	Exp. / An.	Condensation heat transfer	Saturated steam	No	0.38	155 - 2500	N/A	- Analytical considerations equivalent to Sparrow and Gregg [76].

									- Experimentally measured heat flux exceeds analytical prediction; results are attributed to wave formation.
Butuzov and Rifert [78]	1972	Exp. / An.	Condensation heat transfer	Steam	No	0.3	95 - 2139	N/A	- Experimental heat transfer results 5 - 10% below analytical prediction, comparable to analysis by Sparrow and Gregg [76]. - For $\omega > 497$ rpm, heat transfer coefficient proportional to $\omega^{0.5}$. - Rotation enhances heat transfer by a factor of 3 to 5.
Wood and Watts [96]	1973	Exp.	Sensible heat transfer	Water, viscostatic oil	No	0.34	320 - 2200	6.3 - 252	- Heat transfer coefficient increases with flow rate, contrary to expectations. - Heat transfer not correlated to rotational speed at low liquid flow rates (6 - 25 g/s). - Heat transfer increases with rotational speed at high flow rates (above 50 g/s).
Jachuck and Ramshaw [11]	1994	Exp.	Sensible heat transfer	Water	No	0.36	250 - 890	30 - 70	- Tailored disk surfaces improve film heat transfer by up to 77 % compared to smooth disk. - Maximum average film heat transfer coefficient of 18 kW/(m^2·K) achieved by disk with surface grooves. - Positive effect of increasing rotational speed on heat transfer only up 650 rpm.
Al-Baroudi and Klein [79]	1995	Exp.	Condensation heat transfer	Steam	No	0.30	200 - 400	N/A	- Empirical results show satisfactory agreement with correlation by Sparrow and Gregg [76].
Aoune and	1999	Exp.	Sensible heat transfer	Water, water/pro	No	0.5	286 - 955	35 - 80	- Local film-side heat transfer coefficient alternates around Nusselt prediction, depending on experimental parameters.

Ramshaw [13]				pylene glycol					
Oxley et al. [83]	2000	Exp.	Chemical reactions	Various reactants	Yes	0.15	Up to 5000	Up to 4.5	- Calculated local overall heat transfer coefficient values between 0.4 and 4.2 kW/(m^2·K).
Burns and Henderson [86]	2007	P.	Internal heat transfer enhancement	N/A	Yes	N/A	N/A	N/A	- Machining of profile into back surface of cooling channel to optimize trade-off between pressure drop and heat transfer performance.
Burns and Henderson [106]	2008	P.	Internal heat transfer enhancement	Water	Yes	0.3	650	15	- Disk with spirally wound quadratic channel (10 mm channel width, 2 mm fin thickness) achieves an overall heat transfer coefficient of 9.7 kW/(m^2·K). - Rotational speed not critical to heat transfer performance.
Present study	2018	Exp.	Absorption	Aqueous lithium bromide	Yes	0.30	100 - 500	6 - 16	- Film-side heat transfer coefficient enhanced by factor of 4.7 compared to falling film on tube banks. - Film-side heat transfer increased by a factor of 2.2 when rotational speed accelerated from 100 to 500 rpm. - Heat transfer performance highest at medium/high mass flow rates.

* Abbr.: An.: Analytical methods; Exp.: Experimental; P.: Patent.

An early work by Rees [107] on sensible heat transfer on rotating disks is reported by Khan [108] and Wood and Watts [96]. Rees developed an analytical model based on the assumption that the flow is laminar and can be described by the Nusselt model. Further, no shear is assumed at the free surface and no slip boundary condition is assumed at the surface of the disk. He assumed a cubic the temperature profile with the boundary conditions:

$$T = T_w \; and \frac{d^2T}{dz^2} = 0 \; at \; z = 0 \qquad 2\text{-}19$$

$$T = T_s \; and \frac{dT}{dz} = 0 \; at \; z = \delta \qquad 2\text{-}20$$

From the boundary conditions, the temperature profile follows as given in Eq. 2-21 which can be written according to Eq. 2-22.

$$\frac{T - T_w}{T_s - T_w} = \left(\frac{3}{2}\frac{z}{\delta} - \frac{1}{2}\frac{z^3}{\delta^3}\right) \qquad 2\text{-}21$$

$$T = T_w - \frac{3}{2}\frac{z}{\delta}(T_w - T_s) + \frac{(T_w - T_s)}{2}\frac{z^3}{\delta^3} \qquad 2\text{-}22$$

Then the average temperature at any radial position is given by Eq. 2-23.

$$T_{ave} = \frac{\int_0^\delta uTdz}{\int_0^\delta udz} = \frac{1}{80}(61T_s + 19T_w) \qquad 2\text{-}23$$

The surface heat flux is given by Fourier's law, Eq.2-24, and it must be equal to the rate of heat transfer through the liquid film (Eq. 2-25). Equating Eqs. 2-24 and 2-25, the heat transfer coefficient follows as function of film thickness (Eq. 2-26.)

$$q'' = -k\frac{dT}{dz}\Big|_{z=0} = -\frac{k}{\delta}\frac{3}{2}(T_s - T_w) \quad \text{2-24}$$

$$q'' = h(T_{ave} - T_w) = \frac{61}{80}h(T_s - T_w) \quad \text{2-25}$$

$$h = \frac{120}{61}\frac{k}{\delta} \quad \text{2-26}$$

Wood and Watts [96] compared experimental data to this model and verified the dependence of heat transfer coefficient on angular velocity. However, they could not find the negative dependence on volumetric flow rate that is implicit due to the appearance of the film thickness in the denominator in the correlation. Based on their results, the model overestimates heat transfer at low volumetric flow rates and underestimates heat transfer at high flow rates. The deviation at high flow rates is explained by the heat transfer enhancement through surface waves present at these conditions.

Aoune and Ramshaw [13] performed a Nusselt model analysis similar to Rees's work but assumed a parabolic temperature profile. After applying standard conditions ($T = T_w \ at\ z = 0,\ T = T_{int} \ at\ z = \delta,\ dT/dz = 0\ at\ z = \delta$), the parabolic profile is given by Eq. 2-27. From the temperature profile, they deducted an average temperature (Eq. 2-28), which lead to heat transfer coefficient given in Eq. 2-29.

$$T = T_w - \frac{2(T_w - T_s)}{\delta}z + \frac{(T_w - T_s)}{\delta^2}z^2 \quad \text{2-27}$$

$$T_{ave} = \frac{3}{5}T_s + \frac{2}{5}T_w \quad \text{2-28}$$

$$h = \frac{5}{3}\frac{k}{\delta} \qquad 2\text{-}29$$

However, Appendix II shows that correct evaluation of Eq. 2-30 with parabolic temperature and velocity profile and standard boundary conditions leads to the average temperature profile given in Eq. 2-31.

$$T_{ave} = \frac{\int_0^{\delta} uTdz}{\int_0^{\delta} udz} \qquad 2\text{-}30$$

$$T_{ave} = \frac{4}{5}\,T_s + \frac{1}{5}T_w \qquad 2\text{-}31$$

Moreover, the heat flux evaluated through application of Fourier's law to the parabolic temperature profile is given by Eq. 2-32 from the factor "2" was omitted in [13]. Thus, the correct analytical heat transfer coefficient for parabolic temperature and velocity profiles is given by Eq. 2-33 and is 50% larger than the value reported by Aoune and Ramshaw.

$$q" = -k\frac{dT}{dz}\Big|_{z=0} = -\frac{2k}{\delta}(T_w - T_s) \qquad 2\text{-}32$$

$$h = \frac{heat\ flux}{T_{ave} - T_w} = \frac{2k}{\delta}\frac{(T_w - T_{s)}}{(\frac{4}{5}T_w - \frac{4}{5}T_s)} = \frac{5}{2}\frac{k}{\delta} \qquad 2\text{-}33$$

In the experimental part of their paper, Aoune and Ramshaw measured film and surface temperature at 7 radially distributed locations on a disk of 0.5 m diameter. For water, they found the experimental heat transfer coefficient to be higher than analytically expected at radii below 0.125 m and above 0.21 m and below predictions at radii in between. However, Mikielewicz argued in a letter to the editors [109] that

this distribution of local heat transfer coefficients was merely a result of non-monotonic wall heat fluxes. Using an aqueous propylene glycol solution of with viscosity of 0.01 Pa·s, Aoune and Ramshaw found the Nusselt prediction to be a closer match of experimental results. In that case, experimental heat transfer coefficient monotonically increases with radius while showing overall less variation over radial position. Experimental values are however larger than the analytical predictions, which may be due to the incorrectly low values of the analytical solution.

A series of publications by Faghri, Ozar, Cetegen and their contributors [81,82,88,90,91,110–113] reported experimental data, analytical predictions and semi-empirical correlations for heat transfer on stationary disks and disks rotating to at maximums speed of 200 to 500 rpm. A short overview on the efforts was provided in Table 2-5. Their experimental setup utilized a special arrangement for deposition of liquid on the disk (see Figure 2-8). A collar of 10.2 cm diameter – basically a second, smaller disk – was located parallel to the main disk and rotated with the disk. In most investigations, the distance between the two solid surfaces was 0.254 mm which led to creation of a fully developed parabolic Poiseuille velocity profile. This feed system was analyzed using jet impingement theory originally developed by Watson [114] and reviewed by Webb and Ma [115]. As shown in Figure 2-8, the liquid is ejected at high velocity and film thickness increases due to friction. Once centrifugal forces become sufficiently strong, film thickness decreases again.

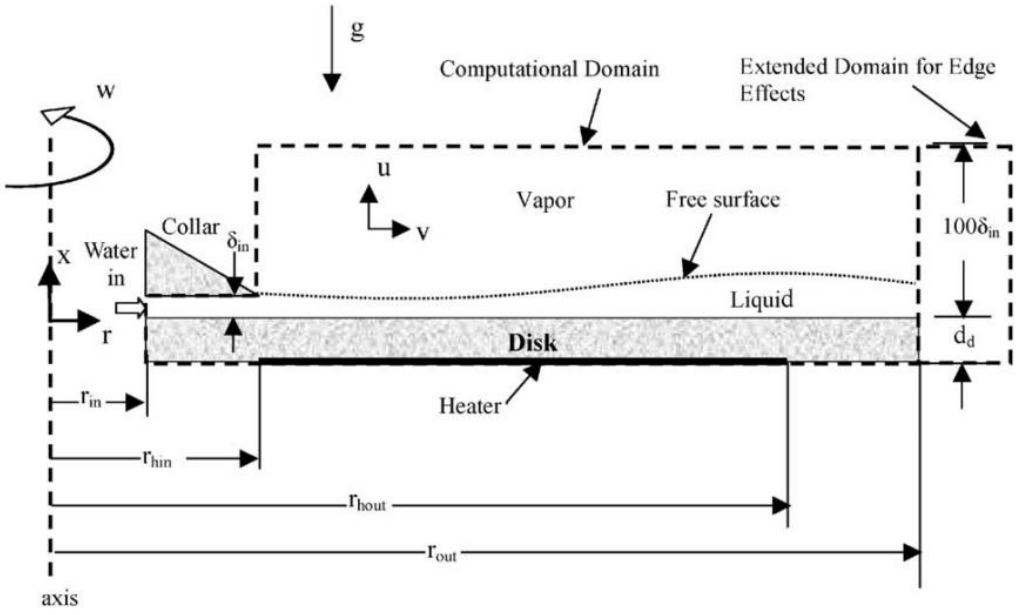

Figure 2-8: Schematic of spinning disk with controlled impingement used in research by Faghri, Ozar, Cetegen, Rice and contributors. Figure from [91].

Basu and Cetegen [81,113] analyzed hydrodynamics and heat transfer by integral method. They deducted equation 2-34, which can be numerically integrated to determine the non-dimensionalized film thickness over the disk surface. If inertia is negligible, e.g. in a case without the ejector effect of the flow through the color, the first two terms disappear and the equation collapses back to Nusselt's equation of film thickness for laminar flow.

$$\frac{d\tilde{\delta}}{d\tilde{r}} + \frac{\tilde{\delta}}{\tilde{r}} + \frac{5}{6Ro_c}\tilde{r}^3\tilde{\delta}^3 = \frac{5}{2Re_{r_c u_c}}\left(\frac{r_c}{h_c}\right)^2 \tilde{r} \qquad 2\text{-}34$$

With respect to heat transfer, they showed that the thermal entry length for moderate Péclet number ($Pe_c = \mathrm{u_c r_c}/\alpha$) is small enough to be neglected. The Nusselt number increased for higher inlet Reynolds numbers due the thinning effect of

increased inertia of the ejected fluid. At high rotational speeds or low values of the Rossby number ($Ro_c = u_c^2/(\omega^2 r_c^2)$) , the Nusselt number increased very strongly. As the strongest effect of heat transfer enhancement due rotation was experienced at smaller radii, the maximum Nusselt shifted to smaller radial coordinates at higher rotational speeds. The effect of Rossby number on average Nusselt number was found to be non-linear and was described by an inverse power law with different coefficients for constant wall temperature and constant wall heat flux boundary conditions. Basu and Cetegen compared the Nusselt numbers by integral method to experimental heat transfer data by Ozar et al. [90] and found them to agree well. Generally, Nusselt numbers determined by experiments showed much less variation with local position than when calculated by integral method.

Ozar et al. [90] and Quinn and Cetegen [82] reported experimental heat transfer data for the same experimental setup. They described the advantages of the collar feed system over conventional jet impingement as better flow control and well-defined inlet conditions. Ozar et al. divided the liquid flow over the rotating disk into a zone I, which encompassed the thermal entry length, and a zone II that covered the thermally developed region. However, under the assumption that the temperature of the free surface does not deviate significantly from the inlet temperature of the liquid, the heat transfer correlation for both zones collapsed to the same form. The heat transfer coefficient depended on the thickness of thermal boundary layer in zone I and on the film thickness in zone II. The Prandtl number was used to correlate thermal and velocity boundary layer thickness in zone I. Thus, in both zones the heat transfer coefficient

depended on the film thickness, which was defined by two complementing factors. Inertial effects of the flow impingement were more important in the zone adjacent to the collar, while centrifugal forces dominate at larger radii. It was found that Nusselt numbers increased with angular velocity and Reynolds number, e.g. liquid flow rates, the correlations were fitted for local and average Nusselt numbers, Eqs. 2-35 and 2-36, respectively. The experiments were conducted with water at constant inlet temperatures such that the Prandtl number dependence was replaced by a constant. From an analytical point of view, the Prandtl number dependence is only warranted for the thermal entry region anyway.

$$Nu_r = 0.088\, Re_{r_c u_c}^{0.66} Pr^{0.33} + 0.436 \left(\frac{Re_\omega}{Ro^{0.5}}\right)^{0.39} Pr^{0.33} \qquad 2\text{-}35$$

$$\overline{Nu} = 1.595 \left(2Re_{r_c u_c}\right)^{0.79} Pr^{0.33} + 2.692 \left(\frac{Re_{\omega r_o}}{Ro_{ro}^{0.5}}\right)^{0.30} Pr^{0.33} \qquad 2\text{-}36$$

Quinn and Cetegen [82] extended the experiments to evaporation of water into air at 70°C. In order to develop functional dependences to correlate experimental data, they modified the integral analysis in [81] to account for evaporation effects. The mass transfer dependence was deducted from an assumed similarity condition between heat and mass transfer. The Sherwood number for external flow with laminar boundary layer along flat plates and low mass transfer rates given by Eq. 2-37 [116] was modified for high mass transfer using a correction factor. Quinn and Cetegen evaluated liquid phase Reynolds number Re_r instead of Re_x and used liquid kinematic viscosity and diffusivity of water vapor into air to calculate the Schmidt number. Since the

correlation rests on the analogy of momentum, heat and concentration boundary layers Eq. 2-37 does not seem to have been applied correctly in the reported case.

$$Sh = 0.332\, Sc^{\frac{1}{3}} Re_x^{\frac{1}{2}} \qquad 2\text{-}37$$

In line with this consideration, Quinn and Cetegen reported that visual observation yielded high cooling effect due to evaporation while the model predicted only a small effect. Nusselt numbers from experimental data were about 50% less than expected based on integral method [81] and numerical simulation [91] while the authors of [81] and [91] had validated their models against data as well. Thus, Quinn and Cetegen proposed a new Nusselt number correlation based on twofold contributions from heating and evaporation.

Jachuck and Burns [14] provided a formula for film heat transfer coefficient based on similarity to liquid-solid mass transfer by confusion. They first derived a liquid-solid mass transfer coefficient for a diffusive process under laminar flow conditions. Then, they replaced mass diffusivity with thermal diffusivity and received Eq. 2-38. No experimental validation was provided.

$$h = 0.71 \left(\frac{\omega^4 k^6 Q c_p^3 \rho^3}{R^2 \nu^2} \right)^{\frac{1}{9}} \qquad 2\text{-}38$$

Jachuck and Ramshaw [11] tested heat transfer on rotating disks utilizing four different types of surfaces finish: smooth, metal sprayed and two types of grooves. They found that each of the surface modifications enhanced the heat transfer coefficient. The disk with rectangular grooves provided the highest enhancement of up

to 77% compared to the smooth surface. They also found that increasing rotational speed caused a monotonic increase in heat transfer coefficient only at the highest volumetric flow rate. They suggested that at lower flow rates, surface waviness reduced at high rotational speeds, which caused heat transfer coefficient to flatten or even to decline.

In conclusion, the research community has not yet reached full agreement on the nature of sensible heat transfer on spinning disks. A large part of the literature concerns spinning disks with a special jet impingement collar feed system that may not be generalized to regular spinning disks. The Nusselt model has been shown to be a good starting point for evaluation of spinning disk systems. Based on operating parameters and properties, it may be over- or underestimating experimental results. Generally, the dependence of heat transfer on rotational speed is well established while the effect of flow rate/film thickness has not been confirmed in most experiments.

2.4.3. Latent external heat transfer

Early studies on spinning disk reactors examined pure condensation without bulk flow that is present in an absorption process. These papers relied on adoption of Nusselt's [95] model on the process of laminar film condensation along a vertical plate which is subject of standard text books on heat transfer (e.g. [94]). In this model, a linear temperature profile and a parabolic velocity profile are assumed. Equations for film thickness (Eq. 2-39), heat transfer coefficient (Eq. 2-40) and average heat transfer coefficient (Eq. 2-41) are derived.

$$\delta = \left(\frac{4k_l\mu_l(T_{sat} - T_w)x}{g\rho_l(\rho_l - \rho_v)h_{fg}}\right)^{\frac{1}{4}} \quad \text{2-39}$$

$$h = \left(\frac{g\rho_l(\rho_l - \rho_v)k_l^3 h_{fg}}{4\mu_l(T_{Sat} - T_w)x}\right)^{1/4} \quad \text{2-40}$$

$$\bar{h} = 0.943\left(\frac{g\rho_l(\rho_l - \rho_v)k_l^3 h_{fg}}{\mu_l(T_{Sat} - T_w)L}\right)^{\frac{1}{4}} \quad \text{2-41}$$

Espig and Hoyle [105] extended the analysis of laminar film condensation to rotating disks and kept the assumption of a linear temperature profile. They derived Eq. 2-42 for film thickness that does not depend on radial location and used Fourier's law to derive the (mean) isothermal heat transfer coefficient (Eq. 2-43).

$$\delta = \left(\frac{1.5\mu_l k_l(T_s - T_w)}{\rho_l^2\omega^2 h_{fg}}\right)^{\frac{1}{4}} \quad \text{2-42}$$

$$h_{th} = 0.903\left(\frac{\omega^2\rho_l^2 k_l^3 h_{fg}}{\mu_l(T_{sat} - T_w)}\right)^{\frac{1}{4}} \quad \text{2-43}$$

To test the validity of their model experimentally, they used a setup in which dry, saturated steam condensed on one face of a rotating disk that was cooled on the back face by cooling water spray. They found that experimentally measured values exceeded theoretical predictions and that the correction applied in Eq. 2-44 most accurately described the deviations. Temperatures values in Eq. 2-44 are in units of Fahrenheit. The deviation of experiments and theory was explained by the presence of surface waves.

$$h_{exp} = 113\, f^{-0.415}(T_{sat} - T_w)^{-0.6} h_{th} \qquad 2\text{-}44$$

Sparrow and Gregg [76] derived the same mean transfer coefficient as Espig and Hoyle but opted to present it in terms of the Prandtl number (Eq. 2-45). Eq. 2-45 represented the solution for a thin layer of condensate where energy convection and inertia terms are regarded as negligible. However, numerical solution of Navier-Stokes, energy equation and conservation of mass without deleting energy and inertia terms showed that solutions only deviate from Eq. 2-45 for cases that were less likely to occur from an engineering and fluid properties point of view. At Prandtl numbers between 10 and 100, energy convection was shown to become relevant and the pre-factor was to exceed 0.904, but significantly so only for values of $c_p \Delta T / h_{fg} > 0.1$.

$$\frac{h\left(\frac{\nu}{\omega}\right)^{\frac{1}{2}}}{k} = 0.904 \left(\frac{Pr}{c_p(T_{sat} - T_w)/h_{fg}}\right)^{\frac{1}{4}} \qquad 2\text{-}45$$

In an additional publication, Sparrow and Gregg [104] reassessed the assumption of no shear at the gas-liquid interface made in [76]. Again, they studied numerically a variety of cases and concluded that inclusion of shear at the vapor interface only has a small effect of few percent points at most. Largest influence was found for either very thin or very thick films, and heat transfer was found to decrease or increase depending on conditions.

Nandapurkar and Beatty [77] experimentally studied condensation of three different fluids on a rotating water-cooled disk. Results were about 25-30% below the theoretical prediction of Eq. 2-41. However, the confirmed the propagated

dependencies of Eq. 2-41. The mass transfer coefficient was shown to be proportional to $\omega^{0.45}$ and to vary with fluid properties as expected. Butuzov and Rifert [78] also compared experimental data to Eq. 2-41 and found good agreement with experimental values 5-10% below theoretical prediction for rotational speeds above 52 rad/s. For these experimental runs, they also confirmed the exponent of 0.5 for angular velocity. Results lower angular velocities were adversely affected by the setup, which employed a downward facing condensation surface. Butuzov and Rifert reported heat transfer coefficients of above 90 kW/(m^2·K) at 2139 rpm and the lowest heat flux studied. Typical for film condensation, higher heat fluxes lead to thicker films and therefore lower heat transfer coefficients. They estimated heat transfer enhancement of rotating disks over condensation on vertical surfaces to equal a factor of 3 to 5. This statement agrees with Sparrow and Gregg's [76] estimation that enhancement factor E equals Eq. 2-46. Thus, the heat transfer of rotating disks was said to overtake the heat transfer from vertical condensation surfaces when the condition given in Eq. 2-47 is fulfilled.

$$E = \frac{h_{rot}}{h_{grav}} = \left(\frac{8}{3}\frac{x\omega^2}{g}\right)^{\frac{1}{4}} \qquad 2\text{-}46$$

$$\omega^2 > \frac{3g}{8x} \qquad 2\text{-}47$$

Overall, latent heat transfer of spinning disk seems to be better understood in the research community than sensible heat transfer. With latent heat transfer, the flow rate on over the disk is less uncertain as it can be calculated from the similar problem of condensation on vertical planes. Experimental results agree well with theory and

confirm the substantial enhancement potential of spinning disk reactors in this field. However, there no studies on the latent heat transfer when bulk flow is present such as the absorption process in an absorption cooling system.

2.4.4. Internal heat transfer

Few studies have incorporated an internal cold wall into the design of a spinning disk reactor. While internal circulation of a heat transfer fluid is the expected heat removal method for most actual applications, studies on heat transfer characteristics largely relied on heat flux from an internal electric heater to the outside film. Usually, the disk itself consists of a highly conductive material or a sub-disk made of highly conductive material is used. Heating elements below the disk provide the heat input. An arrangement of that form can only be used for experiments in which heat is added, not removed. However, exothermic reactions require cooling by a heat transfer fluid circulating within the disk. Usage of a heat transfer fluid may also be advantage in some heating applications. Hence, circulating heat transfer fluid is the prime mode of heat transfer in most applications. Notwithstanding, little attention has been spent on the internal heat transfer resistance of spinning disks used as heat exchangers in the available literature. For example, studies regarding production of chemicals using spinning disk reactors that included internal cooling emphasized its effectiveness but did not measure heat transfer rates [27,28].

One exemption is a publication on manufacturing of pharmaceuticals by Oxley et al. [83] who used the Colburn j_h factor (Eq. 2-48, found e.g. in [117]) for heat transfer on the surface of a disk that had a diameter of 0.15 m.

$$Nu = j_h Re\ Pr^{\frac{1}{3}} \left(\frac{\mu_{bulk}}{\mu_{wall}}\right)^{0.14} \qquad 2\text{-}48$$

The disk was cooled through a fluid circulating through a channel below the surface of the disk. They chose the film thickness as characteristic length for the Nusselt number but did not provide further info on the j_h factors that had been applied. Using water as heat transfer fluid at a volumetric flow rate of 100 mL/s and a brass disk with a cooling channel width of 3 mm, values for the overall heat transfer coefficient vary between 2200 W/(m^2·K) at 20 mm radial distance from center and 1100 W/(m^2·K) at 60 mm radial distance from center according to their calculations. Decreasing the width of the cooling channel to 1 mm, U-values increase to 4400 W/(m^2·K) and 2700 W/(m^2·K) respectively. The authors stated that experimental results agreed with the calculations but do not disclose the level of agreement. They further detailed that a smaller channel promoted turbulence. However, given flow rates and dimensions, flow should be laminar.

The internal heat transfer of spinning disk heat exchangers was topic of two patents by Burns and Henderson [86,106]. One patent [106] disclosed a spinning disk with spiral passageway for the heat transfer fluid on the internal face of the spinning disk. A prototype was fabricated using copper. The disk was 5 mm thick and spiral channels had dimensions of 10 mm times 10 mm with 2 mm fin thickness. 300 mL/s of water

were pumped as heat transfer fluid through the spirals and 15 mL/s of water were flowing over the top surface while the assembly was rotating at 650 rpm. The inventors claimed that an overall heat transfer coefficient of 9.7 kW/(m^2·K) was realized with this setup. While not provided in the patent disclosure, simple analysis suggests that internal heat transfer has to be on the order of 27 kW/(m^2·K) to achieve the cited overall heat transfer coefficient. This is roughly in line with the prediction of the Dittus-Boelter-equation. In the second patent [86], the same authors described an enhanced spreader plate. They suggested profiling of the surface that serves as the lower plate of the cooling channel the upper plate of which is the backside of the spinning disk. The profile of this surface could be modified in a way to make the height of the gap between the two surfaces inversely proportional to the radial position. Thus, radial velocity could be kept constant and heat transfer could get enhanced without too much penalty in terms of an increase in pressure drop.

Recently, the concept of flat plate manifold-microchannel heat exchangers has received a lot of attention as experimental and numerical investigations revealed favorable heat transfer and pressure drop characteristics of this type of heat exchanger [21,22]. Single-phase experiments with water in a low heat flux setting found the heat transfer coefficient to be as high as 66,000 W/m^2K for counter flow configuration [21]. The microchannel plate was made of copper. Width of microchannels was 40 μm and fin height and width was 360 μm and 90 μm, respectively. High heat transfer enhancement is achieved because the water entering the microchannel exhibits developing flow characteristics; Andhare et al. [21] report Nusselt number of 7.58 for

a Reynolds number of 30. Still, pressure drop stays low because many microchannels are operated in parallel. While the concept of manifold-microchannels has not been applied or proposed to rotating disk applications, it certainly offers an interesting way to enhance heat transfer on the internal face of the disk. Difficulties expected to lie in machining the microchannel into the surface of the disk and in the unusual geometrical configuration.

In summary, the internal heat transfer process of spinning disk reactors has not been subject to detailed studies although it is very important for industrial applications of the concept. Most researchers describing chemical processes carried out on spinning disk reactors with internal cooling do not specify the cooling performance. Two patents have been filed to increase the effectiveness of internal heat transfer. Adaption of innovative concepts such as manifold-microchannel technology could improve the overall heat transfer performance of spinning disk reactors substantially.

2.4.5. Mass transfer

There are two different types of mass transfer operations that are enhanced by the use of centrifugal forces in spinning disk reactors. The solid-liquid mass transfer at the interface of disk surface and liquid is the more commonly studied and has found its way into standard textbooks (e.g. [118]). Boundary layer analogies apply at the laminar flow of liquid over the disk surface where the process takes place. The problem of gas absorption differs in that the vapor-liquid mass transfer takes place at the free surface where the standard assumption is no shear and boundary layer analogies do not apply.

Several theoretical models were developed by Venkatamaran [119]. Wood and Watts [96] cited Venkatamaran's model for small depth of penetration in different form but it can be shown to collapse to Eq. 2-49 with α equal to 0.764. They compared it to experiments of absorption of carbon dioxide into water and found it to agree reasonably well. Lim [120] compared his results to Venkataraman's "approximate" model, which can be shown to be equal to Eq. 2-49 with α equal to 0.431. His experiments of absorbing oxygen into water yielded mass transfer coefficients approx. 25-100% above model predictions. The results of the earlier works of Lim and Wood and Watts are thus in disagreement with the later investigation of Aoune and Ramshaw [13], who found experiments using an oxygen-water system to surpass predictions based on their version of the Higbie model by a factor of 5.

$$\bar{h}_m = \alpha \left(\frac{Q^2 \omega^2 D^3}{\nu r_o^4} \right)^{\frac{1}{6}} \qquad 2\text{-}49$$

Rahman and Faghri [89] developed an analytical and numerical solution for both vapor-liquid and solid-liquid mass transfer. They assumed an inlet where the fluid is discharged from a pressurized container at a certain inlet radius equivalent to the controlled liquid jet entrance condition in later works. However, a parabolic velocity typical for free surface flow was assumed at the entrance without the consequences of shear stress that would result from a stationary disk restricting the flow in z direction. After discharge, the flow was driven by both inertial and centrifugal forces. After simplifying assumptions, the concentration equation reduced to Eq. 2-50.

$$u\frac{\partial C}{\partial r} = D\frac{\partial^2 C}{\partial z^2} \qquad 2\text{-}50$$

From the momentum equation, they obtained the basic Nusselt equation but used the free surface as the zero coordinate in axial direction instead of the standard convention of setting z = 0 at the wall surface. Equations were non-dimensionalized such that the concentration equation became Eq. 2-51. ψ, ξ, ζ, Z were non-dimensionalized concentration (Eq. 2-52), radial coordinate (Eq. 2-53), radial coordinate combined with fluid and flow parameters (Eq.2-55), and axial coordinate (Eq. 2-54), respectively. The definition of Z (Eq. 2-54) was changed to stay with notation used here of axial coordinate equal to zero at the disk surface.

$$(1 - Z^2)\frac{\partial \psi}{\partial \zeta} = \frac{\partial^2 \psi}{Z^2} \qquad 2\text{-}51$$

$$\psi = \frac{C_s - C}{C_s - C_{in}} \qquad 2\text{-}52$$

$$\xi = \frac{r}{r_{in}} \qquad 2\text{-}53$$

$$Z = \frac{\delta - z}{z} \qquad 2\text{-}54$$

$$\zeta = 0.1733 Re_{r,in}^{-\frac{4}{3}} E_{r,in}^{-\frac{2}{3}} Sc^{-1}[\xi^{\frac{8}{3}} - 1] \qquad 2\text{-}55$$

The non-dimensionalized transport equation was solved by separation of variables using the standard boundary conditions ($Z = 0, \psi = 0; Z = 1, \partial\psi/\partial Z = 0; \zeta = 0, \psi = 1$) and Eq. 2-56 followed. In Eq. 2-56, M are hypergeometric functions and λ_n eigenvalues, values of C_n and λ_n were given in a Table [89].

$$\psi(\zeta, Z) = \sum_{n=1}^{\infty} C_n \exp(-\lambda_n^2 \zeta) \exp\left(-\frac{\lambda_n Z^2}{2}\right) \lambda^{\frac{1}{2}} \zeta M\left(\frac{3-\lambda_n}{4}, \frac{3}{2}, \lambda_n Z^2\right) \qquad 2\text{-}56$$

As outlined by Rahman and Faghri in an earlier work [88], the numerical part of their work solved equations of motion and transport for a pie shaped flow domain. With respect to film thickness, the numerical simulation for intermediate Ekman numbers showed an initial increase in film thickness due to frictional effects on the inertial forces at the entrance. Further downstream, centrifugal effects were more important and caused a decrease in film thickness. The peak occurred at smaller radii for higher rotational speeds. The analytical solution did not include inertial entrance effects and thus showed monotonically decreasing film thickness while the numerical study accurately captures the trends in film thickness. In [88] the authors further showed that the numerical simulation resulted in an approximately parabolic velocity profile. As can be expected from the differences in the flow field, numerical and analytical solutions for mass transfer differed more at smaller radii [89]. Mass transfer results were presented in terms of Sherwood number, Sh_{ff}, based on kinematic viscosity and gravitational constant, which was said to be common in thin falling film literature. The numerical solution showed a strong decrease of Sherwood number in the entrance region due to the developing concentration boundary layer. It was followed by a minimum that corresponded to the maximum in film thickness. Analytically and numerically derived Sherwood numbers were in good agreement at larger radii. The effect of parameter variations on the Sherwood number was also investigated. An increase in inlet Reynolds number increased mass transfer in the entrance region where

inertia was increased but decreased mass transfer at larger radii where film thickness increased. The rate of absorption over the whole disk increased with decreasing inlet Ekman number; it doubled when rotational speed tripled.

Peev et al. [121] reviewed the work of Rahman and Faghri [89] and developed a simplified model based on the same analytical approach. In the theory of diffusion into liquid falling film, the simplification can be made that the absorbate does not penetrate far into the liquid film if the diffusion is slow, e.g. for the absorption of oxygen into water [122]. Then it can be assumed that the whole concentration boundary layer is located in a zone where velocity equals maximum velocity. Peev et al. [121] assumed that this assumption was justified because residence time of liquid on the spinning disk is low and the transport equation simplified to Eq. 2-57.

$$u_s \frac{\partial C}{\partial r} = D \frac{\partial^2 C}{\partial z^2} \qquad 2\text{-}57$$

Using the boundary conditions ($r = R_{in}, C = C_{in}; z = \delta, C = C_s, z = 0, C = C_{in}$) and referring to the solution of a similar problem in [122], the local mass flux followed (Eq. 2-58) and the mean mass flux was found by integration (Eq.2-59). This allowed to define the average mass transfer coefficient, Eq. 2-60.

$$N" = (C_s - C_{in}) \left(\frac{D u_s}{\pi r}\right)^{\frac{1}{2}} \qquad 2\text{-}58$$

$$\bar{N}'' = 0.468 \frac{r_o^{\frac{4}{3}} - r_{in}^{\frac{4}{3}}}{r_o^2 - r_{in}^2} (C_s - C_{in}) D^{\frac{1}{2}} Q^{\frac{1}{3}} \omega^{\frac{1}{3}} \nu^{-\frac{1}{6}} \qquad 2\text{-}59$$

$$\bar{h}_m = \frac{\bar{N}''}{C_s - C_{in}} \qquad 2\text{-}60$$

The average Sherwood number with disk radius as characteristic length is given by Eq. 2-61. The Sherwood number can be written in terms of Ekman, Reynolds and Schmidt numbers and Eq. 2-62 follows if the liquid feed is discharged at the center of the disk.

$$\overline{Sh}_{r_o} = \frac{\bar{h}_m r_o^{\frac{1}{3}}(r_o^2 - r_{in}^2)}{D(r_o^{\frac{4}{3}} - r_{in}^{\frac{4}{3}})} \qquad 2\text{-}61$$

$$\overline{Sh}_{r_o} = \frac{\bar{h}_m r_o}{D} = 0.864 Ek_{r_o}^{-\frac{1}{3}} \mathrm{Re}_{\mathrm{r_o,Q}}^{\frac{1}{3}} Sc^{\frac{1}{2}} \qquad 2\text{-}62$$

It can be shown that this result by Peev et al. is equivalent to the application of the so called Higbie penetration model to the problem. Higbie [123] described that industrial absorption equipment is characterized by short contact times of gas phase and a usually laminar layer of liquid. Thus, the depth of the boundary layer is very thin, e.g. 15 µm for the absorption of carbon dioxide into water after 0.01 seconds of exposure time. The mass transfer coefficient than results as in Eq. 2-63.

$$\bar{h}_m = \sqrt{\frac{4D}{\pi t_e}} \qquad 2\text{-}63$$

Different authors proposed to use average [14] and surface residence time [13] in Eq. 2-63. Using the definitions of average and surface residence time, the average mass transfer coefficient in Eq. 2-49 follows with factors parameter α equal to 0.59 and 0.72. Following the definition of the average Sherwood number in terms of dimensionless

numbers, Eq. 2-64 gives the Sherwood number following the Higbie model. β equals 1.085 and 1.329 for the cases of average and surface residence time, respectively.

$$\overline{Sh}_{r_o} = \frac{\bar{h}_m r_o}{D} = \alpha(2\pi)^{\frac{1}{3}} Ek_{r_o}^{-\frac{1}{3}} \mathrm{Re}_{\mathrm{r_o,Q}}^{\frac{1}{3}} Sc^{\frac{1}{2}} = \beta Ek_{r_o}^{-\frac{1}{3}} \mathrm{Re}_{\mathrm{r_o,Q}}^{\frac{1}{3}} Sc^{\frac{1}{2}} \qquad 2\text{-}64$$

Peev et al. compared dimensionless concentration calculated from Rahman and Faghri's numerical and analytical results and their own analytical solution and found average concentration from numerical solution to be highest as only numerical accounts for convective mass transfer in more than one direction. However, neither model was found to adequately capture the experimental results reported by Aoune and Ramshaw [13] which was contributed to the omission of wave effects in all models. Still, it was established that the optimized coefficients for the dimensionless numbers shown in Eq. 2-65 allowed to fit Aoune and Ramshaw's experimental data with an average error of 6%.

$$\overline{Sh}_{r_o} = 10.8 \cdot 10^{-4} Ek_{r_o}^{-0.94} \mathrm{Re}_{\mathrm{r_o,Q}}^{0.24} Sc^{\frac{1}{2}} \qquad 2\text{-}65$$

It shall be noted the experimental data did not include variations in Schmidt number. Eq. 2-65 also worked reasonably well when Aoune and Ramshaw's local mass transfer coefficients where plotted and correspondently local Reynolds and Ekman numbers employed. Peev et al. compared the semi-empirical correlation to the analytical model and contributed differences to the mass transfer enhancement of surface waves (Eq. 2-66). It is stated that enhancement due to flow waviness, which is calculated as increase of best-fit mass transfer correlation above initial theoretical prediction, lies in between 6 and 13.

$$\frac{\bar{h}_m}{\bar{h}_{m,th}} = 12.5 \cdot 10^{-4} Ek_{r_o}^{-0.64} Re_{r_o,Q}^{-0.09} \qquad 2\text{-}66$$

The effect of wave regime on vapor-liquid mass transfer was studied numerically by Sisoev et al. [124]. They found that wave formation led to deformation of the diffusion boundary layer, which increased gas absorption. Woods [97] estimated the additional surface area due to waves to be close to 1 percent and thus ruled out that increase in surface area is responsible for high mass transfer rates of spinning disk devices. Sisoev et al. described in another publication [125] how grooved patterns on the disk surface increase waviness. Based on their own numerical waviness model and the experimental data by Aoune and Ramshaw, Sisoev et al. formulated a quantitative model to calculate mass transfer that has been reported by Jachuck and Burns [14]. In their correlation, Sisoev et al. proposed to use a characteristic film thickness defined in Eq. 2-67. Mass transfer coefficient and Sherwood number based on characteristic film thickness are given in Eqs. 2-68 and 2-69, respectively. The Sherwood number showed a positive relationship with both rational speed and liquid flow rate which was attributed to increased surface waviness with an increase of these parameters. The model by Sisoev et al. is the only correlation that includes surface tension, a parameter that can be expected to be relevant if surface waviness increases mass transfer.

$$\delta_c = \frac{2}{3}\bar{\delta} = \left(\frac{3Q\mu}{2\pi r_o^2 \omega^2 \rho}\right)^{\frac{1}{3}} \qquad 2\text{-}67$$

$$h_m = 0.154\left(\frac{\delta_c^5 \omega^8 r_o^4 \rho D^3}{\nu^3 \sigma}\right)^{\frac{1}{6}} \quad 2\text{-}68$$

$$Sh_{\delta_c} = \frac{h_m \delta_c}{D} = 0.154\left(\frac{\delta_C^{11} \omega^8 r_o^4 \rho}{D^3 \nu^3 \sigma}\right)^{\frac{1}{6}} \quad 2\text{-}69$$

In conclusion, a number of different formulas to calculate mass transfer of spinning disks have been brought forward by different researchers. Early models were based on the Higbie penetration model and some researchers found reasonably good agreement with experiments, albeit experimentally deducted values were usually higher. Aoune and Ramshaw [13] reported experimental mass transfer rates far above those predicted by the Higbie model and two research groups developed semi-empirical mass transfer correlations based on the experiments reported by Aoune and Ramshaw. Peev et al. [121] expressed the Higbie model using non-dimensional numbers and changed coefficients based on a data fit. Sisoev et al. [14] developed a correlation by fitting Aoune and Ramshaw's experimental data to their model on absorption into wavy surface. Thus, overall the uncertainty over the scale of mass transfer enhancement is still substantial.

2.5. Previous development of a rotary heat pump

Several patents and publications report on the opportunities to enhance heat and mass transfer of absorption heat pumps through the use of centrifugal forces [17–19,72,74,75]. The earliest reference is a patent filed by Cross and Ramshaw of Imperial Chemical Industries (UK) in 1984 [17]. The invention was designed to provide heating

at a COP greater than one using a gas-fired boiler as heat input. All mass transfer units of the heat pump were flat plates mounted on one rotary shaft (Figure 2-9). The pump was to supposed to be of rotary type, also being driven by the rotational shaft. Absorber and evaporator were integrated into one unit consisting of several plates, where condensable vapor and lean solution were fed on one face the plates while the liquid refrigerant coming from the condenser was fed on the other. This subchapter will expand on the overview provided in Table 2-6.

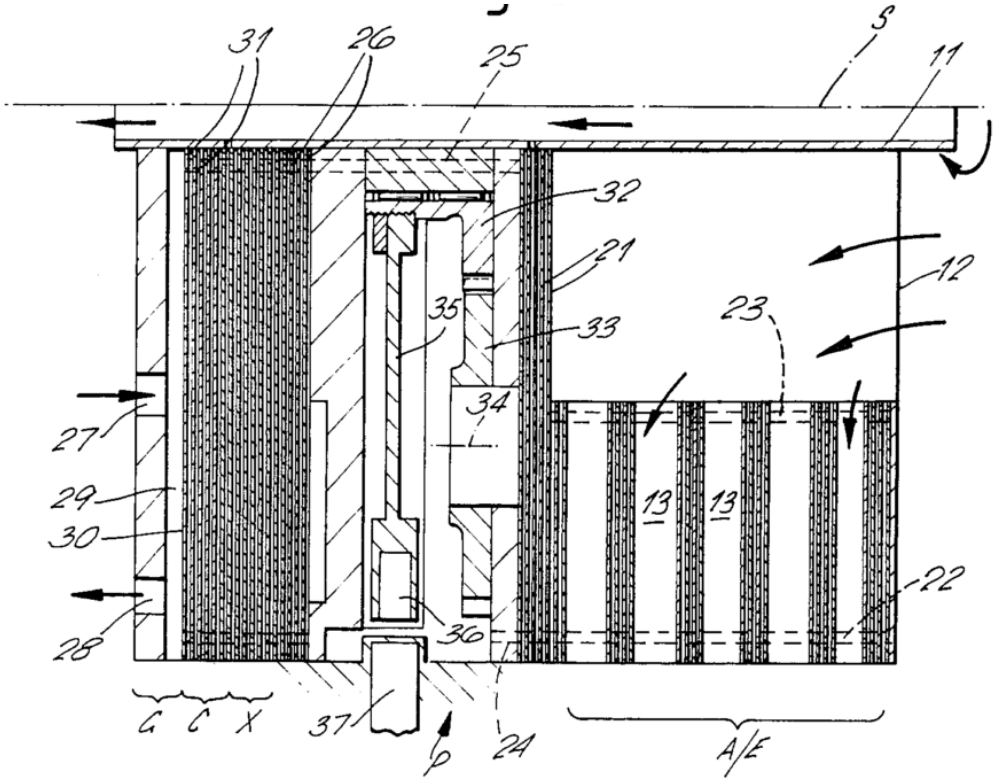

Figure 2-9: Centrifugal heat pump. G = Vapor generator, C = Condenser, X = Solution heat exchanger, P = Rotary pump, A = Absorber, E = Evaporator. Figure from [17].

Results of a first prototype, called “Rotex” are reported in [72]. The design, shown in Figure 2-10, exhibits some deviations from the previously filed patent. In the revised design, condenser and absorber unit were integrated into one unit consisting only of one plate. As both units reject heat, internal cooling was introduced. The evaporator was changed to oval tube type and refrigerant flow was recirculated in evaporator to improve wetting. The absorbent was a mixture of very strong solutions of potassium hydroxide (KOH) and sodium hydroxide (NaOH) which can withstand high heat input temperatures in the generator and can generate a high temperature lift. Caesium hydroxide was added to influence crystallization and vapor pressure behavior. Refrigerant in this system was water. The prototype achieved a COP of 1.2 in heating mode at 30°C temperature lift.

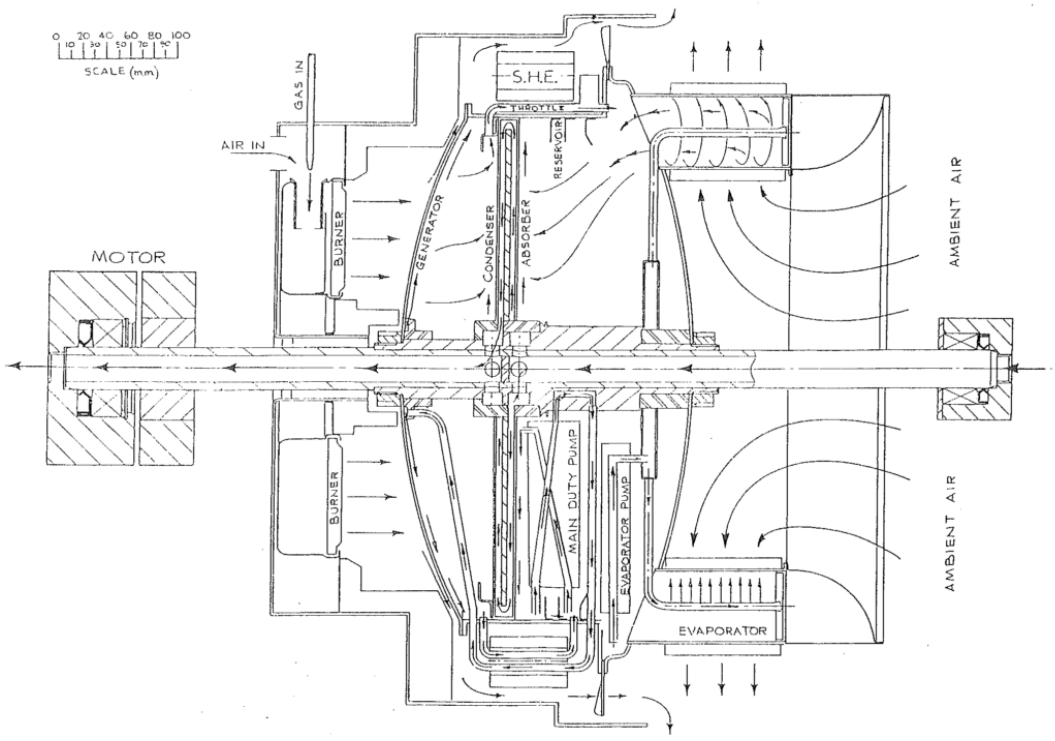

Figure 2-10: First prototype of centrifugal absorption heat pump "Rotex". Figure from [72].

Several problems with respect to operation and performance of the prototype were reported:

1) Vacuum sealing and built-up of non-condensable gases.
2) Heat spreading in the unit.
3) Splashing.
4) Distribution of absorbent on the generator plate.

As the price of natural gas declined during the development phase, the objective to commercialize the heat pump as a high efficiency heating device became less attractive. An international consortium with Spanish, American and British companies was

formed to redesign the product into a double-effect heat pump for cooling purposes, called “Interotex” [73]. Substantial efforts were made to advance the project, with a total of 9 engineers plus additional manpower from the consortia members assigned to work it. The machine design was changed again, partially to reflect double-effect operation with three pressure levels (Figure 2-11).

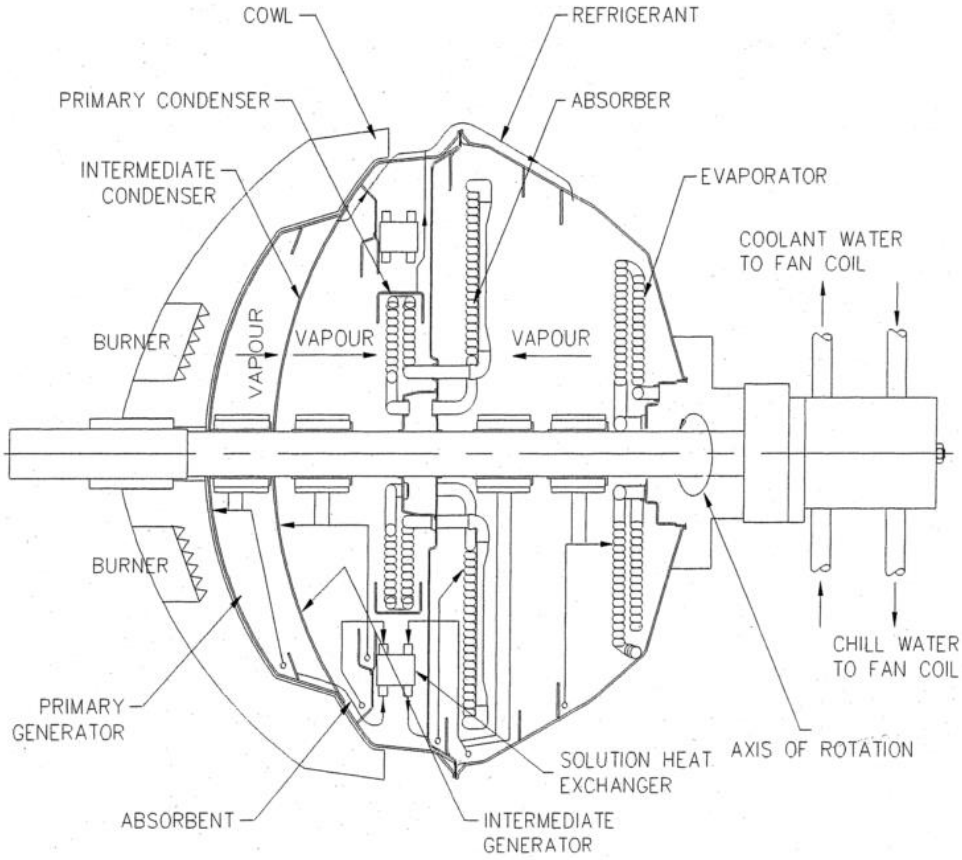

Figure 2-11: Drawing of double-effect rotary heat pump design Interotex. Figure from [74].

Further, the absorber and primary condenser were changed from flat plate type to coil type. Experimental results are reported in [74]; the hydroxide absorbent allowed to

reject heat at a high cooling water exit temperature of 52°C which resembles dry cooling and would not be possible with conventional water/lithium bromide system due to crystallization limitations. COP was 0.76 at 8.8 kW cooling capacity for a system with a diameter of 0.5 m and a length of 0.5 m. The target COP from modeling the system was 0.9, indicating unpredicted inefficiencies in the machine. Corrosion issues with the KOH/NaOH mixtures proved to be persistent and the developers switched to lithium bromide as absorbent [75]. With water/lithium bromide as working fluid, the rotary chiller achieved a performance of 10.5 kW cooling capacity at a COP of 0.9 at ambient temperature of 32°C, indicating that dry heat rejection in moderate climate is possible. Operated in double effect configuration, the chiller used flat plates for primary and intermediate generators. The film heat transfer coefficient of the intermediate generator was 9 kW/(m^2·K) and overall heat transfer coefficient of the intermediate condenser/intermediate generator 6.5 kW/(m^2·K). The intermediate generator operated at a temperature of 107 °C and a pressure of 12 kPa, one order of magnitude higher than the typical pressure for absorbers. While the whole chiller was integrated in one rotating enclosure, it was reported that highest process intensification was achieved through the flat disk generators. The absorber was listed as the major area of future development as it is the mass transfer units with tightest temperature, concentration and pressure drop operation windows and most challenging fluid properties. The unit of 0.5 m diameter and 0.5 m length was supposed to deliver a cooling capacity of 10.5 kW.

The Spanish companies Fagor Electrodomesticos s.Coop. and gasNatural SDG S.A. continued the development work and commercialized a single-effect rotary

absorption chiller “Rotartica” [19,126], pictured in Figure 2-12. A tube heat exchanger provided the dry heat rejection of the cooling fluid to ambient air. A review on heat absorption machines in 2011 listed Rotartica as one of only two lithium bromide – water absorption machines that allow dry cooling [127]. The unit was marketed for solar absorption cooling applications and operational data is reported in [93]. A 20 days test trial in summer climate in Madrid, Spain, resulted in average COP of 0.49. Conventional electric resistance heating was used as heat source. If electric power for auxiliary units and the respective generation efficiency is taken into account, the COP based on primary energy decreases to 0.37. As of 2017, Rotartica is believed to be out of business with the exact cause for the commercial failure unknown. However, it seems likely that the performance of the device was not strong enough to justify the additional expenditures associated with rotation of the assembly.

Figure 2-12: Rotartica 045 rotary absorption chiller. Figure from [126].

In summary, a substantial research effort has been invested in the development of rotary absorption heat pumps from the 1980's until the early 2000's. Patents and published performance data has proven the viability of the concept. However, since the development was advanced by commercial companies throughout, no detailed design data, operating conditions and performance correlations are available in the published literature. The design of the machine went through several iterations, some associated to changes do the objective due to economic considerations. While the first design used flat disk for all transfer units, later stages switched to coil type designs for evaporator and absorber. The reasons for the design change were not discussed in the open literature. Still, the flat disk designs of intermediate generator/condenser unit were said to have achieved the highest process intensification. The combined intermediate condenser / intermediated generator achieved an overall heat transfer coefficient of 6.5 $kW/(m^2 \cdot K)$ with lithium bromide – water as working fluid.

3. Experimental study of spinning disk absorber

This chapter describes the development, design and fabrication of a first generation spinning disk absorber. Further, experimental test results are presented and discussed. Figure 3-1 shows a graphical abstract of the work presented in this chapter.

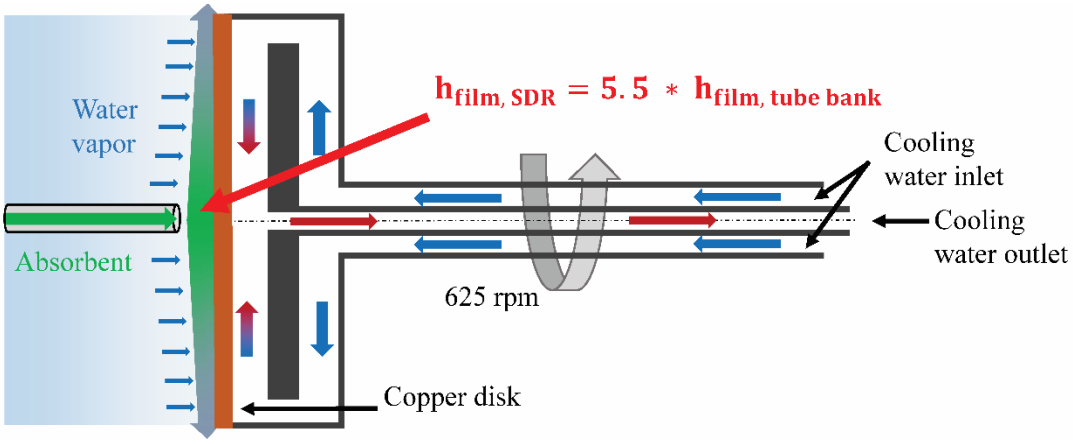

Figure 3-1: Graphical abstract of work presented in chapter 3.

3.1. Description of absorber design and experimental setup

3.1.1. Design of the test section

A spinning disk reactor used as the absorber increases heat transfer through and mass transfer into the liquid absorbent film. For the reactor to take full advantage of this enhancement, good heat rejection capabilities are required throughout the whole assembly. The wall in contact with the absorbent solution should exhibit low thermal resistance, while heat losses everywhere else and heat transfer between the hot and cold sides of the cooling water should be mitigated. At the same time, operation under vacuum requires effective vacuum sealing and structural reliability. Figure 3-2 shows

a schematic of the spinning disk reactor assembly used in this work. The axis of rotation of the disk aligned horizontally. The surface of the disk assembly that was in contact with the absorbent solution consisted of a 6.35 mm-thick copper plate of a diameter of 0.305 m. The plate was cooled internally using a thin channel of 0.263 m diameter. Cooling water flowed through the channel in counter flow operation. The backside of the channel was constricted by an acetal disk that also prevented heat transfer between the hot and cold sides of the cooling water through its low thermal conductivity. Both cooling water supply and return flowed through co-axial tubing in the drive shaft. Here, air insulation (not shown in Figure 3-2) between the cold and hot sides prevented heat transfer. A rotary feedthrough inserted into the vacuum chamber incorporated bearings and lip seals and aided to secure the disk assembly. The drive shaft was connected to the cooling water loop by a custom-designed rotary duo-flow valve.

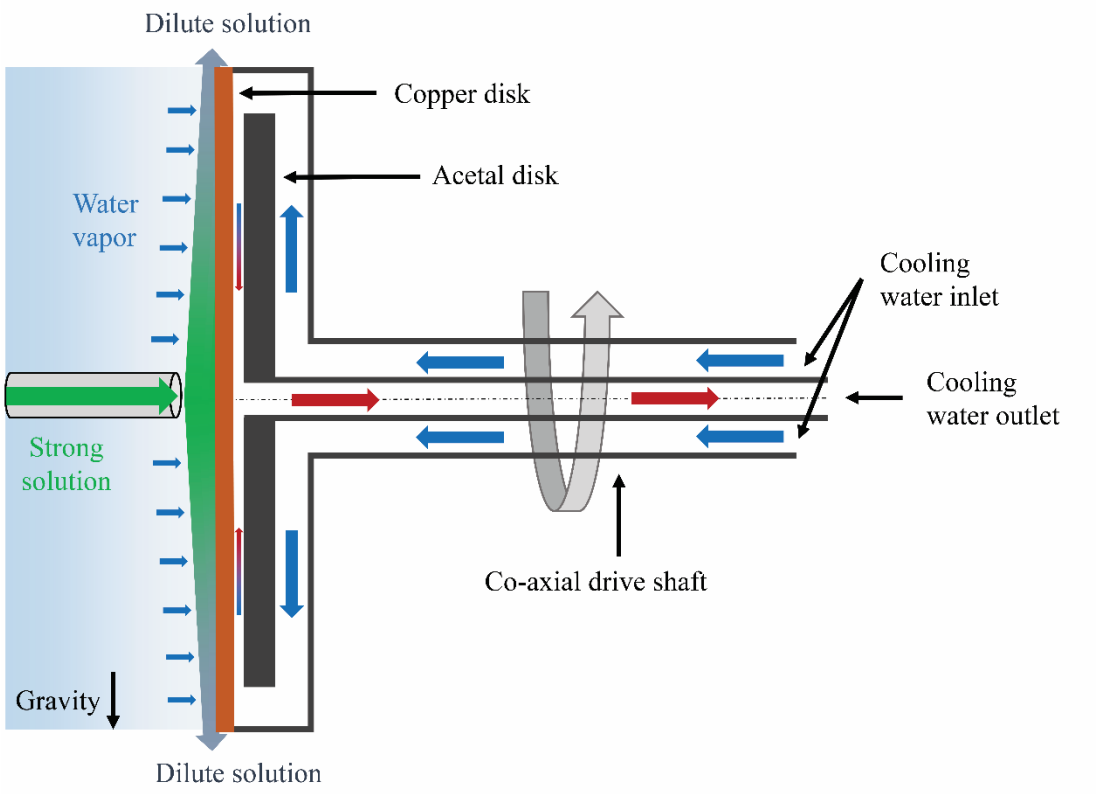

Figure 3-2: Schematic of spinning disk assembly.

Figure 3-3 shows the various components in more detail with additional specifications as follows:

1: The surface disk in contact with the absorbent solution has a radius of 0.15 m, a thickness of 6.2 mm and is made out of copper. Copper ensures minimal heat transfer resistance while deformation at 1.5 bar pressure difference is 0.44 mm.

2: Stainless steel sealing ring with O-ring glands on both surfaces. Components 1, 2 and 3 all have 36 thru-holes for fastening.

3: Back disk, similar dimensions as 1 but made out of stainless steel.

4: Delrin plate of 0.13 m diameter. The width of the cooling channel between 1 and 4 defines the internal heat transfer coefficient and influences pressure drop. Low conductivity of Delrin (also known as polyoxymethylene or acetal) minimizes heat transfer between hot and cold side of cooling fluid.

5: 12 sealing screws on two different radii in conjunction with shim washers control the width of the cooling channel. The width of the cooling channel is thus flexible and can be changed by adding shim washers.

6: Outer shell of the shaft. Cooling fluid enters disk assembly through annular gap between outer and inner shell of shaft and flows along back surface of copper disk in counter flow direction to absorbent on top surface of the copper disk. It exits through 7.

7: Inner shell of the shaft actually consists of two thin tubes welded together with a small air gap in between for insulation.

8: Two consecutive lip seals for vacuum sealing

9: Bearings.

10: Aluminum tubing that to keep bearings in place.

11: Keyless timing pulley.

12: Stationary duo-flow rotary valve facilitates connection between cooling water supply/return and rotating disk assembly.

13: Nut tightening in direction of spinning disk to prevent movement in axial direction towards top disk.

14. Cover plate which provides support to bearing, connected to rotary feedthrough.

15. Rotary feedthrough: Connects to feedthrough of vacuum chamber and provides housing for bearing and sealing. Prevents movement in axial direction.

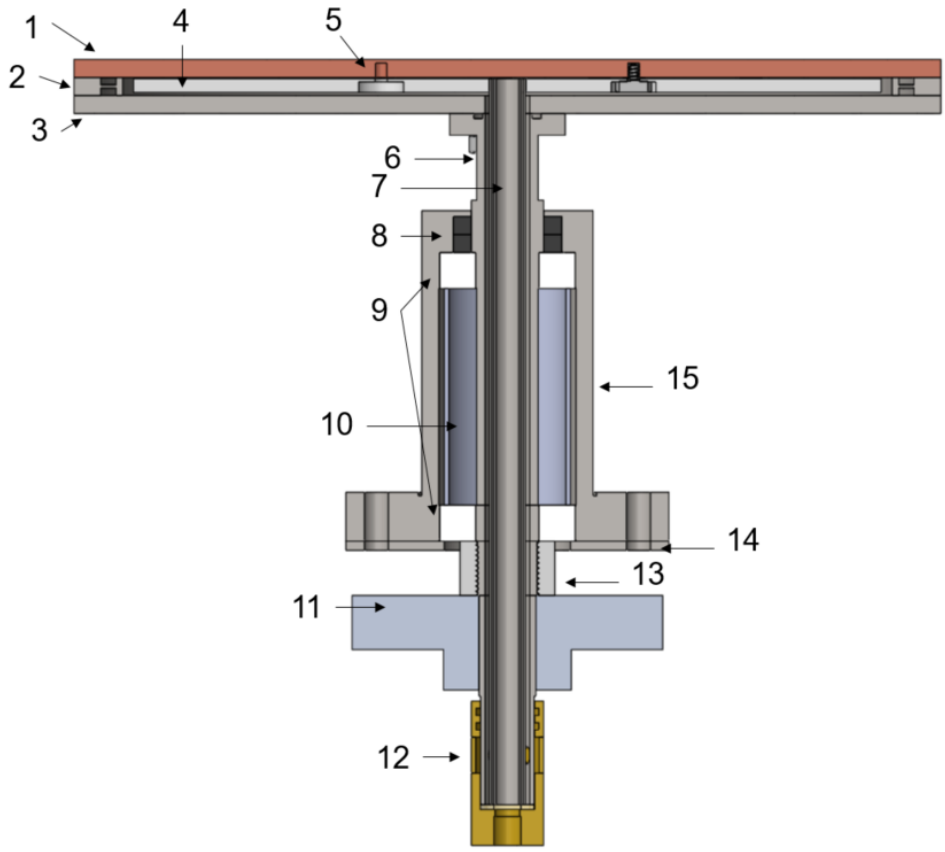

Figure 3-3: Drawing of spinning disk absorber including auxiliary parts.

The disk assembly shown in Figure 3-3 is held in place by a rotary feedthrough that is inserted into a feedthrough of the vacuum chamber. A drawing of the vacuum chamber with its support structure is shown in Figure 3-4. The spinning disk absorber is operated in with the axis of the drive shaft in aligned with the horizontal. This arrangement allowed direct connection to the evaporator of a full loop absorption cooling system for later stage testing.

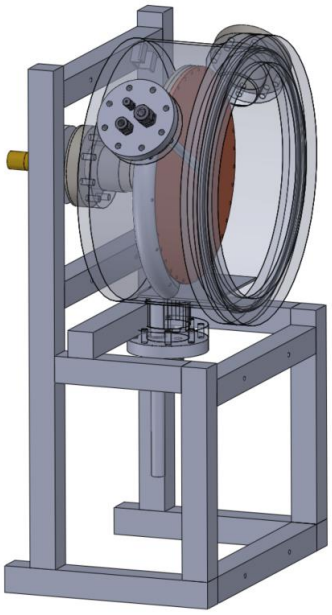

Figure 3-4: Drawing of spinning disk absorber, vacuum chamber and support structure.

3.1.2. Experimental setup

Figure 3-5 and Figure 3-6 show a schematic and a picture, respectively, of the test setup, which consisted of a combined absorber/generator chamber that operated at one pressure level. The spinning disk reactor served as the absorber, and an electric heater was used as generator. The strong solution was fed at the center of the disk by a nozzle located 3 mm from the surface of the disk. The disk rotated at velocities between 125 and 625 rpm. To measure the temperature of the solution as it was thrown off the disk, the solution was partially captured by two 3D-printed run-off trays. The trays were located to the lower left and upper right side of the spinning disk. From the trays, the solution flowed by gravity towards a 7.5 kW electric heater. A stainless-steel plate

between the generator and absorber sections prevented the violently boiling solution from throwing regenerated liquid back towards the disk. The plate is not shown in Figure 3-5 for simplicity. Heat transfer between the vacuum chamber and ambient was minimized by foam rubber insulation of 12.7 mm thickness. The lid of the vacuum chamber was made of Pyrex to allow visual access to the surface of the disk and the path of the fluid within the chamber.

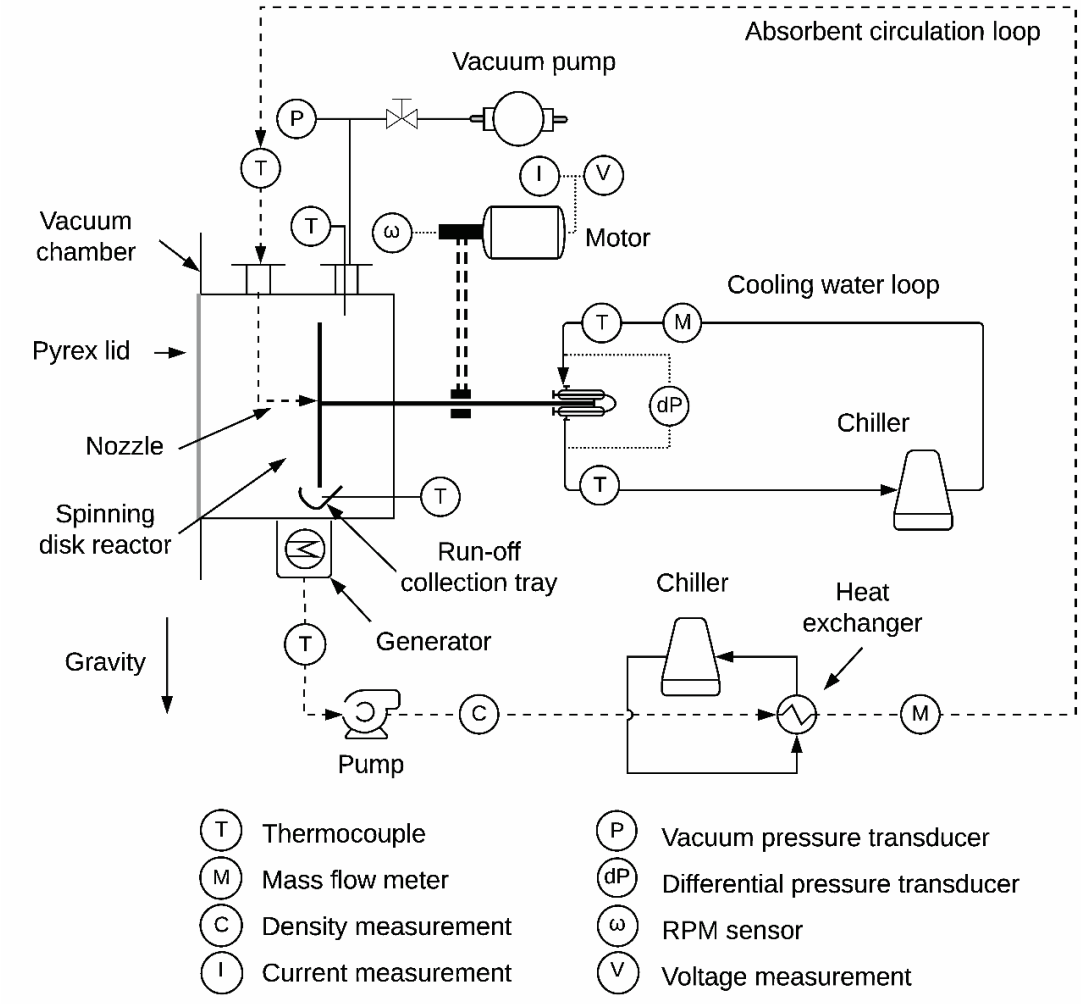

Figure 3-5: Schematic of the experimental setup.

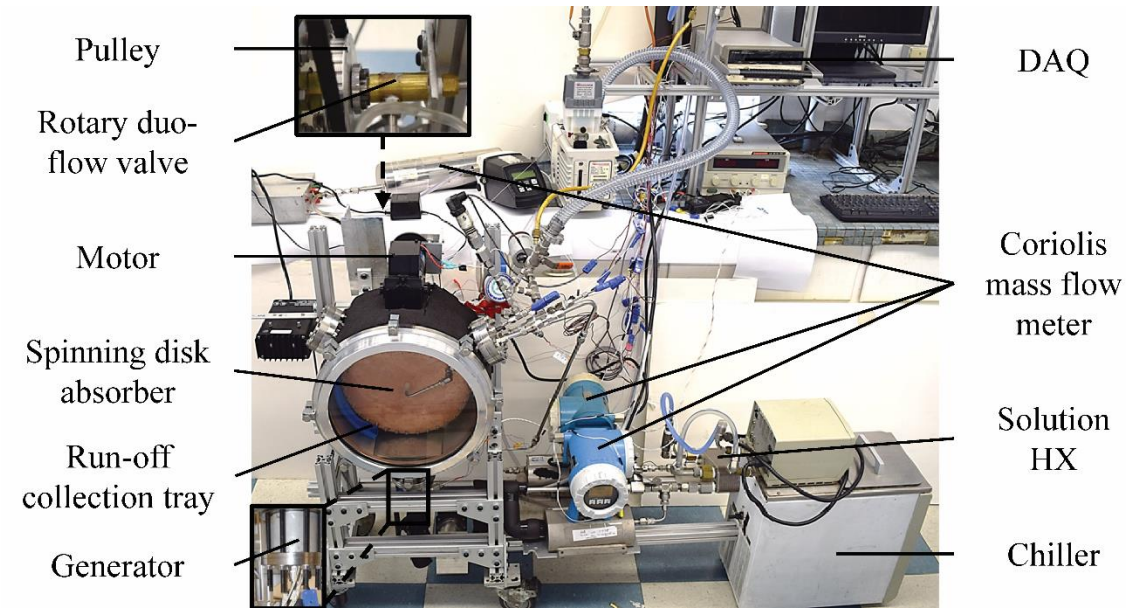

Figure 3-6: Photograph of the experimental setup.

Two Coriolis flow meters measured the flow rate and density of the solution. A plate heat exchanger connected to a chiller pre-conditioned the solution before it was recirculated to the absorber. Concentration of lithium bromide was controlled to an accuracy of ± 0.1 wt.-% and subcooling of the solution to ± 1 K. Subcooling is defined as the difference between saturation temperature of the solution at the inlet to the absorber, which depends on pressure and concentration, and its actual temperature. A positive value indicates that the solution needs to absorb water vapor to reach equilibrium, while a negative value signifies a supersaturated solution. Experiments have shown that the effect of subcooling on film-side heat transfer coefficient is approximately 1% reduction in film-side heat transfer coefficient per 1 K of subcooling at the conditions relevant for the current study [43]. Cooling water for internal cooling

of the disk was supplied and exited through the drive shaft of the disk. A 0.5 hp DC motor connected to a variable power supply rotated the disk. A shaft speed sensor measured rotational speed of the motor shaft.

Figure 3-7 shows an image of the spinning disk absorber during operation. The liquid feed is impinging in the middle of the disk and is driven outward by centrifugal forces. The blue trays to the left and right of the disk capture liquid as it is thrown of the disk. A T-type thermocouple probe inserted at the lower end of the trays measures the temperature of the liquid. The solution flows towards a feedthrough at the lowest location of the vacuum chamber by gravity. The stainless steel plate can be seen just below the rotating disk.

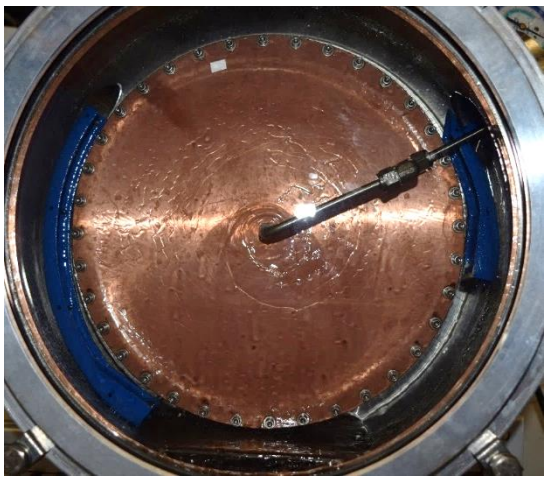

Figure 3-7: Front view on spinning disk absorber during operation.

3.1.3. Characteristics of operation

Table 3-1 lists operating conditions during the experiments and specifications of the absorber. Data related to relevant tests of a conventional absorber by Kyung and Herold [43,128] are included for comparison purposes. Most experiments were carried out at constant pressure of 1100 Pa. A few data sets investigated the effect of pressure and included data acquisition at 1100 Pa and 2000 Pa. Changes of any experimental parameter caused the equilibrium pressure of the system to shift. Therefore, the voltage supplied to the generator, and thus the heat input into the system, was controlled to achieve constant pressure at otherwise varying operating conditions. In this manner, pressure was controlled within ± 10 Pa. Once the system reached steady state, data were logged over a period of one minute for subsequent analysis.

Table 3-1: Absorber specifications and operating conditions.

Parameter	**Current study**	**Kyung and Herold** [43,128]
Absorber type	Spinning disk	Horizontal tube bundle (4 tubes)
Internal/film-side heat transfer surface area of absorber [m^2]	0.054 / 0.073	0.072 / 0.086
Inlet mass fraction [wt.-% LiBr]	57.2 / 60	60
Mass transfer enhancing surfactant	None	None
Solution mass flow rate [kg/s]	0.010 - 0.0275	0.01 - 0.035
Inlet subcooling [°C]	1.0	0.0
Cooling water mass flow rate [kg/s]	0.090	0.126
Cooling water supply temperature [°C]	30.5	30.0
Pressure [Pa]	1100 / 2000	1093

To prevent corrosion, the setup was pressurized with nitrogen whenever not in operation to avoid the introduction of oxygen. At the start of experiments, the system was purged with a vacuum pump while circulating the absorbent solution. Vacuum leakage rate was less than 0.5 Pa/min, and purging was performed at regular intervals to prevent build-up of air inside the system.

3.2. Data reduction and analysis

Researchers most commonly analyze the flow of a liquid over rotating disks by adapting Nusselt's [95] description of condensation on vertical plates as described by Wood and Watts [96] and Bell [100]. If gravitational acceleration is replaced by centrifugal acceleration, local film thickness and radial velocity profile and are given by Eqs. 3-1 and 3-2, respectively [13]:

$$\delta = \left(\frac{3\mu\dot{m}}{2\Pi r^2\omega^2\rho^2}\right)^{\frac{1}{3}} \qquad 3\text{-}1$$

$$u = \frac{r\omega^2\rho}{\mu}\left(z\delta - \frac{z^2}{2}\right) \qquad 3\text{-}2$$

Although more sophisticated models of the hydrodynamics have been developed, the Nusselt model captures the dominant characteristics of thin films flowing over rotating disks [70,97]. Integration of Eq. 3-1 yields the average film thickness over the disk surface (Eq. 3-3):

$$\bar{\delta} = \frac{\int_0^{2\pi}\int_0^R\int_0^\delta r\, dzdrd\phi}{\pi r^2} = \left(\frac{81\dot{m}\mu}{16\pi R^2\omega^2\rho^2}\right)^{\frac{1}{3}} \qquad 3\text{-}3$$

Different researchers proposed the use of different temperature profiles to derive average temperature of liquid film and heat transfer coefficient. For the case of sensible heat transfer, Wood and Watts [5] and Bell [100] assumed a cubic polynomial, while Aoune and Ramshaw [13] assumed a parabolic temperature profile. The standard assumption for laminar film condensation is a linear temperature profile [94]. The basic process of deducing average temperature and heat transfer coefficient is given by Aoune and Ramshaw [13]. However, there are inconsistencies in their derivation of both average temperature profile and heat transfer coefficient. Appendix I shows the calculations that lead to Eqs. 3-4 and 3-5 for average temperature and heat transfer coefficient, respectively, for a parabolic temperature profile. The value for heat transfer coefficient derived here is 50% higher than the value given in [13]:

$$T_{ave,par} = \frac{1}{5}T_w + \frac{4}{5}T_s \qquad 3\text{-}4$$

$$h_{par} = \frac{5}{2}\frac{k}{\delta} \qquad 3\text{-}5$$

Nusselt originally modeled a condensation process that results in heat transfer across a gas-liquid interface. For the thin film that follows, he assumed a linear temperature profile. The average temperature of the liquid is given in Eq. 3-6, which, together with a parabolic velocity profile, leads to the heat transfer coefficient in Eq. 3-7 as shown in Appendix II.

$$T_{ave,lin} = \frac{3}{8}T_w + \frac{5}{8}T_s \qquad 3\text{-}6$$

$$h_{lin} = \frac{8}{5}\frac{k}{\delta} \qquad 3\text{-}7$$

Thus, a parabolic temperature profile results in a 56% higher heat transfer coefficient than a linear temperature profile. While the Nusselt profile and its assumptions are accepted for film condensation [94], its applicability to water absorption into lithium bromide solution is more ambiguous. Kyung et al. [129] analyzed the absorption process over tube banks in a 2D model and concluded that the temperature profile is non-linear for the first quarter of the flow distance. Therefore, the most accurate description may lie between the coefficients deducted for linear and parabolic temperature profiles.

Inserting average film thickness (Eq. 3-3) and a coefficient β instead of the constants in Eqs. 3-5 and 3-7, the average film-side heat transfer coefficient can be written as Eq. 3-8:

$$\bar{h} = \beta k \left(\frac{81\dot{m}\mu}{16\pi R^2\omega^2\rho^2}\right)^{-\frac{1}{3}} \qquad 3\text{-}8$$

The heat transferred to the cooling water loop of the absorber was calculated from the mass flow rate of cooling water and the temperature difference across return and supply lines (Eq. 3-9):

$$\dot{Q}_{CW} = \dot{m}_{CW} c_{p,CW} (T_{CW,out} - T_{CW,in}) \qquad 3\text{-}9$$

The efficiency of the electrical motor that spun the disk was taken from the motor curve. The power used for rotation after accounting for inefficiencies of the motor is given by Eq. 3-10. It was assumed that this power was lost due to friction in the sealing assembly.

The resulting heat was assumed to be picked up by the cooling water. Thus, the heat rejected during the absorption process was calculated as heat transferred to cooling water minus power used for rotation (Eq. 3-11):

$$P_{rot} = \eta\, I_M V_M \tag{3-10}$$

$$\dot{Q}_{abs} = \dot{Q}_{CW} - P_{rot} \tag{3-11}$$

In the absorption literature, log mean temperature difference in the absorber is commonly defined using saturation temperatures on the solution side as shown in Eq. 3-12 [10,20,43]:

$$\Delta T_{lm} = \frac{(T^{sat}_{sol,in} - T_{CW,out}) - (T^{sat}_{sol,out} - T_{CW,in})}{\ln\left[(T^{sat}_{sol,in} - T_{CW,out})/(T^{sat}_{sol,out} - T_{CW,in})\right]} \tag{3-12}$$

At the inlet to the absorber, saturation temperature can be calculated from the measured variables mass fraction and pressure. The saturation temperature at the outlet of the absorber depends on the mass fraction of lithium bromide at the outlet, which is given by Eq. 3-13. The mass flow rate of water vapor in Eq. 3-13 is unknown and must be determined through mass and energy balances, Eqs. 3-14 and 3-15, respectively:

$$x_{LiBr,out} = \frac{\dot{m}_{LiBr,in}}{\dot{m}_{sol,in} + \dot{m}_{H_2O(g)}} \tag{3-13}$$

$$\dot{m}_{sol,out} = \dot{m}_{sol,in} + \dot{m}_{H_2O(g)} \tag{3-14}$$

$$\dot{Q}_{abs} = h_{sol,in}\dot{m}_{sol,in} + h_{H_2O(g)}\dot{m}_{H_2O(g)} - h_{sol,out}\dot{m}_{sol,out} \tag{3-15}$$

The area of fluid flow over the surface of the absorber serves as control volume for the energy and mass balances. Eqs. 3-13 to 3-15 include the unknowns$x_{LiBr,out}$, $\dot{m}_{H_2O(g)}, h_{sol,out}\ and\ \dot{m}_{sol,out}$, which leaves the system of equations unspecified.

Yuan and Herold [130] developed a property expression for specific enthalpy of aqueous lithium bromide as a function of mass fraction, temperature and pressure. Since temperature and pressure are known, this equation can be used to solve the system of equations and to determine the mass of water vapor absorbed and related unknowns.

Once concentration at the outlet of the absorber is specified, the saturation temperature can be calculated. Then, overall heat transfer coefficient follows from Eq. 3-16. Since the heat removal ability ultimately depends on the internal heat transfer, the area of the channel inside the disk, i.e. only the actively-cooled area of the copper disk, was used to calculate U:

$$U = \frac{\dot{Q}_{abs}}{\Delta T_{lm} A_{ch}} \qquad 3\text{-}16$$

The flow in the internal cooling channel is laminar up to a radial distance to center of 13 mm. Thus, the turbulent area is negligible, and the Nusselt number for laminar flow between parallel plates with one heated and one insulated plate applies. Assuming an uniform temperature profile, the Nusselt number is equal to 4.86 [116]. With an average cooling channel width of 0.329 mm, the average hydraulic diameter is equal to 0.658 mm, and the internal heat transfer coefficient has a value of 4455 W/(m^2·K). This leads to an internal thermal resistance of 0.0041 K/W, while the copper plate has a conductive thermal resistance of 0.0003 K/W.

The combined conductive and internal convective resistances were further confirmed from experimental data by adaption of the Wilson plot technique [131]. The

total thermal resistance of the system is given by Eq. 3-17 and can be expressed by its individual components (Eq. 3-18):

$$R_{tot} = \frac{1}{UA_{ch}} \tag{3-17}$$

$$R_{tot} = R_{int} + R_{cond} + R_{film} \tag{3-18}$$

The internal resistance was constant, since flow was laminar and the cooling water mass flow rate did not change. Thus, Eq. 3-18 can be rewritten as a function of a constant, α, and the film-side heat transfer coefficient, Eq. 3-8, which leads to Eq. 3-19. If Eq. 3-8 is inserted while replacing the exponents for rotational speed and film thickness with γ and ϵ, respectively, Eq. 3-20 describes total resistance:

$$R_{tot} = \alpha + \frac{1}{A_{film}\bar{h}_{film}} \tag{3-19}$$

$$R_{tot} = \alpha + \frac{1}{A_{film}\beta k}\left(\frac{81\dot{m}\mu}{16\pi R^2 \omega^{\gamma}\rho^2}\right)^{\epsilon} \tag{3-20}$$

Eq. 3-20 can be fitted to measured values of total thermal resistance to quantify the unknowns α, β, γ and ε. Since the equation cannot be linearized in terms of these variables, a minimization scheme is needed [131], and an algorithm to solve non-linear least-squares problems was used. The variable of interest in Eq. 3-20 is α, the combined internal and conductive resistance, while the additional variables are included due to inherent uncertainty of Eq. 3-8 to predict the film-side heat transfer coefficient accurately. Initial fits revealed that Eq. 3-20 represents experiments at different rotational velocities reasonably well, but that the effect of changes in mass flow rate was not in agreement with the prediction of Eqs. 3-8 and 3-20.This observation is

consistent with previously reported experimental data [11,82,96] and most likely caused by increased mixing at higher flow rates [99,102]. Thus, Eq. 3-20 was fitted separately to seven data sets covering different vapor pressures, concentrations and mass flow rates. Film temperatures and concentrations were used to calculate thermo-physical properties. Each data set contained data from four different rotational velocities between 250 and 625 rpm. Data at 125 rpm, which were deemed to be influenced by the gravitational acceleration due to the vertical orientation of the disk's surface, were omitted. Each fit revealed values of the variables within the expected range: for example, β between 8/5 and 5/2, γ close to 2, and ϵ close to -1/3. The average value of α was 0.0045 K/W at an uncertainty of ± 8% in accordance with a 95% confidence interval. Thus, the measured combined internal and conductive resistance was close to the expected value based on design calculations. Accordingly, the Wilson plot technique confirmed that the performance agreed with expectations based on the design of the device within anticipated tolerances.

Although the experimental setup did not include a designated evaporator for production of chilled water, it is possible to calculate cooling capacity from the mass flow rate of water vapor that is absorbed. Since the absorption process releases heat of vaporization and heat of dilution, the cooling capacity must be based on the heat of vaporization of water only and not on the heat rejected by the absorber. The cooling capacity based on the mass flow rate of water vapor and enthalpy of vaporization is given by Eq. 3-21. The enthalpy of water was evaluated at the measured pressure.

Moreover, saturation was assumed since an evaporator would operate at saturated conditions.

$$\dot{Q}_{CC} = \dot{m}_{H_2O\,(g)}(h_{H_2O\,(g)} - h_{H_2O\,(l)}) \qquad 3\text{-}21$$

According to Kyung and Herold [43], the heat transfer coefficient is an appropriate gauge of the overall performance in absorption cooling systems because the heat and mass transfer processes are closely related. Therefore, heat and mass transfer coefficients convey largely similar information. In the present case, the solution leaving the disk is close to saturation, which makes calculation of a log mean concentration difference and a mass transfer coefficient highly uncertain, as it relies on a very small concentration difference at the exit. Thus, it is more reliable to measure the heat transfer coefficient, whose measurements are more accurate.

Table 3-2 lists limits of error of measurement variables. Equipment suppliers commonly do not differentiate between random and systematic uncertainties and therefore the uncertainty analysis in this study includes both types of errors. However, in order to further minimize the effect of random errors, measurements were collected over a time interval of 1 minute and averaged. Thermocouples that measured the temperature of cooling water were calibrated using high accuracy resistance temperature detectors. Uncertainty of measurement results was evaluated using the procedure outlined in NIST Technical Note 1297 [132]. According to the Technical Note, the uncertainty $u(y)$ of the output variable y, which is a function of input estimates x_1, x_2, …, x_N, can be calculated from the sensitivity coefficients $\partial f/\partial x_i$, the

standard uncertainty of the input measurement $u(x_i)$ and covariances $u(x_i, x_j)$ (Eq. 3-22).

$$u(y) = \sqrt{\sum_{i=1}^{N} \left(\frac{\partial f}{\partial x_i}\right)^2 u^2(x_i) + 2\sum_{i}^{N-1} \sum_{j=i+1}^{N} \frac{\partial f}{\partial x_i} \frac{\partial f}{\partial x_j} u(x_i, x_j)} \quad 3\text{-}22$$

If individual measurements are uncorrelated and random, the covariances in Eq. 3-22 are zero and the formula shortens to Eq. 3-23.

$$u(y) = \sqrt{\sum_{i=1}^{N} \left(\frac{\partial f}{\partial x_i}\right)^2 u^2(x_i)} \quad 3\text{-}23$$

Standard uncertainties in output quantities of interest are listed in Table 3-2. The main source of uncertainty of output variables was uncertainty of temperature measurements. Measurement of cooling water temperatures generated 98.7% and 95.4% of the uncertainty of overall heat transfer coefficient at minimum and maximum heat transfer rate recorded in the experiments, respectively. At the minimum heat transfer rate, 90.8% of the uncertainty of film-side heat transfer coefficient was caused by uncertainty of cooling water temperatures. At the maximum heat transfer rate, uncertainty of internal thermal resistance generated 63.2% of the uncertainty of the film-side heat transfer coefficient with the remainder due to uncertainty of temperature measurements. Uncertainty of cooling capacity and mass flow rate of vapor was almost exclusively caused by uncertainty of temperature measurements while uncertainty of power consumption was due to uncertainty of current measurement.

Table 3-2: Limits of errors of measurement variables.

Measurement variable	Instrument/sensor used (Manufacturer, model)	Error source	Proportional error	Absolute error	Total error at typical conditions
Cooling water mass flow rate	Coriolis flow meter (FCI, FlexCor Model CMF Series)	Measurement, transmitter, current	± 0.36%	± 0.14 g/s	± 0.51%
Solution density	Coriolis mass flow measuring system (Endress + Hauser, Proline Promass 83A)	Measurement, current	-	± 1 kg/m3	± 0.06%
Solution mass flow rate	Mass flow measurement system (Endress + Hauser, Promass 63A)	Measurement, current	± 0.16%	-	± 0.16%
Vacuum pressure	Capacitance manometer (MKS Instruments, Baratron Type 622C)	Measurement	± 0.25%	± 0.13 Pa	± 0.26%
Rotational speed	Shaft speed sensor (Electro Sensors, ST420)	Measurement	-	± 4.2 RPM	± 1.12%
Motor voltage	Data acquisition system (Keysight Technologies, 34970A)	DAQ	± 0.0035%	± 0.00005 V	± 0.004%
Motor current	Current probe (Amprobe Test Tools, CT238A)	Measurement, DAQ	± 1%	± 0.003 A	± 1.05%
Temperature	Copper/copper-nickel thermocouple (Omega Engineering, T-type wire SLE)	Measurement, DAQ	-	± 1.5 °C	± 3.26%
Temperature of cooling water	Calibrated copper/copper-nickel thermocouple (Omega Engineering, T-type wire SLE)	Measurement, DAQ	-	± 0.2 °C	± 0.63%
Internal thermal resistance	-	Measurement	-	0.00038 K/W	± 8.5%

Table 3-3: Uncertainty of output quantities.

	Uncertainty at minimum heat transfer rate	**Uncertainty at maximum heat transfer rate**
Overall heat transfer coefficient [W/(m^2·K)]	10.5%	4.2%
Film-side heat transfer coefficient [W/(m^2·K)]	17.5%	20.3%
Mass flow rate of vapor [g/s]	10.8%	4.5%
Cooling capacity [W]	10.8%	4.5%
Power consumption [W]	1.0%	1.0%

3.3. Results and discussion

3.3.1. Heat transfer performance

Figure 3-8 shows the relationship between overall heat transfer coefficient and rotational speed at different mass flow rates. In an absorption chiller, low solution flow rates are preferred as they curtail efficiency losses associated with solution circulation. However, too little solution flow can lead to poor wetting of the heat transfer surface in the absorber. Hence, the present experiments were conducted at relatively low flow rates that were still high enough to guarantee good wetting of the surface of the disk. The overall heat transfer coefficient increased strongly with rotational speed. This effect was larger at lower rpms: on average, the overall heat transfer coefficient increased by 14% when rotational speed changed from 250 rpm to 375 rpm, while the value at 625 rpm was 6% above the value for 500 rpm. Visual observation suggested that the disk's horizontal axis influenced operation at 125 rpm. At slow rotational speeds, the liquid did not immediately reach the disk's angular velocity. Thus, gravity

forced the flow to move downwards and out of center, leading to non-uniform film thickness with a substantially thinner film on the upper half of the disk. In addition, a small part of the liquid was thrown off the disk directly as it experienced fast acceleration out of a relatively thick layer of fluid. The effect of mass flow rate on overall heat transfer coefficient is ambiguous, which hints at more complicated phenomena than the simple Nusselt model being present on the disk. According to Nusselt's solution, higher mass flow rate causes a thicker film. This causes higher thermal resistance, which causes an inversely proportional relationship between heat transfer coefficient and mass flow rate. In the present experiments, however, higher mass flow rates outperformed lower mass flow rates. This finding is in agreement with previously reported data for sensible heat transfer [11,82,96] and mass transfer [13].

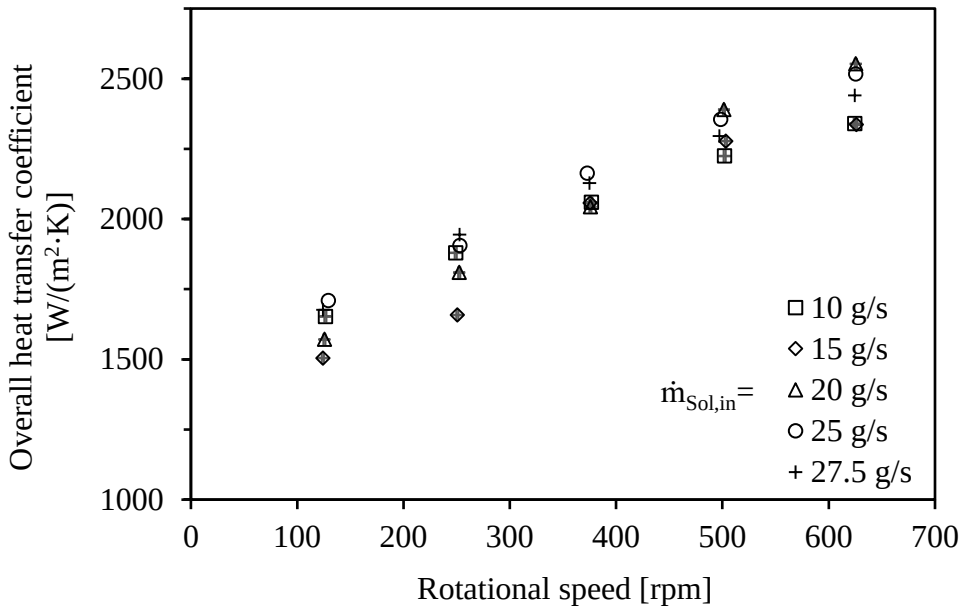

Figure 3-8: Effect of rotational speed and solution mass flow rate on overall heat transfer coefficient.

The results can be explained by the effects of surface waves that cause mixing within the film [99,102]. High quality images taken a with Nikon D5300 camera revealed that the flow over the disk surface at low flow rates of 10 and 15 g/s was smoother than at higher flow rates. Figure 3-9 to Figure 3-13 show images of absorption tests at a rotational speed of 375 rpm and solution mass flow rates between 10 g/s and 27.5 g/s. At 10 g/s and 15 g/s (Figure 3-9 and Figure 3-10, respectively), the liquid film is relatively smooth. Film waviness is clearly visible at 20 g/s (Figure 3-11) and increases with higher solution mass flow rates of 25 g/s and 27.5 g/s (Figure 3-12 and Figure 3-13, respectively).

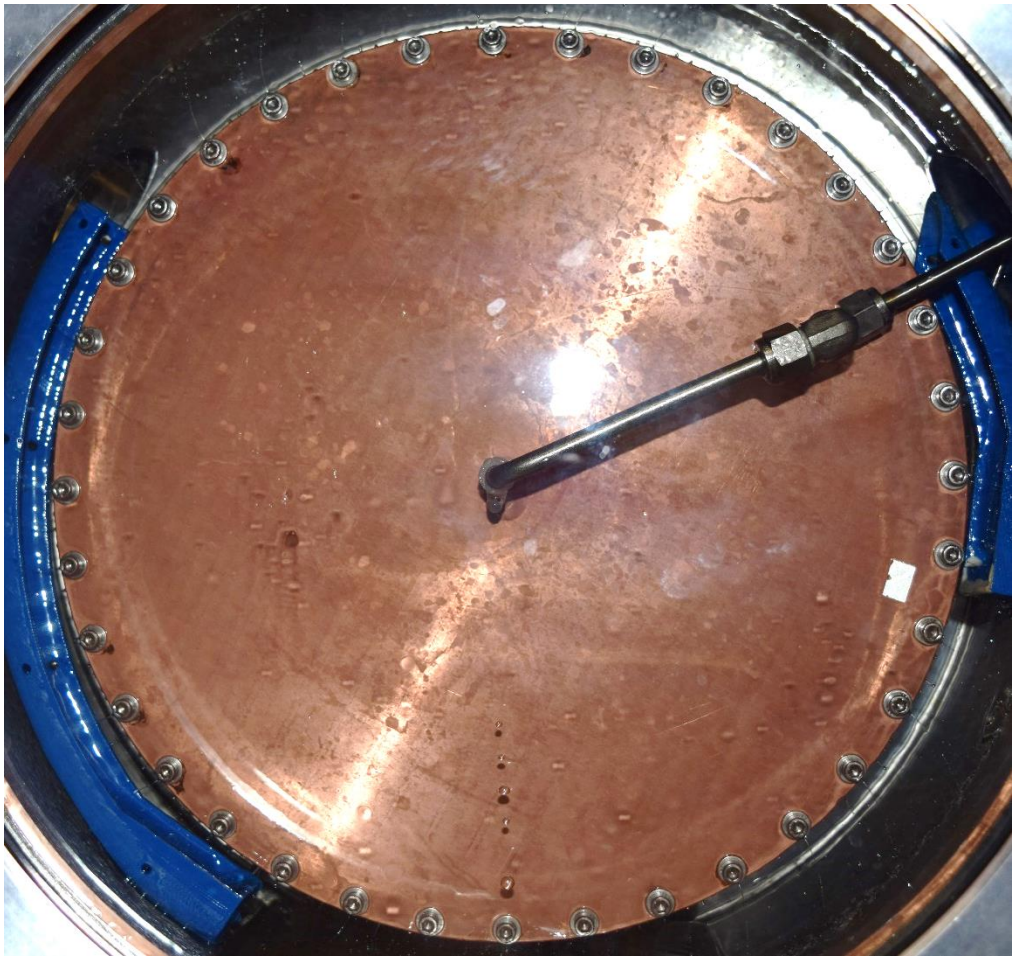

Figure 3-9: Image taken at a rotational speed of 375 rpm and a solution mass flow rate of 10 g/s.

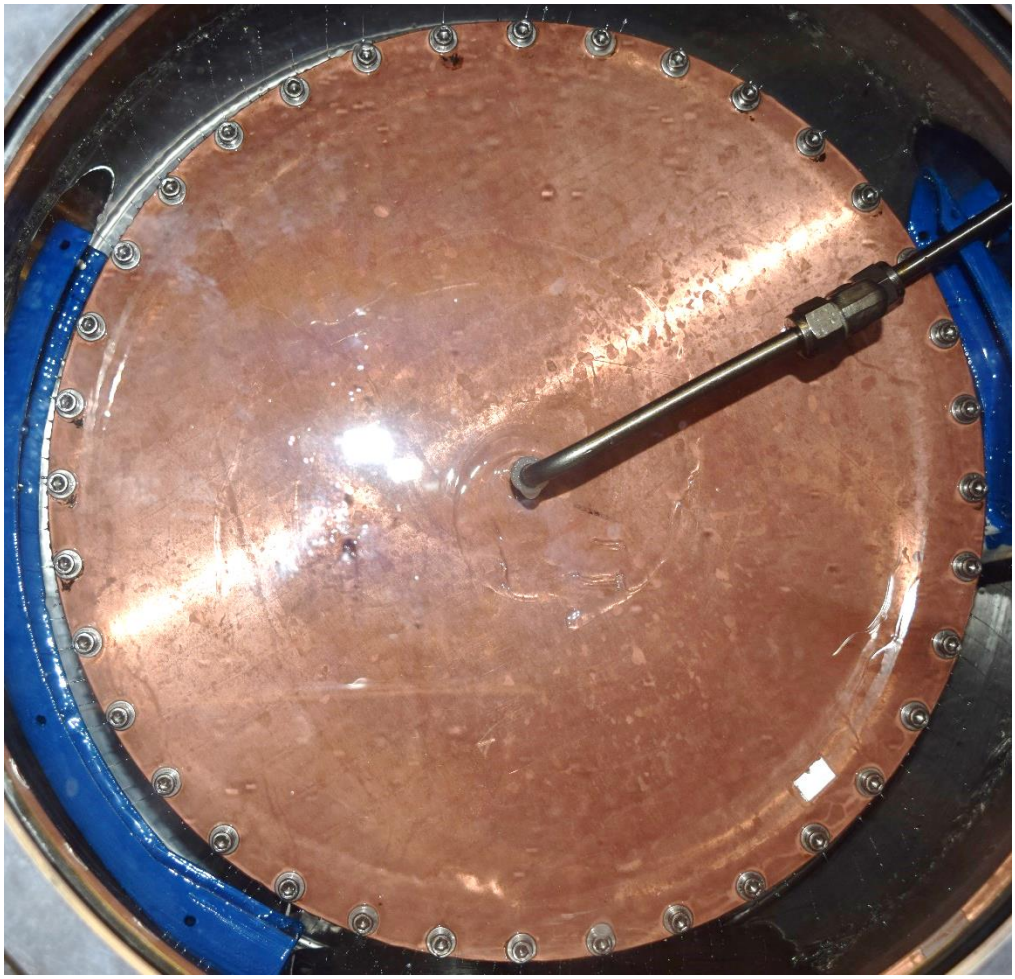

Figure 3-10: Image taken at a rotational speed of 375 rpm and a solution mass flow rate of 15 g/s.

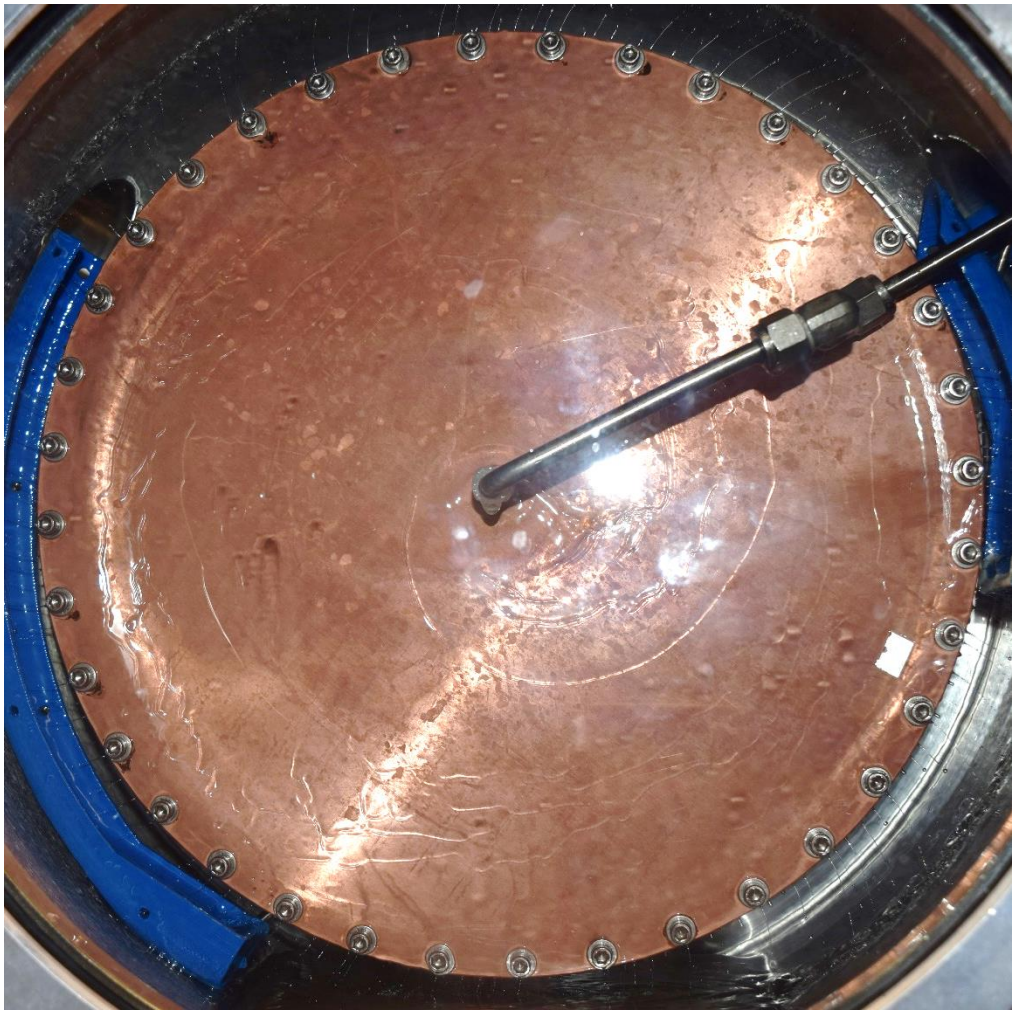

Figure 3-11: Image taken at a rotational speed of 375 rpm and a solution mass flow rate of 20 g/s.

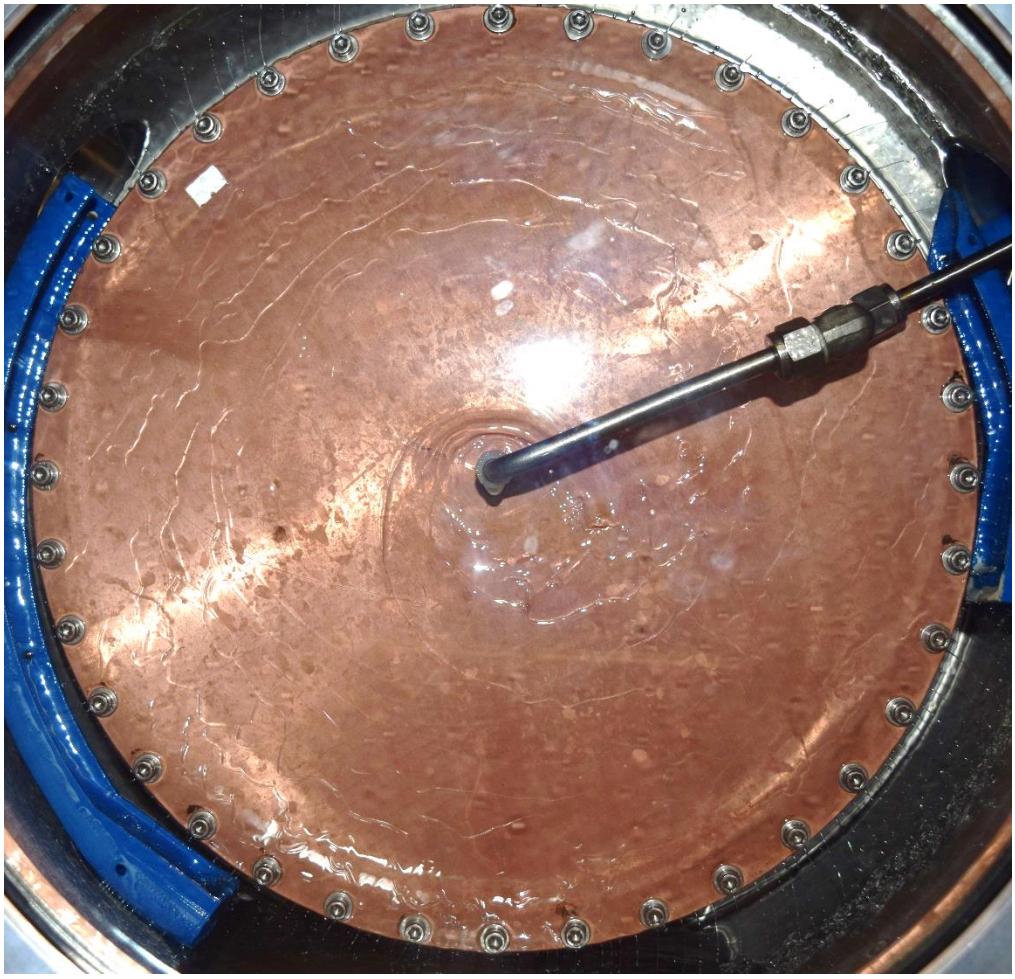

Figure 3-12: Image taken at a rotational speed of 375 rpm and a solution mass flow rate of 25 g/s.

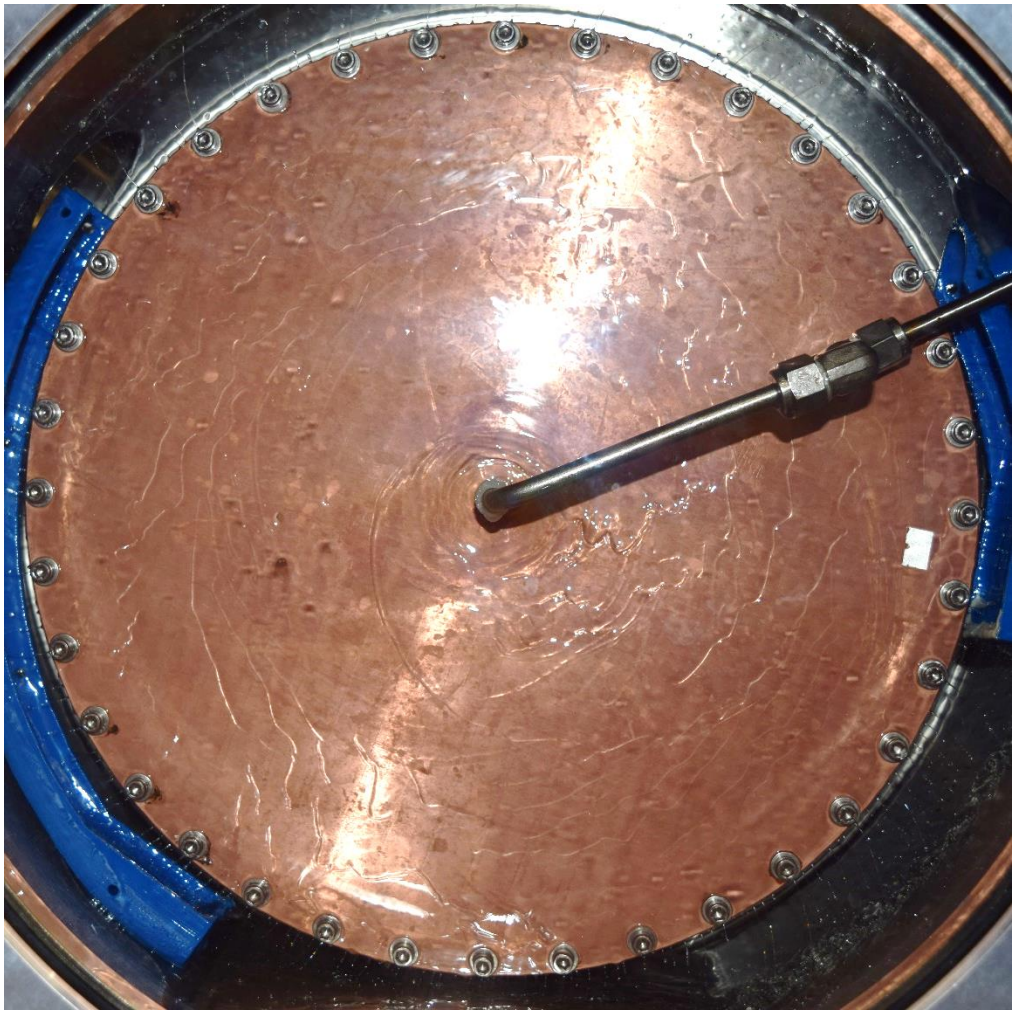

Figure 3-13: Image taken at a rotational speed of 375 rpm and a solution mass flow rate of 27.5 g/s.

Figure 3-14 to Figure 3-17 show images of absorption test at a constant solution mass flow rate of 20 g/s and increasing rotational speed. At a rotational speed of 125 rpm (Figure 3-14), the liquid film appears thick and a wave related to the influence of gravity appears. At 250 rpm (Figure 3-15), the influence of gravity reduces and the film

thins. Wave formation accelerated from rotational speeds of 375 rpm (Figure 3-11) and higher (Figure 3-16 and Figure 3-17). At 625 rpm (Figure 3-17), the clearly shows a characteristic wave pattern depending on radial location. Closer to the center of the disk, waves were of spiral type. Moving radially outwards, the wave pattern broke down and gave way to smaller, three-dimensional ripples. This pattern largely followed the observations described by Woods [97]. However, film waviness is dampened at low solution mass flow rates as image even if rotational speed is high (Figure 3-18). This observation agrees with the large divergence in results between high and low mass flow rates at higher rpm.

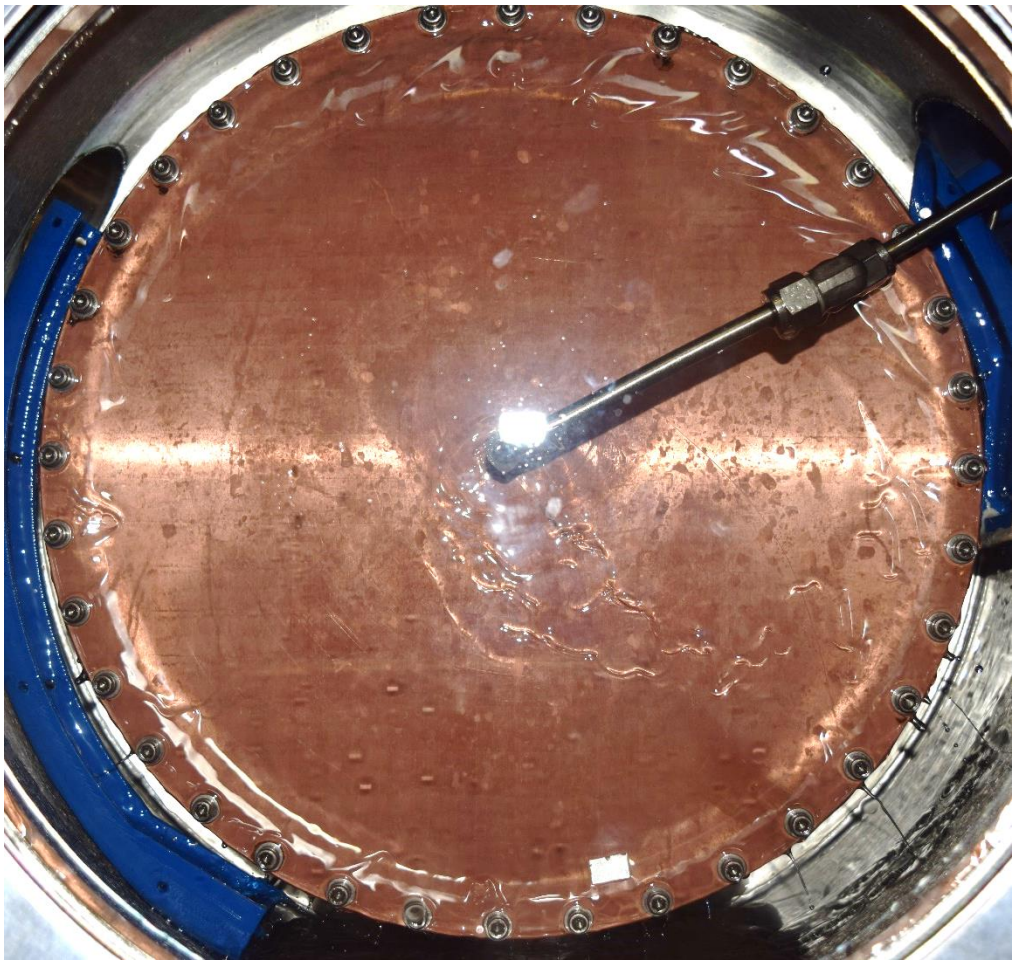

Figure 3-14: Image taken at a rotational speed of 125 rpm and a solution mass flow rate of 20 g/s.

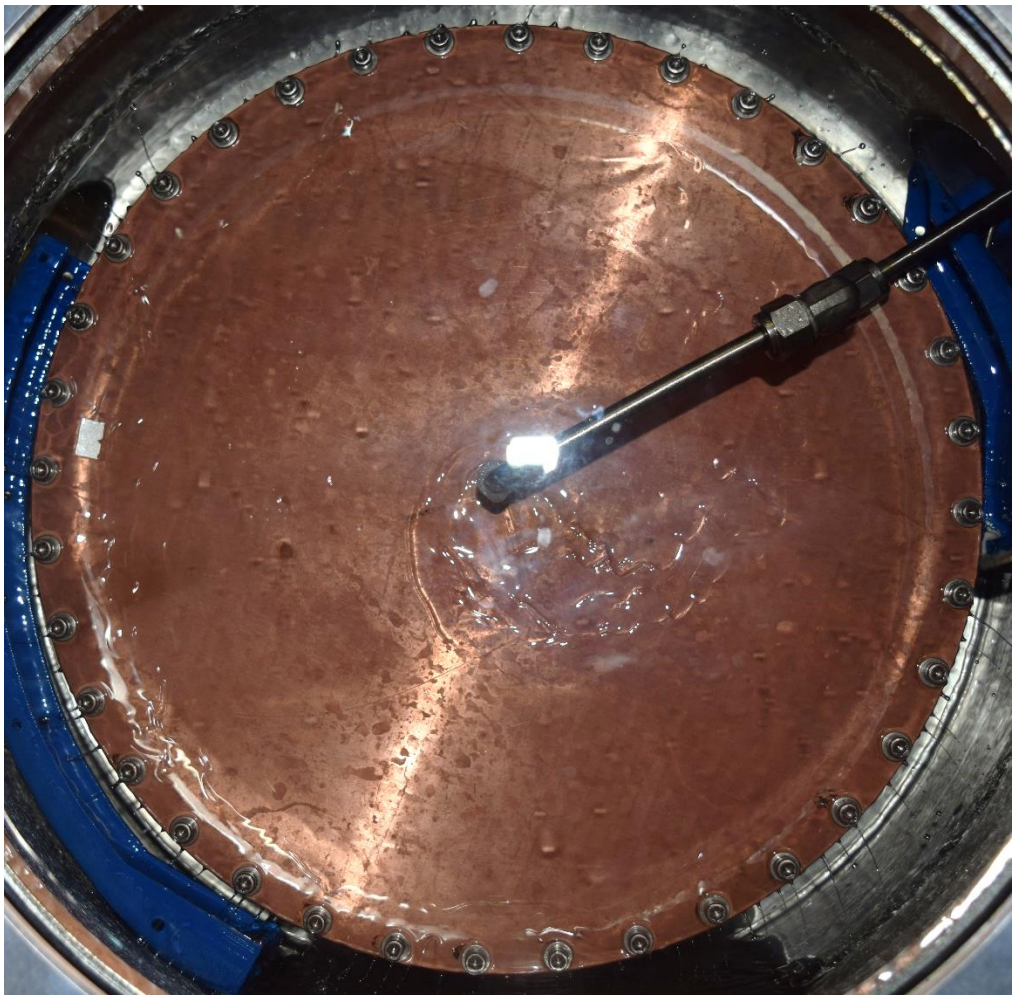

Figure 3-15: Image taken at a rotational speed of 250 rpm and a solution mass flow rate of 20 g/s.

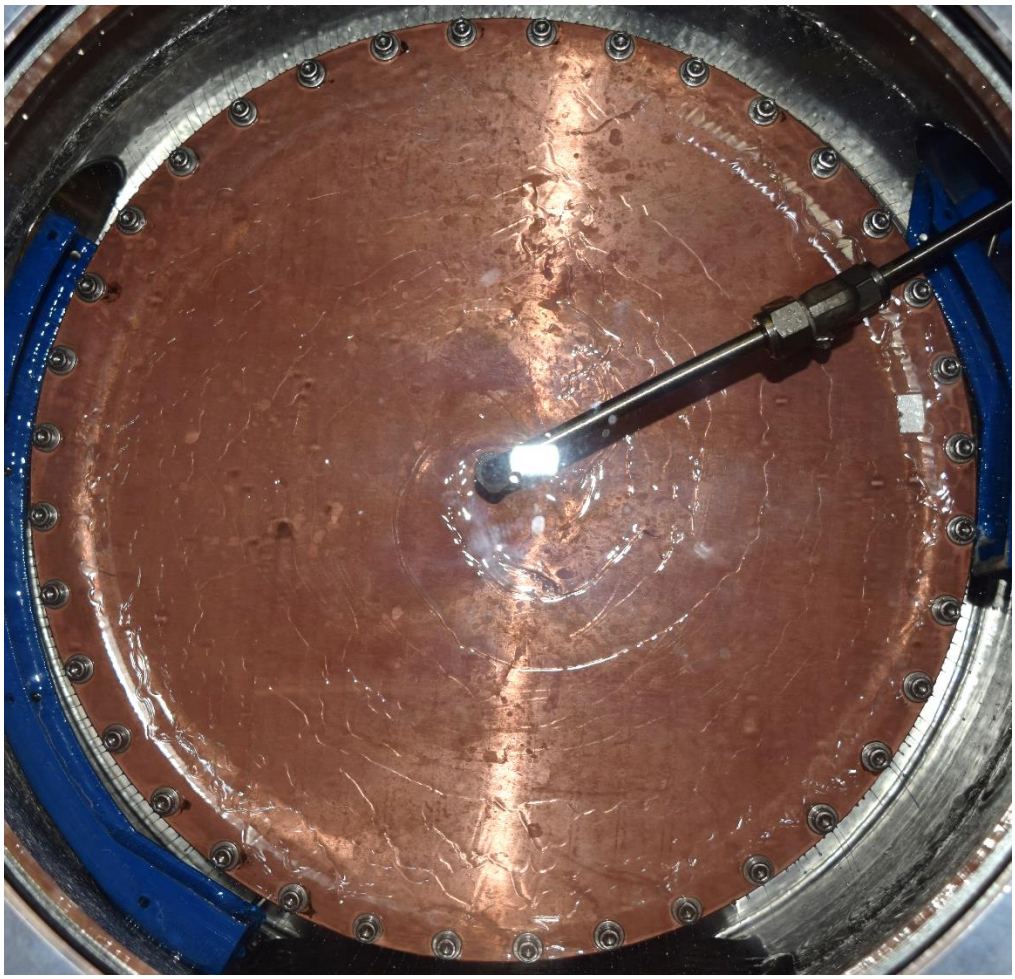

Figure 3-16: Image taken at a rotational speed of 500 rpm and a solution mass flow rate of 20 g/s.

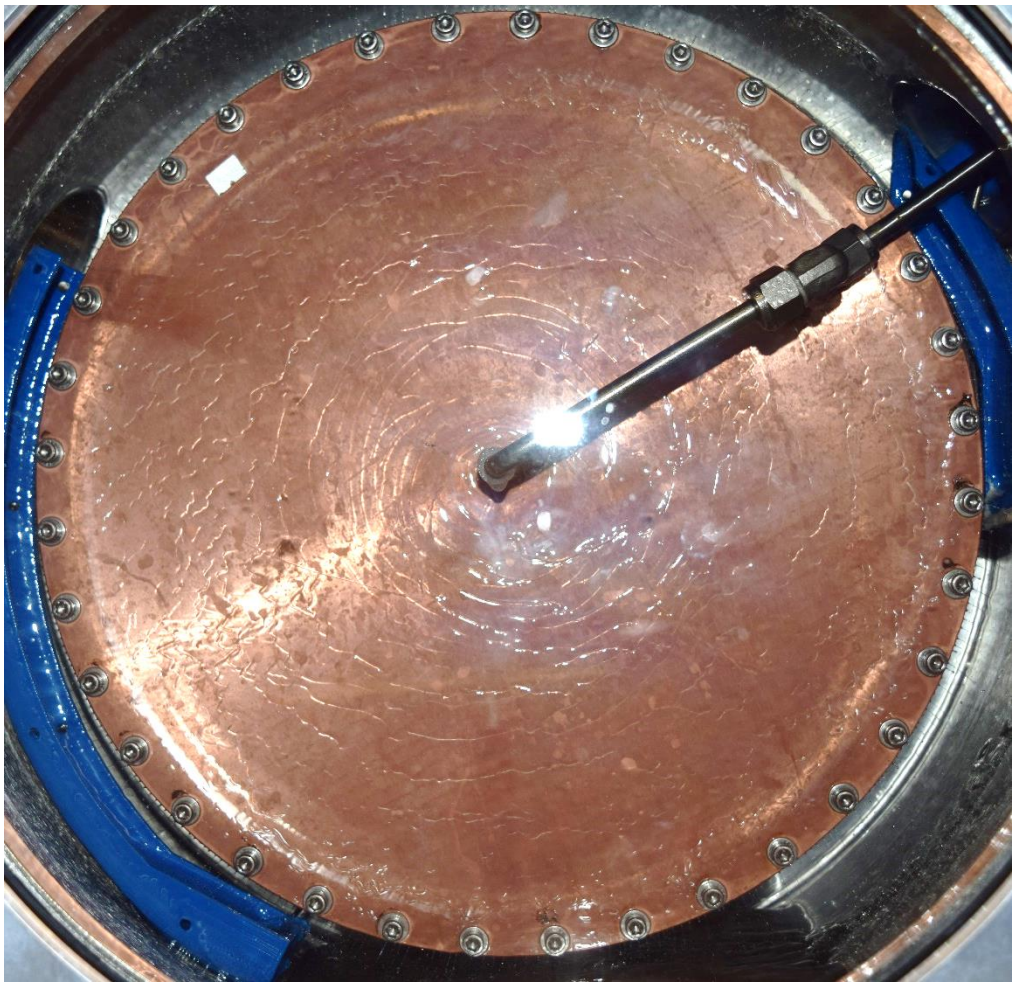

Figure 3-17: Image taken at a rotational speed of 625 rpm and a solution mass flow rate of 20 g/s.

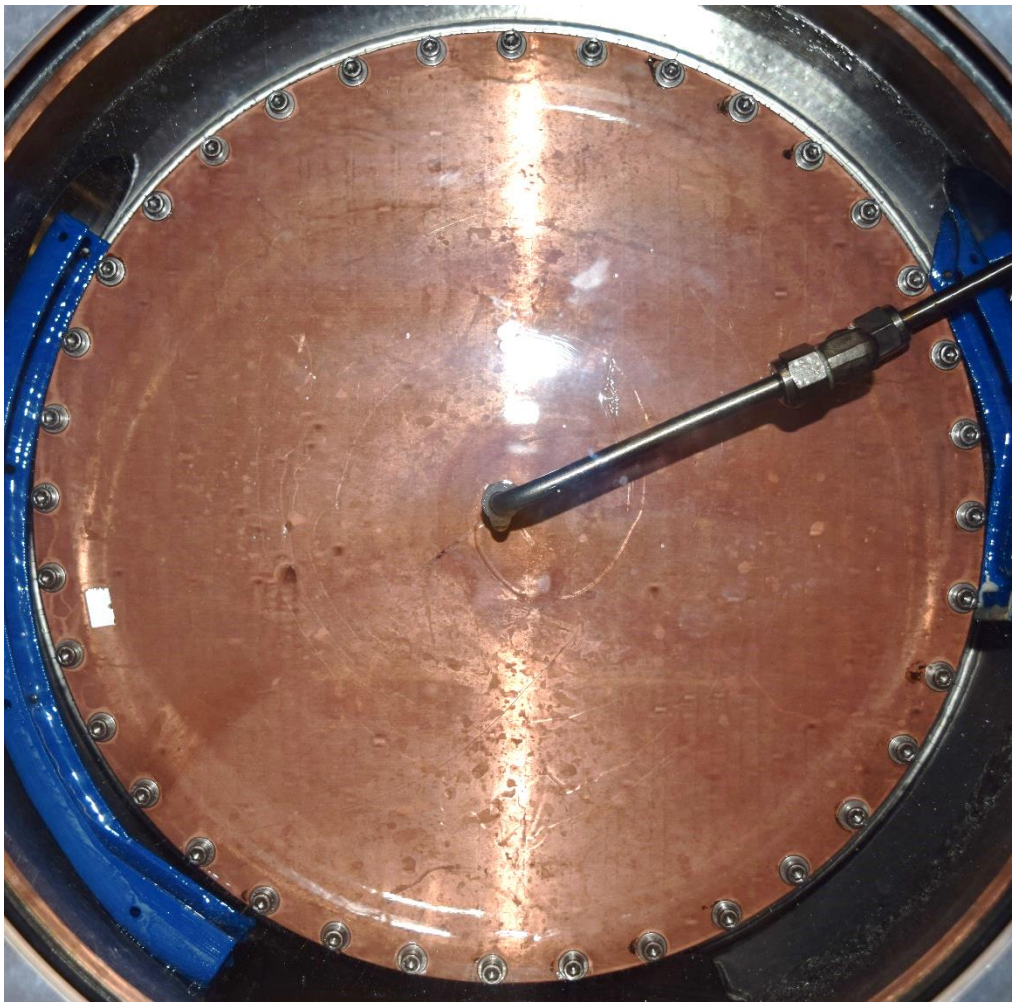

Figure 3-18: Image taken at a rotational speed of 625 rpm and a solution mass flow rate of 10 g/s.

The surface area increments per increment in radial location are steadily increasing in radial direction. Therefore, the local film thickness decreases (Eq. 3-1) and the local heat transfer coefficient increases in radial direction (Eqs. 3-5, 3-7). Hence, a larger diameter of the disk may enhance the performance of the spinning disk absorber per surface area. In the present study, the internally cooled area of the spinning disk

absorber is smaller than the external surface area of the disk. The area close to the perimeter of the disk can be compared to the droplet formation regime in horizontal tube absorbers, for which an adiabatic condition is commonly assumed [30,129,133]. The area is hence characterized by heat/mass transfer into a subcooled absorbent solution that continues even in the absence of heat rejection to cooling water. Subjecting the complete external surface area to active internal cooling through better packaging, e.g. reducing the area needed for sealing and fasteners, would increase the heat rate for given dimensions of the disk assembly. However, the overall heat transfer coefficient may remain approximately constant because it is based on the actively cooled surface area in this study. Further discussion of the absorption and heat transfer behavior would require better insight into the simultaneous heat and mass transfer process. Experimentally validated design models for spinning disk absorbers, similar to those developed for tube-type absorbers [30,128,133], may lead to designs that further intensify the absorption process and chapter 5 will present such a model.

Figure 3-19 displays the film-side heat transfer coefficient at different operating conditions. On average over different mass flow rates, the film-side heat transfer coefficient increased by a factor of 2.3 when the rotational speed accelerated from 125 to 625 rpm. The highest film-side heat transfer coefficient of 5098 W/(m^2·K) was observed at a solution mass flow rate of 20 g/s and rotational speed of 625 rpm. This result was higher by a factor of 2.7 than the value at similar solution mass flow rate and rotational speed of 125 rpm. At a solution mass flow rate of 10 g/s, the film-side heat transfer coefficient was higher by a factor of 2.0 when the rotational speed increased to

625 rpm from 125 rpm. The lesser enhancement was attributed to lower wave formation and subsequently less disturbance of the concentration boundary layer at the vapor-liquid interface.

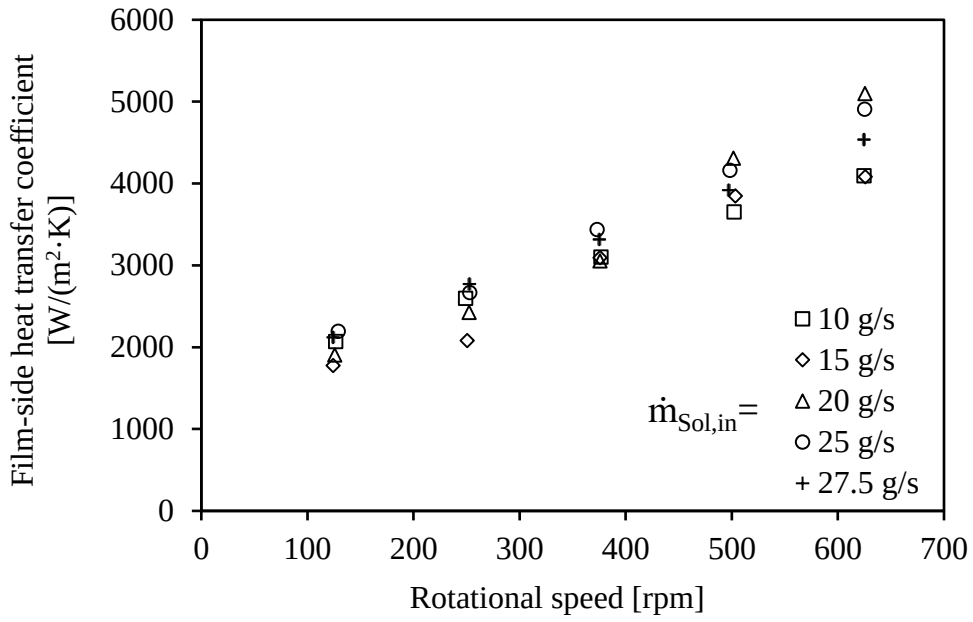

Figure 3-19: Effect of solution flow rate and rotational speed on the film-side heat transfer coefficient.

The results can be analyzed in terms of thermal resistances as discussed in section 3.2. Fitting Eq. 3-24 to the 28 data points for rotational speeds between 250 and 625 rpm resulted in coefficients of 2.10 for β, 2.14 for γ and -0.36 for ϵ. The values of the coefficients indicate the following:

- The temperature profile is between parabolic and linear form. As shown in section 3, the value of beta is equal to 2.5 if a parabolic temperature profile is present and 1.6 if the temperature profile is linear.

- The formula for average film thickness, Eq. 3-3, is a valid parameter in the calculation of thermal resistance, but actual resistance is higher than predicted by the formula for film thickness alone.
- $\gamma \cdot \epsilon$ = -0.76: The exponent of rotational speed in Eq. 3-8 holds even though overall resistance is higher. Thus, the heat transfer coefficient is proportional to (rotational speed)$^{0.76}$:

$$R_{tot} = 0.0045 + \frac{1}{A_{film}\beta k}\left(\frac{81\dot{m}\mu}{16\pi r^2 \omega^{\gamma}\rho^2}\right)^{\epsilon} \qquad 3\text{-}24$$

Figure 3-20 displays that Eq. 3-24 predicts the actual thermal resistance within ± 25%. The deviations are mainly due to the film-side resistance, which does not depend on the mass flow rate as predicted by Eq. 3-8.

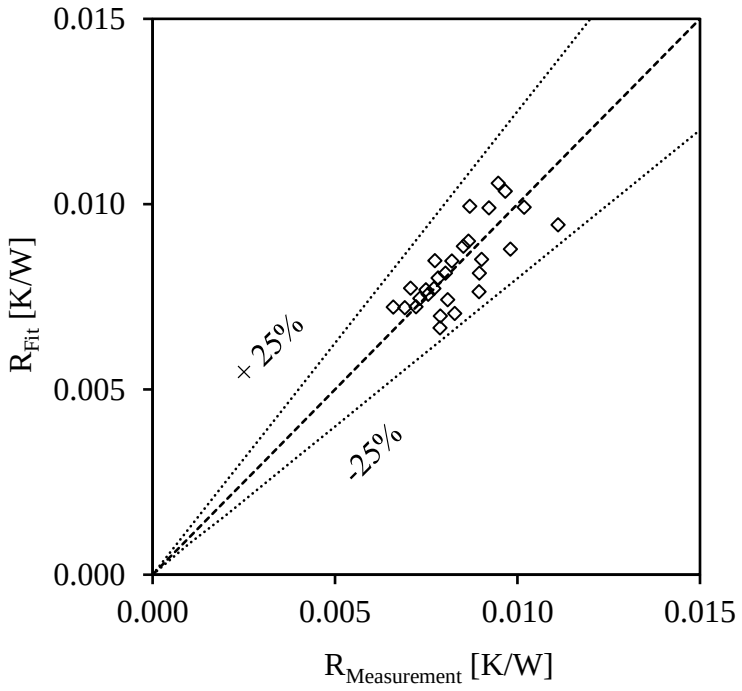

Figure 3-20: Fitted vs. measured values of overall thermal resistance.

3.3.2. Comparison to traditional absorbers

The maximum overall heat transfer coefficient of the spinning disk absorber was 2553 W/(m^2·K), while the value for horizontal tube bank absorbers at comparable operating conditions is 768 W/(m^2·K) if based on the outer diameter of the tubes [43]. Thus, the spinning disk absorber increased overall heat transfer by an enhancement factor of 3.3. The film-side heat transfer coefficient reported by Kyung and Herold with a conventional tube bundle absorber was 930 W/(m^2·K), albeit at higher mass flow rates [43]. The spinning disk absorber increased that value by an enhancement factor for film-side heat transfer of 5.5. It is worth noting that other researchers reported lower film-side heat transfer coefficients of tube bundles: Remec et al. [134], Beutler et al. [10] and Nomura [29] reported 510, 793 and 850.6 W/(m^2·K) respectively. Beutler et al. reported that a surface-enhanced tube achieved 957 W/(m^2·K).

The value and make-up of overall resistance of the conventional absorber in [43,128] and the spinning disk absorber in this study reveal the differences between the two design concepts. The spinning disk absorber had 52% lower thermal resistance than the tube bank absorber, even though its film-side surface area was 15% smaller. Figure 3-21 shows that contributions from individual resistances change significantly as well. Thermal resistance of the conventional absorber is dominated by film-side resistance. The largest contribution to thermal resistance of the spinning disk absorber rotating at 625 rpm came from internal resistance: film-side resistance was responsible for only 37% as compared to 83% for the conventional absorber. The dominance of internal resistance opens new possibilities for further optimization: whereas internal

heat transfer enhancement has limited effect in a conventional tube bundle, innovative approaches to improve internal heat transfer in spinning disk reactors will have a much more immediate effect on overall performance.

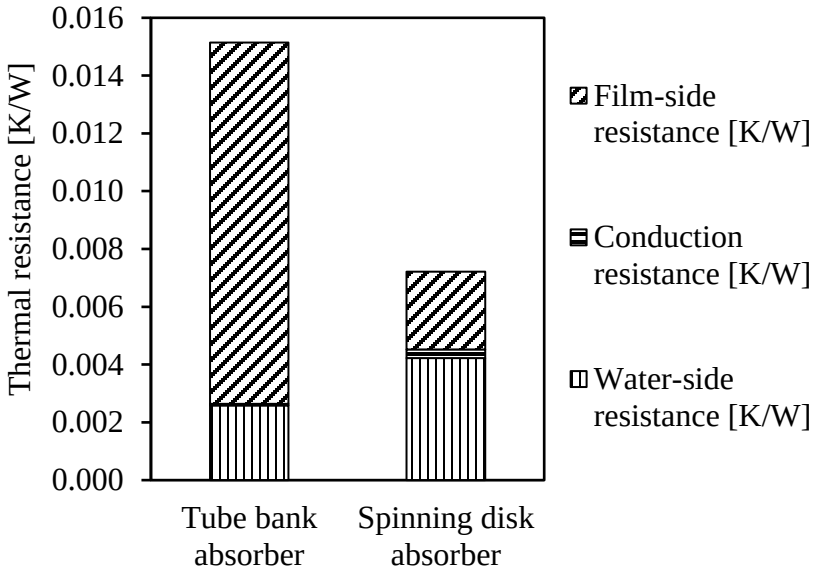

Figure 3-21: Thermal resistance breakdown for stationary conventional tube bundle [43] and spinning disk absorber rotating at 625 rpm.

3.3.3. Effect of pressure and concentration

The overall heat transfer ultimately depends on the mass of water vapor absorbed at the vapor-liquid interface that then releases its latent heat and causes heat of dilution. The driving force for vapor absorption is the difference between the concentration of water in the bulk solution and the equilibrium concentration of water at the gas-liquid interface, which strongly depends on the pressure of the vapor phase. Figure 3-22 shows that the overall heat transfer coefficient and film-side heat transfer coefficient increased by 4 to 10% and by 7 to 22%, respectively, when the pressure in the absorber

increased from 1100 Pa to 2000 Pa. In a full loop absorption cycle, these pressures correspond to temperatures of 8.37 °C and 17.50 °C, respectively, in the evaporator. Both data sets were taken at a mass flow rate of 20 g/s and a content of 60 wt.-% lithium bromide in the solution. Solution inlet temperature at 2000 Pa was higher, since inlet subcooling was kept constant.

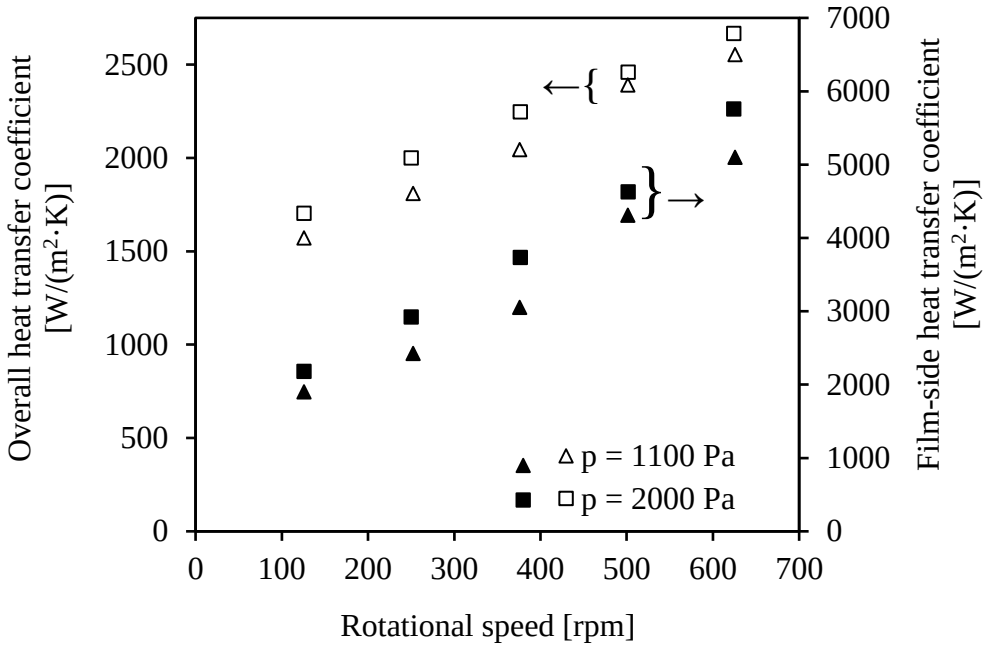

Figure 3-22: Effect of pressure on overall and film-side heat transfer coefficient.

An alternative way to change the driving force of the mass transfer is to change the mass fraction of lithium bromide at the inlet to the absorber. A higher concentration of lithium bromide lowers the saturation vapor pressure of the solution and therefore increases the driving force for mass transfer. Given a constant pressure of water vapor in the absorber vessel, a stronger solution leads to a higher saturation temperature. These effects oppose each other if the system is analyzed in terms of the overall heat

transfer coefficient. A stronger solution increases the heat flux, but log mean temperature difference is higher as well. Figure 3-23 shows that the effects offset each other in this study. The slight increase of higher overall heat transfer coefficients at lower concentration of lithium bromide is within uncertainty limits. However, higher concentration of lithium bromide leads to a significantly higher mass flow rate of water across the gas-liquid interface. Thus, a stronger solution leads to higher cooling capacity at similar operating conditions.

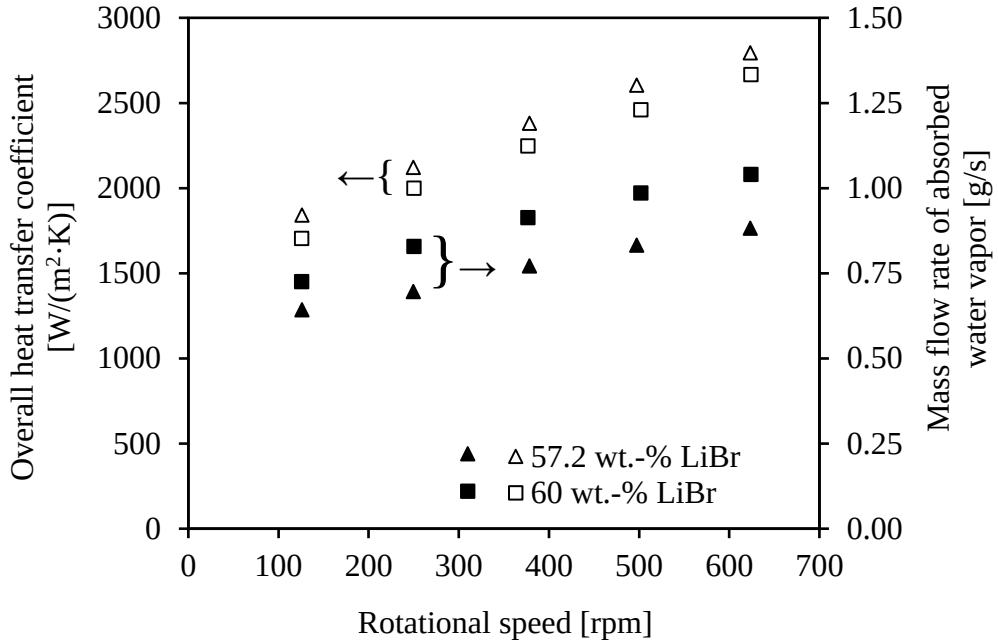

Figure 3-23: Effect of mass concentration on overall heat transfer coefficient and mass flow rate of vapor at pressure of 2000 Pa.

3.3.4. Cooling capacity and power consumption

Cooling capacity of the device strongly depended on the set point for pressure and rotational speed. At any mass concentration and pressure tested in this study, the

cooling capacity increased strongly with rotational speed. Depending on operating conditions, the increase in cooling capacity was between 65% and 76% when rotational speed increased from 125 to 625 rpm. Figure 3-24 shows cooling capacities at different operating conditions. Assuming no pressure loss between the evaporator and the absorber of a full absorption cooling loop, the pressure levels of 1100 Pa and 2000 Pa corresponded to temperatures of 8.37 °C and 17.50 °C in the evaporator, respectively. The maximum cooling capacity at a pressure of 1100 Pa was 1559 W. While maximum cooling capacity at solution mass flow rates between 20 and 27.5 g/s was almost constant, the value was about 11% less for the lowest flow rates of 10 and 15 g/s. Different mass concentrations of lithium bromide were tested at a pressure of 2000 Pa, and the results show that a stronger solution increased cooling capacity by up to 20%. Mass concentrations of up to 65 wt.-% lithium bromide are possible in industrial applications if the absorption machine is equipped with an adequate control system and a high temperature heat source is available [23]. The associated increase in driving force for mass transfer is expected to significantly increase the cooling capacity of the spinning disk absorber and thereby decrease power consumption relative to cooling capacity.

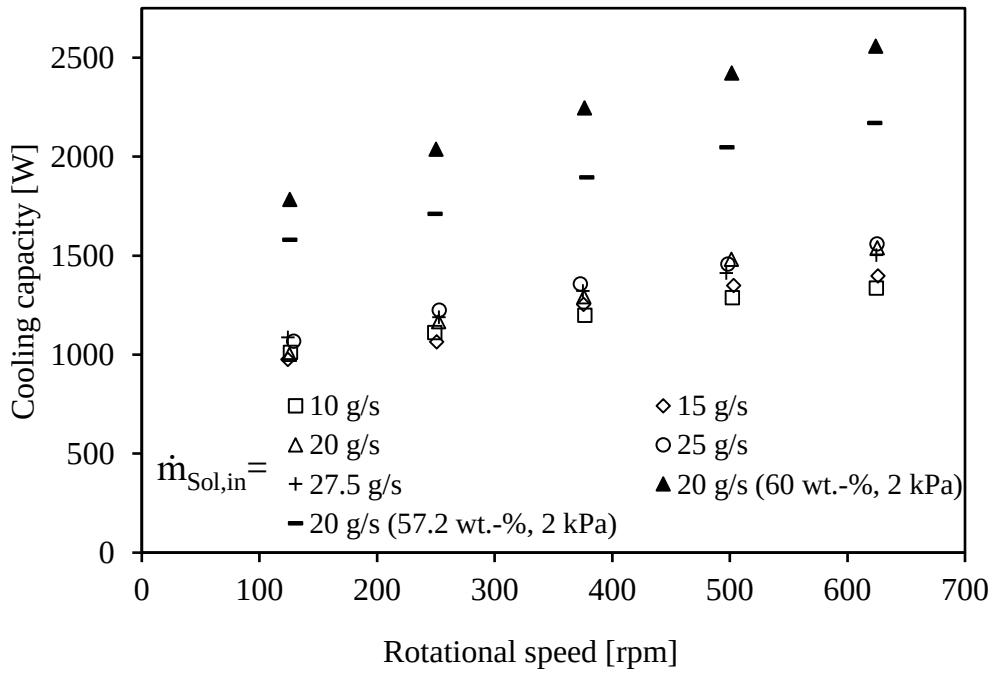

Figure 3-24: Cooling capacity at various operating conditions. If not specified otherwise, mass concentration and pressure were 60 wt.-% LiBr and 1.1 kPa, respectively.

Figure 3-25 shows the dependence of power consumption on rotational speed and solution mass flow rates. The main source of power consumption of the spinning disk absorber was expected to be frictional losses in the sealing mechanism. Indeed, small misalignments of the rotary seal and subsequent non-uniform pressure on the sealing O-rings caused power consumption to spike. Maximum total power consumption was 77 W at the maximum, of which 50 W were caused by the spinning disk itself after accounting for inefficiencies of the motor. Power consumption depended only slightly on the solution mass flow rate, which confirmed that power lost due to liquid acceleration was minor. On average over all experiments, power consumption was

3.1% of cooling capacity. At the lower pressure level and mass flow rate of 20 g/s, the power consumption as percentage of cooling capacity varied between 2.1% at 125 rpm and 4.6% at 625 rpm. If inefficiencies of the motor are neglected, the power required to spin the disk was between 1.3% and 3% of cooling capacity. The prevalence of sealing losses suggests that any scale-up to a multi-disk device should aim to add several disks on a single drive shaft to minimize power consumption.

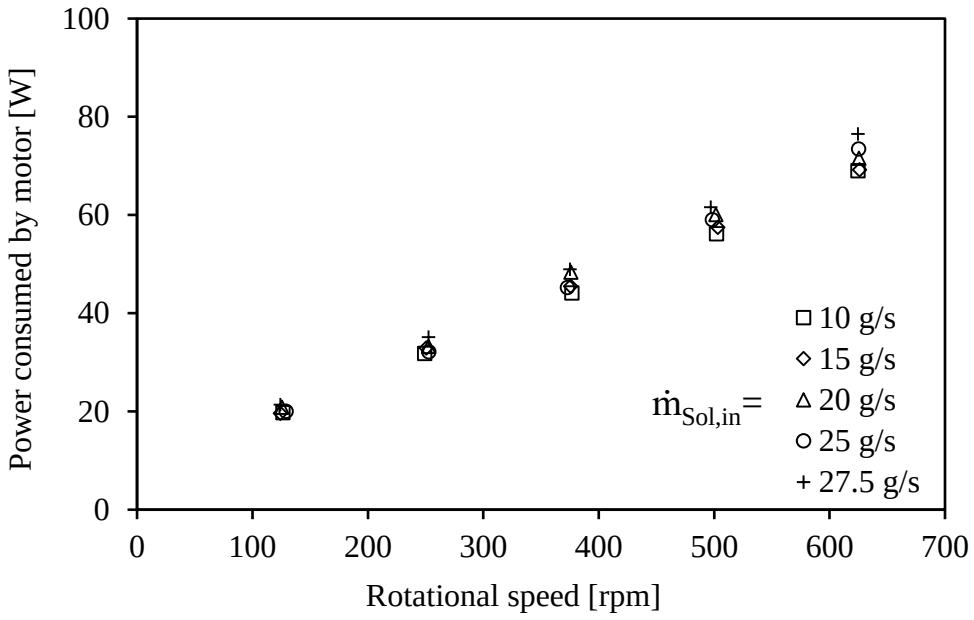

Figure 3-25: Total power consumed by motor at different mass flow rates of solution and rotational speed.

3.4. Chapter conclusions

Since the absorber is the most critical component of absorption chillers, any process intensification that can boost its performance will have a direct benefit in the overall

system performance. Although process intensification by centrifugal acceleration has been studied before, no detailed performance data have been available so far.

To quantify the performance enhancement achieved by replacing gravitational acceleration with centrifugal acceleration, a spinning disk reactor was operated as the absorber in a vapor absorption system that used aqueous lithium bromide as working fluid. Parametric studies quantified the effect of rotational speed and mass flow rate of solution at standard operating conditions of lithium bromide absorption chillers. Spinning the disk at 625 rpm increased the film-side heat transfer coefficient by a factor of 5.5 compared to conventional tube bundle absorbers. The overall heat transfer coefficient increased by a factor of 3.3 and was ultimately limited by internal resistance. Thus, the film-side performance enhancement shifted the dominating thermal resistance from the film-side to the inside, thereby opening the door for future improvements that incorporate internal enhancements.

Cooling capacity of the system and power consumption of the electric motor increased with rotational speed. At typical operating conditions, power consumption was 2.1% of cooling capacity at 125 rpm and 4.6% at 625 rpm rotational speed. Power consumption was driven by frictional losses in the sealing of the drive shaft and motor inefficiencies. These losses can be minimized by using low friction sealing materials and a high-efficiency motor. Further, any scale-up should add more disks in parallel on the same drive shaft, which would increase cooling capacity without significantly increasing power consumption.

This research has shown that centrifugal acceleration is a promising process intensification method for absorption chillers using conventional working fluids. Its effects may be even more pronounced and important when combined with novel high-efficiency absorbents that exhibit more challenging thermo-physical properties. Future research is needed to assess the performance enhancement when these new absorbents are utilized and to further improve the device's performance by incorporating internal heat transfer enhancement. Such an enhanced spinning disk absorber with innovative water-side heat transfer enhancement will be shown in the next chapter.

4. Development and experimental study of enhanced spinning disk absorber

Chapter 4 will present the development and experimental testing of an enhanced spinning disk absorber. A graphical abstract of the research is shown in Figure 4-1.

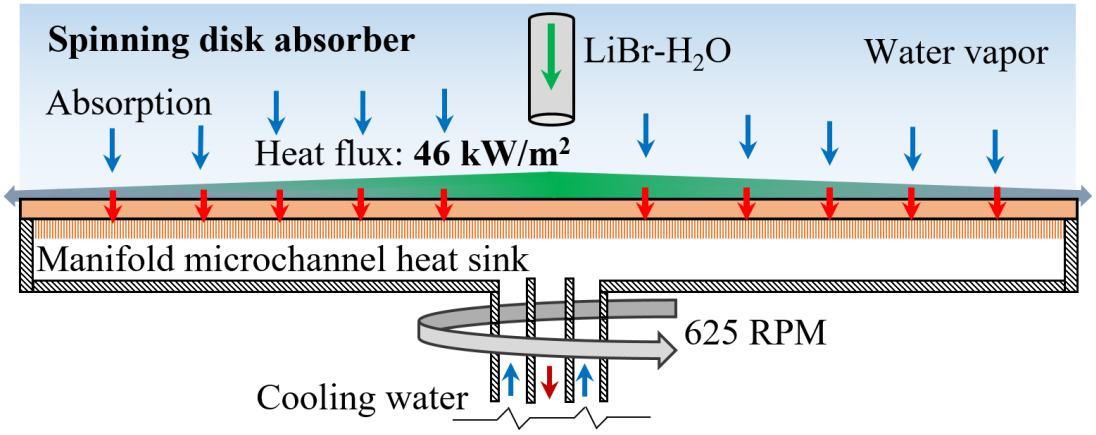

Figure 4-1: Graphical abstract of research presented in chapter 4.

4.1. Motivation

One interesting conclusion from chapter 0 was that the film-side resistance decreases with increasing rotational speed and, ultimately, falls below the water-side resistance. In conventional absorbers, water-side heat transfer enhancement does not strongly influence performance due to the dominance of film-side resistance [20]. However, as the spinning of the heat transfer surface minimizes the coupled film-side thermal and mass transfer resistance, water side thermal resistance must fall to reduce the size of the absorber further. The device studied in this chapter utilizes microchannel

surfaces in combination with an additively manufactured manifold to reduce the water-side resistance in a spinning disk absorber.

Manifold microchannel heat exchangers are commonly manufactured in rectangular shape and have been shown to achieve equal or better heat transfer performance than conventional microchannels while reducing the pressure drop penalty considerably [21,22]. Another noteworthy advantage of manifold-microchannel technology is their flexibility. The introduction of a flow distribution manifold as a separate part makes it possible to easily adjust the heat exchanger for different operating conditions. E.g., if cooling water flow rate is required to increase strongly, it is possible to switch more microchannels in parallel flow configuration simply by swapping the polymer manifold. This effect will be discussed further in chapter 8.2 when describing scale-up strategy.

4.2. Design of the experimental apparatus

4.2.1. Numerical optimization of manifold geometry

Manifold-microchannel technology was first introduced by Harpoe and Eninger in 1991 [135]. They concluded that a manifold-microchannel heat sink with optimized design parameters for single phase flow can achieve an effective heat transfer coefficient of on the order of 100 kW/(m^2·K). Since this first publication, the technology has received widespread attention for applications as varied as high heat flux electronics cooling [136], high performance plate heat exchangers [21] and high temperature heat exchangers. The reader is referred to Ohadi et al. for a comprehensive

discussion manifold-microchannel technology [137]. For the purpose of this study, a conceptual introduction and discussion of design determination are sufficient.

A schematic of a manifold-microchannel plate heat exchanger is shown in Figure 4-2. Fluid enters a manifold, from where is force into microchannels. The fluid only travels through the microchannels for the fin width of the manifold before it escapes into an adjacent manifold cell. The heat transfer occurs in the microchannels. Since the passage through the microchannel is short, the fluid flow stays in hydrodynamically and thermally developing flow regime for a significant part of the passage. This results in increased heat transfer coefficients and decreased pressure drop per unit length as compared to flow in longer microchannels with fully developed flow. The performance of a manifold microchannel plate heat exchanger increases by dividing the heat exchanger base area into several manifold microchannel segments such that flow alternates between adjacent manifold cells. The main optimization parameters for the manifold in such a system are the manifold fin width, the manifold channel width and the length of one manifold cell.

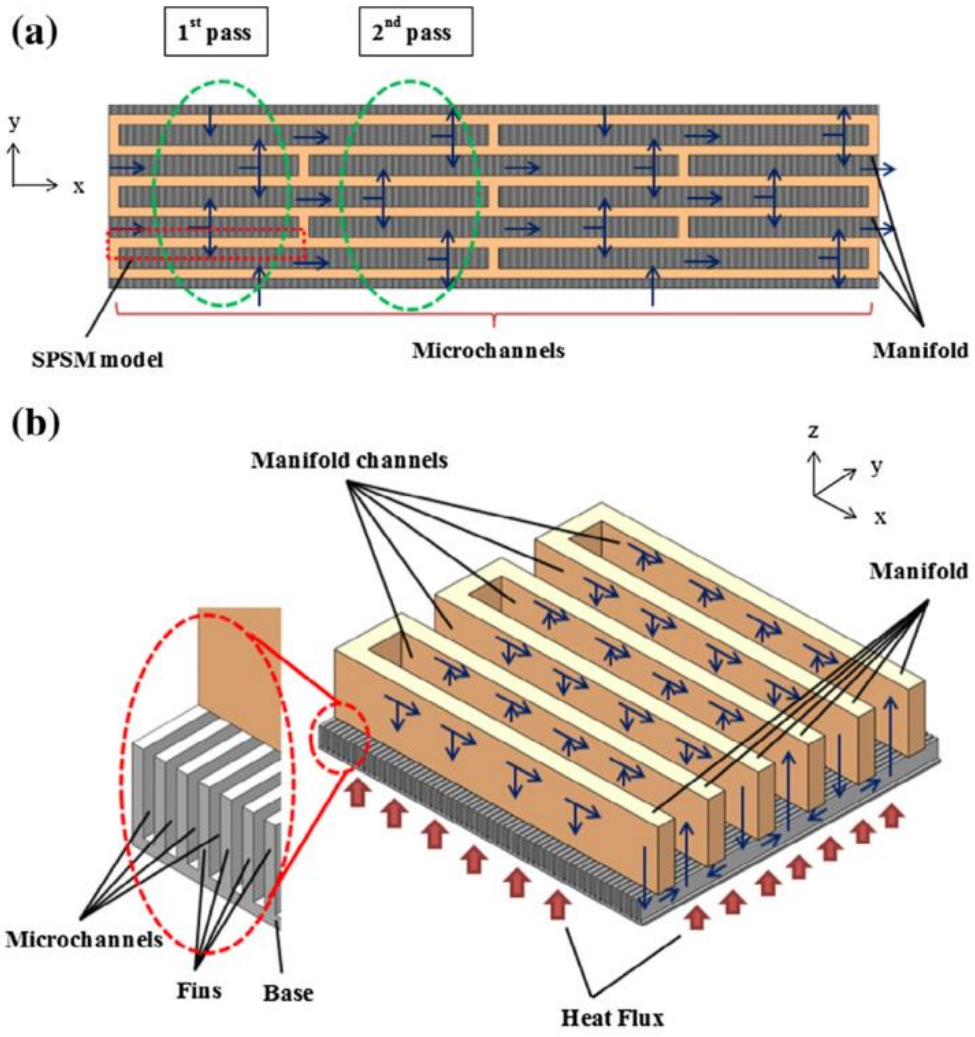

Figure 4-2: Schematic of manifold microchannel plate heat exchanger: (a) Top view of heat exchanger, (b) 3D view of one segment of the heat exchanger. Figure from [22].

Design choices of the microchannel heat sink for this study are limited to commercially available options due to cost considerations. Copper microchannel plates produced by micro deformation technique are commercially available from MicroCool, a division of Wolverine Tube [138], and the microchannel heat sink used in this study

is a sample provided by Wolverine Tube. Therefore, the design variables are limited to those dependent on the geometry of the manifold. This allows to perform an optimization based on CFD simulations only without building a metamodel as it is generally done if more design variables were present [22,139]. A bi-objective optimization was used to optimize manifold specifications using unit cell CDF model, shown in Figure 4-3. The geometry of interest for one pass encompasses part of the manifold channel, the microchannel and the volume of conductive material related to one flow path through a microchannel. Assuming symmetry boundary conditions, the computational domain is reduced to one half of fin width, manifold entry width and microchannel width. Since conductivity of the material of the manifold is low, the manifold fin is not included in the domain.

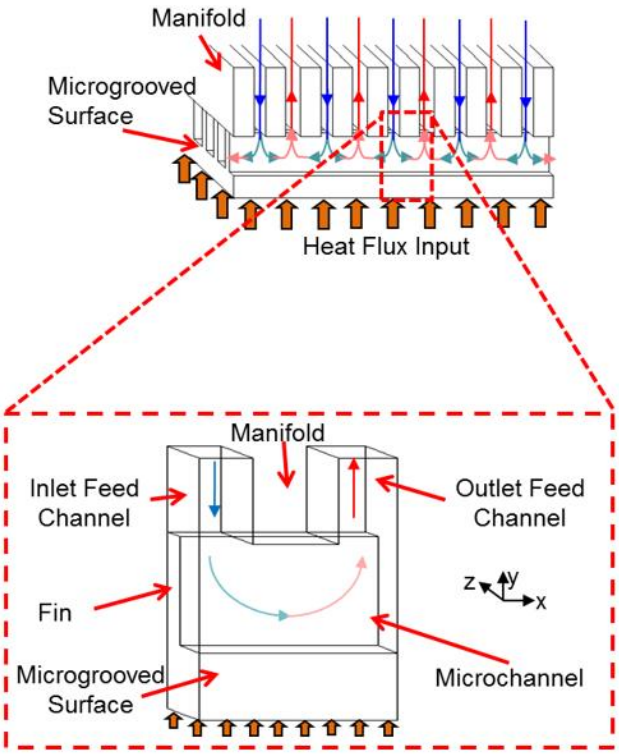

Figure 4-3: Unit cell CFD model for optimization of manifold microchannel heat sink. Figure from S2TS lab.

The optimization is performed as connection of MATLAB, ICEMCFD and ANSYS Fluent software packages (Figure 4-4). The problem is formulated in MATLAB and variable assignment and parametrization are performed there as well. The software then successively feeds necessary information first to ICEMCFD, for geometry and mesh generation, and then to ANSYS Fluent for CFD simulation. The analysis of CFD results is again performed in MATLAB.

Objectives and parameters of the problem are formulated as:

Minimize: negative heat transfer coefficient

Minimize:	Pressure drop
Subject to:	0.5 mm < Inlet feed channel length < 10 mm
	1 mm < Manifold fin width < 20 mm
	1 < Number of passes < 20
With:	Inlet feed channel length = outlet feed channel length
	Microchannel length = manifold fin width + (Inlet feed channel length)/2 + (Outlet feed channel length)/2
	Length of manifold cell = function (Number of passes)

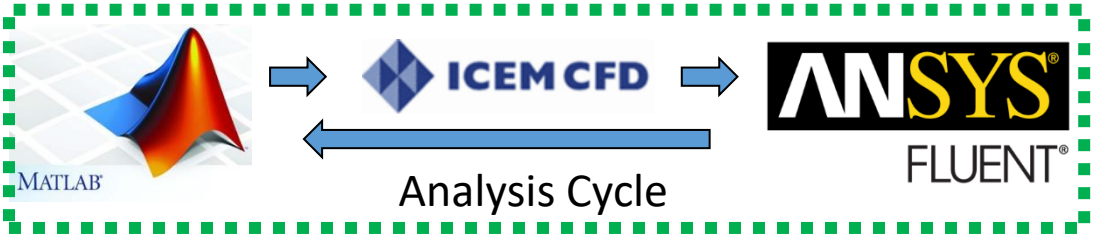

Figure 4-4: Software interaction for optimization of manifold geometry.

Results of the optimization are presented in Figure 4-5. As expected, a trade-off between high heat transfer coefficient and low pressure drop exists. The chart shows results for two different cooling water flow rates. When the cooling water flow rate increases by one order of magnitude, variations in manifold geometry make it possible to achieve similar pressure drops using the same microchannel disk. These optimization results obtained for a simple unit cell were used to design the manifold with varying cell geometries over the whole cooling area of the spinning disk absorber. The adaption was made such that width of the manifold fin changes over the course of the disk. For areas with shorter length between inlet and outlet and thus less number of passes

through microchannels, the fin width increases. Therefore, the length of each pass through the microchannels increases, leading to overall similar pressure drop for different areas of the disk. The design concept will be discussed in more detail in chapter 4.2.3.

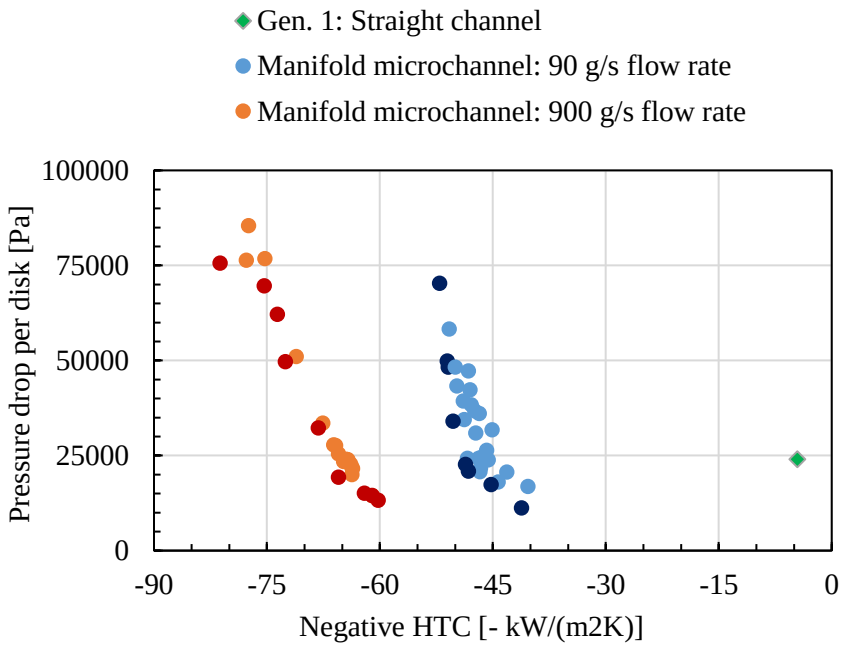

Figure 4-5: Optimization results for manifold microchannel system and comparison to conventionally cooled spinning disk reactor

4.2.2. Design of test section

A schematic diagram of the absorber used in this part of the work is shown in Figure 4-6. The absorber is composed of an internally cooled, disk-shaped heat exchanger that spins at up to 625 rpm. The absorbent solution is fed to the center of the top surface of the absorber from which it flows radially outward due to centrifugal acceleration. The

thickness of the solution film depends on the disk's rotational speed. The absorbent solution absorbs water vapor as it flows over the surface of the disk. The water absorption causes enthalpy of condensation and heat of mixing, which are rejected into the rotating disk assembly. The disk is cooled internally by cooling water, which is supplied and returned through the drive shaft.

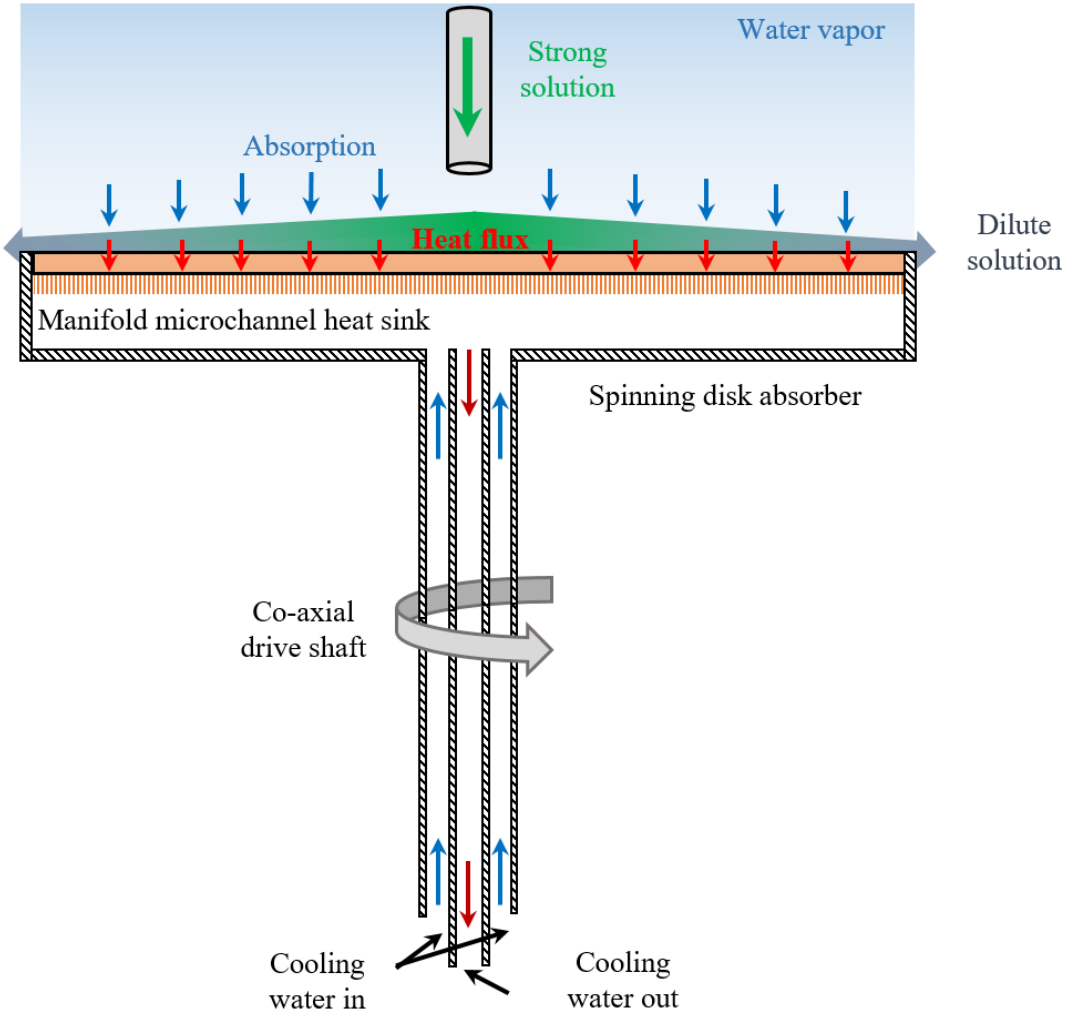

Figure 4-6: Schematic of spinning disk absorber assembly.

The spinning disk assembly consists of four layers: a top disk, microchannel disk, manifold disk and back cover (Figure 4-7). Microchannel and manifold disks are encircled by sealing rings. Table 4-1 lists geometrical dimensions, Figure 4-8 provides photographs of the significant parts of the assembly. The top disk is made of copper and has a surface area of 0.073 m^2 with an active area (i.e., the cooled area) of 0.057 m^2. A disk with microchannels is soldered to the internal (water-side) face of the top disk. Figure 4-9 shows the microchannels, which are made using micro-deformation technology. The microchannels run in parallel; therefore, microchannels located near the center of the disk are longer than those located further from the center. The third layer is an additively manufactured manifold for distribution of cooling water into the microchannels. The manifold was treated with a low viscosity, penetrating epoxy to make it leak-proof. It is attached to the copper heat sink by fasteners (Figure 4-8c). The microchannel and manifold disks are surrounded by metal rings that contain sealing and space for fasteners. The disk assembly ends with a back cover that is fastened to the drive shaft. The drive shaft consists of an external and internal tube to separate cooling water supply and return (Figure 4-7).

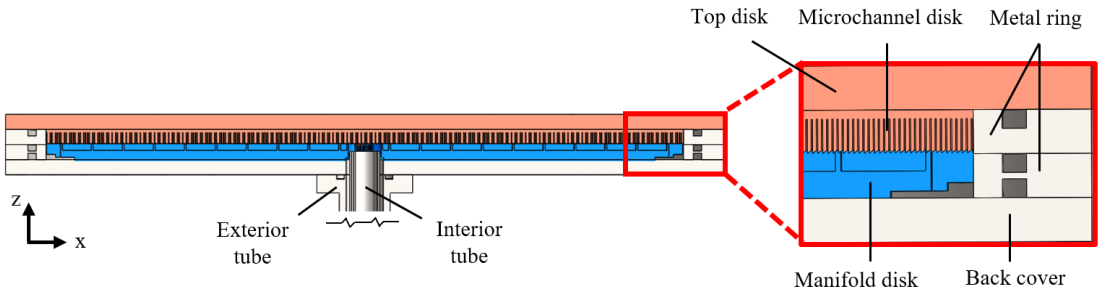

Figure 4-7: Cross-section cut through center of spinning disk assembly.

Table 4-1: Geometrical dimensions of enhanced disk assembly.

Component (Material)	Radius	Thickness	Fin height | fin width | channel width
Top disk (copper)	0.152 m	6.35 mm	-
Microchannel disk (copper)	0.135 m	1.2 mm (Base)	5 mm | 0.55 mm | 0.2 mm
Manifold disk (ABS)	0.135 m	3.9 mm (Base)	3 mm | 5.4 mm - 16.9 mm | 4.5 mm
Back cover (stainless steel)	0.152 m	6.35 mm	-

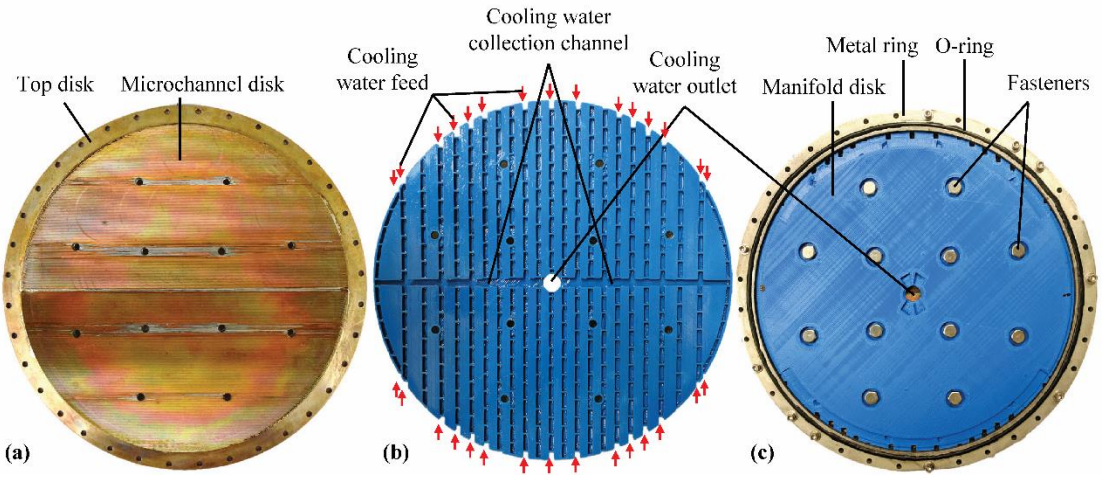

Figure 4-8: Manifold-microchannel disk heat exchanger: (a) Microchannel disk soldered to top disk, (b) Additively manufactured polymer manifold disk, (c) Manifold fastened to copper disk and encircled by metal ring.

Figure 4-9: Detail view of microchannels.

4.2.3. Water-side heat transfer enhancement

Ideally, the absorbent solution and cooling water would flow in counter-current operation. The flow path of the absorbent solution is determined by centrifugal acceleration and therefore lies in the radial direction. Thus, preferably, the cooling water would flow radially inward from the circumference of the cooling area to an exit located centrally in the drive shaft. The parallel orientation of the microchannels, however, poses a challenge as to the desired routing of the cooling water. A solution to this problem was developed by adapting an established manifold-microchannel technology [21,22], as explained in the following paragraphs.

Manifold-microchannel heat exchangers are commonly manufactured in a rectangular shape and have been shown to achieve equal or better heat transfer performance than conventional microchannels while considerably reducing the pressure drop penalty. Figure 4-10 shows the arrangement of the top disk, microchannels and manifold in the present embodiment. The manifold has openings to

feed the cooling water into the microchannels over a length of two thirds of its perimeter (see cooling water feed locations in Figure 4-8b and Figure 4-10). In the manifold, cooling water travels in the ± x-direction, while movement in the microchannel is restricted to the ± y-direction. Detail view A within Figure 4-10 shows the manifolding system. Cooling water enters a manifold cell through an opening in the base of manifold (step 1). As the path into the x-direction is blocked within a short distance from the point of entry, the cooling water is forced into several microchannels in parallel (step 2). It is required to flow through the microchannels for the width of the manifold's fin (step 3). Once it passes the edge of the manifold fin, it escapes into an adjacent manifold cell (step 4). Within the manifold cell, the cooling water travels a short distance in the x-direction (step 5) before a wall forces it to return into the microchannels (step 6). After travelling for the length of the manifold fin (step 7), it reaches a cell located at the same y-coordinate at which its journey started but at an advanced x-coordinate (step 8). From here, the passage repeats itself throughout the manifold-microchannel system until the cooling water reaches a horizontal coolant collection channel (Detail view B in Figure 4-10). The collection channel gathers the cooling water and leads it to the outlet at the center of the disk.

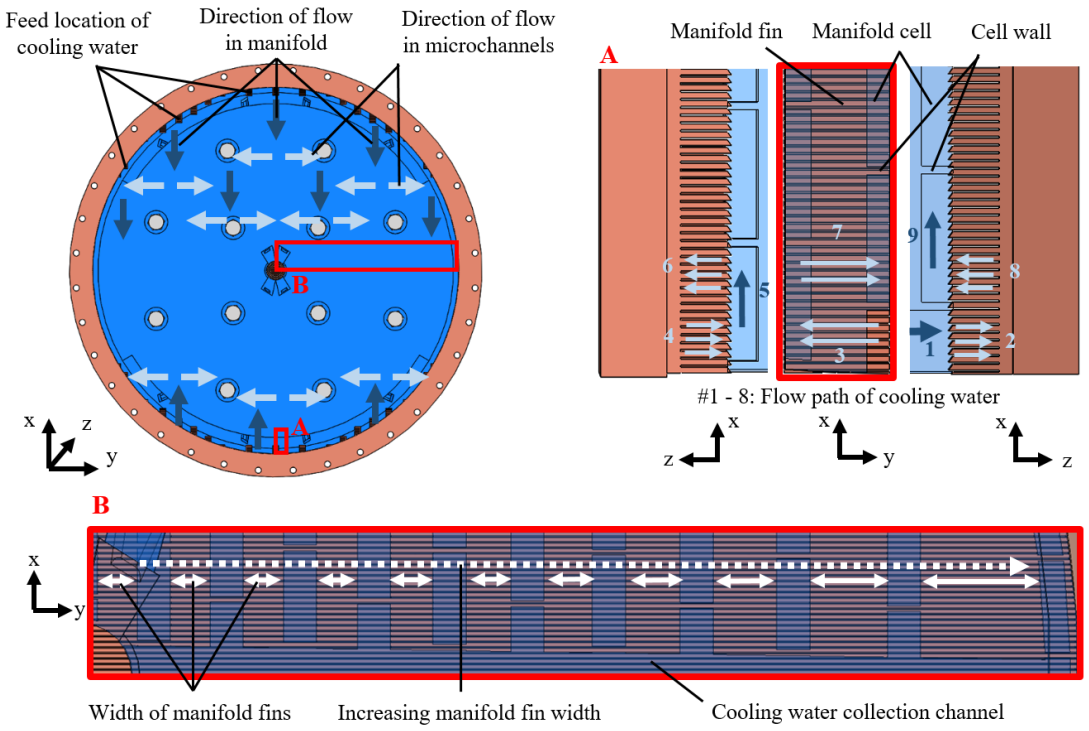

Figure 4-10: Geometrical configuration of disk-shaped manifold-microchannel heat exchanger. Detail view A: Feed system; Detail view B: Varying manifold fin width in y-direction.

The description of the flow path in detail view A of Figure 4-10 is slightly simplified in that the cooling water can always flow into adjacent cells in the positive and negative y-direction. Ultimately, all cells connect with each other through their neighbors, and cross-talk between the different pathways ensures good flow distribution. The feed location of the cooling water into the manifold determines the flow length into the x-direction. The number of serial passes through the microchannels and the pressure drop depend on the flow length in x-direction. Therefore, the manifold was designed to achieve uniform mass flow of cooling water per microchannel as

shown in detail view B of Figure 4-10. The fin width of the manifold cells increases from the center towards the perimeter in the positive and negative y-direction. The increase in fin width results in longer flow length through the microchannels as well as higher pressure drop per pass. The fin width was adapted such that the total pressure drop trough the manifold-microchannel system was the same independent of feed location. This adaption of manifold-microchannel technology makes it possible to use parallel straight microchannels in near-counterflow configuration to a fluid flowing radially on the opposite side. Conventional heat exchangers are usually limited to standard shapes such as shell-and-tube or flat plates. However, the actual volume available for heat exchanger deployment in space-limited applications may have a non-standard shape. The design proposed here makes it possible to customize manifold-microchannel technology to optimally use space in such applications.

4.2.4. Experimental setup

Figure 4-11a and Figure 4-12 show a photograph and a schematic of the experimental setup, respectively. The setup consists of a closed loop vacuum system that operates at a single pressure level. 20 g/s of concentrated water/lithium bromide solution is fed to the center of the spinning disk absorber, which rotates in a vacuum chamber filled with pure water vapor. The water/lithium bromide solution, flowing in radial direction over the disk (Figure 4-11b), absorbs water vapor and gets diluted in the process. The diluted solution flows directly into the generator, which is located in the bottom of the vacuum chamber and consists of 5 cartridge heaters of 1.5 kW

capacity each. A stainless steel plate between the generator and absorber sections prevents back-splashing of the boiling solution into the absorber. From the generator, the solution is pumped into the solution line while the water vapor flows directly back into the absorber section. The solution line contains Coriolis flow meters that measure density and mass flow rate. A heat exchanger controls the temperature of the concentrated solution before it is fed back to the absorber. A drive shaft connects the spinning disk absorber assembly with a pulley and motor. Sealing and bearings of the shaft are integrated in a rotary feedthrough. The end of the drive shaft rotates in a stationary duo-flow valve, which connects to cooling water supply and return lines. RTDs measure temperature of the cooling water while thermocouples measure other temperatures. More details on the experimental setup used in this study and its operation can be found in chapter 3.1.2 and chapter 3.1.3.

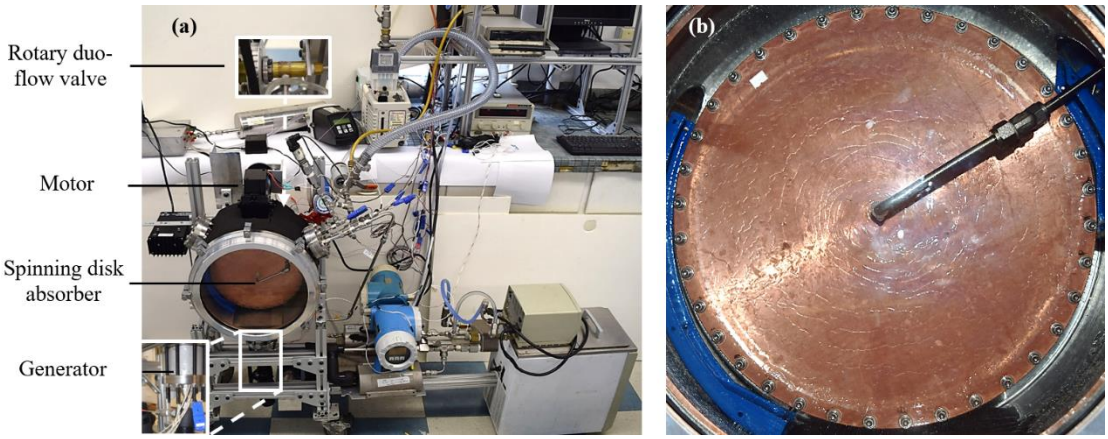

Figure 4-11: Photograph of the (a) experimental setup and (b) the absorber surface while operating.

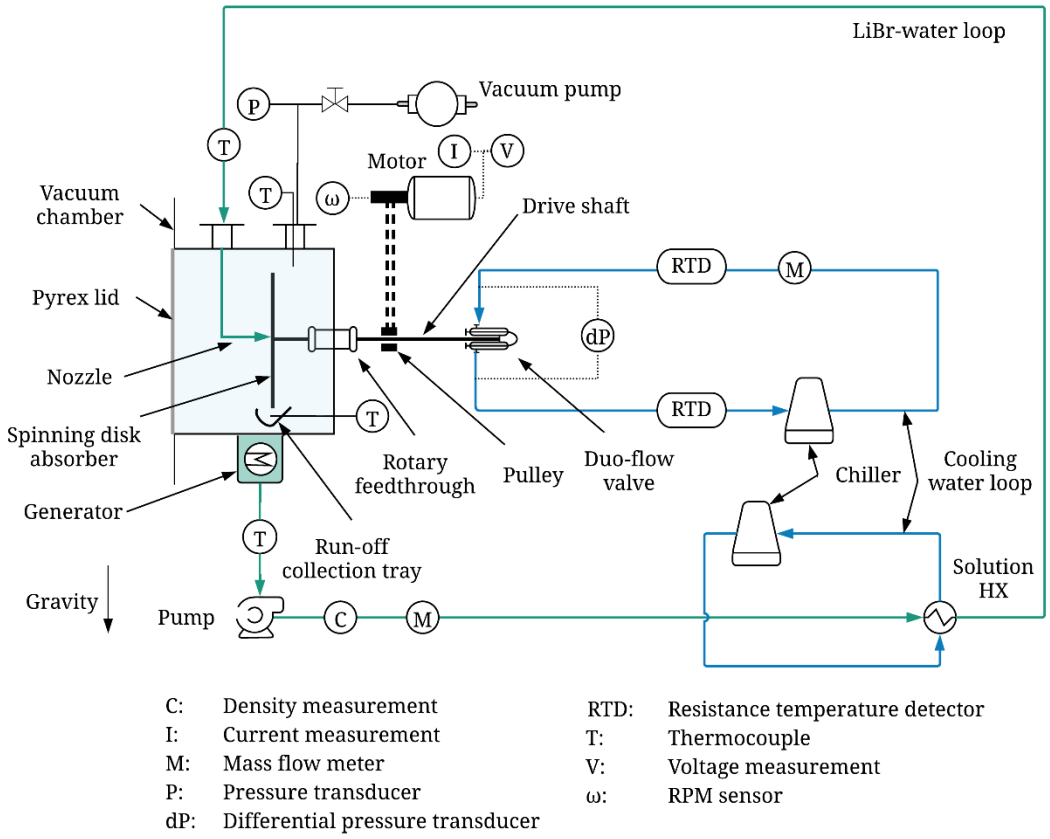

Figure 4-12: Schematic diagram of the experimental setup.

4.3. Data reduction experimental uncertainty

4.3.1. Data reduction

Absorber heat load is based on the heat rejected to cooling water less frictional heating of rotation. It is assumed that rotational power is converted into frictional heating which is ultimately rejected to the cooling water. The share of frictional heating was less than 2% of overall heat rejection load.

$$\dot{Q}_{abs} = \left(T_{CW,out} - T_{CW,in}\right) c_{p,CW} \dot{m}_{CW} - \eta_M I_M V_M \quad 4\text{-}1$$

The absorber heat flux is heat load divided by active heat exchange area.

$$\dot{q}''_{abs} = \frac{\dot{Q}_{abs}}{A} \quad 4\text{-}2$$

The absorber heat load can also be calculated from the solution side, Eq. 4-3.

$$\dot{Q}_{abs} = \dot{m}_{Sol,in} h_{Sol,in}(T_{Sol,in}, x_{Sol,in}) + \dot{m}_{H_2O,(g)} h_{H_2O} - h_{Sol,out} \dot{m}_{Sol,out}(T_{Sol,out}, x_{Sol,out}) \quad 4\text{-}3$$

Eq. 4-3 can be solved numerically [44] using partial and overall mass balance of substances and thermodynamic property routines developed reported by Yuan and Herold [130], yielding the absorbed mass of water vapor $\dot{m}_{H_2O}$ and related parameters. The absorber mass flux or rate of absorption is equal to the mass transfer over area.

$$N''_{H_2O} = \frac{\dot{m}_{H_2O(g)}}{A} \quad 4\text{-}4$$

The cooling capacity is calculated from the absorbed mass of water vapor and the enthalpy of vaporization at the measured pressure.

$$\dot{Q}_{CC} = \dot{m}_{H_2O\,(g)} (h_{H_2O\,(g)} - h_{H_2O\,(l)}) \quad 4\text{-}5$$

4.3.2. Experimental uncertainty

Limits of error of individual measurements are listed in Table 4-2. Temperatures were measured with class 1/10 DIN RTD sensors and T-type thermocouples with special limits of error. Table 4-3 lists the estimated uncertainties in output quantities based on an error propagation analysis as outlined in NIST Technical Note 1297 [132]. Equipment suppliers commonly do not differentiate between random and systematic

uncertainties (see Table 4-2) and therefore the uncertainty analysis in this study includes both types of errors. However, in order to further minimize the effect of random errors, measurements were collected over a time interval of 1 minute and averaged.

Table 4-2: Limits of error of measurement quantities.

Measurement variable	**Error source**	**Proportional error**	**Absolute error**	**Total error at typical conditions**
Cooling water mass flow rate	Measurement, transmitter, current	± 0.36%	± 0.14 g/s	± 0.47%
Solution density	Measurement, current	-	± 1 kg/m3	± 0.06%
Solution mass flow rate	Measurement, current	± 0.16%	-	± 0.16%
Vacuum pressure	Measurement	± 0.25%	± 0.13 Pa	± 0.26%
Rotational speed	Measurement	-	± 4.2 rpm	± 1.12%
Motor voltage	DAQ	± 0.0035%	± 0.00005V	± 0.004%
Motor current	Measurement, DAQ	± 1%	± 0.003 A	± 1.05%
Pressure drop	Measurement	± 0.15%	± 155 Pa	± 0.31%
Temperature (RTD)	Measurement, DAQ	-	± 0.106 °C	± 0.106 °C
Temperature (TC)	Measurement, DAQ	-	± 1.5 °C	± 1.5 °C

Table 4-3: Uncertainty of calculated variables.

Variable	**Uncertainty at minimum heat transfer rate**	**Uncertainty at maximum heat transfer rate**
Absorption rate [kg/(m^2·K)]	6.9%	4.0%
Overall heat transfer coefficient [W/(m^2·K)]	5.8%	3.9%
Heat flux [W/m^2]	5.1%	3.0%
Cooling capacity [W]	7.0%	4.1%
Power consumption [W]	1.0%	0.9%

4.4. Results and discussion

4.4.1. Absorption rate

The absorption rate is plotted against the rotational speed in Figure 4-13. The absorption rate increases continuously with rotational speed. The highest rate of absorption was 0.016 kg/(m^2·s) at a rotational speed of 625 rpm. This value was 77% higher than the rate measured at the minimum rotational speed of 128 rpm. The significant enhancement of absorption rate with rotational speed is attributed to the effect of rotational speed on both heat and mass transfer rates. Heat transfer benefits from higher rotational speed due to the decreasing film thickness caused by stronger centrifugal acceleration. Also, the increased intensity of film waviness with rotational speed leads to stronger disturbance of the concentration boundary layer and hence mass transfer enhancement.

Figure 4-14 shows a comparison to absorption rates reported in literature for various absorber types. The operating conditions of the studies plotted in Figure 4-14 are given in Table 2-1 and Table 2-4. Wherever possible, the maximum absorption rate values measured at solution concentrations, solution temperatures and cooling water temperatures closest to those of the present study were chosen for this comparison. Most studies were conducted at operating conditions relatively similar to the ones present here and hence the results are comparable. Notable expectations are lower cooling water temperatures used by Mortazavi et al. [62] and by Isfahani and

Moghaddam [58] and higher cooling water temperatures by Miller and Perez-Blanco [42] and by Miller and Keyhani [140].

The average value of all the data points from the literature plotted in Figure 4-14 is an absorption rate of 0.003 kg/(m^2·s) at a vapor pressure of 1.35 kPa. The highest absorption rate recorded in the present study was 0.016 kg/(m^2·s), which is 5.3 times higher. Most studies with conventional tube-type absorbers report absorption rates in the range of 0.002 – 0.003 kg/(m^2·s), but some values are as low as 0.001 kg/(m^2·s). One notable positive exception is the result with both internally and externally enhanced tubes given by Atchley et al. [32]. They tested a variety of different enhanced tubes of which the best-performing is plotted in Figure 4-14. Even higher absorption rates were achieved in tests with vertical plates by Michel et al. [61] and Mortazavi et al. [62] and a membrane-based reactor by Isfahani and Moghaddam [58]. However, the solution at the absorber inlet was substantially subcooled during these studies. Further, cooling water temperature in the studies by Mortazavi et al. and Isfahani and Moghaddam was relatively low which makes a direct comparison to the present study difficult. Lower cooling water temperature increases the rate of absorption by providing faster heat rejection.

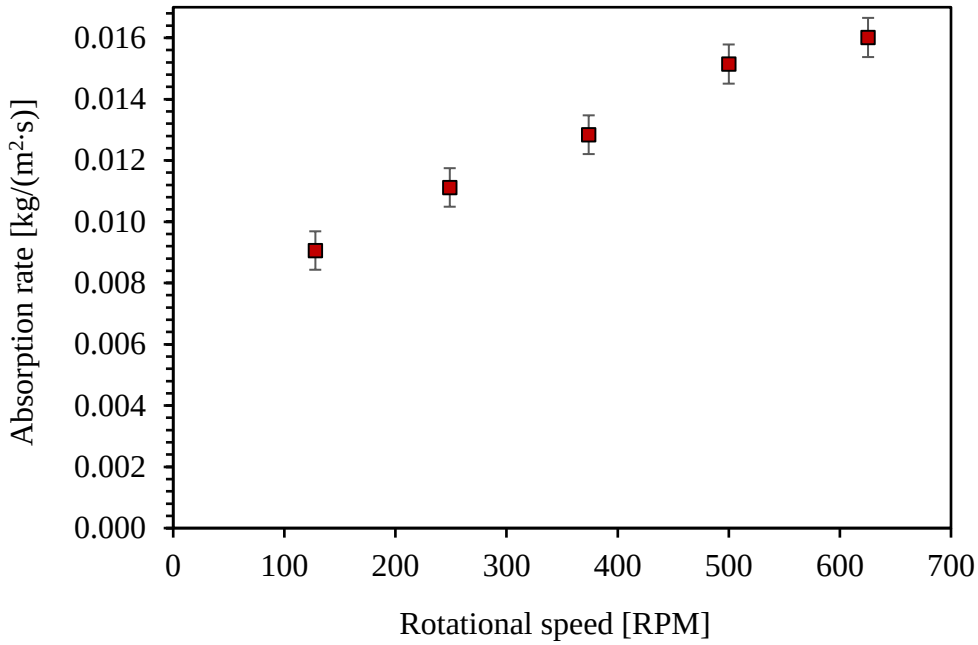

Figure 4-13: Absorption rate vs. rotational speed.

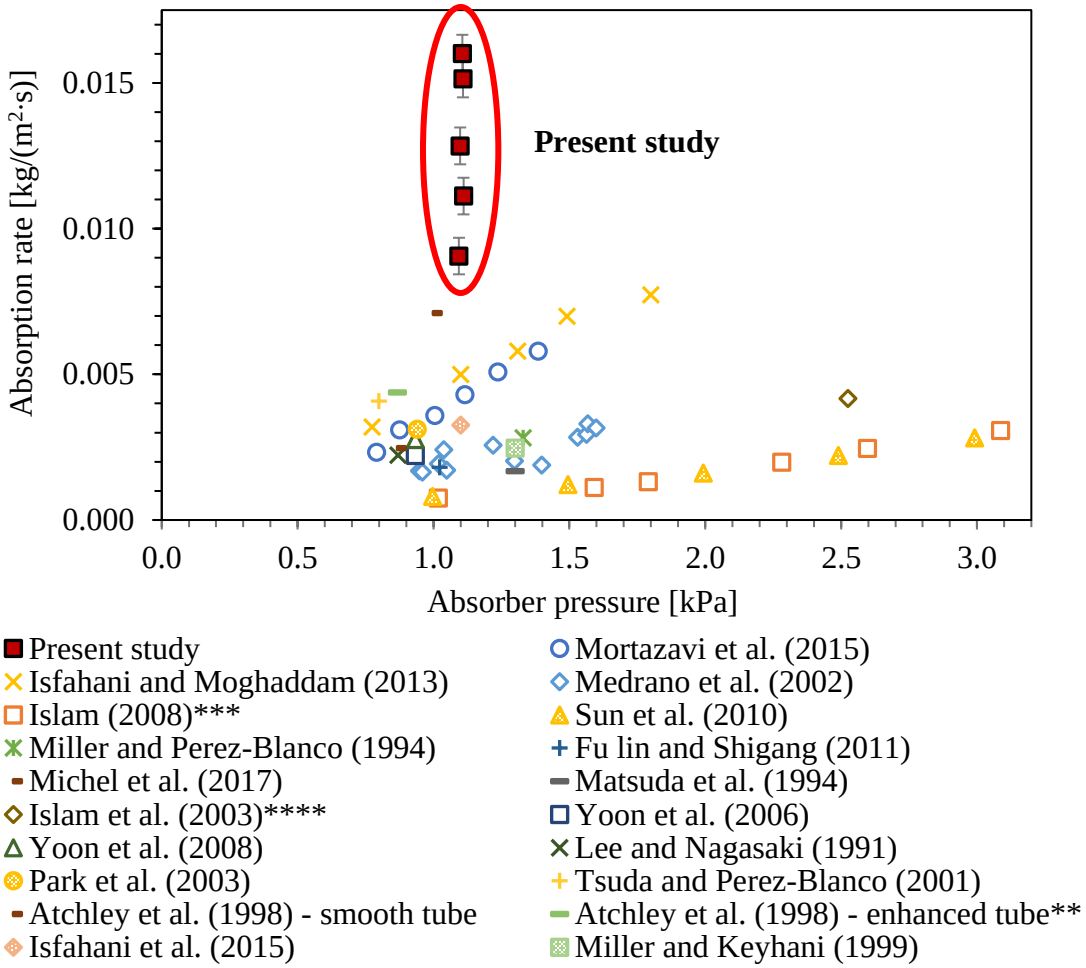

Figure 4-14: Absorption rates reported in the literature at different absorber pressures.

4.4.2. Heat transfer performance

Figure 4-15 shows the effect of rotational speed on overall heat transfer coefficient in the present study and compares it to results for a spinning disk absorber without internal enhancement reported in chapter 3. In the present experiments, the overall heat transfer coefficient increased continuously from 1851 W/(m^2·K) to 3622 W/(m^2·K) at rotational speed varying from 125 rpm to 625 rpm. The improvement in heat transfer

coefficient compared to spinning disk without internal enhancement amounts 18% at the lowest speed to 42% at the highest speed. This intensification of the transfer process is attributed to the use of manifold-microchannel technology to enhance heat transfer on the water side.

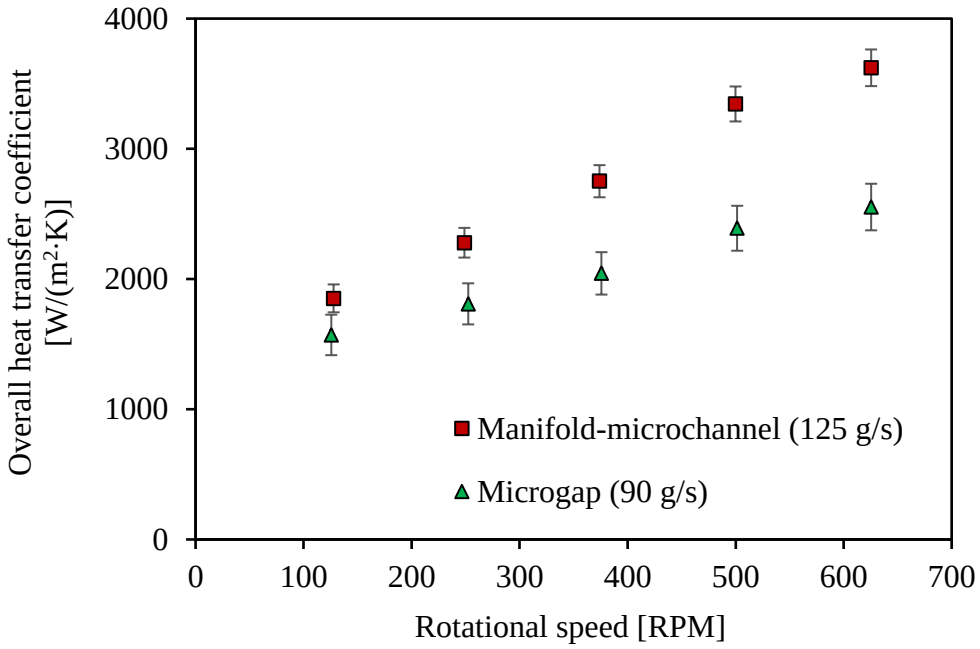

Figure 4-15: Comparison of overall heat transfer coefficient in the present experiments with those presented in chapter 3.3.1.

Table 2-3 in chapter 2.2 listed values of the overall heat transfer coefficients of conventional heat/mass exchangers reported in the literature. The large spread in absolute values reflects the influence of differences in operating conditions and analytical methodologies—mainly, the temperature difference from which the heat transfer coefficient is derived [58]. Results for tube banks operated at similar conditions and analyzed with the same methodology as the present study were reported by Kyung and Herold [13]. The absorber in the present study achieved a maximum enhancement factor of 4.7 at 625 rpm and a minimum enhancement factor of 2.4 at 128 rpm. This result points to the opportunity to significantly reduce the size of absorbers in water/lithium bromide absorption chillers. In the enhanced spinning disk absorber, the heat transferred per active surface area increased almost fivefold which should translate into equal reduction in absorber volume with well-designed packaging.

Figure 4-16 shows a comparison of thermal resistances in fast-rotating spinning disk absorbers with microgap cooling and manifold-channel cooling. The resistances in the present test section were calculated by an adaption of the Wilson plot technique as outlined in chapter 3.2. The chart shows that the increase in overall heat transfer is due to the improvement of the water-side heat transfer; the water-side resistance decreases by 66% while solution-side and conduction resistance are approximately constant. The heat transfer resistance of the manifold-microchannel spinning disk absorber is dominated by solution-side resistance, which accounts for 59% of overall resistance. Thus, surface modifications on the solution-side of the absorber should be considered to enable further performance enhancement. In experiments with water,

grooves in the disk surface have been shown to increase heat transfer by more than 60% over smooth disks [11]. However, the influence of water-side resistance is also significant such that further refinement of the manifold-microchannel system may also lead to further process intensification.

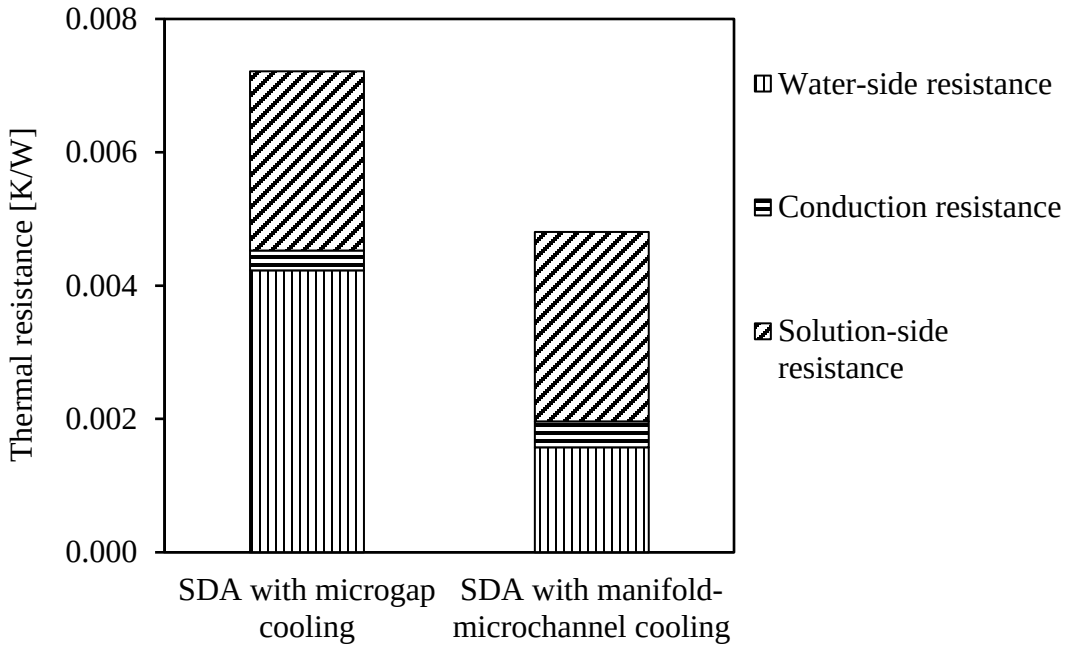

Figure 4-16: Thermal resistance breakdown of spinning disk absorbers (SDA) with microgap (chapter 3.3.2) and manifold-microchannel water-side cooling (this set of experiments) rotating at 625 rpm.

Another metric to compare heat transfer performance is the absorber heat flux. Figure 4-17 plots heat flux of various studies against their respective vapor pressure and results from the present study with the respective rotational speed.

Table 2-2 listed the details of the devices and test conditions of the studies presented in Figure 4-17. As expected, the absorber heat flux of the present heat/mass exchanger increases with rotational speed. It reaches a maximum of 45.6 kW/(m^2·K) at 625 rpm. The cited studies report significantly lower values between 5.4 and 16.6 kW/(m^2·K).

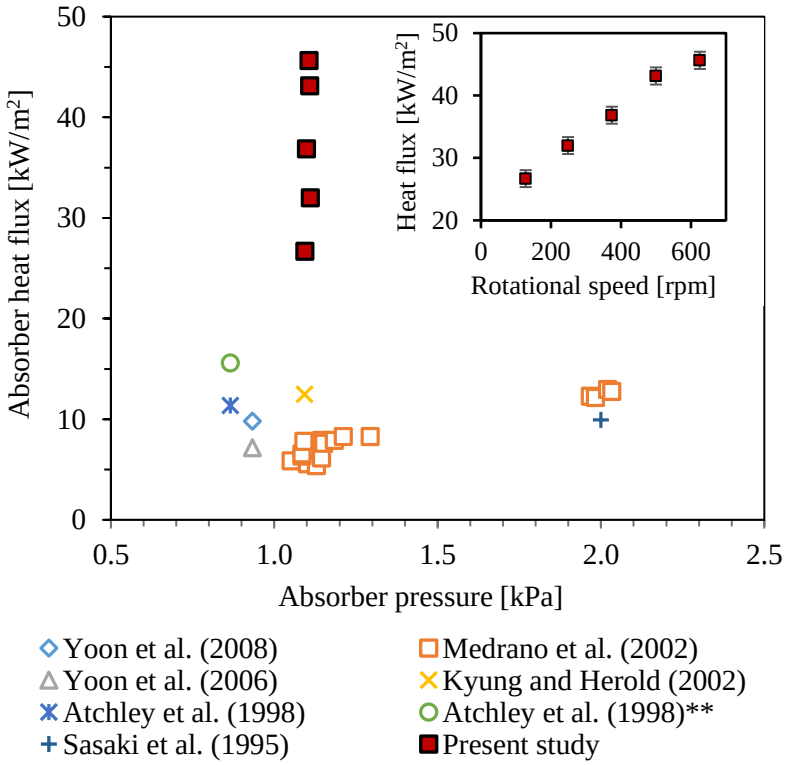

Figure 4-17: Absorber heat flux in comparison to literature values.

4.4.3. Cooling capacity and power consumption

The cooling capacity continuously increases from 1292 W to 2283 W with increase in rotational speed (Figure 4-18). The present experiments were conducted at a pressure of 1.1 kPa, and thus the minimum chilled water temperature at which the reported cooling capacity can be achieved is 8.4 ºC. The use of manifold-microchannel

technology increased cooling capacity by up to 48% compared to a spinning disk absorber without water-side enhancement operated at similar conditions except for lower cooling water flow rate.

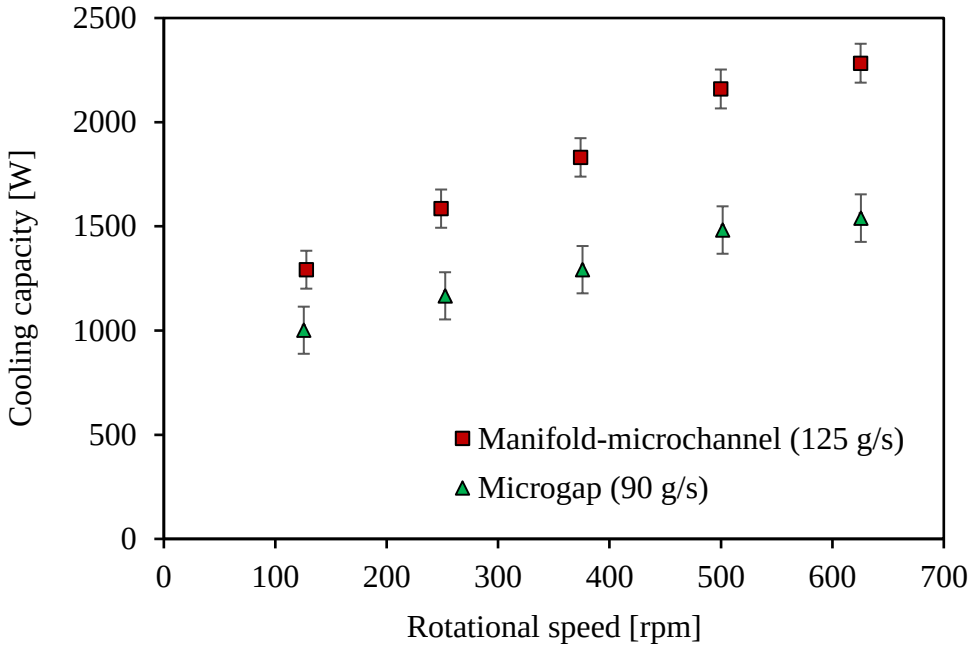

Figure 4-18: Effect of rotational speed on the absorber cooling capacity.

The increase in cooling capacity with faster rotation comes at the cost of higher power consumption of the electric motor. Figure 4-19 shows the power consumption of the electric motor and the power consumed by rotation of the disk. Rotational power is consumed primarily to overcome bearing and sealing friction with a minor contribution by the centrifugal acceleration of the liquid (see chapter 3.3.4). Total power consumption additionally includes the losses at the motor level. Rotational power and the total power consumption were 53 W and 81 W at the maximum rotational speed. The motor's efficiency was calculated from the motor curve based on the measured

voltage. It was between 63% and 66% throughout the experiments, which was close to the motor's maximum efficiency of 71.6%. This means that around a third of the power draw was lost in the motor's windings. This energy loss can easily be reduced by a more efficient motor. The bulk of the rotational power loss is due to frictional losses in the sealing. Here, the use of more efficient low-friction sealing materials could reduce power consumption.

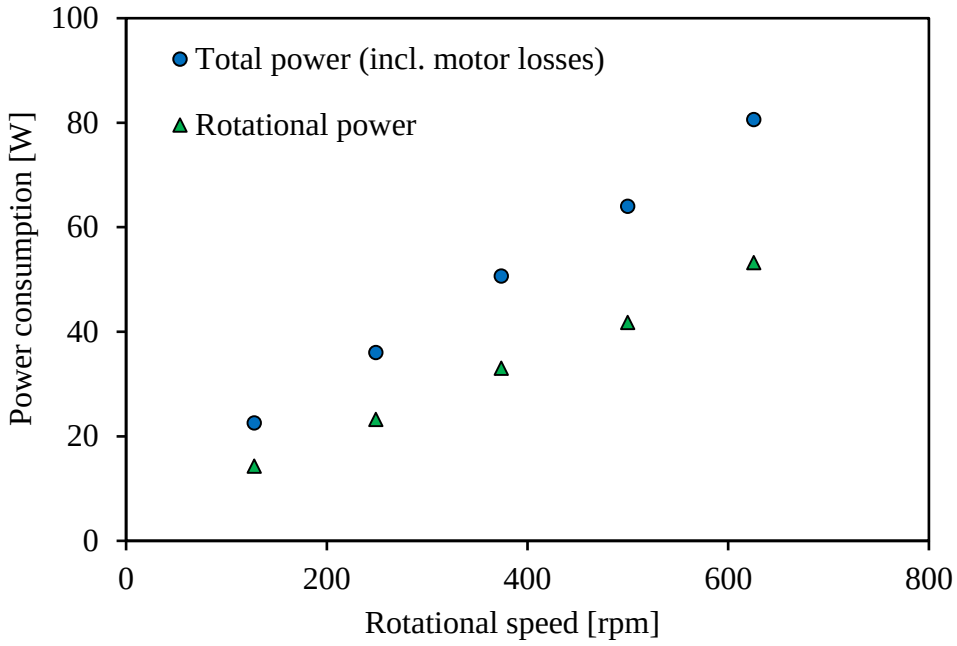

Figure 4-19: Power consumption caused by rotation of the disk.

Power consumption rose more quickly than cooling capacity with increasing rotational speed. This is in line with theoretical considerations: Keyvani and Gardner [141] estimate power consumption for bearing friction to be proportional to rotational speed. Assuming applicability of the Nusselt model, the solution-side heat transfer coefficient is proportional to $\omega^{2/3}$ [13]. Since other heat transfer resistances (e.g.

conduction and water-side heat transfer resistances) do not decrease with rotational speed, cooling capacity is expected to rise less than $\omega^{2/3}$. Hence power consumption rate, defined as power consumption over cooling capacity, rises with rotational speed. Figure 4-20 shows power consumption rate based on both total power draw and rotational power. The rotational power consumption rate has a minimum of 1.1 % and a maximum of 2.3 %, measured at minimum and maximum rotational speeds, respectively. This result indicates that there is a trade-off between increasing cooling capacity and most efficient provision of cooling.

Since the power is lost mainly in the sealing of the drive shaft, it will scale favorably with scale-up of the device. The device can likely be scaled up by stacking several disks in parallel on a single drive shaft, and cooling capacity will increase proportionally to the number of disks. Even if shaft diameter increases to accommodate higher cooling water flow rates, frictional losses will increase less than proportional to the number of disks. Hence, cooling capacity is expected to increase faster than power consumption.

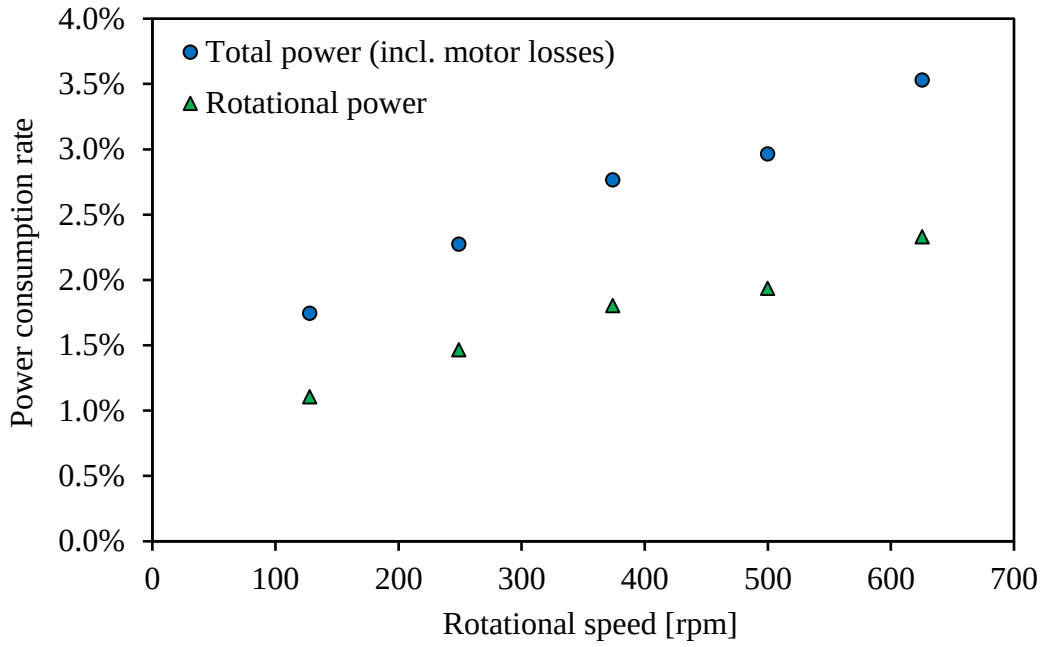

Figure 4-20: Spinning disk power consumption as a fraction of absorber's cooling capacity.

Figure 4-21 shows the pressure drop performance of the spinning disk absorber heat exchanger at a cooling water flow rate of 125 g/s. Independent of rotational speed, the pressure drop was measured at values around 50,000 Pa which was deemed acceptable for the application. The present heat exchanger has relatively large microchannels and if the attempt is made to improve heat transfer characteristics by reducing channel width, a trade-off between channel size and pressure drop is expected to arise. The pressure drop with manifold-microchannel technology at 125 g/s was less than maximum pressure drop recorded with microgap cooling. With microgap cooling, the cooling water pressure drop increase with rotational speed. The reason for this behavior could be established with certainty.

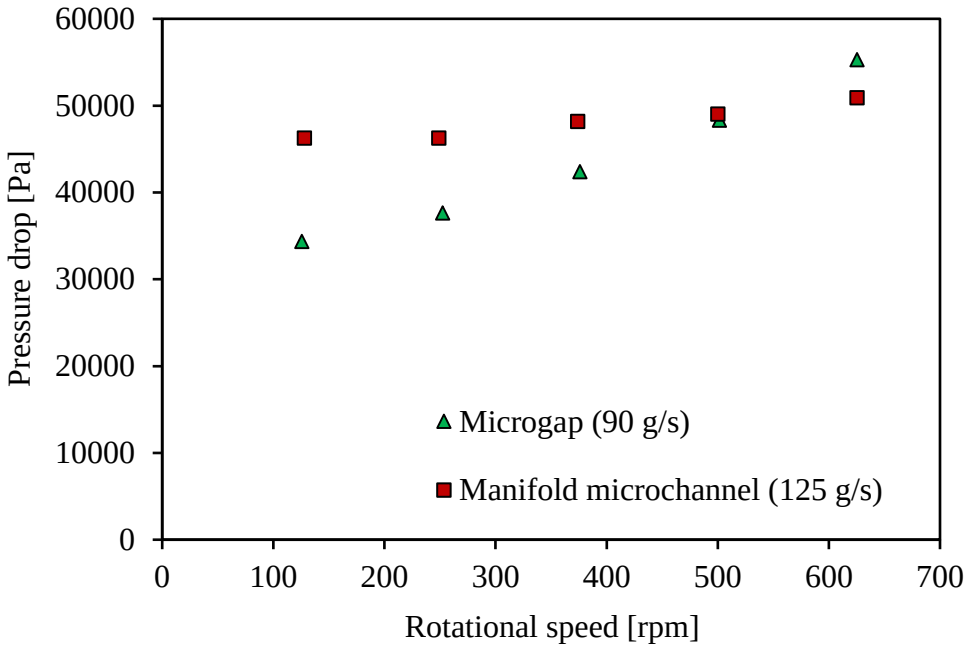

Figure 4-21: Pressure drop performance of spinning disk absorber.

4.5. Chapter conclusions

Almost one half of the world's primary energy consumption is rejected as low temperature waste heat. Water/lithium bromide absorption cooling is an efficient process to recover this waste heat for cooling purposes. However, the coupled heat/mass transfer process in absorbers of water/lithium bromide absorption chillers is slow, which makes the absorption systems bulky. The high heat transfer resistance also causes crystallization issues in air-cooled systems.

To reduce the size of absorption cooling systems, a novel manifold-microchannel assisted spinning disk absorber was fabricated. Spinning of the disk improved the

solution-side performance while the manifold-microchannel provided water-side enhancement. Combination of these process intensification methods increased the overall heat transfer coefficient by a factor of 4.7 over a conventional tube bank absorber. The rate of absorption increased by a factor of 4 to 10 over tube banks and by at least a factor of 2 over state-of-the-art absorption technologies.

The spinning disk absorber achieved a heat flux of 46 kW/(m^2·K), which led to a cooling capacity of 2.3 kW for the single-disk design used in this study. Power required for spinning the disk ranged between 1.1% and 2.3% of cooling capacity. The majority of power consumption was caused by friction of the drive shaft's sealing. Therefore, a scaled-up multi-disk absorber is expected to have a much lower power consumption relative to cooling capacity.

The enhanced spinning disk absorber requires about one fifth or less of the surface area of conventional absorbers for equal performance. The process intensification can lead to significantly smaller absorbers and more compact absorption chillers. The enhancements also help operate the absorber at higher heat rejection temperatures, which can facilitate air-cooling of the system. Such a compact, air-cooled absorption chiller could substantially reduce cost of absorption cooling systems and make otherwise wasted energy available for cooling applications. Further areas of research include optimization of enhancement concepts, and fabrication of a scaled-up absorber design and will be discussed in chapter 0.

5. A model of a water/lithium bromide spinning disk absorber

Chapter 5 describes the development of an analytical model of water absorption into aqueous lithium bromide on a spinning disk reactor. After a short introduction, related literature is reviewed in section 5.2. Two different research areas are relevant for the present study: Models of water absorption into aqueous lithium bromide on tube-type absorbers and studies on heat/mass transfer behavior of spinning disk reactors. Based on the reviewed literature, a modeling approach for a spinning disk absorber is discussed in section 5.3. Finally, the model results are presented and compared to experimental data.

5.1. Introduction

Conventional shell and tube absorbers have been extensively studied experimentally and, additionally, several analytical models have been published. Such analytical models give insight into the absorption process and are used to optimize absorber designs [142]. The experimental studies presented in chapters 0 and 4 have shown the potential to enhance transfer processes by replacing shell and tube absorbers with spinning disk reactors. The experiments have shown that spinning disk absorbers indeed lead to significant enhancement of the rate of absorption of water vapor in the absorbent solution. However, no analytical model for spinning disk absorbers is available in the literature so far. The objective of the present study is to develop a

simple analytical model for absorption of water vapor into aqueous lithium bromide on spinning disk absorbers. The custom-made program code for the model is implemented in MATLAB. In line with one type of models of tube-type absorbers, the model uses a predefined velocity profile and transfer coefficients. Modeling results are compared to experimental data available in the literature. Analysis of the differences leads the way to model calibration and the development of a semi-empirical mass transfer correlation. The modeling effort aims to give additional insight into the absorption process on spinning disk absorbers. A better understanding of the process will help to develop further optimized spinning disk absorber designs.

5.2. Discussion of previous work

5.2.1. Analytical/numerical models of falling film absorption

The current study concerns the absorption of the refrigerant water by the non-volatile absorbent lithium bromide. Therefore, the review of the literature in this section does not cover ammonia/water systems, which are characterized by a volatile absorbent. A wide-ranging review of falling film absorption with volatile and non-volatile absorbents published up to the year 2001 is provided by Killion and Garimella [27]. Most models solve the governing partial differential equations for energy and mass diffusion, Eqs. 5-1 and 5-25-4, but often under a varying set of simplifying assumptions.

$$\rho\left(\frac{\partial h}{\partial t}+u\frac{\partial h}{\partial x}+v\frac{\partial h}{\partial y}\right)=\frac{\partial}{\partial x}\left(k\frac{\partial T}{\partial x}\right)+\frac{\partial}{\partial y}\left(k\frac{\partial T}{\partial y}\right) \qquad 5\text{-}1$$

$$\left(\frac{\partial C_A}{\partial t} + u\frac{\partial C_A}{\partial x} + v\frac{\partial C_A}{\partial y}\right) = \frac{\partial}{\partial x}\left(D_{AB}\frac{\partial C_A}{\partial x}\right) + \frac{\partial}{\partial y}\left(D_{AB}\frac{\partial C_A}{\partial y}\right) \quad 5\text{-}2$$

Three common assumptions are constant thermophysical properties, negligible mass diffusion and heat conduction in stream-wise direction, which yield equations for simplified energy and mass diffusion, Eqs. 5-3 and 5-4.

$$u\frac{\partial T}{\partial x} + v\frac{\partial T}{\partial y} = \alpha\frac{\partial^2 T}{\partial y^2} \quad 5\text{-}3$$

$$u\frac{\partial C_A}{\partial x} + v\frac{\partial C_A}{\partial y} = D_{AB}\frac{\partial^2 C_A}{\partial y^2} \quad 5\text{-}4$$

Widely accepted is the assumption of vapor pressure equilibrium at the gas-liquid interface. The momentum equation is either solved or a linear, parabolic (i.e. the Nusselt model) or other velocity profile is assumed. Killion and Garimella distinguish between models that assume laminar, turbulent and wavy film and those assuming transport coefficients. With respect to the assumption of laminar film, the authors conclude “the practical usefulness of laminar-film models is not well established since laminar films are rarely encountered in actual absorbers”. Turbulent models add an eddy diffusivity factor to the constants for thermal and mass diffusivity, α and D_{AB}, in the governing equations. The value of eddy diffusivity factor depends on the location within the film and is assumed based on profiles reported in the literature. The need to define an eddy diffusivity profile is a major drawback according to Killion and Garimella, since there is no agreement on the appropriate form of the profile. The assumption of wavy films constitute the third category of models. Since Killion and Garimella emphasize the instability of falling films which leads to development of

various types of waves, wavy film flow seems to be their preferred description of falling films. However, wavy-film models commonly rely on significant assumptions such as a priori assumed velocity profiles and negligence of fluid recirculation. Given the lack of agreement on the nature of hydrodynamics and transport processes of falling films and the difficulties in describing them, it is no surprise that a fourth category of models emerged that assumes transport coefficients based on experimental work. Kirby and Perez-Blanco [133] developed one early model in this category. The model is important for two reasons: It describes horizontal tube banks, which are much more common in industry and experimental research, while the majority of publications treats vertical tubes or plates. Further, the model by Kirby and Perez-Blanco was the first to distinguish three mass transfer regimes: falling film, droplet formation and droplet fall. For each mass transfer regime, mass and energy balances were solved. Results from the model were in qualitative agreement with the experimental data by Nomura et al. [29], e.g. they showed the fall and rise of the temperature of the solution in falling film and droplet fall regimes, respectively. The model pointed to the substantial contribution of the droplet formation to overall mass transfer. Later, Jeong and Garimella [30] expanded on Kirby and Perez-Blanco's work by incorporating incomplete wetting of tubes and considering lower Reynolds number flows. They also provided more details on modeling results, including a comparison of mass transfer in the three regimes. The contribution of droplet fall to overall mass transfer is minimal because the time duration is very short. The total amount of mass transfer in falling film and droplet formation are comparable; the mass transfer coefficient in droplet formation is higher but time

duration is less than in falling film, resulting in almost identical water absorption. They assumed that droplet formation is best represented by an internal circulation model with uniform droplet temperature, which increased the mass transfer coefficient in that regime significantly. In the falling film regime, they assumed linear temperature profile across the film except close to the vapor interface where heat of condensation leads to a steeper temperature gradient. They assumed a constant temperature difference between interface and bulk flow for lack of knowledge about the actual temperature profile. For the concentration profile, Jeong and Garimella assume that the concentration profile develops much slower than temperature and velocity profiles such that the concentration boundary layer exhibits interface velocity. This effectively also means that much of the solution flow does not participate in the absorption process. However, they assume perfect mixing as the solution starts its flow around each tube. Kyung et al. [129] published another model that divides the absorption process into three mass transfer regimes. They improve on the resolution of earlier models by solving two-dimensional energy and mass diffusion equations in the falling film regime. The resulting 2D model allows analyzing the evolution of concentration and temperature profiles in transverse direction. In a later publication, the model was also compared to experimental results [128].

In summary, models on gravity-driven falling film absorption show considerable disagreement with respect to modelling approach and exhibit difficulties accurately describing the more complex phenomena observed in experiments. The present study concerns a film flow accelerated by a centrifugal force that is much larger than gravity.

Hence, precise description of the flow and in consequence the transfer processes is even more difficult. Therefore, this study aims to develop a simplified analytical model based on transfer coefficients which are discussed in the next section.

5.2.2. Transfer coefficients of spinning disk reactors

5.2.2.1. Heat transfer coefficient

Heat transfer coefficients in the literature on falling film absorption are commonly based on saturation temperatures [9]. Consequently, Chapters 3 and 4 analyzed experiments conducted with a spinning disk absorber in the same manner. However, heat transfer coefficients based on saturation temperature do not describe actual driving forces and are therefore not suitable for usage in an analytical model. Exothermic absorption combines characteristics of both sensible and latent heat transfer and a review for the case of spinning disk reactors was provided in Chapters 2.4.2 and 2.4.3. Similar to condensation, energy input in absorption takes place at the gas-liquid interface. However, unlike to rotating condensation, the absorbent film on the disk forms a blanket with additional heat transfer resistance. In a theoretical problem of rotating condensation, Sparrow and Gregg [76] found the liquid film to have a linear temperature profile. Experimental investigations can be regarded by and large as affirmative of the heat transfer predictions by Sparrow and Gregg: two studies found satisfactory agreement [78,79], one study found 25% lower [77] while another one found 50-200% higher heat transfer rates [105]. The heat transfer coefficient of liquid films on rotating disks, based on the simple Nusselt model, is given in Eq. 5-5.

$$h = \beta \frac{k}{\delta} \qquad 5\text{-}5$$

The value of thermal conductivity is a known and Burns et al. [70] showed that the Nusselt model gives acceptable estimates of film thickness under most operating conditions, which leaves only β to be determined. The constant β has a value of 2.5 in case of a parabolic temperature profile (Eq. 2-33) and 1.6 in case of linear temperature profile (Eq. 3-7). Linear temperature profiles are generally associated with latent heat transfer into falling films [94] while parabolic temperature profiles are associated with sensible heat transfer. Aoune and Ramshaw [13] reported results for sensible heat transfer and assumed a parabolic temperature profile, although they derived a value for β of 1.67. With a viscous working fluid (μ = 0.01 Pa·s), the experimental heat transfer coefficient surpassed the theoretical prediction. The deviation may be caused by the artificially low value of β Aoune and Ramshaw applied to calculate the prediction; however, in experiments with water they reported local heat transfer coefficients that alternated around the prediction. Jachuck and Ramshaw [11] reported average heat transfer coefficients of 6.0 to 9.4 kW/(m^2·K) for experiments with a water at a flow rate of 0.03 L/s on a smooth disk rotating at 300 – 890 rpm. Per the author's calculations, these values are significantly below the predictions of the Nusselt model. To the best of the author's knowledge, there are no experiments with latent heat transfer into a bulk flow available in the literature that report heat transfer coefficients based on actual temperatures. Chapters 3 and 4 reported experiments with a spinning disk absorber but the results were derived using saturation temperatures in accordance with standard

analysis. Thus, the value of β cannot be determined with certainty. However, there are reasons to assume that assuming a deviation from the linear temperature profile is warranted. For laminar flow on horizontal tubes, Kyung et al. showed that [129] the profile only becomes linear only past a 45º angle. Killion and Garimella [27] concluded that the predominant flow pattern on vertical plates/tubes is a wavy-film and found the published literature to relate heat and mass transfer enhancement to this waviness. For flow with roll waves over a vertical plate, Patnaik and Perez-Blanco [143] have shown that the temperature profile can exhibit steep gradients as well as almost no gradient towards the gas-liquid interface, depending on the location of the wave front. Studying wavy flow as well, Morioka and Kiyota [144] found the temperature profile to alternate between linear and concave sections depending on the location of the wave front. Looking at turbulent falling film flow, Grossman and Heath [145] and Yüksel and Schlünder [146] assume two temperature boundary layers in vicinity of wall and interface, respectively, with no temperature gradient due to eddy heat transport in between. In the experimental part of their work, Yüksel and Schlünder [147] used an infrared measurement technique to monitor the temperature of the free liquid surface. The measurements confirmed that the surface temperature is elevated. Therefore, even if turbulence is assumed, the eddy transport is dampened near the interface which leads to a temperature gradient. Likewise, studies on spinning disks agree on the waviness of the flow upon them [11,96,97] and associate the waves with enhanced heat transfer [11,96].

5.2.2.2. Mass transfer coefficient

Mass transfer on spinning disk reactors is treated in more detail in Chapter 2.4.5 but shall be summarized here for clarity. Higbie [123] wrote in his development of the penetration theory that industrial absorption equipment is characterized by short contact times of gas phase and a usually laminar layer of liquid. Spinning disk reactors are also characterized by short contact times. Hence, Aoune and Ramshaw [13] used the mass transfer coefficient based on Higbie's penetration theory, Eq.5-6, to predict mass transfer on spinning disks.

$$\bar{h}_m = \sqrt{\frac{4D}{\pi t}} \qquad 5\text{-}6$$

However, Aoune and Ramshaw found experimental mass transfer rates to surpass the prediction by a factor of 5. Peev et al. [121] developed a dimensionless form of the Higbie model by using the outer disk radius as characteristic length of the Sherwood number, Eq. 5-7.

$$\overline{Sh}_R = 0.864 Ek_{out}^{-\frac{1}{3}} \mathrm{Re}_{\mathrm{out}}^{\frac{1}{3}} Sc^{\frac{1}{2}} \qquad 5\text{-}7$$

They further calibrated the dimensionless correlation by fitting the experimental data reported by Aoune and Ramshaw to it (Eq. 5-8).

$$\overline{Sh}_R = 10.8 \cdot 10^{-4} Ek_{out}^{-0.94} \mathrm{Re}_{\mathrm{out}}^{0.24} Sc^{\frac{1}{2}} \qquad 5\text{-}8$$

The differences in mass transfer between analytical model and semi-empirical correlation were contributed to the mass transfer enhancement of surface waves. Peev et al. stated that the enhancement factor due to flow waviness lies in between 6 and 13.

Comparing the mass transfer performance of spinning disk to gravity-driven falling film, they estimated that mass transfer coefficients on spinning disks are up to 14 times higher than those for gravity-driven wavy falling film at similar Reynolds numbers.

The effect of wave regime on vapor-liquid mass transfer was studied numerically by Sisoev et al. [124]. They found that wave formation led to deformation of the diffusion boundary layer which increased gas absorption. Woods [97] estimated the additional surface area due to waves to be close to 1 percent and thus ruled out that increase in surface area is responsible for high mass transfer rates of spinning disk devices. Jachuck and Burns [14] report a quantitative model by Sisoev et al. to calculate mass transfer based. The correlation is based on the earlier numerical work on mass transfer contribution of surface waves and the experimental data by Aoune and Ramshaw. Sisoev et al. proposed to use a characteristic film thickness defined, Eq. 5-95-10, to develop a correlation for mass transfer coefficient and Sherwood number (Eq. 5-10). The Sherwood number exhibits a positive relationship to both rational speed and liquid flow rate which was attributed to increased surface waviness with an increase of these parameters. Notably, the model by Sisoev et al. includes surface tension as a parameter that influences the mass transfer coefficient. It also has a stronger positive dependence on rotational speed. Higher rotational speed increases wave generation and which enhances mass transfer

$$\delta_c = \frac{2}{3}\bar{\delta} = \left(\frac{3Q\mu}{2\pi R^2 \omega^2 \rho}\right)^{\frac{1}{3}} \qquad 5\text{-}9$$

$$\overline{Sh}_{\delta_c} = \frac{\bar{h}_m \delta_c}{D} = 0.154 \left(\frac{\delta_C^{11} \omega^8 R^4 \rho}{D^3 \nu^3 \sigma} \right)^{\frac{1}{6}} \qquad 5\text{-}10$$

In conclusion, a number of different formulas to calculate mass transfer of spinning disks has been suggested in the literature. Experimental mass transfer rates far above those predicted by the Higbie's penetration theory have been reported and two research groups developed semi-empirical mass transfer correlations based on the experiments reported by Aoune and Ramshaw. Peev et al. expressed the Higbie model using non-dimensional numbers and changed coefficients based on a data fit. Sisoev et al. developed a correlation by fitting the data to their model on absorption into wavy surface. However, using the proposed correlations to predict mass transfer coefficients of water absorption into aqueous lithium bromide illustrates the poor agreement between them. Figure 5-1 compares mass transfer coefficients for a spinning disk absorber based on the different correlations to with experimental values reported for tube banks. The range for tube banks is based on the values reported in [25,50]. The correlation by Sisoev et al. clearly surpasses the other correlations for spinning disks and the experimentally derived values for tube banks. Remarkably, the correlation by Sisoev et al. surpasses the correlation by Peev et al. by a factor of 2.6 although both were derived from the same experiments by Aoune and Ramshaw [13]. The correlation by Sisoev et al. predicts a five-fold enhancement over the middle of the range of tube banks.

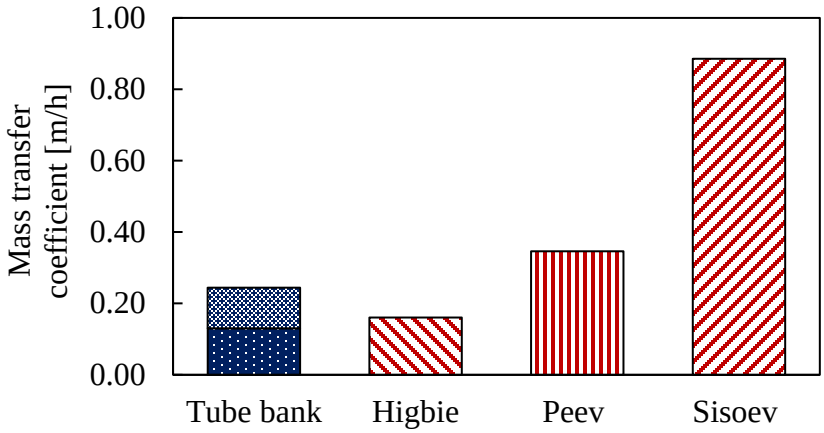

Figure 5-1: Theoretical mass transfer coefficients for disk spinning at 625 rpm and experimental mass transfer coefficient for tube banks.

5.3. Modeling approach

Figure 5-2 shows a schematic of the absorption process investigated in this study. A concentrated absorbent solution is fed to the center of a flat, rotating disk. The liquid solution is accelerated by centrifugal forces and flows radially outward. The gas phase around the disk consists of refrigerant. At the gas-liquid interface, refrigerant vapor is absorbed into the liquid solution, thereby releasing heat of vaporization and heat of mixing. The disk assembly includes internal cooling in counterflow configuration, to which the heat is rejected. The problem is analyzed in terms of an annular control volume that encompasses small absorbent, disk and cooling water elements. However, the cooling water does not reach the edge of the disk assembly such that adiabatic conditions prevail close to the perimeter. In this study, the absorbent consists of

aqueous lithium bromide and the process takes place under vacuum conditions since the refrigerant is water.

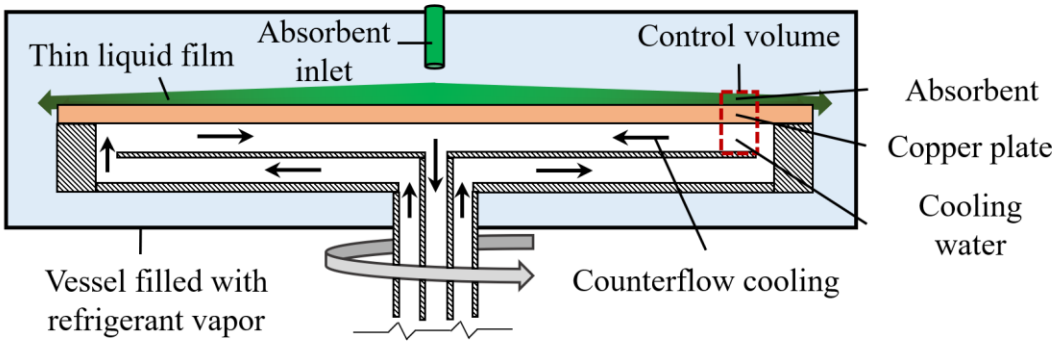

Figure 5-2: Schematic of the absorption process.

5.3.1. Geometrical configuration, assumptions and property data

A schematic of the geometrical configuration of the problem in cylindrical coordinates is given in Figure 5-3. The process is analyzed by in terms of annular control volumes. The solution algorithm steps by small radial increments from center to edge of the disk, thereby solving mass and energy balance of the associated control volumes.

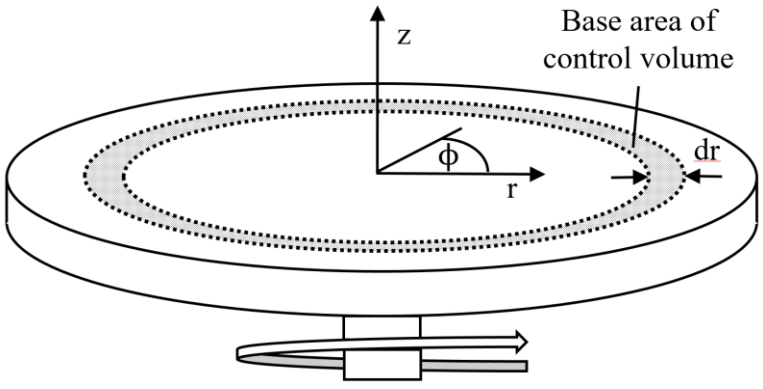

Figure 5-3: Geometrical configuration of the spinning disk absorber model.

The following list gives assumptions that were made to develop the model. Where applicable, examples of falling film absorption models that use similar assumptions are given in parenthesis.

1) Steady state conditions [63,148]
2) Negligible shear stress at the gas-liquid interface [129]
3) Negligible heat transfer between vapor phase and liquid phase [63,129,148]
4) The gas phase consists of pure water vapor without non-condensables; thus, there is no vapor-side resistance to mass transfer [129,148]
5) Laminar or wavy-laminar flow of liquid over the disk surface that can be approximated by the Nusselt model [143,148]
6) The zone of jet impingement in center of the disk is small compared to overall disk surface and its effects on thermal and fluid flow behavior can be neglected.
7) Linear or parabolic temperature profile in the liquid film, both cases will be studied. In case of a parabolic temperature profile, a steep gradient in immediate vicinity to the gas-liquid interface is added to account for the effect of vapor absorption. A steep temperature gradient at the interface has also been assumed in [30].
8) Vapor pressure equilibrium between vapor and liquid phases at the gas-liquid interface [129,143,148,149]
9) 1D heat transfer, e.g. 1D conduction for solid wall and heat transfer coefficient for convection in fluids [150,151]. No heat conduction in radial direction which is most relevant in the last segment of the copper disk close to the perimeter of

the assembly. This assumption implies that heat rejection from the solution to the cooling water stops once the end of the actively cooled area of the disk is reached.

10) The concentration boundary layer is developing slowly and thus only the surface of the solution film is involved in the mass transfer process. The concentration of the core of the film will remain equal to the bulk concentration at the inlet throughout the flow over the disk. This is a standard assumption in falling film absorption that is used e.g. in [30,146] and derived by [128,152,153].

Figure 5-4 shows velocity, temperature and concentration profiles based on these assumptions.

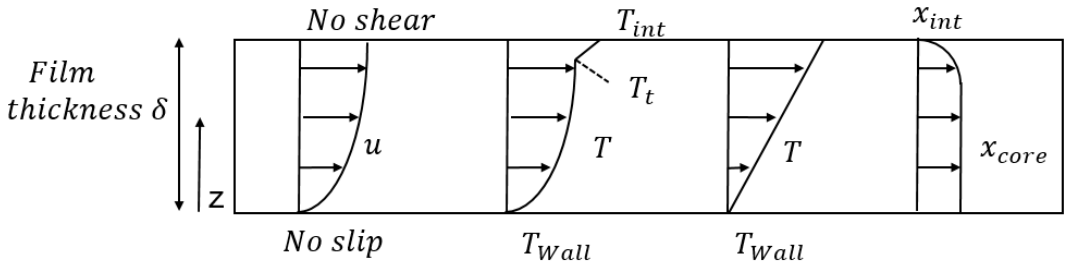

Figure 5-4: Velocity profile, parabolic and linear temperature profiles, and concentration profile used in the numerical model.

The water-side heat transfer coefficient was calculated based on the Wilson plot technique and tests with water without absorption. Its value was 5916 W/(m^2·K), 16611 W/(m^2·K) and 20949 W/(m^2·K) for microgap cooling at 90 g/s cooling water flow rate,

manifold-microchannel cooling at 90 g/s cooling water flow rate and manifold-microchannel cooling at 125 g/s cooling water flow rate respectively.

Most thermodynamic properties of the absorbent solution are based on the correlations developed by Yuan and Herold [130]. Thermal conductivity and dynamic viscosity are calculated according to the property correlations used in the software Engineering Equation Solver (EES) [154]. Surface tension is based on the data by Patterson and Perez-Blanco [155] and the functional form given by Kirby [156]. The most contentious, and by some measures most important, of aqueous lithium bromide properties is mass diffusivity. Kim et al. [157] noted large discrepancies by a factor of two to three between different correlations developed in the 1980's and Killion and Garimella [27] elaborated that many models use the correlation with highest diffusivity. The issue is also discussed by Kyung et al. [128], who opt to use a value in between early correlations and a more recent one developed by Potnis et al. [158]. The present model uses the data presented by Potnis et al., which approximates a steady value of $6.3 \cdot 10^{-10}$ m^2/s for mass concentrations between 44% and 57.4%, the maximum concentration used in their study. It is further assumed that the value stays at the steady value above the maximum concentration.

5.3.2. Governing equations

The rate of vapor absorption depends on the driving potential for mass transfer, i.e. the difference in concentration between the gas-liquid interface and the solution film. The gas-liquid interface is assumed to be at thermodynamic equilibrium, such that the

concentration is equal to the saturation concentration for given interface temperature and vapor pressure. Per the assumptions, the concentration difference used to calculate the driving potential is given by surface and core concentration of refrigerant. Film surface is assumed to be at equilibrium and thus surface concentration is given by saturation at given interface temperature and vapor pressure, Eq. 5-11 [63,133,148]. Eq. 5-11 is calculated according to property correlations given in [130].

$$\tilde{C}_{H_2O,int} = f(P_v, T_{int}) \quad 5\text{-}11$$

Mass transfer over a differential areal segment is given by Eq. 5-12. If the area A is small annular section as shown in Figure 5-3, Eq. 5-12 reduces to 5-16 for sufficiently small dr:

$$d\dot{m}_{Sol} = h_m\left(\tilde{C}_{H_2O,int} - \tilde{C}_{H_2O,c}\right)M_{H_2O}dA \quad 5\text{-}12$$

With

$$dA = \pi(r + dr)r^2 - \pi r^2 \quad 5\text{-}13$$

Which reduces to

$$dA = 2\pi r dr + dr^2 \quad 5\text{-}14$$

And, for small dr the second order term is neglected

$$dA = 2\pi r dr \quad 5\text{-}15$$

Such that:

$$\frac{d\dot{m}_{Sol}}{dr} = h_m\left(\tilde{C}_{H_2O,int} - \tilde{C}_{H_2O,c}\right)M_{H_2O}2\pi\mathrm{r} \quad 5\text{-}16$$

The boundary condition for Eq. 5-16 is given by Eq. 5-17. The mass transfer coefficient h_m in Eq. 5-16 is based on the mass transfer correlation discussed in chapter 5.2.2.2.

$$\dot{m}_{Sol} = \dot{m}_{Sol,in}\ at\ r = r_{in} \qquad 5\text{-}17$$

Energy balance for solution and cooling water are deducted by help of a two-dimensional schematic of the control volume (Figure 5-5).

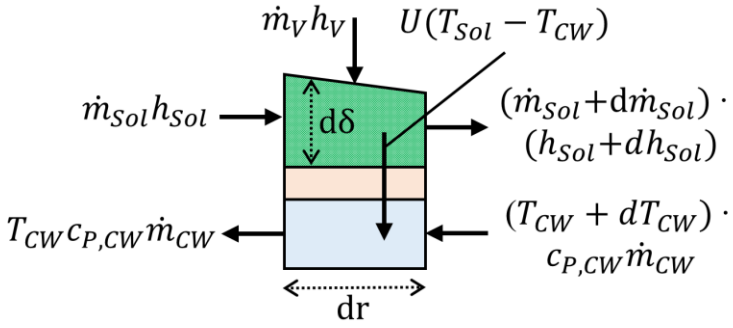

Figure 5-5: Mass and energy flows to, within and from control volume.

The energy for the solution are given by Eq. 5-18 and:

$$\dot{m}_{sol} h_{sol} + \dot{m}_v h_v = (\dot{m}_{sol} + d\dot{m}_{sol})(h_{sol} + dh_{sol}) + U(T_{sol} - T_{cw})dA \qquad 5\text{-}18$$

Where the overall heat transfer coefficient in Eq. 5-18 is defined as:

$$U = \left(\frac{1}{h_{cw}} + \frac{t_{cp}}{k_{cp}} + \frac{1}{h_{film}}\right)^{-1} \qquad 5\text{-}19$$

Notably, the film-side heat transfer coefficient changes depending on film thickness (Eq. 5-5). Thus, the overall heat transfer coefficient is a function of radial location, mass flow rates and other parameters used in calculation of film thickness (Eq. 2-8). The water-side heat transfer also depends on radial location if the cooling water channel width changes in radial direction.

The mass and concentration balances are given by Eq. 5-20 and Eq. 5-21, respectively. The mass balance shows that the change in solution mass flow rate is equal to flow rate of water vapor that crosses the gas-liquid interface.

$$\dot{m}_{sol} + \dot{m}_v = \dot{m}_{sol} + d\dot{m}_{sol} \tag{5-20}$$

$$d\dot{m}_{sol} = -dx_{sol}\frac{\dot{m}_{sol}}{x_{sol}} \tag{5-21}$$

The governing equation for heat transfer is derived from the energy balance in the same way as outlined in [30,156] for the case of absorption into falling film over horizontal tube. The differential of the specific enthalpy is given by

$$dh_{sol} = \left.\frac{\partial h_{sol}}{\partial T_{sol}}\right|_{x_{sol}} dT_{sol} + \left.\frac{\partial h_{sol}}{\partial x_{sol}}\right|_{T_{sol}} dx_{sol} \tag{5-22}$$

Combining the energy balance, Eq. 5-18, with Eqs. 5-15, 5-20, 5-21 and 5-22, and rearrangement leads to expression Eq. 5-23 (Appendix IV).

$$\frac{dT_{Sol}}{dr} = \left[\left(h_v - h_{sol} + x_{sol}\left.\frac{\partial h_{sol}}{\partial x_{sol}}\right|_{T_{sol}}\right)\frac{d\dot{m}_{sol}}{dr} - U(T_{Sol} - T_{CW})2\pi r\right]\frac{1}{\left(\dot{m}_{Sol}\left.\frac{\partial h_{Sol}}{\partial T_{Sol}}\right|_{x_{sol}}\right)} \tag{5-23}$$

The boundary condition for Eq. 5-23 is given by Eq. 5-24

$$T_{Sol} = T_{Sol,in}\ at\ r = r_{in} \tag{5-24}$$

The energy balance for the cooling water loop, which is operated in counterflow configuration, is given by Eq. 5-25 which reduces to Eq. 5-26 for dr → 0.

$$\dot{m}_{CW}c_{P,CW}(T_{CW} + dT_{CW}) + U(T_{Sol} - T_{CW})dA = \dot{m}_{CW}c_{P,CW}T_{CW} \tag{5-25}$$

$$\frac{dT_{CW}}{dr} = -\frac{U(T_{Sol} - T_{CW})2\pi r}{\dot{m}_{CW} c_{P,CW}} \quad 5\text{-}26$$

The boundary condition for Eq. 5-26 is given by Eq. 5-27

$$T_{CW} = T_{CW,out}\ at\ r = r_{in} \quad 5\text{-}27$$

The interface temperature is calculated according to Eq. 5-28.

$$T_{int} = T_{sol} + \frac{3}{8}\delta \frac{dm}{dr} \frac{(h_v + h_{mix})}{k2\pi r} \quad 5\text{-}28$$

Eq. 5-28 results from an energy balance at the interface. This approach has been outlined for a tube-type absorber in [156] and Appendix III shows the adaption of the method for the case of a spinning disk absorber. Once the interface temperature is determined, the interface concentration is calculated according to Eq. 5-11.

At this point, a control step makes sure that all state points are thermodynamically possible. If the value of $d\dot{m}_{sol}/dr$ in Eq. 5-16 is high, it can lead to an interfacial temperature (Eq. 5-28) above saturation of bulk solution. This would mean that water absorption continues beyond saturation, which is not possible. Hence, $d\dot{m}_{sol}/dr$ is restricted to a value that leads to the interface temperature being equal to saturation temperature of bulk solution in such a case. In some instances, this control step is necessary for the stability of the program. If the predicted overshoot of interface temperature is large, it leads to large negative mass transfer in the next Runge-Kutta step. Large negative mass transfer can lead to evaluation of solution properties at an undefined condition and hence to a program error. The model developed by Kirby et al. also implemented a control step within in the Runge-Kutta method. The step is not discussed in the description of the model in [32,133,156] but can be found in the

appended programming code that is provided in [32,156]. Kirby et al.'s control step sets mass transfer to zero if the ODE for mass transfer (similar to Eq. 5-16 in the present program) predicts negative mass transfer. Thus, the control step by Kirby may serve similar purposes as the one used in this work.

In the experiments reported in chapters 3 and 4, solution temperature at the solution inlet is close to saturation while solution-side heat transfer resistance is high due to a thick solution film. These conditions can lead to evaluation of superheated solution conditions within the Runge-Kutta scheme. Patnaik et al. [148] reported the use of a dampening factor to remove instabilities from their model for superheated conditions at the solution inlet. For similar reasons, a dampening factor is applied to the mass transfer coefficient over an entry length of 0.02 m in the present case. The dampening factor starts at 50% and increases linearly to 100%. The area affected by the dampening factor is only 3.6% of total area and the dampening is applied in an area of low heat and mass transfer. Therefore, the effect of the dampening factor on overall results is assumed to be negligible.

5.3.3. Solution approach

Figure 5-6 shows a flow diagram of the solution algorithm that was implemented in MATLAB. First, operating conditions of the absorber such as solution mass flow rate, pressure and cooling water inlet temperature are set. Then, parameters such as mass transfer coefficients and thermophysical properties at the inlet are calculated. Since cooling water flows in opposite direction of the solution film, it is also necessary

to assume an initial cooling water outlet temperature. The initial interface temperature of the solution is assumed to be equal to bulk temperature and initial interface concentration is assumed to be at equilibrium. After the entrance conditions are thus determined, the program steps over the disk surface in radial direction and solves the governing equations for mass transfer, Eq. 5-16, temperature change of solution, Eq. 5-23, and temperature change of cooling water, Eq. 5-26, at each calculation step. The governing equations for mass transport and temperature change of solution are solved simultaneously using a fourth order Runge-Kutta method adapted from Kirby [156] and Atchley et al. [32]. Solution temperature and mass flow and, based on the new values of the former, thermophysical properties are updated. The interface temperature is calculated according to Eq. 5-28 and the interface concentration is updated based on Eq. 5-11 according to the correlations given in [130]. Lastly, the cooling water temperature is calculated according to Eq. 5-26. Once the solution procedure reaches the outer radius of the disk, the model-generated cooling water inlet temperature is compared to the actual set point of the cooling water inlet temperature. If the temperatures deviate by more than 0.01 °C, the core of the program is repeated with an adjusted cooling water outlet temperature. The new estimate of cooling water outlet temperature is given by application of the Golden Section method.

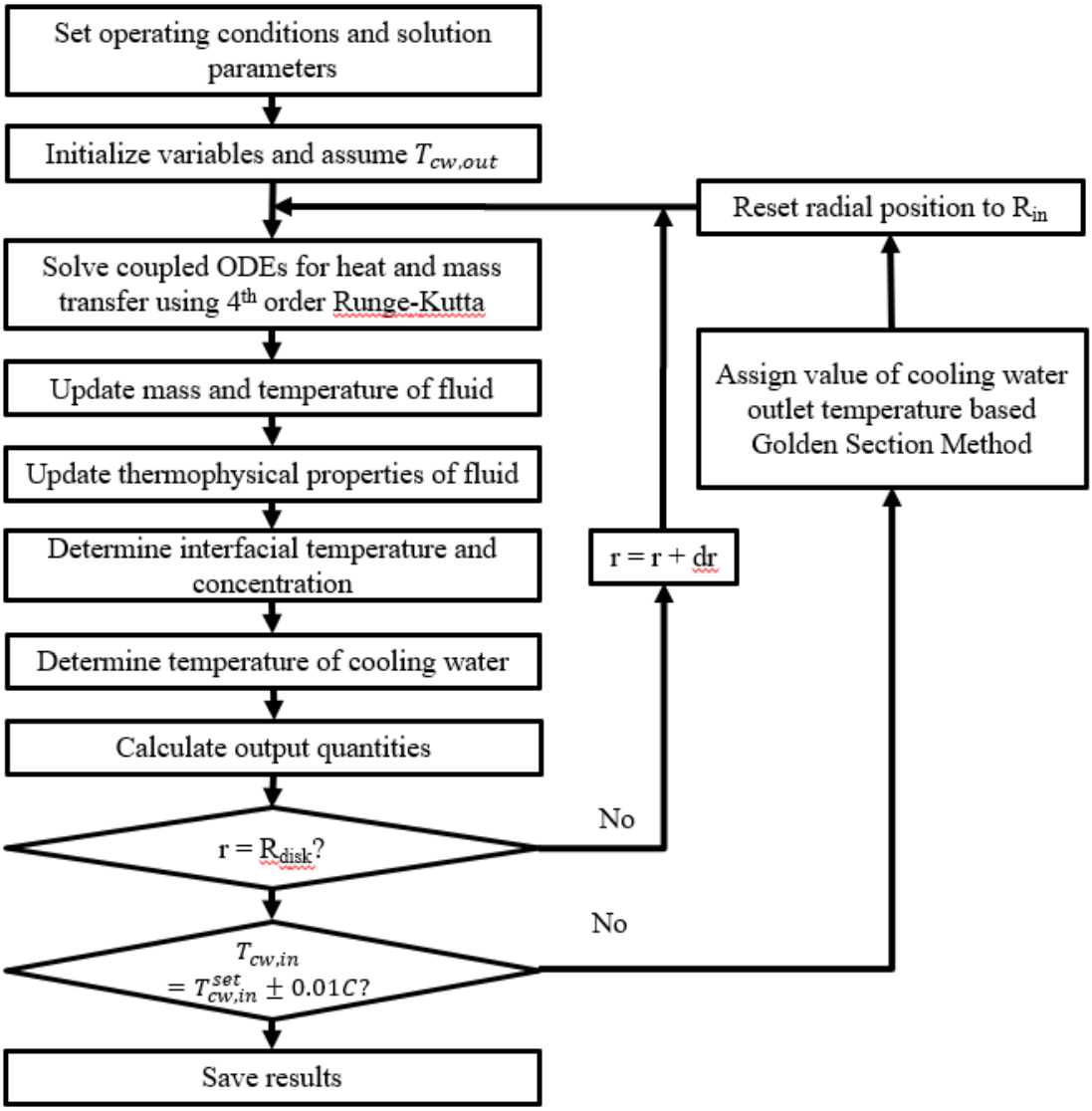

Figure 5-6: Flow chart of computer program.

5.4. Model results and comparison to experimental data

5.4.1. Predictive model

Results of the design model were computed for the two temperature profile options, linear and parabolic, and the three mass transfer correlations to analyze the sensibility of predicted absorption to changes in these parameters. The operating conditions assumed for other parameters are listed in Table 5-1.

Table 5-1: Assumed operating conditions for performance prediction.

Parameter	Value
Solution mass flow rate [g/s]	20
Solution inlet temperature [°C]	46.5
Solution inlet concentration [wt.-% LiBr]	60
Cooling water mass flow rate [g/s	90 - 125
Cooling water inlet temperature [°C]	30
Pressure [kPa]	1.1

Figure 5-7 to Figure 5-9 compare the predictions of the design model with various parameter settings to experimental data. As reported in chapters 3.3.1 and 4.4.2, the absorber heat rate increases with rotational speed and is higher when water-side cooling is provided by manifold-microchannel technology. These observations are correctly predicted by the design model. The choice of heat transfer profile and mass transfer correlation does influence the degree of deviation between model prediction and experiment. In all cases, the prediction accuracy with the mass transfer correlation by Sisoev et al. is highest, followed by Peev, with the Higbie correlation being last. The

correlation by Sisoev et al. is also best at capturing the performance improvement due to increasing rotational speed observed in experiments. Prediction accuracy of all mass transfer correlations is improved if combined with parabolic instead of linear temperature profile. However, the experimentally measured heat rate is higher than the predictions in all investigated cases. The amount of the deviation seems to behave similar for the different water-side cooling options.

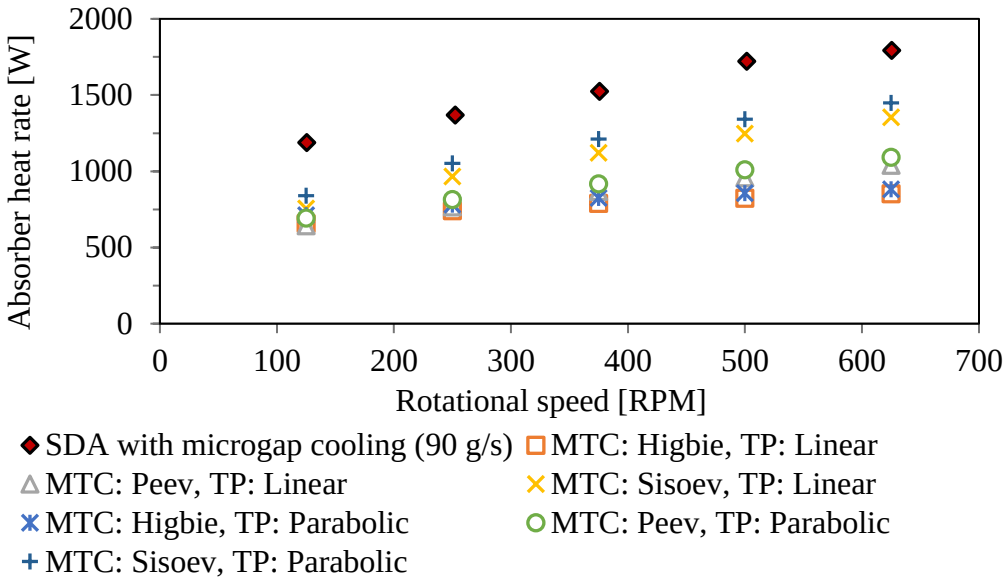

Figure 5-7: Comparison of experimental data of SDA with microgap cooling with design model at varying mass transfer coefficients (MTC), temperature profiles (TP) and rotational speeds.

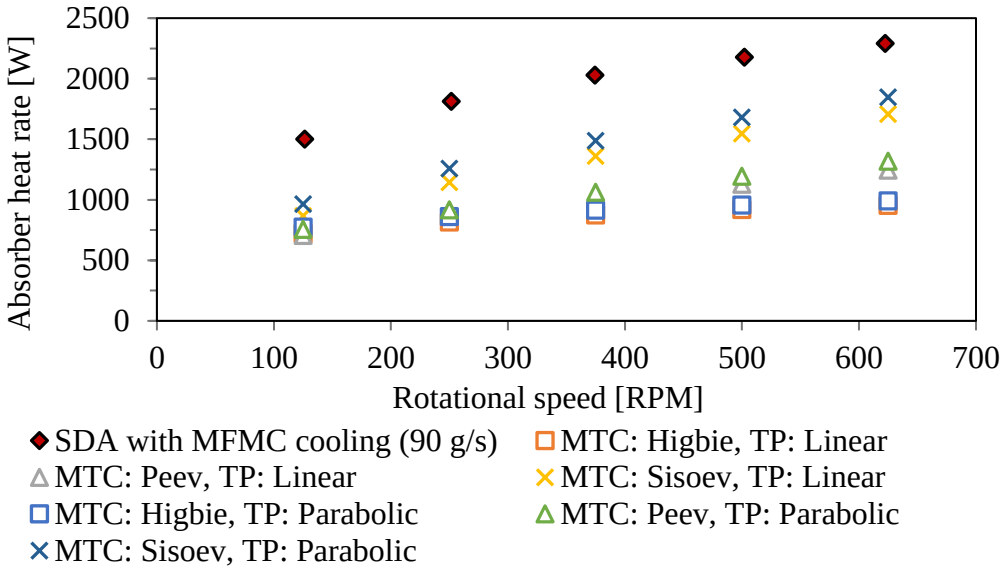

Figure 5-8: Comparison of experimental data of SDA with manifold-microchannel cooling (cooling water flow rate 90 g/s) with design model at varying mass transfer coefficients (MTC), temperature profiles (TP) and rotational speeds.

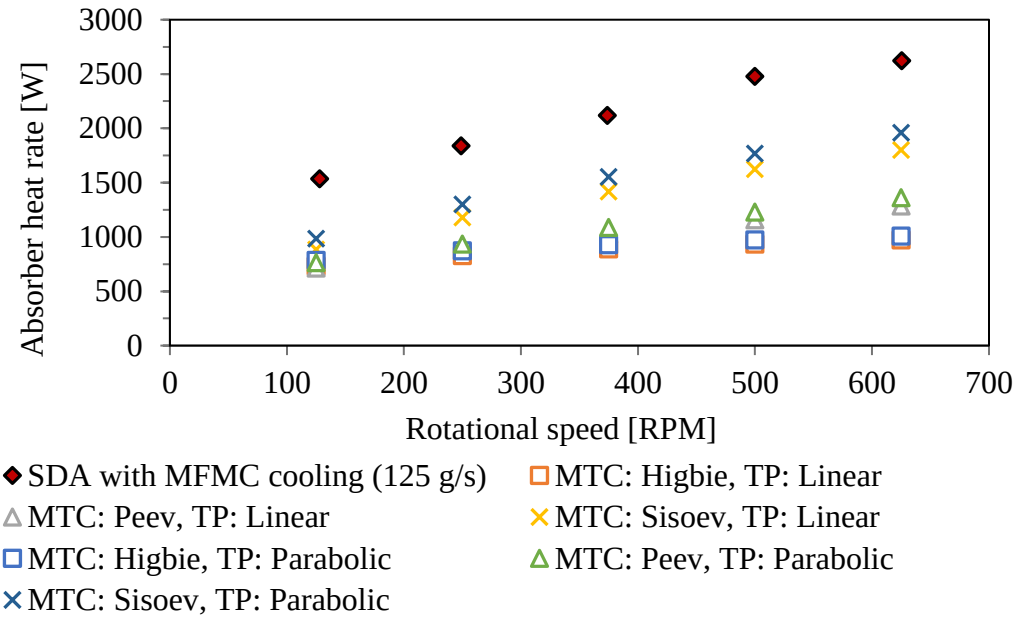

Figure 5-9: Comparison of experimental data of SDA with manifold-microchannel cooling (cooling water flow rate 125 g/s) with design model at varying mass transfer coefficients (MTC), temperature profiles (TP) and rotational speeds.

The underestimation of absorber heat rate is caused by low estimates of mass transfer. In the experimental study, high mass transfer enhancement generates high heat of absorption such that the solution at the outlet of the spinning disk absorber is saturated. In the predictive model, the solution is subcooled at the exit from the absorber disk. The difference between experimental and predicted subcooling is shown for different model parameter settings in Figure 5-10 and Figure 5-11. Figure 5-10 shows results at a rotational speed of 125 rpm and Figure 5-11 at 625 rpm. In the experiments, the measured temperature of the solution was very close to saturation. However, the model predicts strong subcooling and the lower the value of the mass transfer coefficient used in the model is, the higher subcooling will be. The temperature

profile used in the model has a small effect with the parabolic profile generating slightly larger subcooling. The difference between model prediction and experiments is larger at low rotational speeds. This is consistent with the already strong absorption enhancement at low rotational speed observed in experiments. The only model case with low subcooling prediction is when the mass transfer correlation by Sisoev is used at a high rotational speeds.

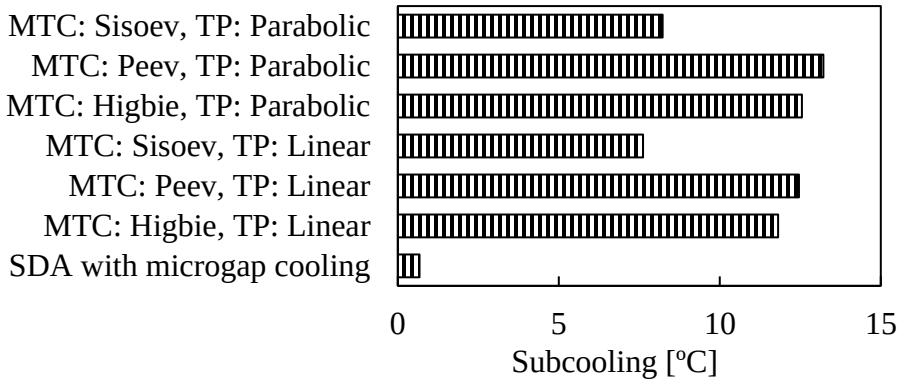

Figure 5-10: Subcooling of solution at rotational speed of 125 rpm in model prediction and experiments.

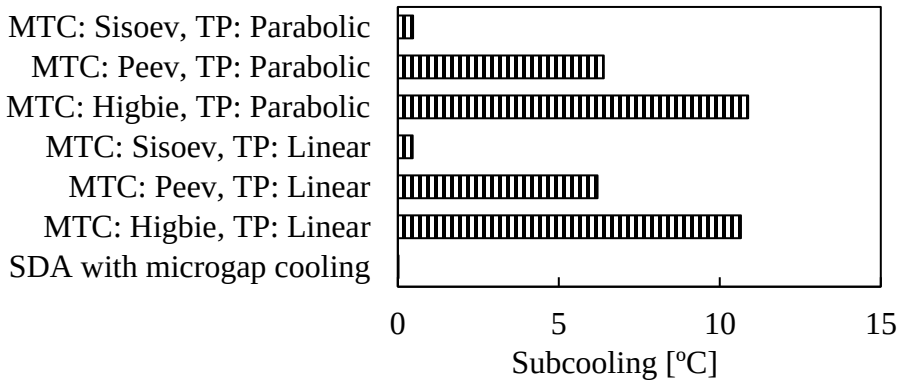

Figure 5-11: Subcooling of solution at rotational speed of 625 rpm in model prediction and experiments.

Temperature profiles that result from low and high mass transfer assumptions display the trends in more detail. Figure 5-12 and Figure 5-13 show temperature profiles at low and high rotational speeds, respectively, when the mass transfer correlation is based on the Higbie model. In both cases, changes in saturation temperature of the bulk solution are fairly small as the predicted changes to the concentration of the solution are low. However, the bulk solution is cooled significantly which results in high subcooling. Interface and solution temperatures decrease relatively slowly close to the center of the disk, where the film is thick and heat transfer through the film is low. Water-side heat transfer resistance also decreases in radial direction. The water-side cooling channel of the disk with microgap cooling had a width of 0.5 mm up to a radial position of 0.044 m. Between a radial location of 0.044 m and 0.095 m the channel width decreased to 0.25 mm and stayed at that value beyond 0.095 m. Hence, heat transfer resistances decrease in radial direction and bulk and interface temperatures fall accordingly. Once the radial location reaches the end of the actively-cooled area, heat rejection stops and solution temperatures begin to rise. In case of higher rotational speed (Figure 5-13), bulk and interface solution temperatures drop faster because of lower solution-side heat transfer resistance. Mass transfer increases which leads to higher cooling water outlet temperature at the center of the disk.

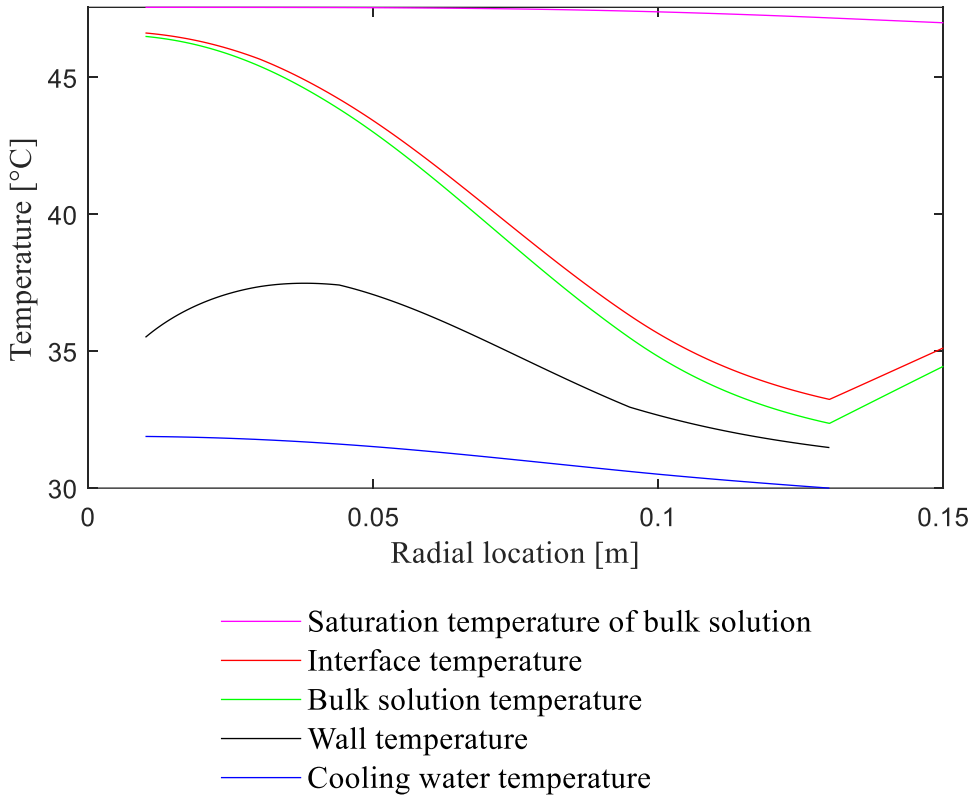

Figure 5-12: Temperature profiles with following model parameters: Rotational speed of 125 rpm, parabolic temperature in film, mass transfer correlation by Higbie, internal cooling by microgap.

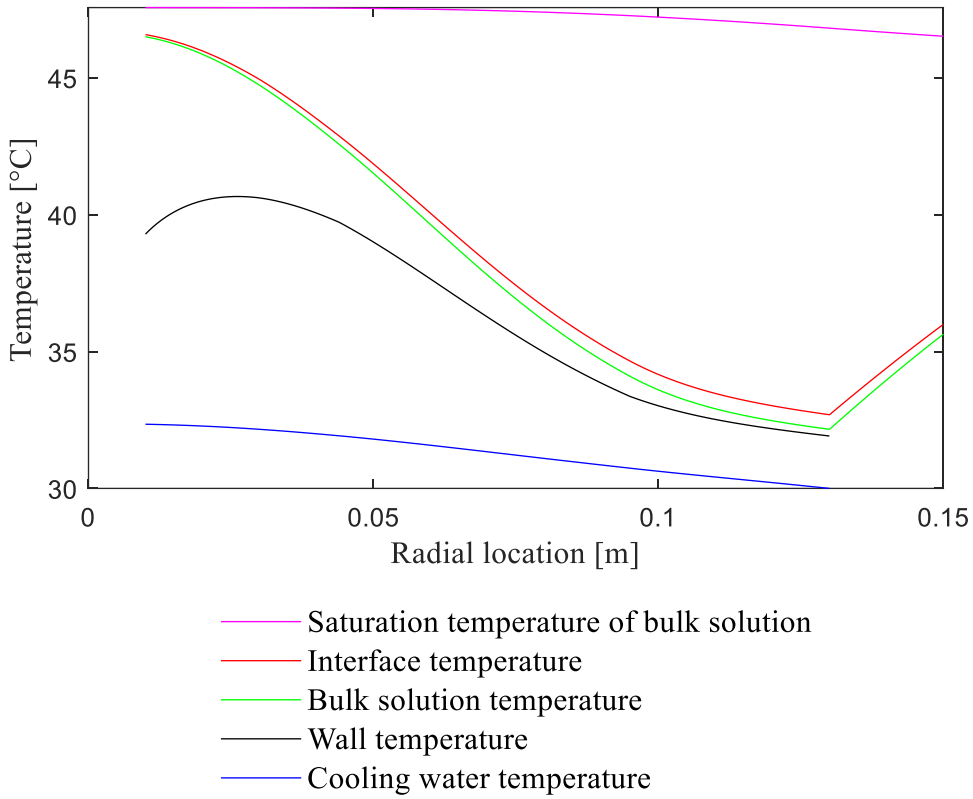

Figure 5-13: Temperature profiles with following model parameters: Rotational speed of 625 rpm, parabolic temperature in film, mass transfer correlation by Higbie, internal cooling by microgap.

Figure 5-14 and Figure 5-15 show again predictions for low and high rotational speed, respectively, but this time when the mass transfer correlation by Sisoev is used. Sisoev et al. predict higher mass transfer, which results in the release of more heat of absorption. Therefore, bulk and interface temperatures are higher than in the previous case of low mass transfer prediction. The larger driving temperature difference between solution and cooling water leads to more heat transfer and hence higher cooling water outlet temperature. At low rotational speed (Figure 5-14) the solution is still subcooled

when it reaches the edge of the disk, but less so than under assumption of the Higbie model for mass transfer. In the case of a high rotational speed of 625 rpm, the solution temperature increases fast once heat rejection stops such that the bulk solution is only slightly subcooled at the end of the disk (Figure 5-15). Therefore, mass transfer correlations that predict higher mass transfer rates yield model results that are in closer agreement to experimental observations.

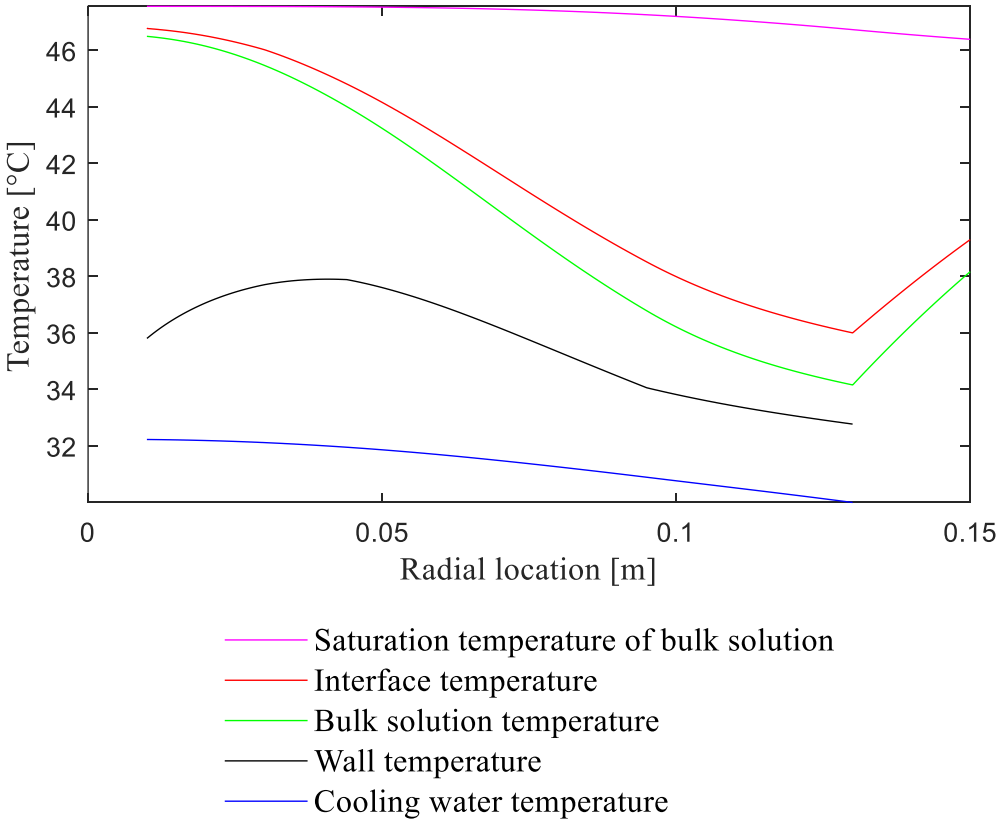

Figure 5-14: Temperature profiles with following model parameters: Rotational speed of 125 rpm, parabolic temperature in film, mass transfer correlation by Sisoev et al., internal cooling by microgap.

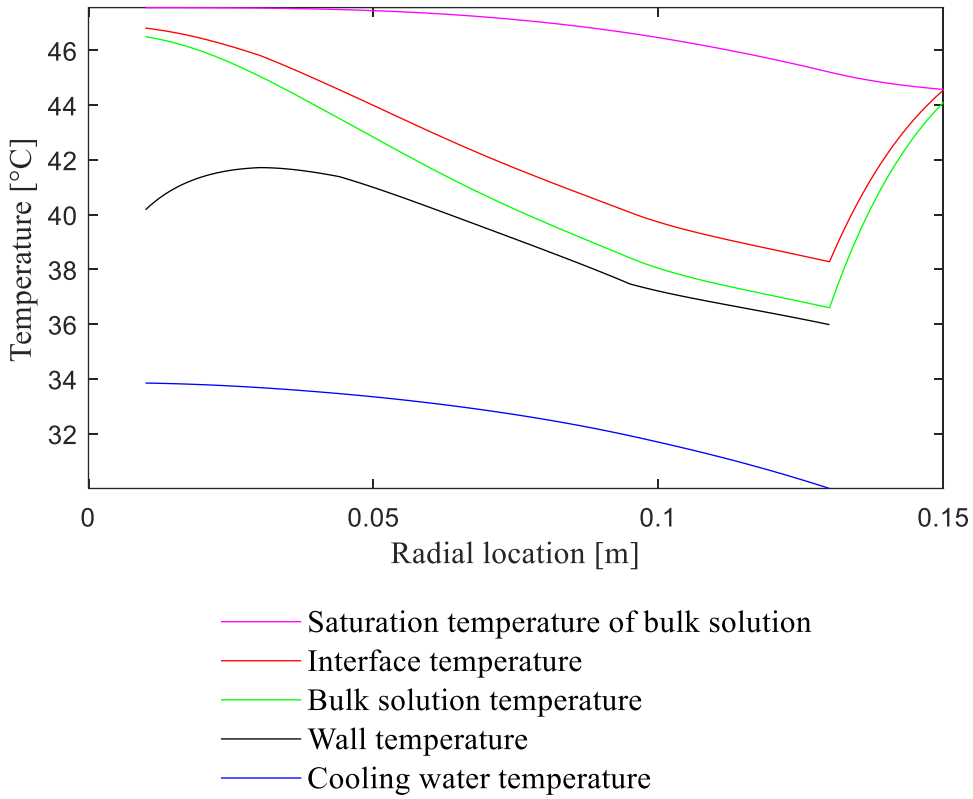

Figure 5-15: Temperature profiles with following model parameters: Rotational speed of 625 rpm, parabolic temperature in film, mass transfer correlation by Sisoev et al., internal cooling by microgap.

5.4.2. Semi-empirical model

A semi-empirical approach of solving the model was developed in order gain additional insight in the absorption process on a spinning disk. The semi-empirical model shown in Figure 5-16 follows mostly the same solution procedure as the predictive model discussed in the previous section. However, in semi-empirical mode, experimental parameters and results are used to calibrate the model. The model calibration is achieved by turning the mass transfer coefficient from an a priori defined

parameter into a changeable variable. In turn, it is necessary to set the cooling water outlet temperature equal to the experimentally recorded value instead of treating it as a variable. Thus, the model is now solved by calculating the mass transfer coefficient that brings cooling water inlet and outlet temperatures in agreement with experimental measurements. The predictive model discussed in the previous section calculated the cooling water outlet temperature that lead to an a priori set cooling water inlet temperature given a fixed mass transfer coefficient. The experimental data gathered in studies with microgap cooling and manifold-microchannel cooling reported in chapters 0 and 4, respectively, is analyzed in this manner. As discussed in chapter 0, the experimental results at a low rotational speed of 125 rpm are influenced by the horizontal orientation of the disk. Therefore, data at 125 rpm is not included in the analysis.

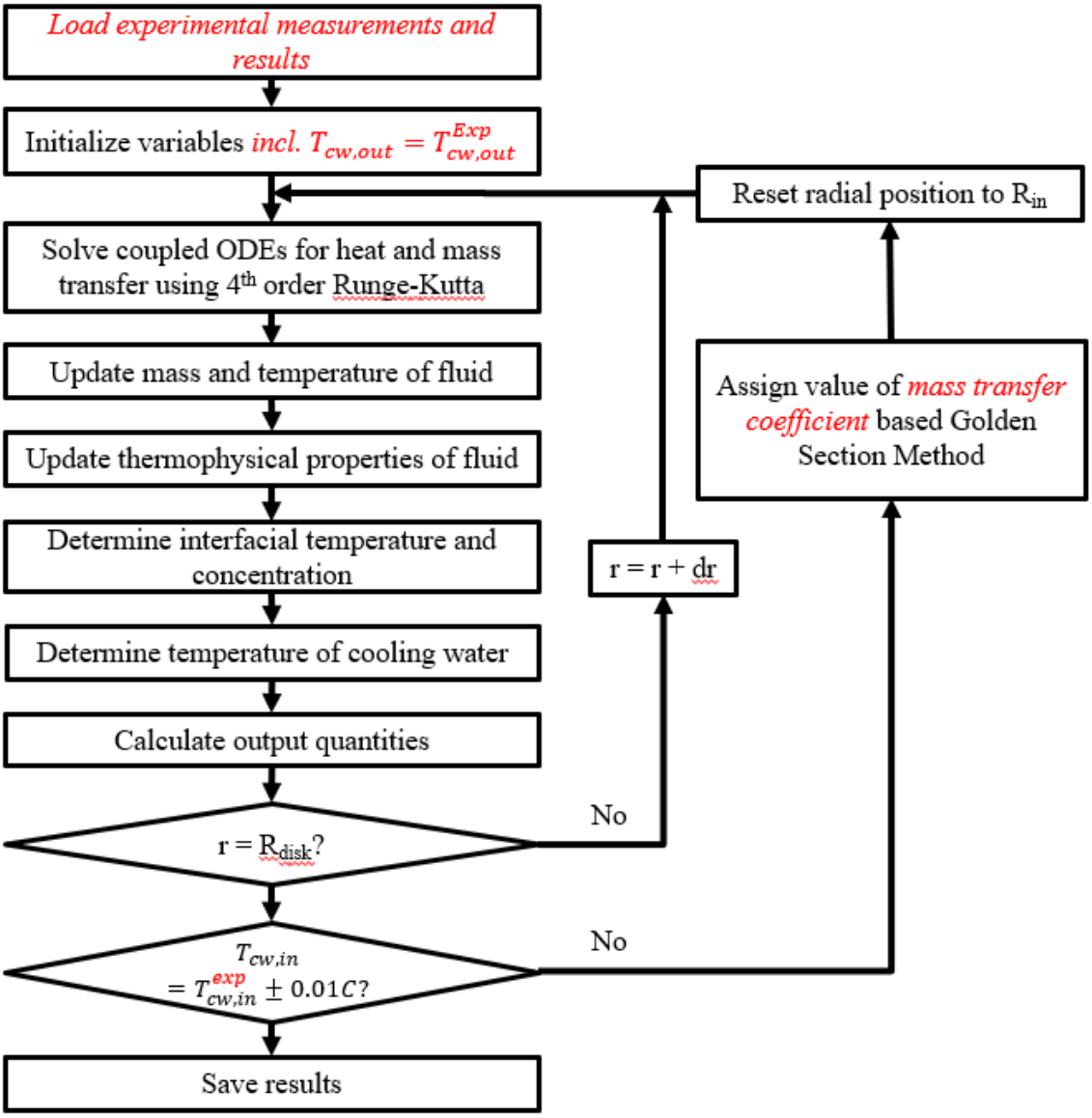

Figure 5-16: Flow chart of semi-empirical computer model.

5.4.2.1. Experiments with microgap cooling on water-side

Figure 5-17 to Figure 5-22 show temperature profiles, concentration profiles, heat flux, mass flux, liquid velocity and film thickness for experiments with microgap cooling at

a rotational speed of 250 rpm. The temperature profiles (Figure 5-17) show some distinctive differences to the profiles generated with the predictive model discussed in section 5.4.1. Since the mass transfer coefficient increases in semi-empirical mode, bulk solution temperature decreases less than before which leads to a higher driving force for heat transfer. The increased value of mass transfer coefficient results in higher mass transfer which causes a larger deviation between interface and bulk temperature (Eq. 5-28). The development of concentration profiles (Figure 5-18) mirrors the temperature profiles. The difference between bulk concentration and interface concentration steadily increases until it reaches a maximum at the end of the actively cooled zone. In the area without heat rejection, the interface concentration increases until it reaches bulk concentration. The heat flux (Figure 5-19) increases from below 15 kW/m^2 at the center of the disk to above 30 kW/m^2 at the end of the actively cooled area; per assumption it is zero beyond that. Thus, the increase in internal and film-side heat transfer coefficients overcome the decrease in temperature difference with radial direction. The profile of the heat flux displays changes in slope at the onset of channel width tightening at 0.044 m and at the end of channel width tightening at 0.095 m. Notably, the behavior of the mass flux (Figure 5-20) deviates to some extent from the heat flux. While the heat flux is relatively high even at the center of the disk, the mass flux is low in the inner region. In this area, sensible heat is removed from the bulk solution. Interface temperature follows the bulk solution temperature and is therefore relatively high. Hence, the interface concentration is not strongly enriched by refrigerant and absorption is low because the driving force for mass transfer is still

relatively low. However, the mass flux continuously increases until it reaches a maximum at the end of the actively cooled zone. Given that outer radial locations have a much larger surface area, the bulk of mass transfer occurs in the outer region of the actively cooled area. Here, the driving force for mass transfer is high due to high solution subcooling. Once heat rejection to cooling water stops, the mass flux does not immediately fall to zero but decreases significantly. Because the solution is subcooled, absorption continues until the heat of absorption brings the solution to saturation temperature. The average liquid velocity (Figure 5-21) decreases from about 0.3 m/s close to the center of the disk to about 0.13 m/s at the outer radius of the disk. The decline in velocity is much stronger at the center than further outwards. The velocity seems to increase slightly at the end of the cooling zone. At this point, the bulk solution temperature increases which leads to lower viscosity and hence faster flow of the liquid film. The profile of the film thickness (Figure 5-22) mostly mirrors the development of velocity. The film is about 0.6 mm thick at the center but it declines to reach 0.1 mm at the outlet. Again, the absolute value of the slope decreases in radial direction. However, the decrease in viscosity leads to a thinner film in the area without cooling.

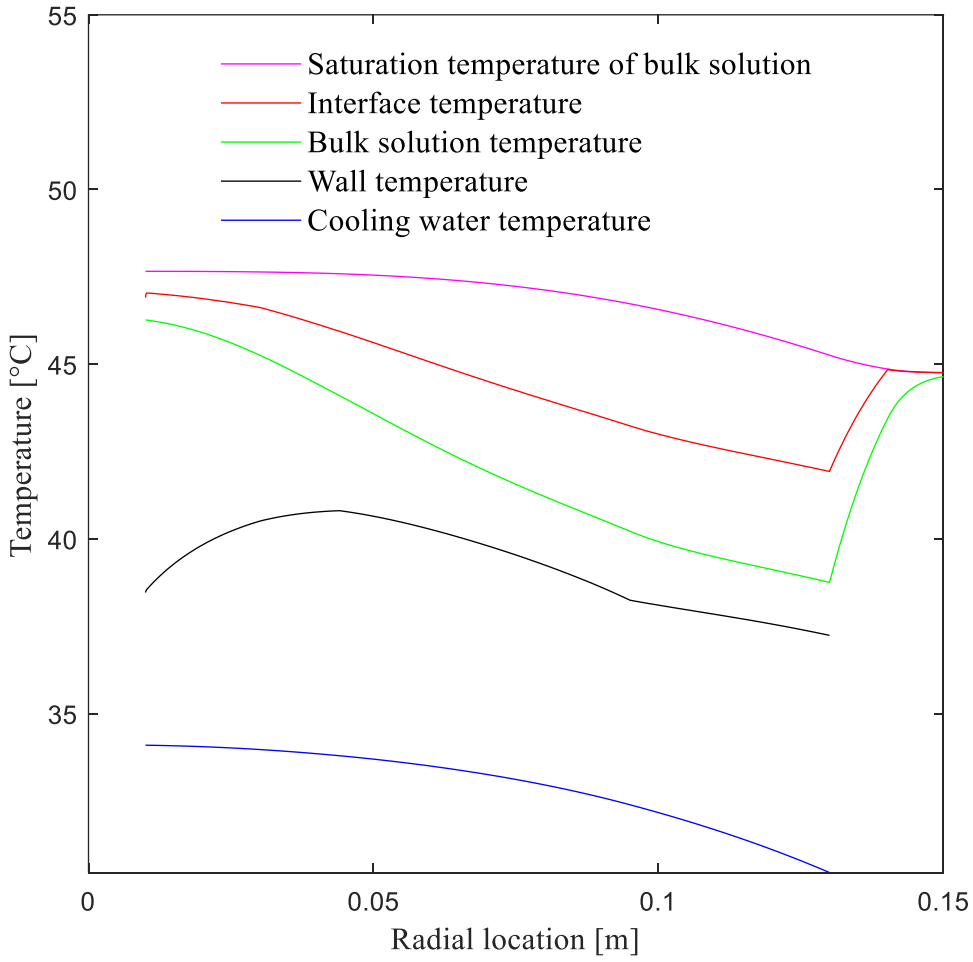

Figure 5-17: Temperature profiles of semi-empirical model with water-side cooling by microgap and rotating at a speed of 250 rpm.

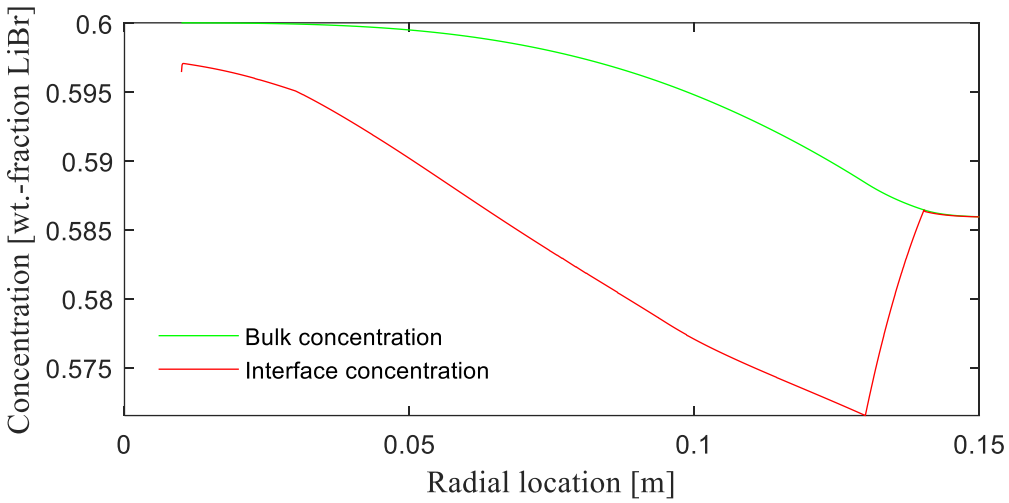

Figure 5-18: Predicted concentration profiles of semi-empirical model with water-side cooling by microgap and rotating at a speed of 250 rpm

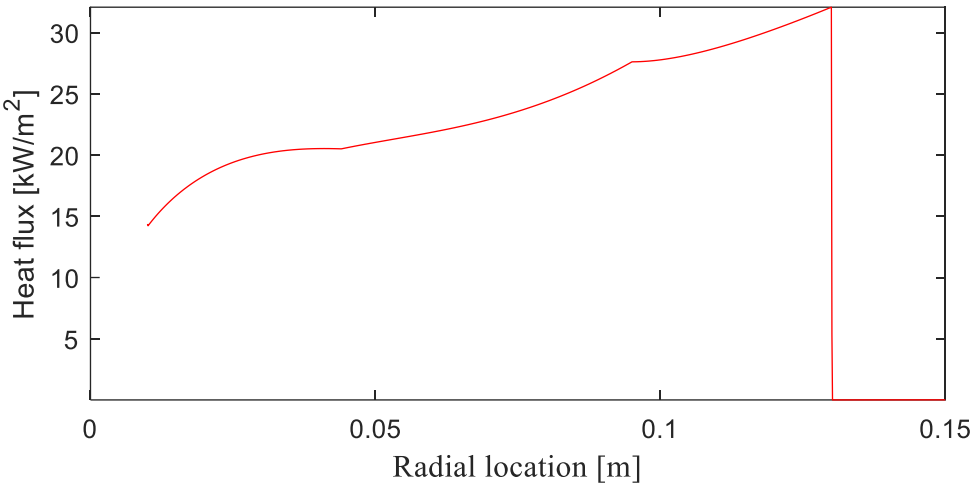

Figure 5-19: Heat flux of semi-empirical model with water-side cooling by microgap and rotating at a speed of 250 rpm.

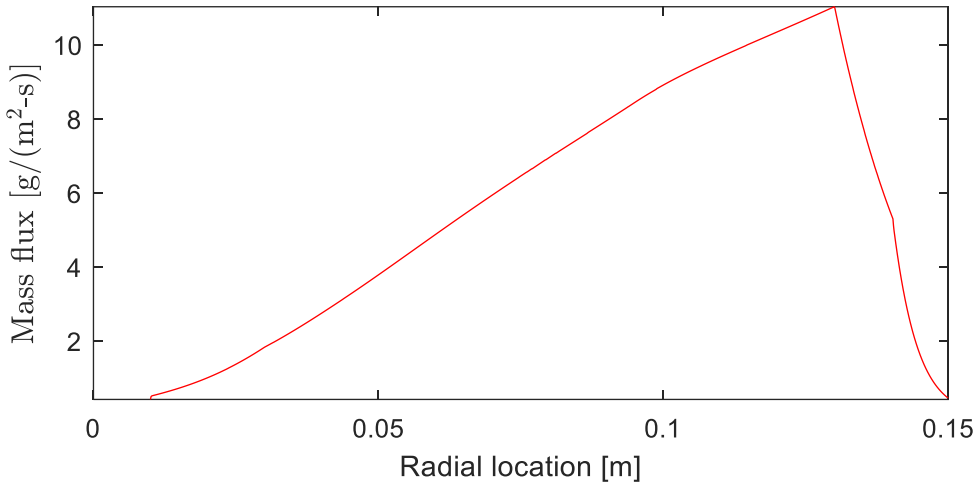

Figure 5-20: Mass flux of semi-empirical model with water-side cooling by microgap and rotating at a speed of 250 rpm.

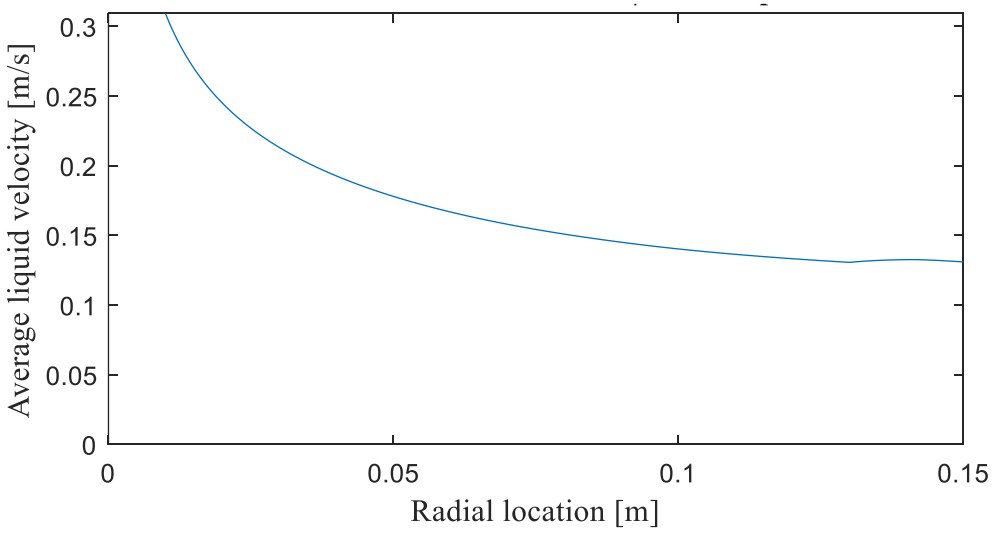

Figure 5-21: Liquid velocity of semi-empirical model with water-side cooling by microgap and rotating at a speed of 250 rpm.

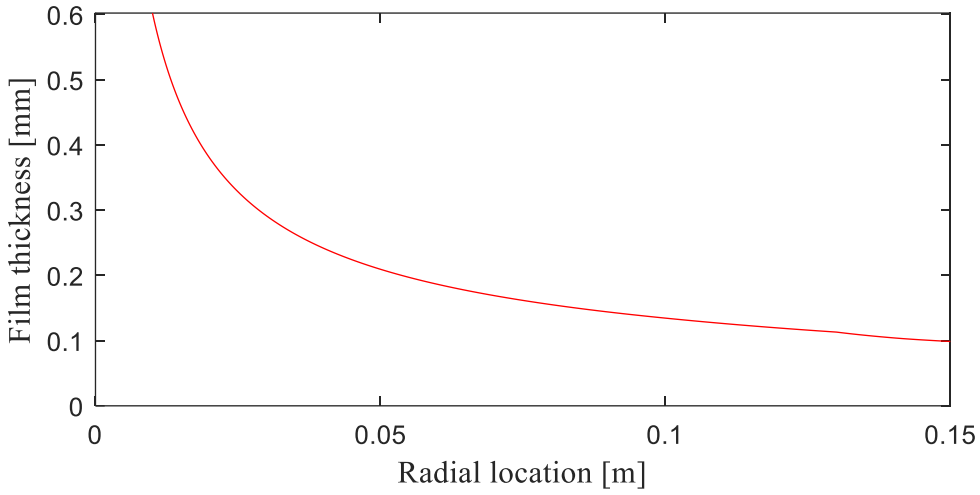

Figure 5-22: Film thickness of semi-empirical model with water-side cooling by microgap and rotating at a speed of 250 rpm.

Figure 5-23 to Figure 5-28 show the same sequence of charts at a faster rotational speed of 625 rpm. Overall, trends are similar to the ones discussed at lower velocity although the magnitude of absolute values may change. E.g. in Figure 5-23, the higher rotational speed strongly decreases solution side temperature difference such that the temperature of the bulk solution is much closer to the wall temperature. As discussed in chapter 3.3.2, the main heat transfer resistance in this configuration lies on the water-side. The heat flux (Figure 5-25) reaches a maximum of above 40 kW/m^2. Particularly at larger radii, the slope of the heat flux curve is much steeper as the film in this area is thinner (Figure 5-28) than at lower rotational speed which increases the film-side heat transfer coefficient. Film velocity (Figure 5-27) is noticeably higher than before and falls to a minimum of below 0.25 m/s. The profile of the mass flux (Figure 5-26)

remains largely the same but it exhibits a steeper slope to reach a higher maximum of almost 16 g/(s·m^2).

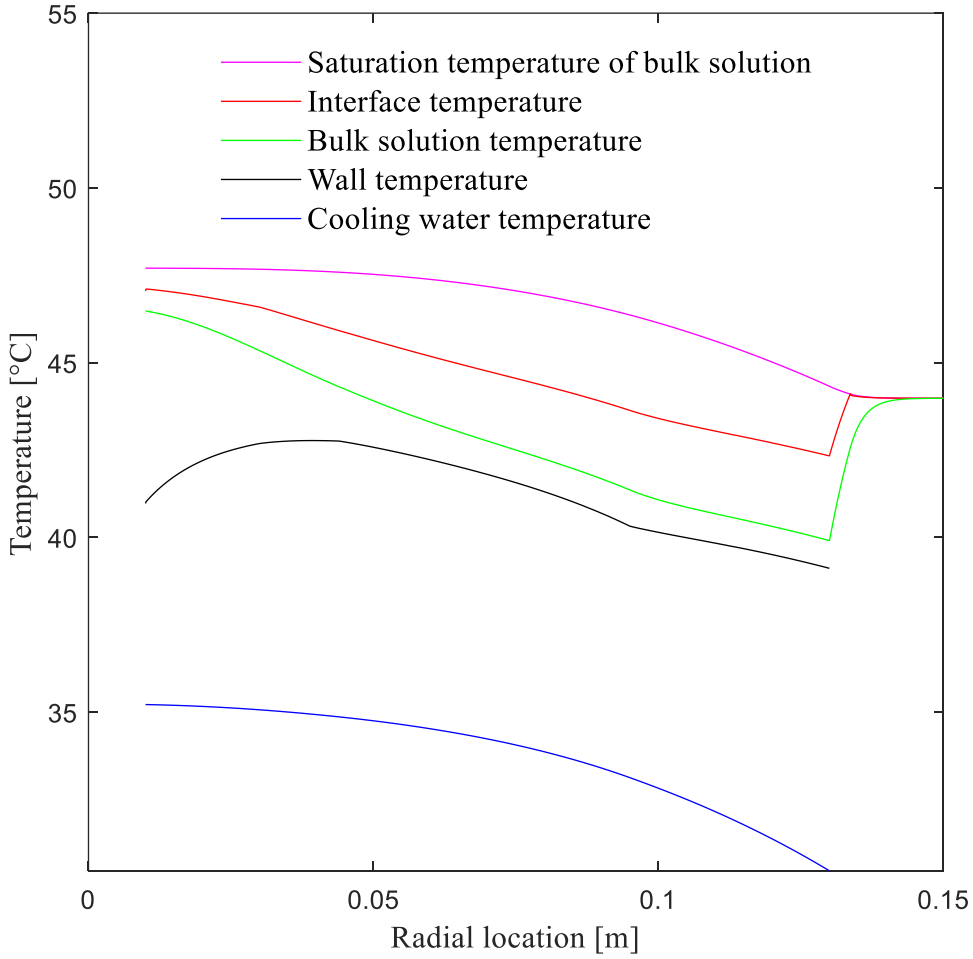

Figure 5-23: Temperature profiles of semi-empirical model with water-side cooling by microgap and rotating at a speed of 625 rpm.

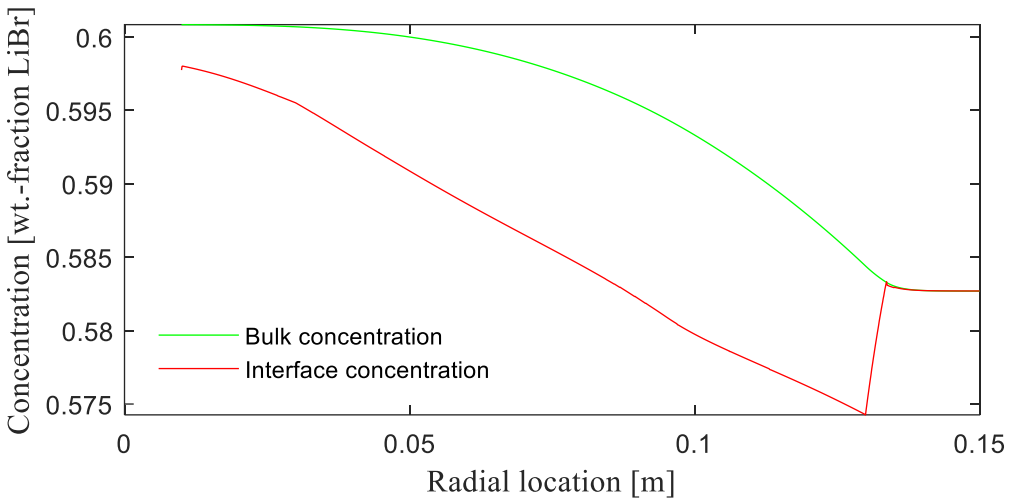

Figure 5-24: Concentration profiles of semi-empirical model with water-side cooling by microgap and rotating at a speed of 625 rpm.

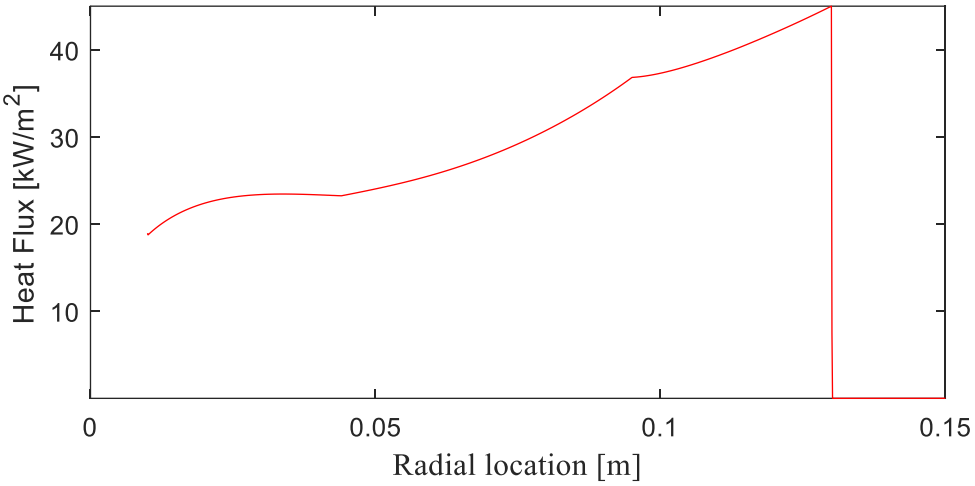

Figure 5-25: Heat flux of semi-empirical model with water-side cooling by microgap and rotating at a speed of 625 rpm.

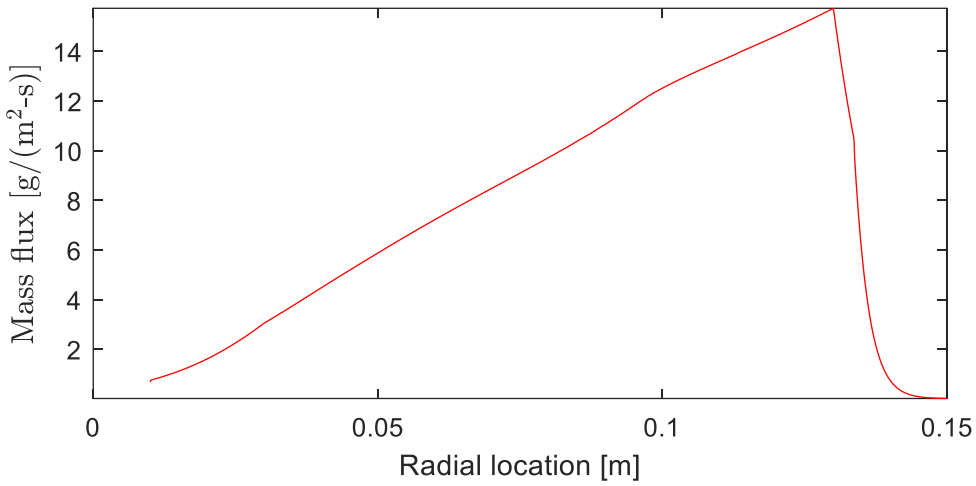

Figure 5-26: Mass flux of semi-empirical model with water-side cooling by microgap and rotating at a speed of 125 rpm.

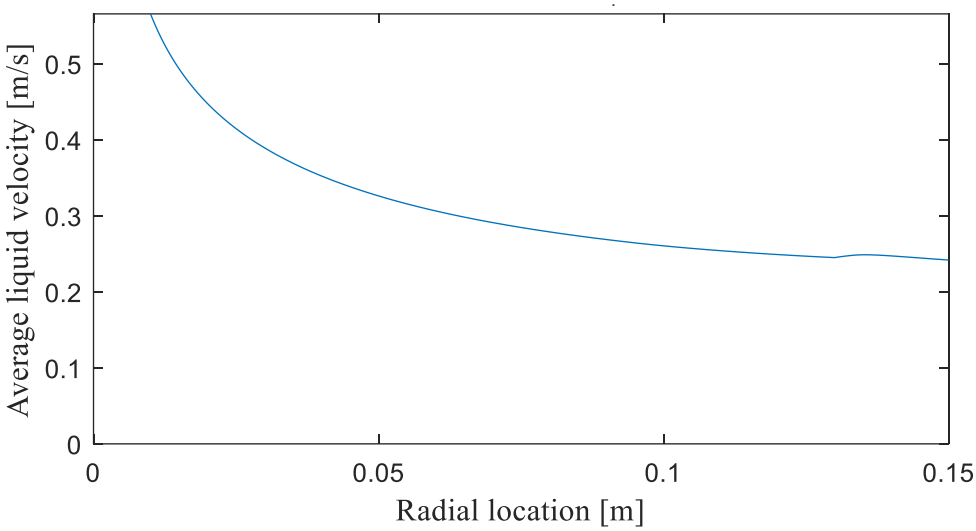

Figure 5-27: Film velocity of semi-empirical model with water-side cooling by microgap and rotating at a speed of 625 rpm.

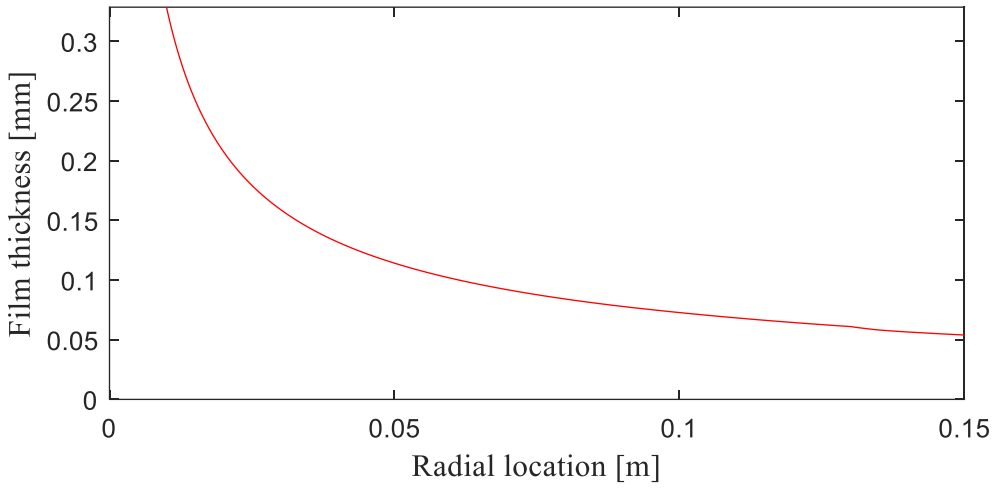

Figure 5-28: Film thickness of semi-empirical model with water-side cooling by microgap and rotating at a speed of 625 rpm.

5.4.2.2. Experiments with manifold-microchannel cooling on water-side

Figure 5-29 to Figure 5-32 show temperature profiles, concentration profiles, heat flux and mass flux for experiments with manifold-microchannel cooling technology on the water-side at a rotational speed of 250 rpm and a cooling water mass flow rate of 125 g/s. Film thickness and liquid velocity profiles develop largely similar to the experiments with microgap cooling and are therefore not repeated. Figure 5-29 shows that the solution temperature decreases faster and to a lower temperature due to the enhanced water-side heat transfer. Consequently, the difference between bulk and interface concentration increases faster and to larger values as well (Figure 5-30). The heat flux in the actively cooled zone lies in between 20 kW/m^2 and more than 35 kW/m^2, with two inflection points: From a low starting point due to the thick film at

the center, it rises as the film thins. As the temperature of the bulk solution decreases, the driving temperature difference diminishes and the heat flux declines. On the outer part of the disk, the heat flux increases again with enhanced absorption due to the low film-side heat transfer resistance. The mass flux (Figure 5-26) is on average 32% larger than in the case with microgap cooling. Beside the difference in absolute value, the mass flux profile behaves differently in the middle part of the disk: Because the solution temperature decreases faster, the mass flux in the middle area is markedly higher.

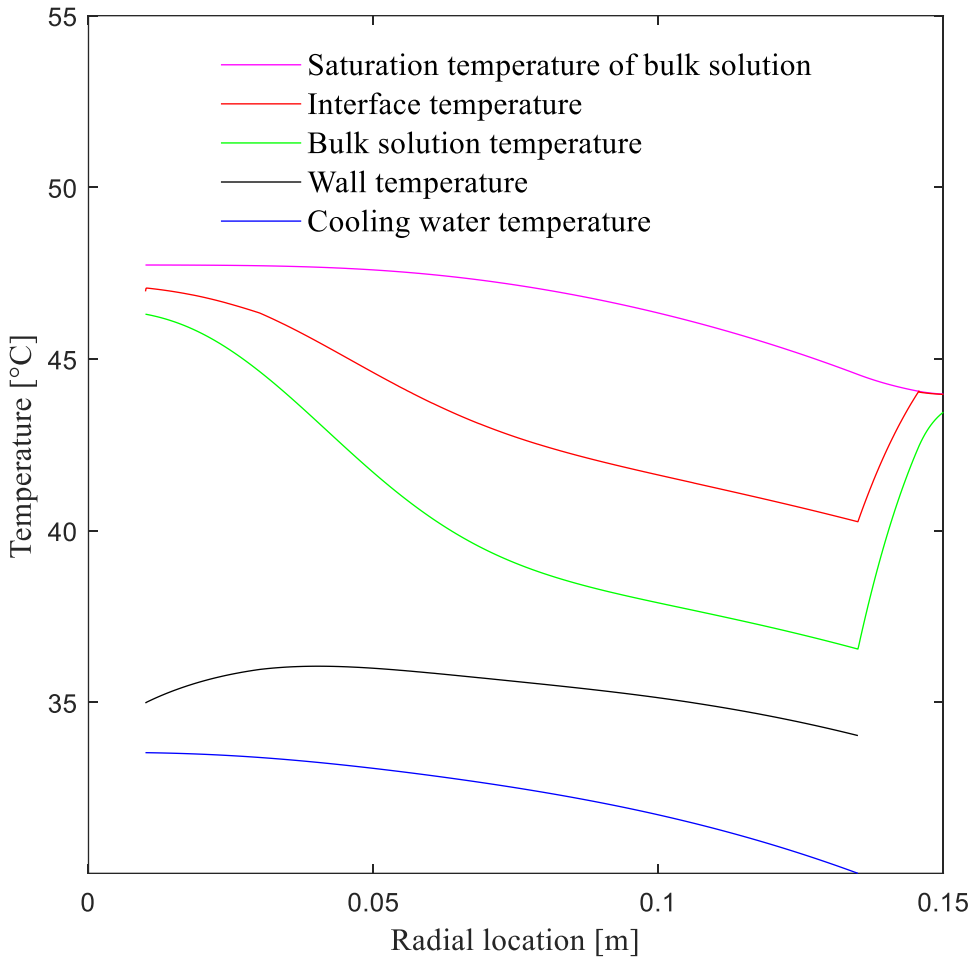

Figure 5-29: Temperature profiles of semi-empirical model with water-side cooling by manifold-microchannel technology and rotating at a speed of 250 rpm.

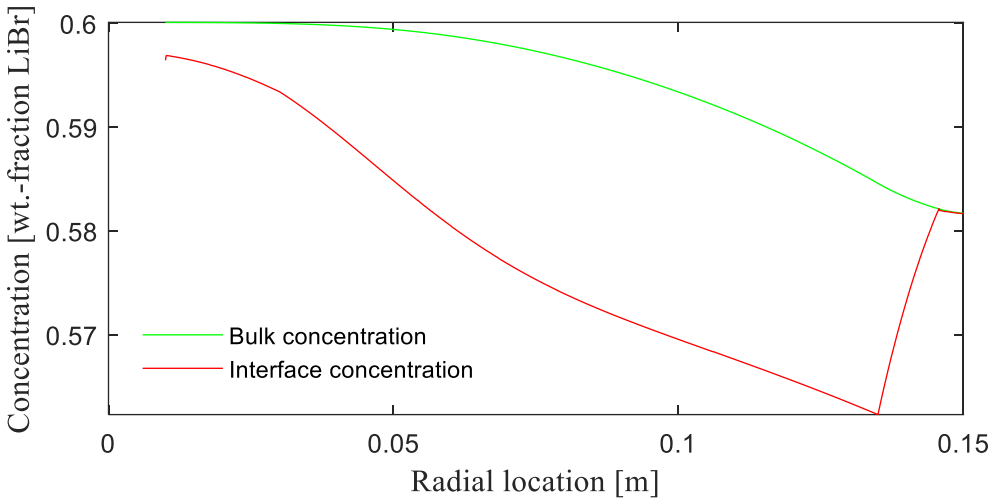

Figure 5-30: Concentration profiles of semi-empirical model with water-side cooling by manifold-microchannel technology and rotating at a speed of 250 rpm.

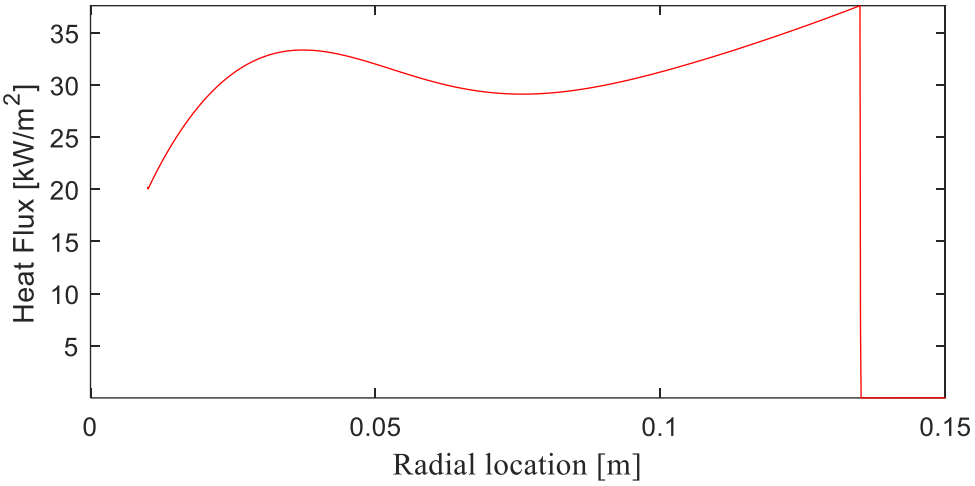

Figure 5-31: Heat flux of semi-empirical model with water-side cooling by manifold-microchannel technology and rotating at a speed of 250 rpm.

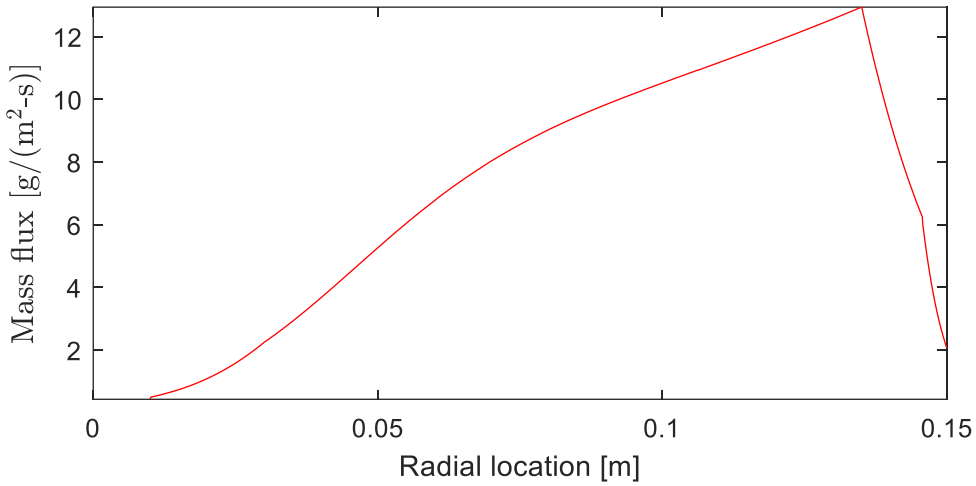

Figure 5-32: Mass flux of semi-empirical model with water-side cooling by manifold-microchannel technology and rotating at a speed of 250 rpm.

Figure 5-33 to Figure 5-36 show results for the same configuration rotating at 625 rpm. Temperature (Figure 5-33) and concentration (Figure 5-34) profiles look relatively similar to the previous case at lower rotational speed. However, the mass flux (Figure 5-35) increases by 42% in average to local values of up to 20 g/(s·m^2). In consequence, the heat flux (Figure 5-36) reaches an average of 46 kW/m^2 in the actively cooled zone.

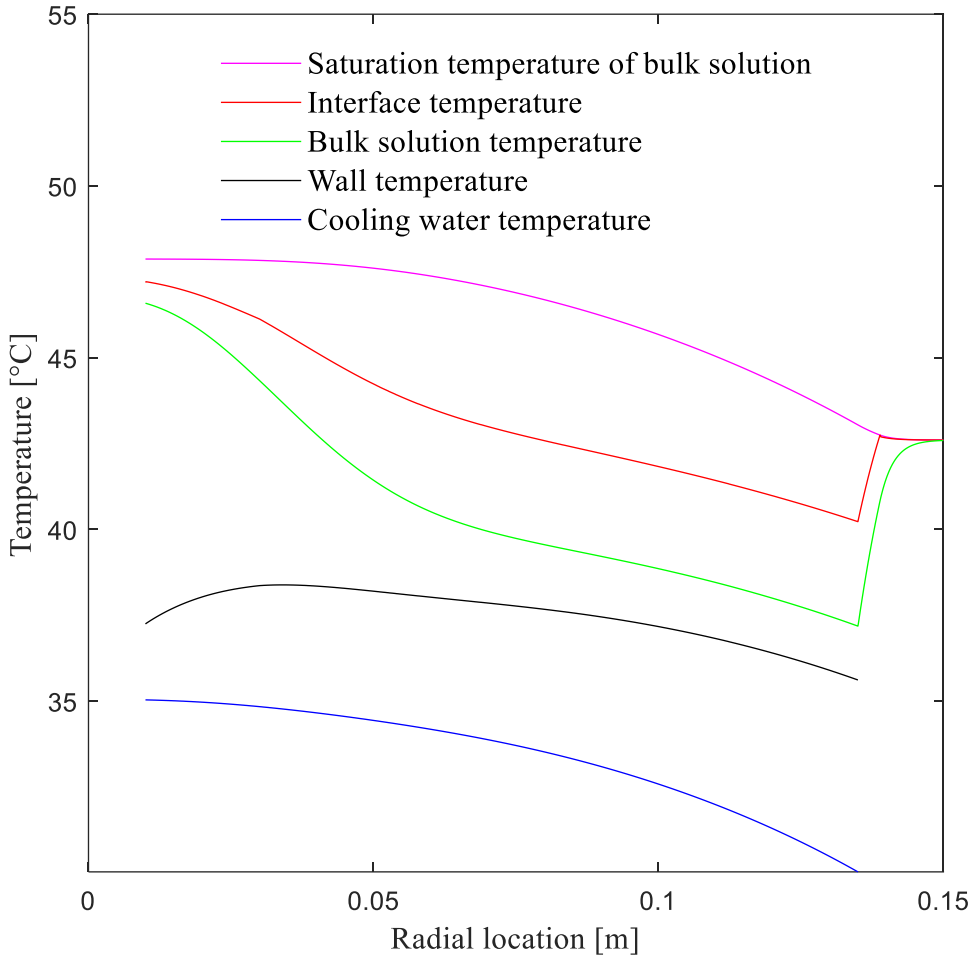

Figure 5-33: Temperature profiles of semi-empirical model with water-side cooling by manifold-microchannel technology and rotating at a speed of 625 rpm.

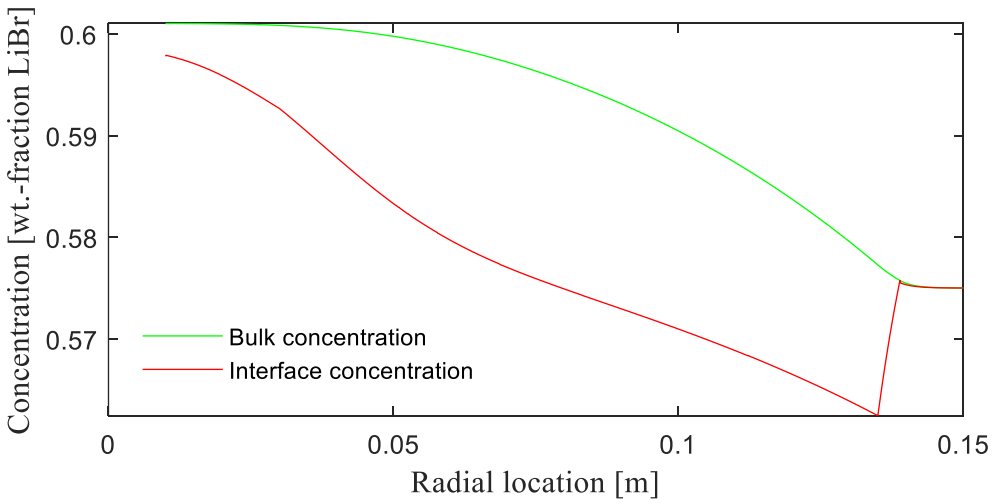

Figure 5-34: Concentration profiles of semi-empirical model with water-side cooling by manifold-microchannel technology and rotating at a speed of 625 rpm.

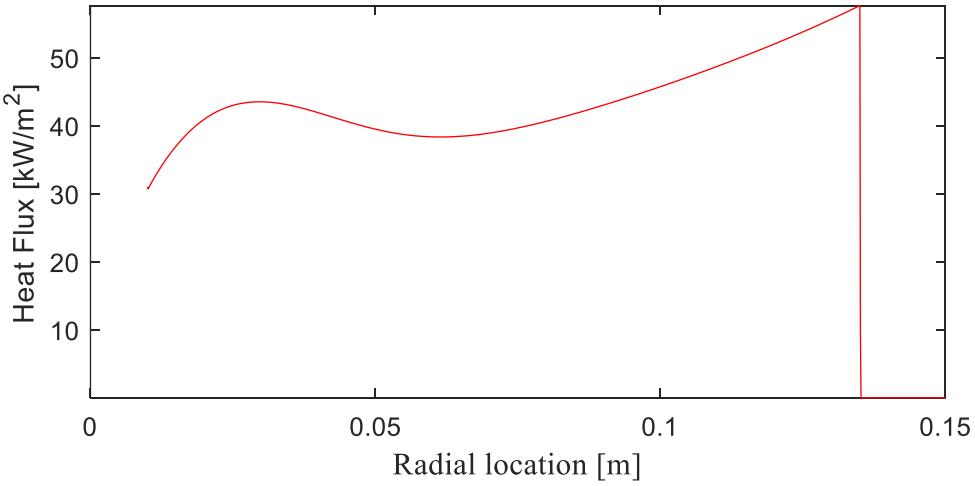

Figure 5-35: Heat flux of semi-empirical model with water-side cooling by manifold-microchannel technology and rotating at a speed of 625 rpm.

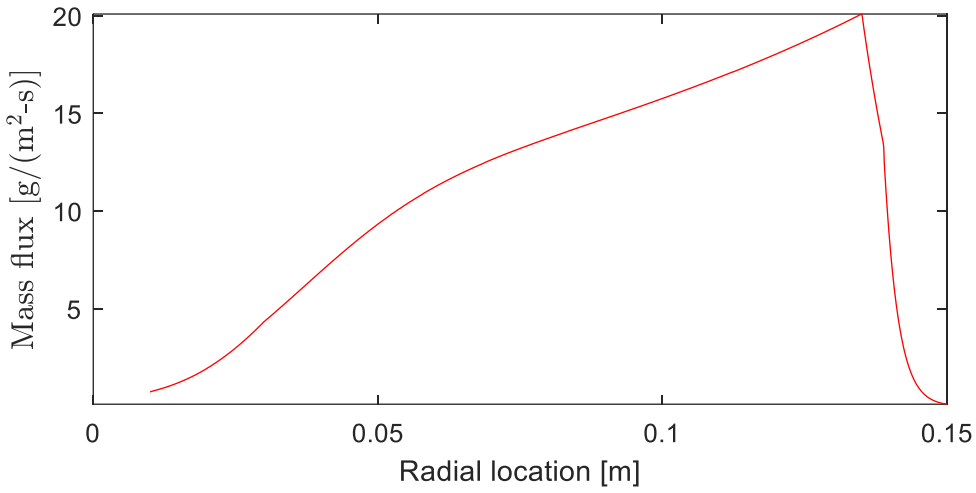

Figure 5-36: Mass flux of semi-empirical model with water-side cooling by manifold-microchannel technology and rotating at a speed of 625 rpm.

5.4.2.3. Summary of semi-empirical model

The semi-empirical mode uses experimental data to calibrate the computer model. By transforming the mass transfer coefficient into a variable, the model is able to replicate the high heat and mass transfer rates observed in experiments. Results show that heat transfer precedes mass transfer, i.e. that the spinning disk absorber produces high heat fluxes from the center of the disk but that meaningful mass flux only starts after approximately a third of the flow distance. Closer to the center, mainly sensible heat is removed and only once the interface temperature is sufficiently lowered does mass flux pick up steam. However, once it has started, mass flux stays high until the end of the actively cooled zone. Thereby, it keeps solution temperature high, which then leads to sustained high heat fluxes. Beyond the actively-cooled zone, the absence of heat rejection reduces mass flux. Yet, small amounts of vapor continue to get

absorbed until the solution is close to saturation at the outer radius of the disk. The results indicate that a larger diameter spinning disk absorber may achieve higher average performance as the heat/muss fluxes are higher in the outer disk area. Also, the area without active cooling should be minimized through more compact packaging of sealing and fasteners.

Both microgap and manifold-microchannel cooling technologies on the water-sider have been analyzed. As expected, high-performance manifold-microchannel cooling cools the absorbent solution faster and to a lower temperature. The lower interface temperature then leads to increased mass flux and higher absorber performance. The mass transfer coefficients that are calculated within the semi-empirical model are subject of the next section.

5.5. Analysis of mass transfer coefficient

As discussed in chapter 5.2.2.2, correlations for gas-liquid mass transfer on spinning disks given in the literature vary significantly. The average gas-liquid mass transfer coefficient in the present study calculated within the semi-empirical model was in between 1.8 m/h at 250 rpm and 2.2 m/h at 625 rpm (Figure 5-37). This constitutes an enhancement by an order of magnitude compared to horizontal tube banks (Figure 5-1). However, it is important to note that the mass transfer coefficient determined in this study is not measured directly but a result of the modeling program. Hence, the value of the mass transfer coefficient depends on modeling assumptions and has an inherent systematic uncertainty that is not possible to quantify.

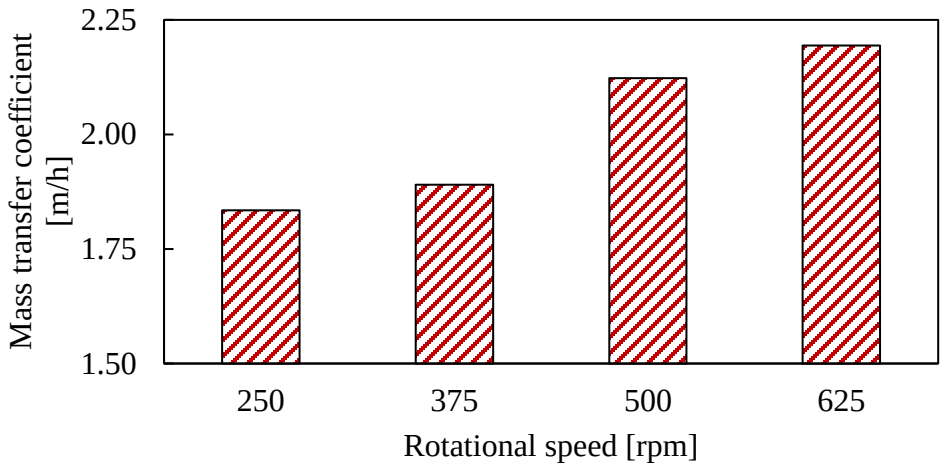

Figure 5-37: Average gas-liquid mass transfer coefficient in present study.

Figure 5-38 shows that the mass transfer determined in this study was larger than predicted based on existing correlations. The enhancement factors were 13.7 to 15.4 over the correlations based Higbie's penetration theory and 2.5 to 4.2 over Sisoev et al.'s theory on absorption into wavy films. The enhancement factor over the correlation by Peev et al. lies in between. Compared with all correlations, yet more strongly compared to the correlation by Peev et al., the enhancement factor is smaller at higher rotational speed. This points to high mixing intensity of the liquid film even at relatively low rotational speed.

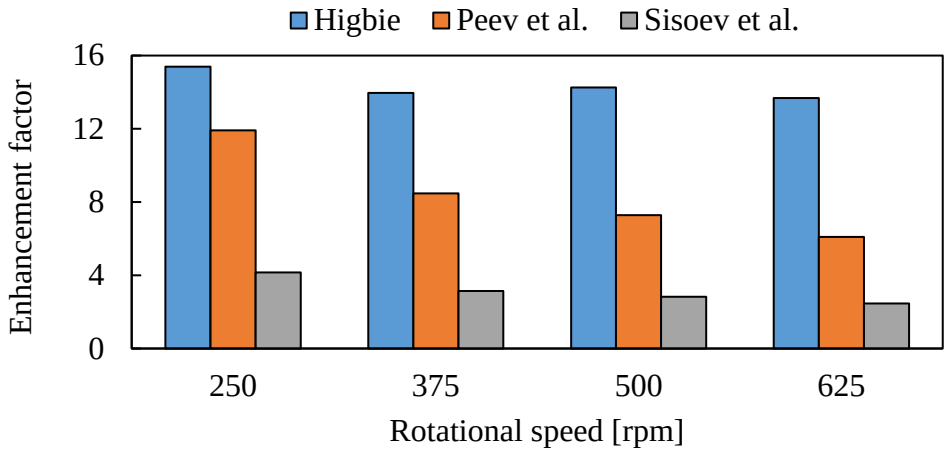

Figure 5-38: Enhancement factor of mass transfer coefficient determined in this study over existing correlations.

Present results have made it clear that the correlations for mass transfer in the literature that were based on absorption of oxygen into water do not capture the present process of absorption of water vapor into lithium bromide accurately. One possible cause for deviations is the inclusion of property data in the correlations that was not or not sufficiently altered in the experiments. Therefore, the theoretical correlation by Peev et al. [121] given in Eq. 5-7 is fitted to a broader set of data. The new data set combines experimental data by Aoune and Ramshaw [13] as analyzed by Peev et al. and data from the present study (Table 5-2).

Table 5-2: Data range used in development of mass transfer correlation.

	Peev et al. / Aoune and Ramshaw	Present study
Ekman	$1.61\text{x}10^{-7}$ - $5.37\text{x}10^{-7}$	$2.0\text{x}10^{-6}$ - $6.8\text{x}10^{-6}$
Reynolds	12.07 - 34.63	1.98 - 7.26
Schmidt	479	3320 - 4819
# data points	25	36

Peev et al. used property data at the outlet from the spinning disk. Since the outlet in the present case is not subject to active cooling, property data was based on values at the end of the actively cooled zone. Fitting the Sherwood number in Eq. 5-7 to the data in Table 5-2 by non-linear least squares method yields the following correlation:

$$\overline{Sh}_{r_o} = 0.0290 Ek_{r_o}^{-0.41} \, \mathrm{Re}_{\mathrm{o,Q}}^{0.62} \, Sc^{1.07} \qquad 5\text{-}29$$

Figure 5-39 shows the quality of the data fit is acceptable with a mean absolute percentage error of 18.2%. The correlation does capture changes in property data values associated with the different operating conditions.

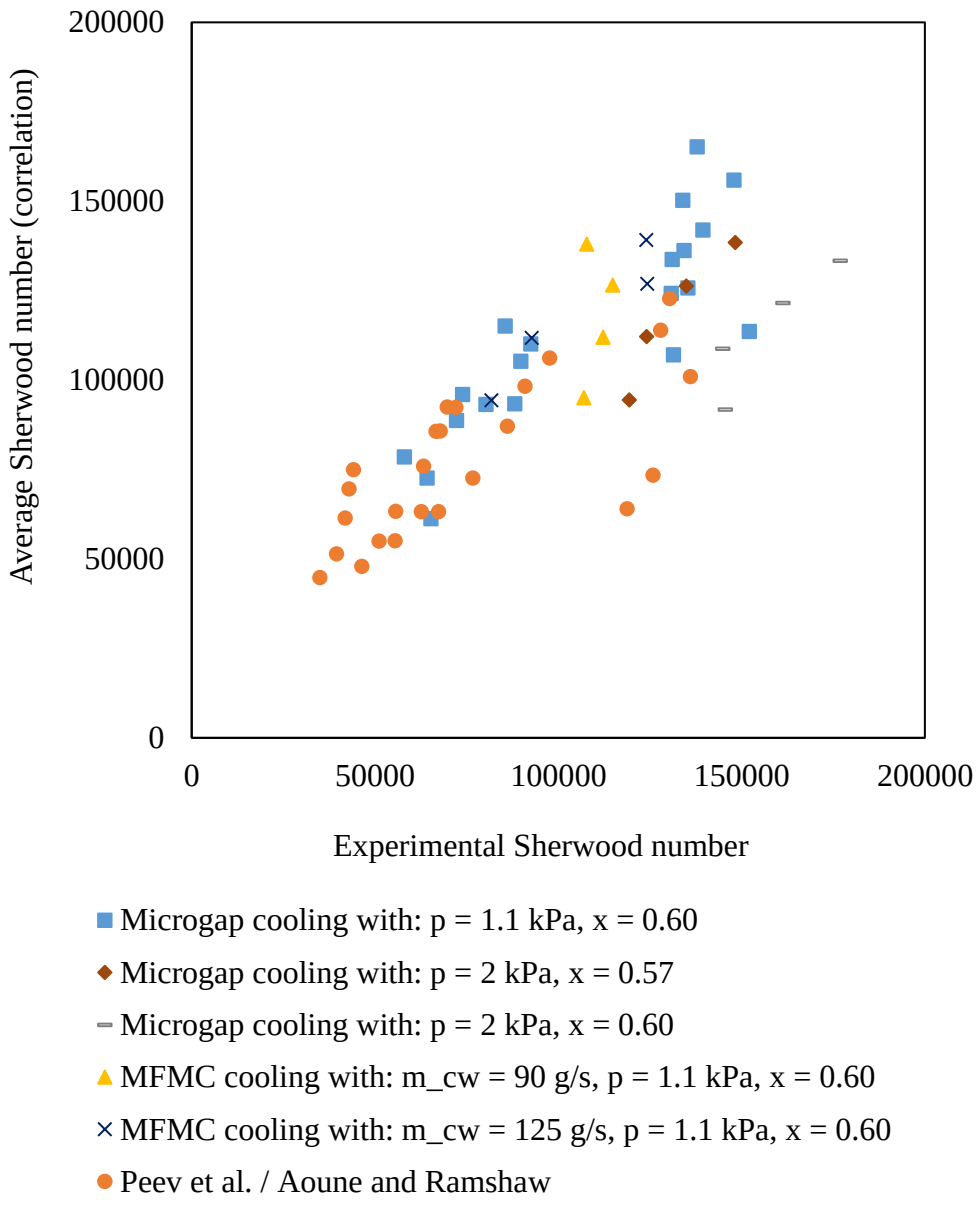

Figure 5-39: Correlation of mass transfer data in this study and by Aoune and Ramshaw [13] based on Eq. 5-29.

5.6. Chapter conclusions

Spinning disk absorbers significantly enhance the absorption process in absorption cooling systems and can therefore lead to smaller and cheaper equipment. However, to the best of the author's knowledge, this study represents the first comprehensive model to describe the simultaneous heat and mass transfer process that takes place during exothermic absorption of a gas into a liquid on a spinning disk reactor.

To describe the absorption process, a set of governing ordinary differential equations for the coupled heat and mass transfer process were identified and solved numerically. Empirical and theoretical correlations for heat and mass transfer coefficients were used. Comparison with experimental data showed that the model can accurately describe the performance of a spinning disk absorber if accurate transfer coefficients are available. Film-side heat transfer based on a parabolic temperature profile was assumed since it showed better match of the absorption performance than linear profile. Temperature and concentration profiles over the radial position were plotted. A new correlation for average Sherwood number was developed based mass transfer coefficient determined within a semi-empirical model and literature data. In case of water/lithium bromide absorption on a spinning disk, the mass transfer coefficient is an order of magnitude higher than conventional horizontal tube absorbers. Both heat and mass transfer increased with rotational speed. Heat flux was significant right from the center and further increased in radial direction with decreasing thickness of the solution film. The mass flux was relatively low at the center but greatly increased

with radial location. This was caused by the increased subcooling in the outer area that amplified the driving force for mass transfer.

The model developed here gives detailed insight into the development of the absorption process and will therefore be a valuable tool in the design optimization of spinning disk absorbers. The proposed non-dimensional correlation for gas-liquid mass transfer on spinning disk may be especially useful when spinning disk absorbers are combined with new absorbers such as Ionic Liquids or microemulsions.

6. Testing of complete absorption chiller

A full absorption chiller with generator, condenser, evaporator and absorber was built by another task group of the overall project. The chiller system was intended to provide a baseline testing scenario for comparison with advanced systems. Unfortunately, preliminary testing failed to produce reliable and accurate baseline data of the chiller and the tubular absorber installed within the chiller. Problems with the baseline tests included lack of reliable concentration, pressure, temperature and cooling water mass flow measurements and the absence of steady-state data. However, the problems with the baseline data were only discovered after the baseline test had concluded and the baseline system had been shut down. Hence, initial loop problems had to be fixed in parallel to testing of the advanced spinning disk absorber that replaced the original tube bank absorber. Figure 6-1 shows a picture of the full absorption chiller with generator, condenser, evaporator and both types of absorbers. Figure 6-2 shows the final test configuration in which the condenser and generator units were directly connected to each other because the tubing connecting the chambers in Figure 6-1 was one source of air leakage into the system.

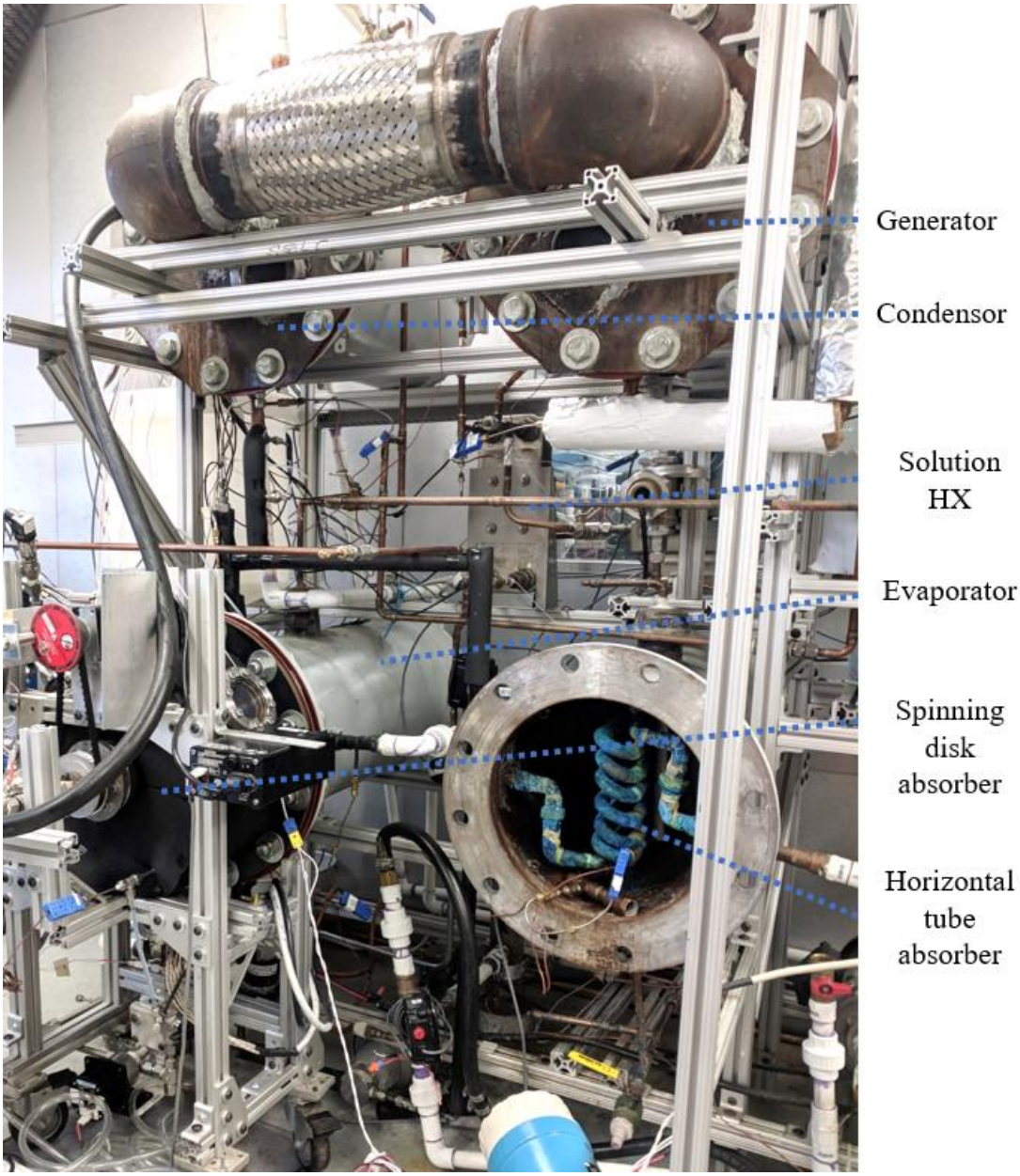

Figure 6-1: Picture of the full absorption chiller test setup.

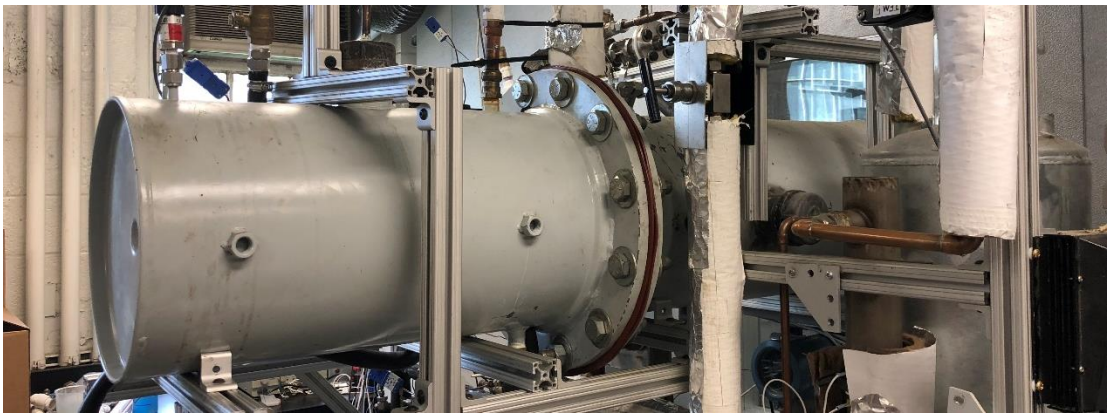

Figure 6-2: Condenser directly connected to generator for final testing.

Operating conditions and results of experimental testing of the absorption chiller are listed in Table 6-1 and Table 6-2, respectively. Cooling capacity (i.e. heat input into the evaporator) of the chiller was slightly below 1 kW, which was less than expected. The low cooling capacity was attributed to very high solution subcooling of 10 to 13°C. This is in stark contrast to previous testing in which the absorbent solution at the absorber was saturated. Even with conventional tube bank absorbers, subcooling is reported to be between 3 and 5°C [20,32].

Typically, heat transfer in absorbers is described by using saturation temperatures. However, given the high subcooling observed at the outlet from the absorber in the complete chiller setup, the saturation temperature of the solution deviates strongly from actual temperatures and is thus not an accurate description of the driving force. Therefore, the overall heat transfer coefficient of the absorber in the complete chiller test in Table 6-2 is based on measured temperatures. The overall heat transfer coefficient was between 2.6 kW/(m^2·K) and 3.1 kW/(m^2·K), which is in line with

previous testing with the mini-test setup (e.g. see Figure 4-15) for the given rotational speed. The accuracy of measurement results can be assessed by separate energy balances over two control volumes (Figure 6-3). Control volume A encompasses only the components at the low pressure stage, i.e. evaporator and absorber. The energy balance over control volume is given by Eq. 6-1. The respective heat flows associated with the four terms in Eq. 6-1 are given in rows one to four of Table 6-2. Eq. 6-1 neglects the power input by rotation due to its low amount relative to other contributions.

$$\dot{m}_{chw,evap} c_{p,H_2O} \left(T_{chw,evap_{in}} - T_{chw,evap_{out}}\right) + \dot{m}_{H_2O,evap_{in}} h_{H_2O(l)} + \dot{m}_{sol,abs_{in}} \left(h_{sol,abs_{in}} - h_{sol,abs_{out}}\right) = \dot{m}_{cw,abs} c_{p,H_2O} \left(T_{cw,abs_{out}} - T_{cw,abs_{in}}\right) \quad 6\text{-}1$$

The energy balance B, encompassing the complete absorption chiller, is given by Eq. 6-2. The pumping power and rotational power inputs are neglected due to their low amounts relative to other contributions.

$$\dot{m}_{chw,evap} c_{p,H_2O} \left(T_{chw,evap_{in}} - T_{chw,evap_{out}}\right) + \dot{m}_{htf,gen} c_{p,htf} \left(T_{htf,gen_{in}} - T_{htf,gen_{out}}\right) = \dot{m}_{cw,cond} c_{p,H_2O} \left(T_{cw,cond_{out}} - T_{cw,cond_{in}}\right) + \dot{m}_{cw,abs} c_{p,H_2O} \left(T_{cw,abs_{out}} - T_{cw,abs_{in}}\right) \quad 6\text{-}2$$

Table 6-1: Operating conditions of complete absorption chiller.

	Unit	Test 1	Test 2
P (Evaporator / absorber)	Pa	1170	1314
T (Evaporator: Chilled water in)	°C	12.0	14.0
T (Evaporator: Chilled water out)	°C	10.4	12.2
Chilled water mass flow rate	g/s	126.2	126.2
T (Absorber: Cooling water in)	°C	19.6	20.1
T (Absorber: Cooling water out)	°C	23.9	25.3
Cooling water mass flow rate	g/s	107.9	107.9
T (Absorber: Solution in)	°C	45.4	49.1
T (Absorber: Solution out)	°C	26.3	26.6
Subcooling (Absorber out)	°C	9.8	13.0
Solution mass flow rate*	g/s	28.9	31.7
x (Absorber in)**	wt.-% LiBr	53.7%	56.2%
x (Absorber out)	wt.-% LiBr	53.4%	56.7%
Rotational speed	rpm	370	463

Notes:

*Only solution mass flow rate of dilute stream, readings of which were more reliable than concentrated stream.

**Concentration: Solution leaving the generator has to be leaner in refrigerant than solution leaving of absorber. Due to small changes in concentration, measurement problems and measurement uncertainty, this is not always fulfilled in this test.

Table 6-2: Test results of complete absorption chiller.

	Units	Test 1	Test 2
Q_{in} (Evaporator: Chilled water)	kW	0.88	0.96
Q_{in} (Evaporator: Refrigerant)	kW	0.04	0.05
Q_{in} (Absorber: Absorbent solution)	kW	1.17	1.36
Q_{out} (Absorber: Cooling water)	kW	-1.91	-2.35
Energy balance (Control volume A: Evaporator / absorber)	-	8.4%	0.9%
Q_{in} (Generator)	kW	2.01	2.68
Q_{out} (Condenser)	kW	-0.99	-1.21
Energy balance (Control volume B: Absorption chiller)	-	-0.7%	2.4%
COP	-	0.44	0.36
Overall heat transfer coefficient	W/(m^2·K)	2620	3054

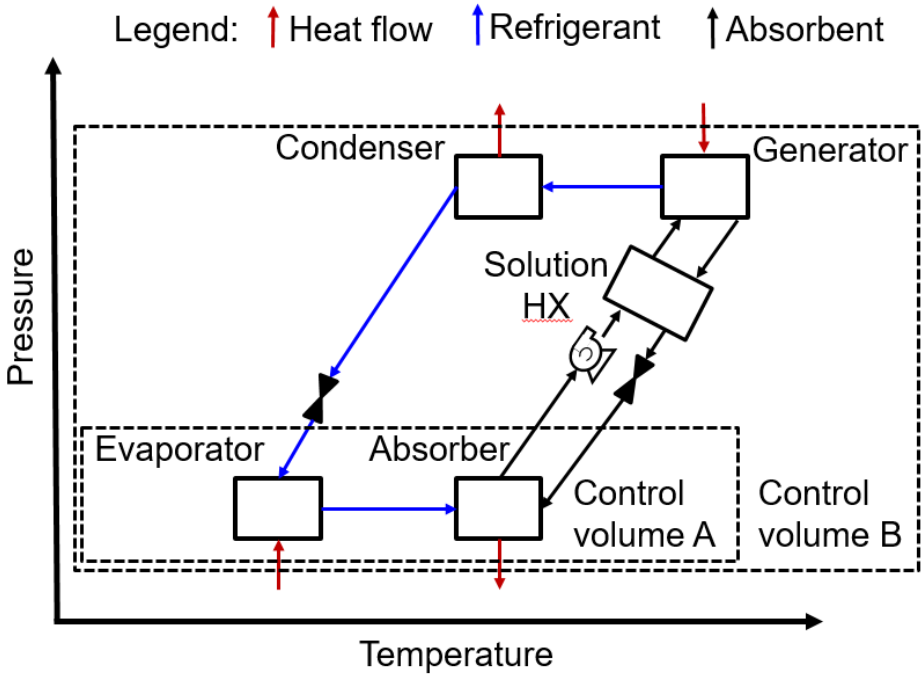

Figure 6-3: Schematic of complete chiller with control volumes for energy balances.

The high subcooling and low cooling capacity were caused by severe corrosion that changed properties of the aqueous lithium bromide solution. Strong corrosion of vacuum chambers and heat/mass exchangers was already noted after conclusion of preliminary testing and further intensified over the time needed to solve operational and measurement problems. An example of heat/mass exchanger corrosion can be seen by the build-up of blue scale on the horizontal tube absorber in Figure 6-1. Vacuum chambers of the absorption chiller were made of carbon steel and strongly corroded as well, in particular because the large system was prone to air leakage and thus oxygen infiltrated the system. In presence of oxygen, aqueous lithium bromide attacks both copper, of which the heat/mass exchangers were made of, and carbon steel. Commercial absorption chillers commonly control the pH value of the absorbent solution to reduce corrosion risk. This measure was not taken in the present case as the system was expected to run for a very short time only. However, the time needed to develop solutions to operational and measurement problems led to prolonged presence of aqueous lithium bromide in the system and hence much higher corrosion risk than anticipated. Although the absorbent solution was refreshed for final testing of the spinning disk absorber, the trend could not be reversed anymore. Figure 6-4 shows the degree of corrosion of the carbon steel vacuum chambers at the example of the generator and the build-up of corroded matter in the spinning disk absorber vacuum chamber after final testing. The photographs were taken after the system had already

been flushed with water multiple times. Unfortunately, the imminent teardown of the building in which the test stand was located prevented further exploration of the problem and development of a corrective measures.

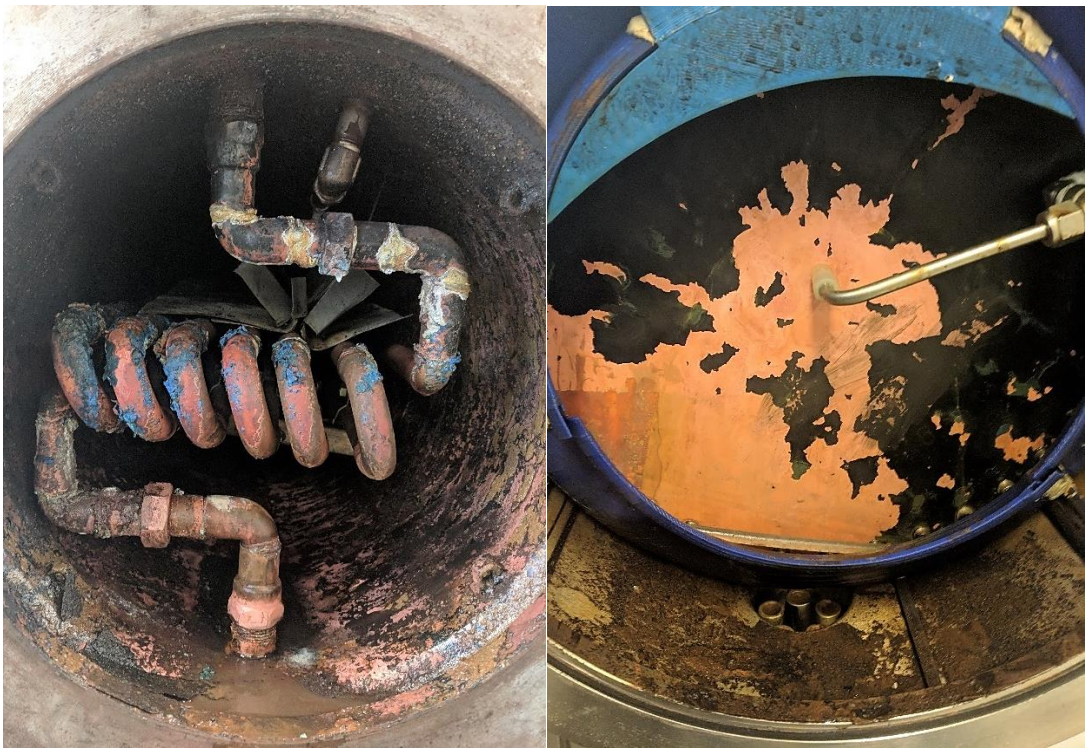

Figure 6-4: Corrosion in generator (left side) and build-up of corroded matter in the spinning disk absorber after testing absorption chiller (right side).

7. Conclusions

This dissertation reports the development of a novel, compact absorber for absorption cooling systems and its experimental and computational analysis. The research demonstrated great potential to intensify absorption cooling systems by rotation of heat/mass transfer surface in the absorber. Based on this body of work the following contributions are drawn:

- Rotation of the heat transfer surface is an efficient technique to intensify heat/mass transfer processes in the absorber component of the absorption chillers. Both heat transfer through the absorbent solution and mass transfer from gas-to-liquid phase are enhanced. In the present study the solution-side heat transfer coefficient increased by up to factor of 5.5. This enhancement is attributed to the thinning of the liquid film by the centrifugal acceleration and mixing of the liquid film. The film-side heat transfer coefficient is higher the faster the heat transfer surface rotates. In the present setup, the film-side heat transfer coefficient was found to be proportional to (rotational speed)$^{0.76}$.
- Rotation of the heat transfer surface ultimately reduced solution-side thermal resistance below the water-side thermal resistance. Conventional tube-type absorbers are strongly dominated by solution-side resistance. Hence, only after intensification of the solution-side process does water-side heat transfer enhancement becomes significant. In the present study, the water-side heat transfer

enhancement led to additional 42% increase in the overall heat transfer coefficient when compared to film-side intensification alone.

- Manifold-microchannel technology can be adapted to highly unconventional geometries and flow arrangements. In the present case, the heat transfer fluid flows in radial direction through a disk-shaped cavity although commercially available microdeformation plates with parallel microchannels are used. The advancement of additive manufacturing has made it possible to design cost-affordable, 3D-printed polymer distribution manifolds that can accommodate a wide range of fluid flow rates and geometries.
- The combination of intensification by centrifugal acceleration on the solution-side and manifold-microchannel technology on the water-side provides very high performance enhancement. Absorption rate of water vapor as high as 16 g/(m^2·s) has been recorded, which is one order of magnitude higher than conventional horizontal tube absorbers and double as high as other novel designs reported in the literature. Overall heat transfer and solution-side heat transfer are 4.7 and 5.5 higher, respectively, than a horizontal tube bank absorber operated at similar conditions. A single disk device achieved a cooling capacity of 2.3 kW at a theoretical chilled water temperature of 8.4 ºC.
- Total power consumption of the optimized device ranged between 23 W and 81 W at 125 rpm and 625 rpm, respectively. Power consumption was 1.7% to 3.5% of cooling capacity with the latter value recorded at 625 rpm and the former at 125 rpm. However, the motor was relatively inefficient. The rotational power

consumption rate alone, excluding motor inefficiencies, was 1.1% to 2.3%. Power is mainly lost due to frictional losses of sealing and bearing and hence will scale favorably with scale-up to a multi-disk design. Also, there are opportunities to reduce power draw by using a high efficiency motor and low-friction seals.

- A computer model was proposed to describe the absorption process on a spinning disk absorber. A set of governing ordinary differential equations was identified and solved numerically. When based on existing mass transfer correlations derived from a different fluid pair, the model under-estimated the absorption/absorber performance. Therefore, a new non-dimensionless mass transfer correlation was derived from semi-empirical version of the computer model that uses experimental data for calibration. According to the proposed correlation, the mass transfer coefficient of the spinning disk absorber surpasses horizontal tube banks by an order of magnitude, which is attributed to the mixing effect of the wavy flow.
- The experimental studies presented in this thesis have shown the significant potential to enhance heat and mass transfer in the absorber section of absorption chillers by rotation of the heat transfer surface. By applying the presented enhancement methods, it will be possible to produce commercial-scale absorption chillers with a higher ratio of cooling capacity to volume, thereby improving their economic appeal. Another potential application area of the developed technology is to use rotating heat transfer surfaces in combination with novel absorbents. Novel absorbents, such as Ionic Liquids or oil-based microemulsions, are often very viscous. High viscosity leads to higher heat transfer resistance of the absorbent

solution on the absorber tubes of conventional shell and tube absorbers and consequently a low ratio of absorber capacity to absorber volume. The solution-side heat transfer enhancement by rotation of the heat transfer surface can mitigate the effects of high absorbent viscosity and will thus be especially useful if combined with novel absorbents.

8. Recommendations for future work

8.1. Further enhancement of heat and mass transfer rates

The discussion of transfer processes in chapter 5 has shown that a disk with a larger diameter is expected to achieve a higher average performance. Enlarging capacity and performance by using a larger diameter disk is especially attractive because it would not increase power consumption, which depends on frictional losses related to rotation of the drive shaft. However, overall dimensions of device in an actual application will likely be restricted and increase in diameter beyond 0.5 m seems unlikely.

However, the performance of the device can increase further even at constant dimensions of the assembly. Jachuck and Ramshaw have shown that just seven radial grooves on the surface of a rotating disk of 0.36 m diameter increase film-side heat transfer by up to 77% [11]. This result was reported for sensible heat transfer experiments and may even be higher in the case of latent heat transfer. It would likely also enhance the mass transfer coefficient significantly as the fluid movement over grooves completely breaks up the concentration boundary layer and leads to thorough re-mixing of the liquid film. Thus, adding concentric grooves to the surface of the disk is likely to promote significant performance improvements at low costs.

Internal heat transfer can further be optimized by continued development of the manifold-microchannel system. The technology presented in chapter 4 succeeded in making the advantage associated with manifold-microchannel improvements available to spinning disks and consequently improved overall performance strongly. However,

it is likely that uniform flow distribution is not achieved, hence leaving room for further improvements.

Any new approach to increase internal heat transfer further should aim to still use commercially available microgrooved heat transfer surfaces plates with parallel microchannel in order to keep production costs low. However, different cutting of the microgrooved plates would enable to achieve more uniform flow distribution. E.g. if the microgrooved surface is cut into four quarters, it will be much easier to design a distribution manifold that achieves uniform flow distribution. A schematic of such a design is shown in Figure 8-1. Microchannels in this design exhibit four 90-degree bends to form a rectangle. Each quarter will be fed individually by the distribution manifold and dividers may be installed between the quarters to prevent flow from one section penetration into the one next to it. Hence, the task reduces to achieving good flow distribution over one quarter which can be replicated three times. Balancing pressure drop and heat transfer capabilities over one quarter will require application of changes in manifold fin width similar to design used in chapter 4.2, maybe encompassed by changes in cell length. Together, these improvements to water-side heat transfer and film-side heat and mass transfer are expected to enhance overall performance significantly.

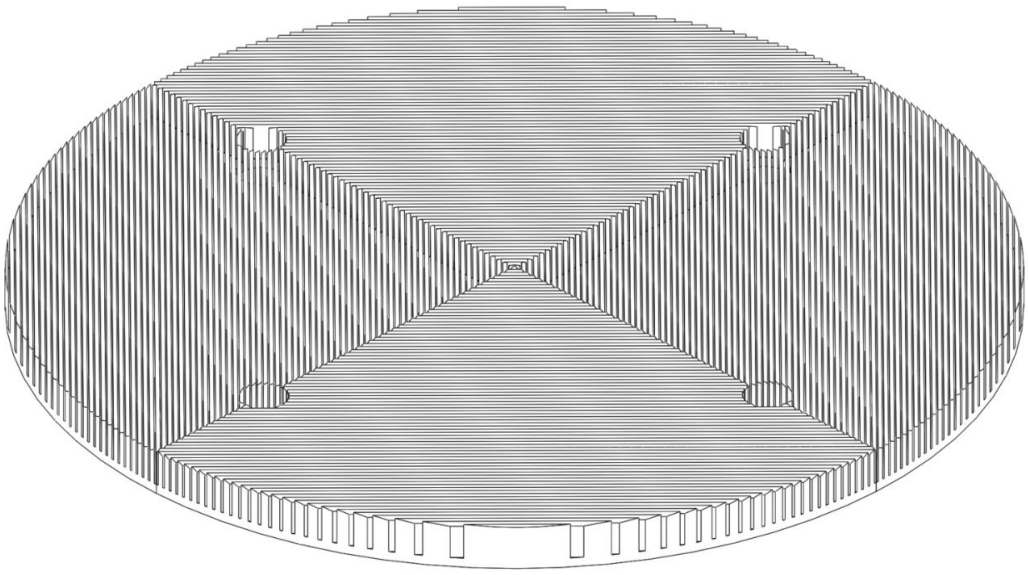

Figure 8-1: Proposed microchannel disk with 90-degree bends.

8.2. Scale-up to commercial capacity

An actual commercial absorption machine requires higher cooling capacity than a single disk design is able to deliver. Hence, a design approach for scale up is necessary. Chapter 3.3.4 has shown that the main power consumption of the spinning disk absorber is caused by frictional losses due to sealing. Therefore, any scale up should include several disks in parallel on the same drive shaft. This design will increase power consumption only due to an inevitable increase in shaft diameter. Such a design is shown in Figure 8-2. To accommodate the higher cooling water flow rate, the shaft diameter increases from approx. 0.75” to 1.5”. At 625 rpm, this will increase power consumption from 76 W to 260 W, an increase by a factor of 3.4 while cooling capacity increases tenfold. Based on the cooling capacity reported in chapter 4.4.3, such a ten-disk design would be able to provide 22 kW (6.25 RT) of cooling at a power

consumption rate of 1.2% before optimization of sealing materials and motor efficiency.

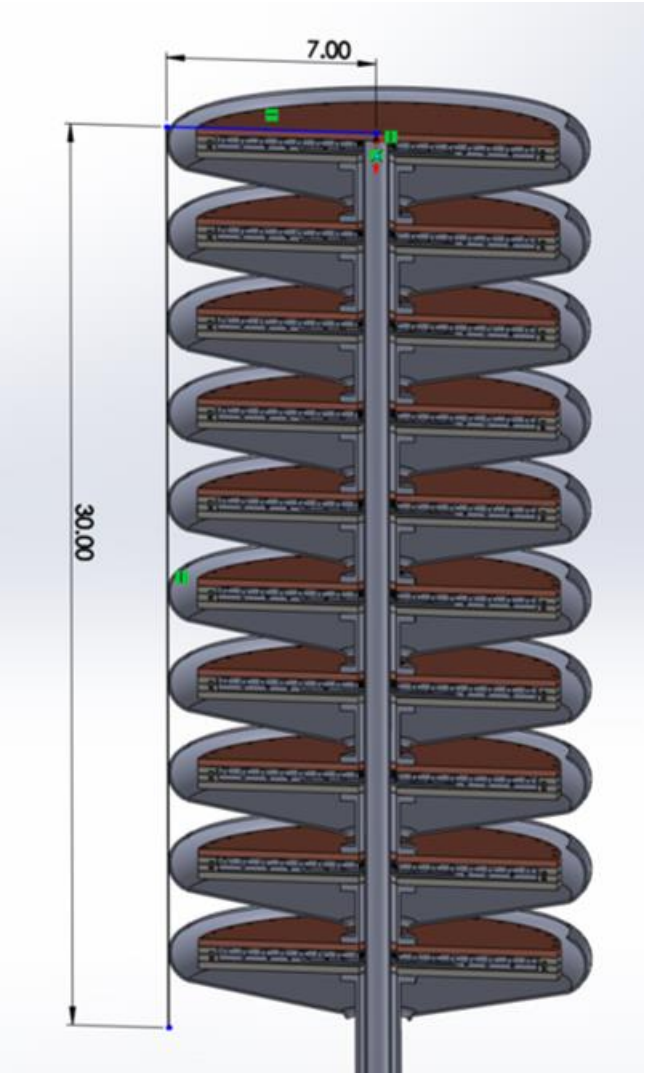

Figure 8-2: Scale-up to 22 kW cooling capacity (Dimensions in inches).

The choice to employ several disks in parallel has a number of consequences. If the shaft axis was aligned with the vertical to be able to use gravity to move absorbent solution between disks. The co-axial shaft design will make it extremely difficult to

achieve good flow distribution between disks and reliable sealing if using a parallel flow configuration. A configuration in series is therefore recommended; cooling water will flow in counterflow direction to absorbent solution to further maximize performance. However, a manifold-microchannel system will allow to achieve very high internal heat transfer coefficients while keeping pressure drop low even if cooling water flow rates increases strongly as was shown in Figure 4-5.

Alternatively, it is still possible to operate a multi-design with a horizontally aligned axis of the drive shaft. In that case, a bearing would most likely be necessary at the top end of the multi-disk assembly to keep the much heavier assembly aligned and reliability high. Horizontal operation would be attractive because it enables to use both sides of the disk for the absorption process, thereby reducing material and space requirements by almost half. Pumping of absorption solution between individual disk surfaces could be achieved by integrating a pitot pump that is driven by the disks rotation. A related approach had been implemented in the development of the Rotex absorption machine [72].

Finally, a complete absorption chiller setup would benefit from application of the process intensification method developed in this work to all heat/mass exchangers. While the absorber is the largest and most critical component by itself, other heat/mass exchangers require a larger combined volume. Hence, to reduce overall system volume and cost, their size needs to reduce as well. All heat/mass exchangers perform conceptually similar process and can hence be intensified by application of centrifugal acceleration. Since the four heat/mass exchangers are commonly integrated in two

pressure vessels, only two drive shafts would be required in total. However, since the temperature levels are different for each component, it may be easier to connect each end of each drive shaft to a rotary valve that delivers heat transfer fluid. This would require four rotary vacuum seals which therefore should be thoroughly engineered for low friction and power consumption.

8.3. Test with the working pair water/Ionic Liquid

Over the last one and a half decades, the concept of replacing conventional absorbents by Ionic Liquids has gathered considerable attention. Ionic liquids are salts composed of an organic cation and an organic or inorganic anion that exist in liquid state at low temperatures. Ionic liquids of interest for absorption refrigeration have a melting point below room temperature and are therefore sometimes referred to as Room Temperature Ionic Liquid (RTIL). This property is different to the common working pair water/lithium bromide, which starts to solidify, i.e. to crystallize, when high concentrations and low temperatures are combined. Crystallization of the lithium bromide salt is commonly regarded as the main drawback that prevents the development of air-cooled absorption refrigeration equipment [159,160]. Moreover, Ionic Liquids exhibit lower corrosion rates than aqueous lithium bromide [161], which should enable longer useful lifetimes of the absorption chiller. Refrigerant pressure as low as 100 Pa has been reported when water is used as refrigerant [161]. Experimental studies and simulations point to that ionic liquid-water system achieve coefficients of performance close to or similar as systems operated with water/lithium bromide [162–

166], Wasserscheid and Seiler [161] reported that a 20 kW commercial chiller was switched from lithium bromide to a proprietary ionic liquid without loss efficiency or cooling capacity. However, a review article stated that Ionic Liquid-based systems generally achieve lower cooling capacities due to lower heat and mass transfer [166]. At study reported a cooling capacity of 1.3 kW for a nominally 10 kW system [163]. The difference was attributed to the high viscosity and poor wetting behavior of Ionic Liquids. An example of poor wetting of Ionic Liquids is shown in Figure 8-3.

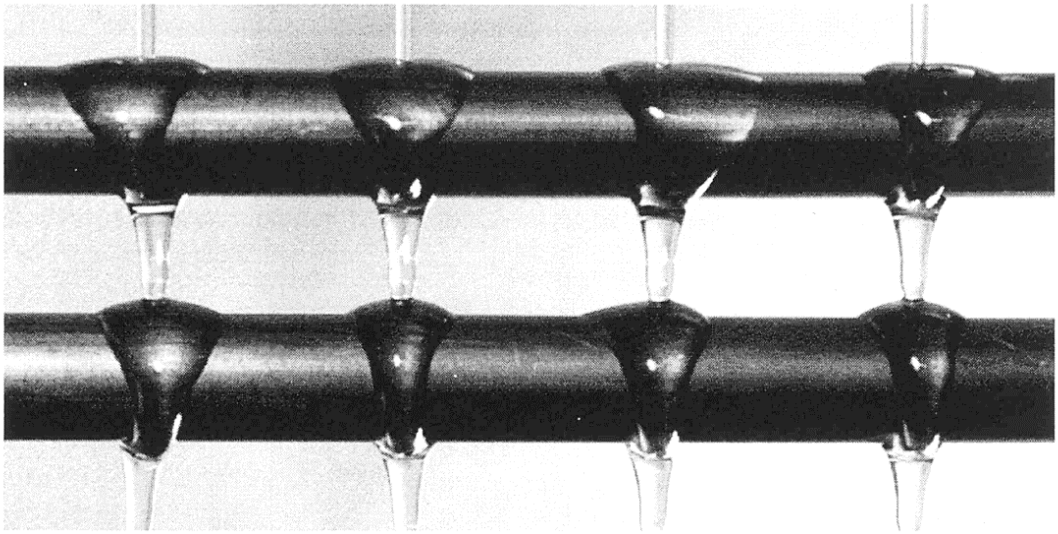

Figure 8-3: Wetting behavior of an Ionic Liquid on a horizontal tube absorber from Römich et al. [163].

Thus, while Ionic Liquid-based absorption machines achieve similar performance than lithium bromide-based ones, they suffer from lower heat and mass transfer performance due to high viscosity and poor wetting. This makes them ideal candidates for testing with the spinning disk absorber.

Appendix I: Deduction of temperature profile and heat transfer coefficient for case of linear temperature profile and parabolic velocity profile

Deduction of linear temperature profile

$T = a + bz$

$BC1: At\ z = 0: T = T_w$

$\rightarrow a = T_w$

$BC2: At\ z = \delta: T = T_s$

$\rightarrow T_s = T_w + bz$

$b = (T_s - T_w)/\delta$

$$T = T_w + \frac{(T_s - T_w)}{\delta} z$$

Deduction of average temperature for linear temperature profile and parabolic velocity profile

$$T_{ave} = \frac{\int_0^\delta uTdz}{\int_0^\delta udz}$$

$$u = \frac{r\omega^2\rho}{\mu}(z\delta - \frac{z^2}{2})$$

$$T = T_w + \frac{(T_s - T_w)}{\delta} z$$

$$T_{ave} = \frac{\int_0^{\delta}\left(\frac{r\omega^2\rho}{\mu}\left(z\delta - \frac{z^2}{2}\right)\right)\left(T_w + \frac{(T_s - T_w)}{\delta}z\right)dz}{\int_0^{\delta}\frac{r\omega^2\rho}{\mu}(z\delta - \frac{z^2}{2})dz}$$

$$= \frac{\int_0^{\delta}\left(T_w z\delta + T_w z^2 - T_w z^2 - \frac{T_w z^2}{2} - \frac{T_s z^3}{2\delta} + \frac{T_w z^3}{2\delta}\right)dz)}{\frac{\delta^3}{2} - \frac{\delta^3}{6}}$$

$$= \frac{3}{\delta^3}\left(\frac{\delta^3}{8}T_w + \frac{5\delta^3}{24}T_s\right)$$

$$T_{ave} = \frac{3}{8}T_w + \frac{5}{8}T_s$$

Deduction of heat transfer coefficient

The surface heat flux, given by Fourier's law, is equal to convective heat flux through liquid film.

Surface heat flux:

$$q''_{Fourier} = -k\frac{dT}{dz}\Big|_{z=0} = \frac{-k(T_s - T_w)}{\delta}$$

Convective heat flux:

$$q''_{Conv} = h(T_w - T_{ave}) = h\left(\frac{5}{8}T_w - \frac{5}{8}T_s\right)$$

Since heat transfer rates must be equal:

$$q''_{Fourier} = q''_{Conv}$$

$$\frac{-k(T_s - T_w)}{\delta} = h\left(\frac{5}{8}T_w - \frac{5}{8}T_s\right)$$

$$h = \frac{8}{5}\frac{k}{\delta}$$

Appendix II: Deduction of temperature profile and heat transfer coefficient for case of parabolic temperature profile and parabolic velocity profile

Deduction of parabolic temperature profile

$$T = a + bz + cz^2$$

$$BC1: At\ z = 0: T = T_w$$

$$\rightarrow a = T_w$$

$$BC2: At\ z = \delta: T = T_s$$

$$\rightarrow T_s = T_w + b\delta + c\delta^2$$

$$BC3: At\ z = \delta: \frac{dT}{dz} = 0$$

$$\rightarrow b = -2c\delta$$

$$T_s = T_w + -2c\delta^2 + c\delta^2$$

$$c = \frac{T_w - T_s}{\delta^2}$$

$$b = \frac{2(T_s - T_w)}{\delta}$$

$$T = T_w + \frac{2(T_s - T_w)}{\delta} z + \frac{(T_w - T_s)}{\delta^2} z^2$$

Deduction of average temperature for parabolic temperature profile and parabolic velocity profile

$$T_{ave} = \frac{\int_0^{\delta} uTdz}{\int_0^{\delta} udz}$$

$$u = \frac{r\omega^2\rho}{\mu}(z\delta - \frac{z^2}{2})$$

$$T = T_w + \frac{2(T_s - T_w)}{\delta}z + \frac{(T_w - T_s)}{\delta^2}z^2$$

$$T_{ave} = \frac{\int_0^{\delta}\left(\frac{r\omega^2\rho}{\mu}\left(z\delta - \frac{z^2}{2}\right)\right)\left(T_w + \frac{2(T_s - T_w)}{\delta}z + \frac{(T_w - T_s)}{\delta^2}z^2\right)dz}{\int_0^{\delta}\frac{r\omega^2\rho}{\mu}(z\delta - \frac{z^2}{2})dz}$$

$$= \frac{\int_0^{\delta}\left(T_w z\delta - \frac{T_w z^2}{2} + 2T_s z^2 - 2T_w z^2 - 2\frac{T_s z^3}{\delta} + 2\frac{T_w z^3}{\delta} - \frac{T_w z^4}{2\delta^2} + \frac{T_s z^4}{2\delta^2}\right)dz}{\frac{\delta^3}{2} - \frac{\delta^3}{6}}$$

$$= \frac{3}{\delta^3}\left(+\frac{1}{15}\delta^3 T_w + \frac{4}{15}\delta^3 T_s\right)$$

$$T_{ave} = \frac{1}{5}T_w + \frac{4}{5}T_S$$

Deduction of heat transfer coefficient:

The surface heat flux, given by Fourier's law, is equal to convective heat flux through liquid film.

Surface heat flux:

$$q''_{Fourier} = -k\frac{dT}{dz}\Big|_{z=0} = \frac{-2k(T_s - T_w)}{\delta}$$

Convective heat flux:

$$q''_{Conv} = h(T_w - T_{ave}) = h\left(\frac{4}{5}T_w - \frac{4}{5}T_s\right)$$

Since heat transfer rates must be equal:

$$q''_{Fourier} = q''_{Conv}$$

$$\frac{-2k(T_s - T_w)}{\delta} = h\left(\frac{4}{5}T_w - \frac{4}{5}T_s\right)$$

$$h = \frac{5}{2}\frac{k}{\delta}$$

Appendix III: Derivation of temperature at the gas-liquid interface for spinning disk absorber

The temperature at the gas-liquid interface can be derived from an energy balance. Kirby describes the procedure for the absorption of water vapor into aqueous lithium bromide flowing over a horizontal tube [156]. The equations can be changed to describe the flow over a spinning disk, which is done here.

The energy balance is given by:

$$\Delta\dot{m}(h_v + h_{mix}) = k\frac{\partial T}{\partial z}(2\Pi r \cdot dr)$$

For Δ and dr $\rightarrow$ 0

$$\frac{\partial\dot{m}}{\partial r} = \frac{\partial T}{\partial z}\frac{k2\Pi r}{(h_v + h_{mix})}$$

If the temperature profile is assumed to be linear, it is given by

$$T = T_w + \frac{(T_s - T_w)}{\delta} z$$

$$\frac{\partial T}{\partial z} = \frac{(T_s - T_w)}{\delta}$$

Average temperature is given by:

$$T_{ave} = \frac{3}{8} T_w + \frac{5}{8} T_s$$

$$T_w = \frac{8}{3} T_{ave} - \frac{5}{3} T_s$$

Such that:

$$\frac{\partial T}{\partial z} = \frac{(T_s - T_{ave})}{\frac{3}{8}\delta}$$

And

$$\frac{\partial \dot{m}}{\partial r} = \frac{(T_s - T_{ave})}{\frac{3}{8}\delta} \frac{k2\Pi r}{(h_v + h_{mix})}$$

Such that

$$T_s = \frac{3}{8} \frac{\partial \dot{m}}{\partial r} \delta \frac{(h_v + h_{mix})}{k2\Pi r} + T_{ave}$$

This approach is not valid with a parabolic temperature profile, where $\partial T/\partial z = 0$ at the interface.

Appendix IV: Derivation of governing equation for heat transfer from energy balance

Energy balance:

$$\dot{m}_{sol}h_{sol} + \dot{m}_v h_v = (\dot{m}_{sol} + d\dot{m}_{sol})(h_{sol} + dh_{sol}) + U(T_{sol} - T_{cw})dA$$

Combined with

$$dA=2\pi r dr$$

And

$$\dot{m}_v = d\dot{m}_{sol}$$

Reduces to

$$d\dot{m}_{sol}h_v = d\dot{m}_{sol}h_{sol} + dh_{sol}\dot{m}_{sol} + dh_{sol}d\dot{m}_{sol} + U(T_{sol} - T_{cw})2\pi r dr$$

And under negligence of the second order term further to

$$d\dot{m}_{sol}h_v = d\dot{m}_{sol}h_{sol} + dh_{sol}\dot{m}_{sol} + U(T_{sol} - T_{cw})2\pi r dr$$

Now we use the differential of specific enthalpy

$$dh_{sol} = \frac{\partial h_{sol}}{\partial T_{sol}}\Big|_{x_{sol}} dT_{sol} + \frac{\partial h_{sol}}{\partial x_{sol}}\Big|_{T_{sol}} dx_{sol}$$

Into which dx_{sol} is substituted

$$dx_{sol} = -\frac{d\dot{m}_{sol}}{\dot{m}_{sol}} x_{sol}$$

$$dh_{sol} = \frac{\partial h_{sol}}{\partial T_{sol}}\Big|_{x_{sol}} dT_{sol} - \frac{\partial h_{sol}}{\partial x_{sol}}\Big|_{T_{sol}} \frac{d\dot{m}_{sol}}{\dot{m}_{sol}} x_{sol}$$

To yield

$$d\dot{m}_{sol}h_v = d\dot{m}_{sol}h_{sol} + \dot{m}_{sol}\frac{\partial h_{sol}}{\partial T_{sol}}\bigg|_{x_{sol}} dT_{sol} - x_{sol}\frac{\partial h_{sol}}{\partial x_{sol}}\bigg|_{T_{sol}} d\dot{m}_{sol}$$

$$+ U(T_{sol} - T_{cw})2\pi r dr$$

And rearranging

$$\left(h_v - h_{sol} + x_{sol}\frac{\partial h_{sol}}{\partial x_{sol}}\bigg|_{T_{sol}}\right)\frac{d\dot{m}_{sol}}{dr} - U(T_{sol} - T_{cw})2\pi r = \dot{m}_{sol}\frac{\partial h_{sol}}{\partial T_{sol}}\bigg|_{x_{sol}}\frac{dT_{sol}}{dr}$$

Bibliography

[1] Forman, C., Muritala, I. K., Pardemann, R., and Meyer, B., 2016, "Estimating the global waste heat potential," Renew. Sustain. Energy Rev., **57**.

[2] Lawrence Livermore National Laboratory, 2018, U.S. Energy Flow Chart 2017.

[3] U.S. Energy Information Administration, 2016, Annual Energy Outlook 2016.

[4] International Energy Agency, "Mexico: Indicators for 2014" [Online]. Available: https://www.iea.org/statistics/statisticssearch/report/?country=Mexico&product=indicators.

[5] OECD/IEA, 2018, The Future of Cooling - Opportunities for energy-efficient air conditioning.

[6] United States Department of Energy, 2017, Combined Heat and Power Technology Fact Sheet Series.

[7] U.S. Department of Energy, 2016, Combined Heat and Power (CHP) Technical Potential in the United States.

[8] York / Johnson Controls, 2017, "Datasheet: York® YHAU-CL-DXS Single-Effect Double Lift Hot Water Absorption Chillers."

[9] Killion, J. D., and Garimella, S., 2003, "A Review of Experimental Investigations of Absorption of Water Vapor in Liquid Films Falling Over Horizontal Tubes," HVAC&R Res., **9**(2), pp. 111–136.

[10] Beutler, A., Hoffman, L., Ziegler, F., Alefeld, G., Gommed, K., Grossman, G., and Shavit, A., 1996, "Expertmental Investigation of Heat and Mass Transfer in Film Absorption on Horizontal and Vertical Tubes," International Ab-Sorption Heat Pump Conference, pp. 409–419.

[11] Jachuck, R. J. J., and Ramshaw, C., 1994, "Process intensification: Heat transfer characteristics of tailored rotating surfaces," Heat Recover. Syst. CHP, **14**(5), pp. 475–491.

[12] Jachuck, R. J., Ramshaw, C., Boodhoo, K., and Dalgleish, J. C., 1997, "Process intensification: the opportunity presented by spinning disc reactor technology," Inst. Chem. Eng. Symp. Ser., (141), pp. 417–424.

[13] Aoune, A., and Ramshaw, C., 1999, "Process intensification: heat and mass transfer characteristics of liquid films on rotating discs," Int. J. Heat Mass Transf., **42**(14), pp. 2543–2556.

[14] Jachuck, R. J. J., and Burns, J. R., 2007, "Spinning Disc Reactor," Encyclopedia of Chemical Processing, S. Lee, ed., Taylor & Francis, pp. 2847–2857.

[15] Boodhoo, K., 2013, "Spinning Disc Reactor for Green Processing and Synthesis," Process Intensification for Green Chemistry, John Wiley & Sons, Ltd, Chichester, UK, pp. 59–90.

[16] Ramshaw, C. (ICI), and Mallinson, R. H. (ICI), 1981, "Mass transfer process," US4283255 A.

[17] Cross, W. T., and Ramshaw, C., 1985, "Centrifugal heat pump," US Patent US4553408 A.
[18] Ramshaw, C., Jachuck, R. J. J., Jones, M., and Henderson, I., 2000, "Rotating surface of revolution reactor with feed and collection mechanisms," Patent US6858189 B1.
[19] Retolaza, X. G., Egaña, U. O., and Rodríguez, J. M. C., 2010, "Rotary Absorption Heat Pump," Patent US 7818977 B2.
[20] Hoffmann, L., Greiter, I., Wagner, A., Weiss, V., and Alefeld, G., 1996, "Experimental Investigation of Heat Transfer in a Horizontal Tube Falling Film Absorber With Aqueous Solutions of Libr With and Without Surfactants," Int.J.Refrig., **19**(5), pp. 331–341.
[21] Andhare, R. S., Shooshtari, A., Dessiatoun, S. V., and Ohadi, M. M., 2016, "Heat transfer and pressure drop characteristics of a flat plate manifold microchannel heat exchanger in counter flow configuration," Appl. Therm. Eng., **96**, pp. 178–189.
[22] Arie, M. A., Shooshtari, A. H., Dessiatoun, S. V., Al-Hajri, E., and Ohadi, M. M., 2015, "Numerical modeling and thermal optimization of a single-phase flow manifold-microchannel plate heat exchanger," Int. J. Heat Mass Transf., **81**, pp. 478–489.
[23] Herold, K. E., Radermacher, R., and Klein, S. A., 2016, Absorption Chillers and Heat Pumps, CRC Press.
[24] Herold, K. E., Radermacher, R., and Klein, S. A., 1996, Absorption Chillers and Heat Pumps, CRC Press, Boca Raton, FL.
[25] Fujita, T., 1993, "Falling liquid films in absorption machines," Int. J. Refrig., **16**(4), pp. 282–294.
[26] Yu, D., Chung, J., and Moghaddam, S., 2012, "Parametric study of water vapor absorption into a constrained thin film of lithium bromide solution," Int. J. Heat Mass Transf., **55**(21–22), pp. 5687–5695.
[27] Killion, J. D., and Garimella, S., 2001, "A critical review of models of coupled heat and mass transfer in falling-film absorption," Int. J. Refrig., **24**(8), pp. 755–797.
[28] Killion, J. D., and Garimella, S., 2004, "Simulation of Pendant Droplets and Falling Films in Horizontal Tube Absorbers," J. Heat Transfer, **126**(6), p. 1003.
[29] Nomura, T., Nishimura, N., Wei, S., Yamaguchi, S., and Kawakami, R., 1993, "Heat and mass transfer mechanism in the absorber of water/LiBr conventional absorption refrigerator: Experimental examination by visualized model," International Absorption Heat Pump Conference vol 31, AES, New York, pp. 203–208.
[30] Jeong, S., and Garimella, S., 2002, "Falling-film and droplet mode heat and mass transfer in a horizontal tube LiBr/water absorber," Int. J. Heat Mass Transf., **45**(7), pp. 1445–1458.
[31] Sasaki, N., Nosetani, T., Furukawa, M., and Kaneko, T., 1995, "Enhanced Heat Transfer Tubes for Film Absorbers of Absorption Chillers/Heaters," HTD-Vol.

316, Proceedings of the 30th 1995 National Heat Transfer Conference - Volume 14, ASME, Portland, Oregon, pp. 91–97.
[32] Atchley, J. A., Perez-Blanco, H., Kirby, M. J., and Miller, W. A., 1998, Final Report - An Experimental and Analytical Study of Advanced Surfaces for Absorption Chiller Absorbers, Gas Reseach Institute / Oak Ridge National Laboratory, Oak Ridge, Tennessee, U.S.A.
[33] York / Johnson Controls, "YIA Single-Effect Absorption Chillers Steam And Hot Water Chillers," Datasheet / Form 155.16-EG3 [Online]. Available: http://www.johnsoncontrols.com/buildings/hvac-equipment/chillers/yia-water-cooled-single-stage-absorption-chiller. [Accessed: 11-Apr-2018].
[34] Bredow, D., Jain, P., Wohlfeil, A., and Ziegler, F., 2008, "Heat and mass transfer characteristics of a horizontal tube absorber in a semi-commercial absorption chiller," Int. J. Refrig., **31**(7), pp. 1273–1281.
[35] Kaynakli, O., 2008, "The first and second law analysis of a lithium bromide/water coil absorber," Energy, **33**(5), pp. 804–816.
[36] Cosenza, F., and Vliet, G. C., 1990, "Absorption in Falling Water/Libr Films on Horizontal Tubes," ASHRAE Trans., **96**(1), pp. 693–701.
[37] Lee, S. K., and Nagasaki, T., 1991, "Water vapor absorption enhancement in LiBr/H2O films falling on horizontal tubes," Exp. Heat Transf., **4**(4), pp. 331–342.
[38] Lu, Z., Li, D., Li, S., and Yu-Chi, B., 1996, "A Semi-Empirical Model of the Falling Film Absorption outside Horizontal Tubes," International Absorption Heat Pump Conference, Montreal, Quebec, Canada, pp. 473–480.
[39] Greiter, I., Wagner, A., Weiss, V., and Alefeld, G., 1993, "Experimental Investigation of Heat and Mass Transfer in a Horizontal-Tube Falling-Film Absorber with Aqueous Solutions," International Absorption Heat Pump Conference, The Advanced Energy Systems Division, ASME, pp. 225–232.
[40] Matsuda, A., Choi, K. ., Hada, K., and Kawamura, T., 1994, "Effect of pressure and concentration on performance of a vertical falling-film type of absorber and generator using lithium bromide aqueous solutions," Int. J. Refrig., **17**(8), pp. 538–542.
[41] Miller, W. A., and Keyhani, M., 1999, "The experimental analysis of local heat and mass transfer data for vertical falling film absorption," AES-Vol.39, Proceedings of the ASME Advanced Energy Systems Division.
[42] Miller, W. A., and Perez-Blanco, H., 1994, "Vertical-tube aqueous LiBr falling film absorption using advanced surfaces," International Absorption Heat Pump Conference, pp. 185–202.
[43] Kyung, I.-S., and Herold, K. E., 2002, "Performance of Horizontal Smooth Tube Absorber With and Without 2-Ethyl-Hexanol," J. Heat Transfer, **124**(1), p. 177.
[44] Medrano, M., Bourouis, M., and Coronas, A., 2002, "Absorption of water vapour in the falling film of water–lithium bromide inside a vertical tube at air-cooling thermal conditions," Int. J. Therm. Sci., **41**(9), pp. 891–898.
[45] Islam, M. R., 2008, "Absorption process of a falling film on a tubular absorber:

An experimental and numerical study," Appl. Therm. Eng., **28**(11–12), pp. 1386–1394.
[46] Sun, J., Fu, L., Zhang, S., and Hou, W., 2010, "A mathematical model with experiments of single effect absorption heat pump using LiBr–H2O," Appl. Therm. Eng., **30**(17–18), pp. 2753–2762.
[47] Fu, L. S. J., and Shigang, Z., 2011, "Experimental study on vertical vapor absorption into LiBr solution with and without additive," Appl. Therm. Eng., **31**(14–15), pp. 2850–2854.
[48] Raisul Islam, M., Wijeysundera, N. ., and Ho, J. ., 2003, "Performance study of a falling-film absorber with a film-inverting configuration," Int. J. Refrig., **26**(8), pp. 909–917.
[49] Yoon, J.-I., Kwon, O.-K., Bansal, P. K., Moon, C.-G., and Lee, H.-S., 2006, "Heat and mass transfer characteristics of a small helical absorber," Appl. Therm. Eng., **26**(2–3), pp. 186–192.
[50] Yoon, J.-I., Phan, T. T., Moon, C.-G., Lee, H.-S., and Jeong, S.-K., 2008, "Heat and mass transfer characteristics of a horizontal tube falling film absorber with small diameter tubes," Heat Mass Transf., **44**(4), pp. 437–444.
[51] Park, C. W., Kim, S. S., Cho, H. C., and Kang, T. Y., 2003, "Experimental correlation of falling film absorption heat transfer on micro-scale hatched tubes," Int. J. Refrig., **26**(7), pp. 758–763.
[52] Miller, W. A., and Keyhani, M., 1999, "The Correlation of Coupled Heat and Mass Transfer Experimental Data for Vertical Falling Film Absorption," AES-Vol. 39, Proceedings of the ASME Advanced Energy Systems Division, pp. 177–187.
[53] Deng, S. M., and Ma, W. B., 1999, "Experimental studies on the characteristics of an absorber using LiBr/H2O solution as working fluid," Int. J. Refrig., **22**(4), pp. 293–301.
[54] Castro, J., Oliva, A., Perez-Segarra, C. D., and Cadafalch, J., 2007, "Evaluation of a Small Capacity, Hot Water Driven, Air-Cooled H2O-LiBr Absorption Machine," HVAC&R Res., **13**(1), pp. 59–75.
[55] Kulankara, S., and Herold, K., 2000, "Theory of Heat/Mass Transfer Additives in Absorption Chillers," HVAC&R Res., **6**(4), pp. 369–380.
[56] Ali, A. H. H., 2010, "Design of a compact absorber with a hydrophobic membrane contactor at the liquid–vapor interface for lithium bromide–water absorption chillers," Appl. Energy, **87**(4), pp. 1112–1121.
[57] Ali, A. H. H., and Schwerdt, P., 2009, "Characteristics of the membrane utilized in a compact absorber for lithium bromide–water absorption chillers," Int. J. Refrig., **32**(8), pp. 1886–1896.
[58] Nasr Isfahani, R., and Moghaddam, S., 2013, "Absorption characteristics of lithium bromide (LiBr) solution constrained by superhydrophobic nanofibrous structures," Int. J. Heat Mass Transf., **63**, pp. 82–90.
[59] Isfahani, R. N., Bigham, S., Mortazavi, M., Wei, X., and Moghaddam, S., 2015, "Impact of micromixing on performance of a membrane-based absorber,"

Energy, **90**, pp. 997–1004.
[60] Bigham, S., Yu, D., Chugh, D., and Moghaddam, S., 2014, "Moving beyond the limits of mass transport in liquid absorbent microfilms through the implementation of surface-induced vortices," Energy, **65**, pp. 621–630.
[61] Michel, B., Le Pierrès, N., and Stutz, B., 2017, "Performances of grooved plates falling film absorber," Energy, **138**, pp. 103–117.
[62] Mortazavi, M., Nasr Isfahani, R., Bigham, S., and Moghaddam, S., 2015, "Absorption characteristics of falling film LiBr (lithium bromide) solution over a finned structure," Energy, **87**, pp. 270–278.
[63] Tsai, B.-B., and Perez-Blanco, H., 1998, "Limits of mass transfer enhancement in lithium bromide-water absorbers by active techniques," Int. J. Heat Mass Transf., **41**(15), pp. 2409–2416.
[64] Tsuda, H., and Perez-Blanco, H., 2001, "An experimental study of a vibrating screen as means of absorption enhancement," Int. J. Heat Mass Transf., **44**(21), pp. 4087–4094.
[65] Ryan, W. A., 1993, "Water absorption in an adiabatic spray of aqueous lithium bromide solution," AES-VoI. 31, International Absorption Heat Pump Conference ASME 1993, pp. 155–162.
[66] Warnakulasuriya, F. S. K., and Worek, W. M., 2006, "Adiabatic water absorption properties of an aqueous absorbent at very low pressures in a spray absorber," Int. J. Heat Mass Transf., **49**(9–10), pp. 1592–1602.
[67] González-Gil, A., Izquierdo, M., Marcos, J. D., and Palacios, E., 2012, "New flat-fan sheets adiabatic absorber for direct air-cooled LiBr/H2O absorption machines: Simulation, parametric study and experimental results," Appl. Energy, **98**, pp. 162–173.
[68] Palacios, E., Izquierdo, M., Lizarte, R., and Marcos, J. D., 2009, "Lithium bromide absorption machines: Pressure drop and mass transfer in solutions conical sheets," Energy Convers. Manag., **50**(7), pp. 1802–1809.
[69] Izquierdo, M., Marcos, J. D., Palacios, M. E., and Gonzalez-Gil, A., 2012, "Experimental evaluation of a low-power direct air-cooled double-effect LiBr-H2O absorption prototype," Energy, **37**(1), pp. 737–748.
[70] Burns, J. R., Ramshaw, C., and Jachuck, R. J., 2003, "Measurement of liquid film thickness and the determination of spin-up radius on a rotating disc using an electrical resistance technique," Chem. Eng. Sci., **58**(11), pp. 2245–2253.
[71] Buhtz, E., 1928, "Verfahren und Vorrichtung zur Durchfuehrung chemischer Reaktionen," Patent DE000000459977 A.
[72] Ramshaw, C., and Winnington, T. L., 1988, "An Intensified Absorption Heat Pump," Proc. Inst. Refrig., **85**, pp. 26–31.
[73] Branson, T., Lorton, R., Winnington, T., Gorrixategi, X., Green, R. J., Sanz Saiz, J., and Uselton, R., 1996, "Interotex: The Development of a High Lift, High Performance Heat Pump," Proc. 1995 Int. Gas Res. Conf., **2**, pp. 1380–1389.
[74] Lorton, R., Gilchrist, K., and Green, R. J., 2000, "Development and operation of a high performance 10kw absorption chiller," Int. J. Refrig., **23**(8), pp. 572–576.

[75] Gilchrist, K., Lorton, R., and Green, R. J., 2002, "Process intensification applied to an aqueous LiBr rotating absorption chiller with dry heat rejection," Appl. Therm. Eng., **22**(7), pp. 847–854.
[76] Sparrow, E. M., and Gregg, J. L., 1959, "A Theory of Rotating Condensation," J. Heat Transfer, **81**, pp. 113–120.
[77] Nandapurkar, S. S., and Beatty, K. O., 1960, "Condensation on a Rotating Disk," Chem. Eng. Prog. Symp. Ser., **56**(30), pp. 129–137.
[78] Butuzov, and Rifert, 1972, "An Experimental Study of Heat Transfer During Condensation of Steam at a Rotating Disk," Heat Transf. - Sov. Reserach, **4**(6), pp. 150–153.
[79] Al-Baroudi, H. M., and Klein, A. C., 1995, "Experimental simulations and heat transfer parameter measurements of film condensation on a rotating flat plate," Exp. Therm. Fluid Sci., **10**(1), pp. 124–135.
[80] Sparrow, E. M., and Gregg, J. L., 1960, "Mass Transfer, Flow, and Heat Transfer About a Rotating Disk," J. Heat Transfer, **82**(4), p. 294.
[81] Basu, S., and Cetegen, B. M., 2006, "Analysis of Hydrodynamics and Heat Transfer in a Thin Liquid Film Flowing Over a Rotating Disk by the Integral Method," J. Heat Transfer, **128**(3), p. 217.
[82] Quinn, G., and Cetegen, B. M., 2011, "Heat Transfer in an Evaporating Liquid Film Flowing Over a Rotating Disk," Exp. Heat Transf., **24**(1), pp. 88–107.
[83] Oxley, P., Brechtelsbauer, C., Ricard, F., Lewis, N., and Ramshaw, C., 2000, "Evaluation of Spinning Disk Reactor Technology for the Manufacture of Pharmaceuticals," Ind. Eng. Chem. Res., **39**(7), pp. 2175–2182.
[84] Moghbeli, M. R., Mohammadi, S., and Alavi, S. M., 2009, "Bulk free-radical polymerization of styrene on a spinning disc reactor," J. Appl. Polym. Sci., **113**(2), pp. 709–715.
[85] Boodhoo, K. V. K., Dunk, W. A. E., Vicevic, M., Jachuck, R. J., Sage, V., Macquarrie, D. J., and Clark, J. H., 2006, "Classical cationic polymerization of styrene in a spinning disc reactor using silica-supported BF3 catalyst," J. Appl. Polym. Sci., **101**(1), pp. 8–19.
[86] Burns, J. R., and Henderson, I., 2007, "Spinning Disc Reactor with Enhanced Spreader Plate Features," Patent US 2007/0297957 A1.
[87] Thomas, S., Hankey, W., Faghri, A., and Swanson, T., 1990, "One-Dimensional Analysis of the Hydrodynamic and Thermal Characteristics of Thin Film Flows Including the Hydraulic Jump and Rotation," J. Heat Transfer, **112**(3), p. 728.
[88] Rahman, M. M., and Faghri, A., 1992, "Numerical simulation of fluid flow and heat transfer in a thin liquid film over a rotating disk," Int. J. Heat Mass Transf., **35**(6), pp. 1441–1453.
[89] Rahman, M. M., and Faghri, A., 1993, "Gas absorption and solid dissolution in a thin liquid film on a rotating disk," Int. J. Heat Mass Transf., **36**(1), pp. 189–199.
[90] Ozar, B., Cetegen, B. M., and Faghri, A., 2004, "Experiments on Heat Transfer in a Thin Liquid Film Flowing Over a Rotating Disk," J. Heat Transfer, **126**(2),

p. 184.
[91] Rice, J., Faghri, A., and Cetegen, B., 2005, "Analysis of a free surface film from a controlled liquid impinging jet over a rotating disk including conjugate effects, with and without evaporation," Int. J. Heat Mass Transf., **48**(25), pp. 5192–5204.
[92] Zaltash, A., Petrov, A., Linkous, R., Vineyard, E., Goodnack, D., and Egilegor, B., 2007, "Performance Evaluation of a 4.5 kW (1.3 Refrigeration Tons) Air-Cooled Lithium Bromide/Water Hot-Water-Fired Absorption Unit," Proceedings of the 2007 ASME International Mechanical Engineering Congress and Exposition (IMECE2007), ASME, Seattle, pp. 197–210.
[93] Izquierdo, M., Lizarte, R., Marcos, J. D., and Gutiérrez, G., 2008, "Air conditioning using an air-cooled single effect lithium bromide absorption chiller: Results of a trial conducted in Madrid in August 2005," Appl. Therm. Eng., **28**(8–9), pp. 1074–1081.
[94] Bergman, T. L., Lavine, A. S., Incropera, F. P., and Dewitt, D. P., 2011, Fundamental of Heat and Mass Transfer, John Wiley & Sons, Ltd.
[95] Nusselt, W., 1916, "Die Oberflaechenkondensation des Wasserdampfes," Z. Ver. Dtsch. Ing., **50**(569–575).
[96] Wood, R. M., and Watts, B. E., 1973, "The flow, heat and mass transfer characteristics of liquid films on rotating discs," Trans. Inst. Chem. Eng., **51**, pp. 315–322.
[97] Woods, W. P., 1995, "The hydrodynamics of thin liquid films flowing over a rotating disc," Ph.D. Thesis, University of Newcastle Upon Tyne.
[98] Hartley, D. E., and Murgatroyd, W., 1964, "Criteria for the break-up of thin liquid layers flowing isothermally over solid surfaces," Int. J. Heat Mass Transf., **7**(9), pp. 1003–1015.
[99] Boodhoo, K. V. K., and Al-Hengari, S. R., 2012, "Micromixing Characteristics in a Small-Scale Spinning Disk Reactor," Chem. Eng. Technol., **35**(7), pp. 1229–1237.
[100] Bell, C., 1975, "The hydrodynamics and heat transfer characteristics of liquid films on a rotating disc," Ph.D. Thesis, University of Newcastle Upon Tyne.
[101] Rauscher, J. W., Kelly, R. E., and Cole, J. D., 1973, "An Asymptotic Solution for the Laminar Flow of a Thin Film on a Rotating Disk," J. Appl. Mech., **40**(1), p. 43.
[102] Mohammadi, S., and Boodhoo, K. V. K., 2012, "Online conductivity measurement of residence time distribution of thin film flow in the spinning disc reactor," Chem. Eng. J., **207**–**208**, pp. 885–894.
[103] Jacobsen, N. C., and Hinrichsen, O., 2012, "Micromixing Efficiency of a Spinning Disk Reactor," Ind. Eng. Chem. Res., **51**(36), pp. 11643–11652.
[104] Sparrow, E. M., and Gregg, J. L., 1960, "The Effect of Vapor Drag on Rotating Condensation," J. Heat Transfer, **82**(1), pp. 71–72.
[105] Espig, H., and Hoyle, R., 1967, "The transfer of heat from condensing steam to a cooled rotating disc," Proc. Inst. Mech. Eng. Conf. Proc. 1967-68, **182**(38), pp. 406–444.

[106] Burns, J. R., and Henderson, I., 2008, “Spinning Disc Reactor with Spiral Passageway for Heat Transfer Fluid,” Patent US 2008/0267843 A1.
[107] Rees, E. L., 1962, “Flow and Heat Transfer of a Rotating Disc,” M.Sc. Swansea University.
[108] Khan, J. R., 1986, “Heat transfer on a rotating surface with and without phase change,” Ph.D. Thesis, University of Newcastle Upon Tyne.
[109] Mikielewicz, J., 2000, “Comments on ‘Process intensification: heat and mass transfer characteristics of liquid films on rotating discs’, A. Aoune and C. Ramshaw,” Int. J. Heat Mass Transf., **43**(15), pp. 2821–2822.
[110] Thomas, S., Faghri, A., and Hankey, W., 1991, “Experimental Analysis and Flow Visualization of a Thin Liquid Film on a Stationary and Rotating Disk,” J. Fluids Eng., **113**(1), p. 73.
[111] Rahman, M. M., and Faghri, A., 1992, “Analysis of heating and evaporation from a liquid film adjacent to a horizontal rotating disk,” Int. J. Heat Mass Transf., **35**(10), pp. 2655–2664.
[112] Ozar, B., Cetegen, B. M., and Faghri, A., 2003, “Experiments on the flow of a thin liquid film over a horizontal stationary and rotating disk surface,” Exp. Fluids, **34**(5), pp. 556–565.
[113] Basu, S., and Cetegen, B. M., 2007, “Effect of Hydraulic Jump on Hydrodynamics and Heat Transfer in a Thin Liquid Film Flowing Over a Rotating Disk Analyzed by Integral Method,” J. Heat Transfer, **129**(5), p. 657.
[114] Watson, E. J., 1964, “The radial spread of a liquid jet over a horizontal plane,” J. Fluid Mech., **20**(03), p. 481.
[115] Webb, B. W., and Ma, C.-F., 1995, “Single-Phase Liquid Jet Impingement Heat Transfer,” Adv. Heat Transf., **26**, pp. 105–217.
[116] Kays, W., Crawford, M., and Weigand, B., 2012, Convective Heat and Mass Transfer, McGraw-Hill.
[117] Coulson, J. M., Richardson, J. F., Backhurst, J. R., and Harker, J. H., 1999, “Volume 1 - Fluid Flow, Heat Transfer and Mass Transfer,” Coulson & Richardson’s Chemical Engineering, Elsevier Butterworth Heinemann.
[118] Bird, R. B., Stewart, W. E., and Lightfoot, E. N., 2005, Transport Phenomena, p. 610-611 & 713-716.
[119] Venkatamaran, R. S., 1966, “Mass Transfer to an Expanding Interface,” Ph.D. Thesis Leeds University.
[120] Lim, S. T., 1980, “Hydrodynamics and mass transfer processes associated with the absorption of oxygen in liquid films flowing across a rotating disc,” Ph.D. Thesis, University of Newcastle Upon Tyne.
[121] Peev, G., Peshev, D., and Nikolova, A., 2007, “Gas absorption in a thin liquid film flow on a horizontal rotating disk,” Heat Mass Transf., **43**(8), pp. 843–848.
[122] Bird, R. B., Stewart, W. E., and Lightfoot, E. N., 2005, Transport Phenomena, p. 558-560.
[123] Higbie, R., 1935, “The rate of absorption of a pure gas into a still liquid during short periods of exposure.,” Trans. Am. Inst. Chem. Eng., **31**, pp. 365–389.

[124] Sisoev, G. M., Matar, O. K., and Lawrence, C. J., 2005, "Gas absorption into a wavy film flowing over a spinning disc," Chem. Eng. Sci., **60**(7), pp. 2051–2060.
[125] Matar, O. K., Sisoev, G. M., and Lawrence, C. J., 2008, "Thin film flow over spinning discs: The effect of surface topography and flow rate modulation," Chem. Eng. Sci., **63**(8), pp. 2225–2232.
[126] Rotartica S.A., "Thermal Solar Line - Datasheet."
[127] Deng, J., Wang, R. Z., and Han, G. Y., 2011, "A review of thermally activated cooling technologies for combined cooling, heating and power systems," Prog. Energy Combust. Sci., **37**(2), pp. 172–203.
[128] Kyung, I., Herold, K. E., and Kang, Y. T., 2007, "Experimental verification of H2O/LiBr absorber bundle performance with smooth horizontal tubes," Int. J. Refrig., **30**(4), pp. 582–590.
[129] Kyung, I., Herold, K. E., and Kang, Y. T., 2007, "Model for absorption of water vapor into aqueous LiBr flowing over a horizontal smooth tube," Int. J. Refrig., **30**(4), pp. 591–600.
[130] Yuan, Z., and Herold, K., 2005, "Thermodynamic Properties of Aqueous Lithium Bromide Using a Multiproperty Free Energy Correlation," HVAC&R Res., **11**(3), pp. 377–393.
[131] Rose, J. W., 2004, "Heat-transfer coefficients, Wilson plots and accuracy of thermal measurements," Exp. Therm. Fluid Sci., **28**(2–3), pp. 77–86.
[132] Taylor, B. N., and Kuyatt, C. E., 1994, NIST Technical Note 1297 (1994 edition) - Guidelines for Evaluating and Expressing the Uncertainty of NIST Measurement Results, Gaithersburg, MD.
[133] Kirby, M. J., and Perez-Blanco, H., 1994, "A design model for horizontal tube water/lithium bromide absorbers," AES-Vol. 32, Heat Pump and Refrigeration Systems Design, Analysis and Applications, ASME, pp. 1–10.
[134] Remec, J., Gjerkes, H., and Gaspersic, B., 1996, "Absorption of Vapour into Liquid Film on Horizontal Tubes," ASHRAE Trans., **102**(1), pp. 973–979.
[135] Harpole, G. M., and Eninger, J. E., 1991, "Micro-channel heat exchanger optimization," 1991 Proceedings, Seventh IEEE Semiconductor Thermal Measurement and Management Symposium, IEEE, pp. 59–63.
[136] Cetegen, E., Dessiatoun, S., and Ohadi, M., 2009, "Multi Objective Optimization of a Force Fed Microchannel Heat Sink," ASME 2009 Second International Conference on Micro/Nanoscale Heat and Mass Transfer, Volume 3, ASME, pp. 93–100.
[137] Ohadi, M. M., Choo, K., Dessiatoun, S., and Cetegen, E., 2013, Next Generation Microchannel Heat Exchangers, Springer New York, New York, NY.
[138] Wolverine MicroCool, "Micro Deformation Technology" [Online]. Available: http://www.microcooling.com/technology/micro-deformation-technology/. [Accessed: 03-Aug-2017].
[139] Abdelaziz, O. A., 2009, "Development of Multi-Scale, Multi-Physics, Analysis Capability and its Application to Novel Heat Exchanger Design and

Optimizaiton," University of Maryland, College Park, MD.
[140] Miller, W. A., and Keyhani, M., 2001, "The Correlation of Simultaneous Heat and Mass Transfer Experimental Data for Aqueous Lithium Bromide Vertical Falling Film Absorption," J. Sol. Energy Eng., **123**(1), p. 30.
[141] Keyvani, M., and Gardner, N. C., 1989, "Operating characteristics of rotating beds," Chem. Eng. Prog., **85**(9), pp. 48–52.
[142] Jeong, S., and Garimella, S., 2005, "Optimal Design of Compact Horizontal Tube LiBr/Water Absorbers," HVAC&R Res. JANUARY, **11**(1).
[143] Patnaik, V., and Perez-Blanco, H., 1996, "A study of absorption enhancement by wavy film flows," Int. J. Heat Fluid Flow, **17**(1), pp. 71–77.
[144] Morioka, I., and Kiyota, M., 1991, "Absorption of Water Vapor into a Wavy Film of an Aqueous Solution of LiBr," JSME Int. journal. Ser. 2, **34**(2), pp. 183–188.
[145] Grossman, G., and Heath, M. T., 1984, "Simultaneous heat and mass transfer in absorption of gases in turbulent liquid films," Int. J. Heat Mass Transf., **27**(12), pp. 2365–2376.
[146] Yüksel, M. ., and Schlünder, E. ., 1987, "Heat and mass transfer in non-isothermal absorption of gases in falling liquid films: Part I: Experimental determination of heat and mass transfer coefficients," Chem. Eng. Process. Process Intensif., **22**(4), pp. 193–202.
[147] Yüksel, M. ., and Schlünder, E. ., 1987, "Heat and mass transfer in non-isothermal absorption of gases in falling liquid films Part II: Theoretical description and numerical calculation of turbulent falling film heat and mass transfer," Chem. Eng. Process. Process Intensif., **22**(4), pp. 203–213.
[148] Patnaik, V., Perez-Blanco, H., and Ryan, W. A., 1993, "A Simple Analytical Model for the Design of Vertical Tube Absorbers," ASHRAE Trans., **99**(2), pp. 69–80.
[149] Grossman, G., 1983, "Simultaneous heat and mass transfer in film absorption under laminar flow," Int. J. Heat Mass Transf., **26**(3), pp. 357–371.
[150] Banasiak, K., and Kozioł, J., 2009, "Mathematical modelling of a LiBr–H2O absorption chiller including two-dimensional distributions of temperature and concentration fields for heat and mass exchangers," Int. J. Therm. Sci., **48**(9), pp. 1755–1764.
[151] Wassenaar, R. H., and Westra, J. J. W., 1992, "Dynamic model of a film absorber with coupled heat and mass transfer," Int. J. Heat Mass Transf., **35**(1), pp. 87–99.
[152] Babadi, F., and Farhanieh, B., 2005, "Characteristics of heat and mass transfer in vapor absorption of falling film flow on a horizontal tube," Int. Commun. Heat Mass Transf., **32**(9), pp. 1253–1265.
[153] Islam, M. A., Miyara, A., and Setoguchi, T., 2009, "Numerical investigation of steam absorption in falling film of LiBr aqueous solution with solitary waves," Int. J. Refrig., **32**(7), pp. 1597–1603.
[154] F-Chart Software LLC, 2018, "Engineering Equation Solver: User manual."

[155] Patterson, M. R., and Perez-Blanco, H., 1988, "Numerical Fits of the Properties of Lithium-Bromide Water Solutions," ASHRAE Trans., **94**(2).
[156] Kirby, M. J., 1995, "A Computer Model of Falling Film Absorption in Horizontal Tube Libr Absorbers," MSc Thesis Pennsylvania State University.
[157] Kim, K. ., Berman, N. ., Chau, D. S. ., and Wood, B. ., 1995, "Absorption of water vapour into falling films of aqueous lithium bromide," Int. J. Refrig., **18**(7), pp. 486–494.
[158] Potnis, S. V., Lenz, T. G., and Dunlop, E. H., 1995, "Measurement of water diffusivity in aqueous lithium bromide and lithium chloride solutions," Chem. Eng. Commun., **139**(1), pp. 41–49.
[159] Zogg, R., and Westphalen, D., 2006, "Developing Air-Cooled LiBr Absorption for Light Commercial Combined Heat and Power Applications," HVAC&R Res., **12**, pp. 731–747.
[160] Wang, K., Abdelaziz, O., Kisari, P., and Vineyard, E. A., 2011, "State-of-the-art review on crystallization control technologies for water/LiBr absorption heat pumps," Int. J. Refrig., **34**(6), pp. 1325–1337.
[161] Wasserscheid, P., and Seiler, M., 2011, "Leveraging Gigawatt Potentials by Smart Heat-Pump Technologies Using Ionic Liquids," ChemSusChem, **4**(4), pp. 459–463.
[162] Chen, W., and Liang, S., 2016, "Thermodynamic analysis of absorption heat transformers using [mmim]DMP/H2O and [mmim]DMP/CH3OH as working fluids," Appl. Therm. Eng., **99**, pp. 846–856.
[163] Römich, C., Merkel, N., Schaber, K., Schubert, T., and Koch, M., 2011, "A Comparison Between Lithiumbromide - Water and Ionic Liquid - Water As Working Solution for Absorption Refrigeration Cycles," Refrigeration for Sustainable Development : 23rd IIR International Congress of Refrigeration, Prague, Czech Republic.
[164] Zhang, X., and Hu, D., 2011, "Performance simulation of the absorption chiller using water and ionic liquid 1-ethyl-3-methylimidazolium dimethylphosphate as the working pair," Appl. Therm. Eng., **31**(16), pp. 3316–3321.
[165] Dong, L., Zheng, D., Nie, N., and Li, Y., 2012, "Performance prediction of absorption refrigeration cycle based on the measurements of vapor pressure and heat capacity of H2O + [DMIM]DMP system," Appl. Energy, **98**, pp. 326–332.
[166] Seiler, M., Kühn, A., Ziegler, F., and Wang, X., 2013, "Sustainable Cooling Strategies Using New Chemical System Solutions," Ind. Eng. Chem. Res., **52**(47), pp. 16519–16546.